Reconstruction of virtual photons from Au+Au collisions at 1.23 GeV/u

TECHNISCHE
UNIVERSITÄT
DARMSTADT

Fachbereich Physik
Institut für Kernphysik

UNIWERSYTET
JAGIELLOŃSKI
W KRAKOWIE

Wydział Fizyki, Astronomii
i Informatyki Stosowanej

Reconstruction of virtual photons from Au+Au collisions at 1.23 GeV/u
Rekonstruktion virtueller Photonen aus Au+Au Stoßen bei 1,23 GeV/u
Rekonstrukcja wirtualnych fotonów w zderzeniach Au+Au przy energii 1,23 GeV/u
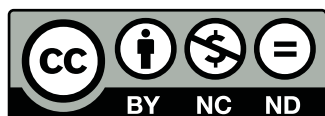
Thesis by M.Sc. Szymon Harabasz from Kraków

1. Supervisor: Prof. Dr. phil. nat. Tetyana Galatyuk
2. Supervisor: Prof. dr hab. Piotr Salabura
1. Referee: Priv.-Doz. Dr. Anton Andronic
2. Referee: Prof. Dr. Bengt Friman

Date of submission: 10.05.2017
Date of defense: 14.06.2017

Darmstadt 2017 — D 17

Erklärung zur Dissertation

Hiermit versichere ich, die vorliegende by ohne Hilfe Dritter nur mit den angegebenen Quellen und Hilfsmitteln angefertigt zu haben. Alle Stellen, die aus Quellen entnommen wurden, sind als solche kenntlich gemacht. Diese Arbeit hat in gleicher oder ähnlicher Form noch keiner Prüfungsbehörde vorgelegen.

Darmstadt, den 10.05.2017

_____

(S. Harabasz)

Oświadczenie

Ja, niżej podpisany Szymon Harabasz, doktorant Wydziału Fizyki, Astronomii i Informatyki Stosowanej Uniwersytetu Jagiellońskiego, oświadczam, że przedłożona przeze mnie rozprawa doktorska pt. „Reconstruction of virtual photons from Au+Au collisions at 1.23 GeV/u" jest oryginalna i przedstawia wyniki badań wykonanych przeze mnie osobiście, pod kierunkiem prof. dra hab. Piotra Salabury i prof. dr phil. nat. Tetyany Galatyuk. Pracę napisałem samodzielnie.

Oświadczam, że moja rozprawa doktorska została opracowana zgodnie z Ustawą o prawie autorskim i prawach pokrewnych z dnia 4 lutego 1994 r. (Dziennik Ustaw 1994 nr 24 poz. 83 wraz z późniejszymi zmianami).

Jestem świadomy, że niezgodność niniejszego oświadczenia z prawdą ujawniona w dowolnym czasie, niezależnie od skutków prawnych wynikających z ww. ustawy, może spowodować unieważnienie stopnia nabytego na podstawie tej rozprawy.

Darmstadt, dnia 10.05.2017

_____

(S. Harabasz)

Abstract

Electromagnetic radiation provides a valuable test to understand the macroscopic properties of strongly interacting matter under extreme conditions. Photons and dileptons themselves are not subject to the strong force, hence their mean-free path is much longer than the size of the hot and dense fireball formed in heavy-ion collisions. This allows them to leave the medium without re-scatterings and be the direct messenger of the processes in which they were created.

As a consequence, photon and dilepton spectra contain contributions from all stages of the reaction: first-chance collisions in the pre-equilibrium phase, QGP and hot hadronic gas, and the meson decays after the freeze-out. Already basic properties of the carefully extracted medium component from the virtual photons spectra give rise to non-trivial information. The yield in the low mass region (LMR, above the π^0 and below the vector meson masses) is the proxy of the life-time of the fireball. The slope of the invariant mass distribution is directly related to the medium's temperature, after appropriate extrapolation to full phase space.

In this context, heavy-ion collisions at lowest beam kinetic energies around 1 GeV per nucleon are highly important not only by completing the beam energy scan and providing a baseline for studies of deconfinement and chiral symmetry restoration. Reactions at these energies explore regions of the QCD phase diagram of highest possible baryon chemical potential and reach conditions, where the quark condensate drops significantly.

This thesis presents data analysis of dilepton excess radiation in Au+Au at $E_{\text{beam}} = 1.23A$ GeV experiment performed by HADES. This starts with an overview of QCD symmetries and its thermodynamics properties, that are essential in situating the current work in the broad context of big questions of contemporary nuclear and particle physics: origin of hadron masses and quark confinement. It is followed by a discussion of details of experimental setup that are necessary to understand the data analysis.

The data analysis is described in the main part of the manuscript. This starts with tools and techniques that have been used. Special effort has been made to "demystify" the usage of a neural network for single lepton identification. An excellent performance in terms of lepton sample purity has been proven. The efficiency is not highest possible and a more sensitive algorithm of reconstructing Cherenkov signal has do be adopted for improvement. The current analysis refrains from this and uses well tested legacy algorithms, the same as in previously published data, in order to provide a clean baseline and cross-check for other independent Au+Au analyses.

It is not possible to divide all e^+ and e^- in a single event into correlated pairs and combinatorial background has to be estimated on a statistical way. The existing formalism which allows to do this with the help of same-event like-sign spectra was slightly extended to introduce in a mathematically correct way a factor which takes into account asymmetry between average probability to reconstruct like-sign and opposite-sign lepton pairs (here called k-factor). It is also argued, that this factor accounts not only for pure geometrical acceptance, but also for track reconstruction efficiency, at least as long as the definitions of "acceptance" and "efficiency" commonly used in HADES are adopted.

Reconstructed signal has to be corrected for efficiency in order to be compared with other measurements and theory predictions. This is done for the first time in HADES by multiplying the signal after background subtraction by a factor depending on the same pair kinematic variable as the signal spectrum. It is argued that this is the best solution considering finite statistics of the April 2012 run. The self-consistency of this correction and resulting systematic error are carefully studied. In the same way extrapolation to full phase-space is performed and as the model used for this is dominated by two-body kinematics, this should be valid at least for extracted medium radiation.

After all the analysis steps spectra are examined in order to make physical statements. The model independent ones come especially from comparison with other experiments. Despite the troubles with statistics, the non-linear scaling with $\langle A_{\text{part}} \rangle$ of the excess yield above conventional hadronic cocktail or NN reference, deduced from previous HADES measurements, has been observed. The point at $\sqrt{s_{NN}} = 2.41$ GeV could be included in beam energy scan of Au+Au collisions. Almost exponential shape of the

dilepton invariant mass spectrum signals radiation from a thermalized source. Average temperature of the medium emitting dileptons was directly extracted from the fit to the invariant mass.

Comparison to model calculations of HSD and Rapp-Wambach spectral function showed their consistency with the data (in spite of small caveats) in various observables. This allowed to extend the set of physical conclusions with a few of model-dependent ones. In particular, lifetime of the fireball, average baryochemical potential and radial flow of dilepton source could be estimated. In spite of different mathematical descriptions, the general physical picture of virtual photon emissivity enhanced by coupling to baryonic resonances is rather clear. The resonance regeneration results then in stronger than linear $\langle A_{\mathrm{part}} \rangle$ dependence.

Kurzfassung

Elektromagnetische Strahlung ermöglicht einen wertvollen Test für das Verständnis der makroskopischen Eigenschaften von stark wechselwirkender Materie unter extremen Bedingungen. Photonen und Dileptonen sind der starken Kraft nicht unterworfen, sodass ihre mittlere freie Weglänge viel größer ist als die Abmessungen des heißen und Dichten Feuerballs, der in Schwerionenkollisionen gebildet wird. Dies macht es ihnen möglich das Medium ohne weitere Wechselwirkungen zu verlassen und als direkte Boten für die Prozesse zu fungieren, in denen sie produziert wurden.

Daher setzten sich Photonen- und Dileptonenspektren aus Beiträgen zusammen, die aus allen Stadien der Reaktion stammen: Von ersten Nukleon-Nukleon Kollisionen aus der Phase bevor die Materie das (thermische) Gleichgewicht erreicht, aus dem Quark-Gluon-Plasma (QGP) und dem heißen Hadronengas, und von Zerfällen von Mesonen nach dem Ausfrieren. Grundlegende Eigenschaften der sorgfältig zu extrahierenden Medium-Komponente der Spektren virtueller Photonen liefern bereits nicht-triviale Informationen. Die Menge an Dileptonen mit kleinen Massen oberhalb der π^0-Masse und unterhalb der Masse der Vektormesonen (engl. Low Mass Range, LMR) dient zur Messung der Lebensdauer des Mediums. Zudem besteht ein direkter Zusammenhang zwischen der Steigung des invarianten Massenspektrums und der Temperatur des Mediums, nachdem eine geeignete Extrapolation der gemessenen Verteilung zum vollen Phasenraum vorgenommen wurde.

Schwerionenkollisionen bei niedrigsten kinetischen Energien von etwa 1 GeV pro Nukleon sind in diesem Kontext von außerordentlich großer Bedeutung. Zum einen wird der Strahlenergie-Scan vervollständigt, zum anderen wird eine Basislinie für weiteren Studien zur Wiederherstellung der chiralen Symmetrie und des Quark-Deconfinement etabliert. Reaktionen bei diesen Energien sondieren die Region des QCD-Phasendiagramms mit dem höchsten möglichen baryochemischem Potential und erreichen Bedingungen, unter denen das Quark-Kondensat bedeutend reduziert wird.

Diese Dissertation stellt die Datenanalyse von Dileptonen in Au+Au Kollisionen bei einer Strahlenergie von $E_{\mathrm{beam}} = 1,23A$ GeV mit dem HADES Experiment vor, die zu Spektren der Dileptonen-Überschussstrahlung führt. Sie beginnt mit einem Überblick über die Symmetrien und die thermodynamischen Eigenschaften der QCD, die für die Platzierung dieser Arbeit in den Kontext großer Fragen der aktuellen Kern- und Teilchenphysik, insbesondere der Herkunft der Hadronenmassen und des Quark-Confinement, notwendig sind. Darauf folgt eine Diskussion der Details des experimentellen Aufbaus, die für das Verständnis der Datenanalyse benötigt werden.

Die Analyse der Daten wird im Hauptteil beschrieben und beginnt mit den verwendeten Hilfsmitteln und Techniken. Ein besonderes Augenmerk liegt hierbei auf der Entmystifizierung der Nutzung eines neuronalen Netzwerks (oftmals als „Black Box" angesehen) für die Leptonenidentifikation. Dessen exzellente Leistung wird in Form der Reinheit der Leptonenauswahl nachgewiesen. Verglichen mit der Methode zur Identifikation von Leptonen, die bereits für frühere Publikationen benutzt wurde und auch in dieser Arbeit zum Einsatz kommt, kann die Detektions-Effizienz für Elektronen mit Hilfe eines empfindlicheren Rekonstruktionsalgorithmus für Cherenkov-Licht weiter erhöht werden. In dieser Analyse wird hierauf jedoch verzichtet, sodass die vorliegenden Resultate als Basislinie und Test für andere unabhängige Au+Au Analysen dient.

Da es nicht möglich ist alle produzierten e+ und e- eines Ereignisses in korrelierte Paare aufzuteilen, muss der kombinatorische Untergrund auf statistischem Wege abgeschätzt werden. Der dazu bereits existierende Formalismus, in dessen Rahmen der kombinatorische Untergrund durch Paare mit gleicher Ladung beschrieben wird, wurde hierzu um einen Faktor erweitert. Diese Korrektur berücksichtigt in mathematisch korrekter Form die Asymmetrie in der Rekonstruktionswahrscheinlichkeit für Paare gleicher und unterschiedlicher Ladung (hier kurz k genannt). Es wird des Weiteren diskutiert, dass in diesen Korrekturfaktor nicht nur die reine geometrische Akzeptanz einfließt, sondern er auch die Rekonstruktionseffizienz der Teilchenspuren innerhalb des Detektors berücksichtigt.

Zum Vergleich mit anderen Messungen und theoretischen Vorhersagen muss das gewonnene Signal noch um die Effizienz korrigiert werden. Dies wird zum ersten Mal in HADES durch die Multiplikation

des Signals, nach Subtraktion des Untergrunds, mit einem Faktor durchgeführt, der von der gleichen Variable wie das Signal abhängt. Es wird argumentiert, das dies die beste Lösung hinsichtlich der begrenzten Statistik des April 2012 Runs darstellt. Die Konsistenz dieser Korrektur wird überprüft und der resultierende systematische Fehler sorgfältig abgeschätzt. Auf ähnliche Weise wird die Extrapolation zum vollen Phasen-Raum der Leptonen durchgeführt. Da das hierzu genutzte Modell von Zweikörper-Kinematik dominiert wird, sollte dieser Ansatz zumindest für die extrahierte Strahlung aus dem Medium gültig sein.

Nach diesen Schritten in der Analyse werden die resultierende Spektren auf ihre physikalischen Aussagen untersucht. Modell-unabhängig sind dabei besonders die Vergleiche zu anderen Experimenten. Trotz der Schwierigkeiten mit der limitierten Statistik, kann die nicht-lineare $\langle A_{\text{part}} \rangle$ Skalierung der Überschussstrahlung über dem konventionellen hadronischen Cocktail oder NN-Referenzspektren aus vorherigen HADES-Messungen bestätigt werden. Der Datenpunkt bei $\sqrt{s_{NN}} = 2{,}41$ GeV fügt sich in den Strahlenergie-Scan von Au+Au Kollisionen ein. Der nahezu exponentielle Verlauf des invarianten Massenspektrums von Dileptonen signalisiert darüber hinaus den thermischen Ursprung der Strahlung. Die mittlere Temperatur des Dileptonen emittierenden Mediums wird durch einen Fit an das invariante Massenspektrum bestimmt.

Der Vergleich mit theoretischen Ergebnissen von HSD und der Rapp-Wambach Spektralfunktion zeigt deren Konsistenz mit den Daten in verschiedenen Variablen (mit kleinen Vorbehalten). Damit kann der Satz an physikalischen Schlussfolgerungen mit Modell-abhängigen Aussagen erweitert werden. Insbesondere die Lebensdauer des Feuerballs, das mittlere baryochemische Potential und der radiale Fluss der Dileptonenquelle kann abgeschätzt werden. Trotz unterschiedlicher mathematischer Ansätze liefern beide Modelle ein gemeinsames physikalisches Bild: Die Emissivität virtueller Photonen wird durch Wechselwirkungen mit baryonischen Resonanzen erhöht. Die Regeneration der Resonanzen resultiert in einer stärker als linearen Abhängigkeit von $\langle A_{\text{part}} \rangle$.

Streszczenie

Jako że fotony nie oddziałują silnie, ich średnia droga swobodna w obszarze gęstej i gorącej materii (ang. *fireball*) formowanym w zderzeniach ciężkich jonów jest dużo większa niż jego rozmiar. Pozwala im to opuszczać ten ośrodek bez oddziaływań rozpraszania i dostarczać bezpośredniej informacji o procesach, w których powstały. W konsekwencji, widma dileptonów zawierają wkłady z każdego stadium reakcji jądrowej: z wczesnych zderzeń nukleonów przed osiągnięciem równowagi termodynamicznej, z plazmy kwarkowo-gluonowej lub gorącego gazu hadronowego, z rozpadów mezonów po wymrożeniu (ang. *freeze-out*). Już podstawowe własności widm wirtualnych fotonów pozwalają na wyciągnięcie nietrywialnych wniosków. Całkowita liczba dileptonów w obszarze masy niezmienniczej powyżej π^0 (0.14 GeV/c^2) i poniżej mas mezonów wektorowych ($\sim$0.78 GeV/c^2) zależy od czasu życia ośrodka. Nachylenie rozkładu masy jest bezpośrednio związane z temperaturą tegoż ośrodka.

W tym kontekście, zderzenia ciężkich jonów przy najniższych energiach wynoszących około 1 GeV na nukleon są niezwykle ważnie dla pełnego zrozumienia diagramu fazowego silnych oddziaływań oraz przywrócenia symetrii chiralnej, podstawowej symetrii QCD spontanicznie złamanej w próżni. W reakcjach przy tak niskich energiach materia znajduje się w obszarach wykresu fazowego chromodynamiki kwantowej, gdzie potencjał chemiczny barionów jest najwyższy i wartość kondensatu kwarkowego, będącego sygnaturą złamania symetrii chiralnej, ulega znaczącej redukcji.

Niniejsza rozprawa przedstawia analizę danych eksperymentalnych prowadzącą do utworzenia widm dileptonów w zderzeniach Au+Au przy $E_\mathrm{beam} = 1.23A$ GeV, przeprowadzonych przez eksperyment HADES. We wstępie omówiono podstawowe symetrie i własności termodynamiczne chromodynamiki kwantowej, które są istotne dla umieszczenia bieżącej pracy w szerokim kontekście istotnych pytań współczesnej fizyki jądrowej i cząstek elementarnych: pochodzenia mas hadronów i uwięzienia kwarków. Po nim następuje opis szczegółów układu detekcyjnego, niezbędnych do zrozumienia analizy danych.

Sama analiza jest opisana w głównej części manuskryptu. Opis ten rozpoczyna się od użytych narzędzi. Sporo miejsca poświęcono wyjaśnieniu użycia sieci neuronowej do identyfikacji leptonów. Wykazane zostało doskonałe działanie sieci neuronowej przy identyfikacji leptonów z wysoką wydajnością i czystością uzyskanej próbki. W wyniku analizy wskazano na elementy algorytmu identyfikacji leptonów w detektorze RICH które wymagają ulepszeń. Zostało to przeprowadzone w alternatywnej analizie. W dalszej części pracy pozostano przy istniejących, dobrze przetestowanych algorytmach, które były już użyte w analizie poprzednio opublikowanych danych, aby dostarczyć punkt odniesienia dla innych, niezależnych analiz eksperymentu Au+Au.

Podstawowym problem analizy par e^+e^- jest oszacowanie tła kombinatorycznego które nie jest możliwe do rozróżnienia od prawdziwego sygnału pochodzącego od emisji z jednego wierzchołka reakcji. Tło kombinatoryczne musi zostać oszacowane metodami statystycznymi. Istniejący formalizm pozwalający dokonać tego oszacowania za pomocą par leptonów tego samego znaku został nieznacznie rozszerzony, aby w sposób matematycznie poprawny wprowadzić czynnik (oznaczany k) uwzględniający asymetrię między prawdopodobieństwem rekonstrukcji par tego samego i różnego znaku w detektorze. Wykazano, że czynnik ten odnosi się nie tylko do geometrycznej akceptancji detektora, lecz również do wydajności rekonstrukcji śladów cząstek w eksperymencie HADES.

Uzyskany sygnał powinien być poprawiony na wydajność, aby możliwe było porównanie z innymi pomiarami i z przewidywaniami modeli teoretycznych. Po raz pierwszy w eksperymencie HADES, jest to osiągane poprzez przemnożenie rozkładów sygnału pozostałych po odjęciu tła kombinatorycznego przez czynnik korekcyjny zależny od tej samej zmiennej kinematycznej co samo widmo sygnału. Dostarczane są argumenty, że jest to najlepsze możliwe rozwiązanie, biorąc pod uwagę ograniczoną statystykę eksperymentu. Test samo-zgodności tej poprawki i oszacowany za jego pomocą błąd systematyczny zostały starannie zbadane. W ten sam sposób przeprowadzona została ekstrapolacja do pełnego zakresu kąta bryłowego oraz pędów leptonów. Użyta funkcja korekcji została oparta o model uwzględniający specyfikę źródeł dielektronowych emitowanych w reakcji Au+Au.

Otrzymane w wyniku analizy rozkłady są badane w celu wyciągnięcia fizycznych wniosków. Te spośród nich, które są niezależne od modelu wynikają głównie z porównania do innych eksperymentów. Pomimo trudności związanych z ograniczoną statystyką, możliwe było potwierdzenie nieliniowej zależności od $\langle A_{\text{part}} \rangle$ natężenia wirtualnych fotonów powyżej konwencjonalnego „koktajlu" hadronowego lub referencyjnego rozkładu NN, wynikającego z wcześniejszych pomiarów na detektorze HADES. Punkt odpowiadający $\sqrt{s_{NN}} = 2.41$ GeV został dołączony do zależności od energii wiązki w zderzeniach Au+Au. Średnia temperatura ośrodka emitującego dileptony została uzyskana bezpośrednio z dopasowania rozkładu Boltzmanna to widma masy niezmienniczej.

Porównanie przewidywań modelowych HSD oraz funkcji spektralnej mezonu ρ^0 wg. modelu Rappa i Wambacha do danych eksperymentalnych wykazało, że są one (z niewielkimi zastrzeżeniami) zgodne. Uzyskana zgodność pozwoliła na wyznaczenie istotnych parametrów zderzenia takich jak czas życia ośrodka, średni potencjał chemiczny barionów i radialny pływ dileptonów. Pomimo różnic w opisie modeli, uzyskano ogólny obraz emisji wirtualnych fotonów istotnie zwiększonej wskutek sprzężenia do rezonansów barionowych. Regeneracja rezonansów skutkuje zależnością od $\langle A_{\text{part}} \rangle$ silniejszą, niż liniowa.

Contents

List of Figures

List of Tables

1 Strongly interacting matter and its electromagnetic probes

According to the Standard Model of elementary particles and their interactions, there exist four types of fundamental *forces*. Gravitation and electromagnetism are familiar from everyday observation. Microscopically, electromagnetism is described by a quantum field theory – Quantum Electrodynamics (QCD). It is now the most precisely tested theory in physics, among the results that it provides, Lamb shift and anomalous magnetic moment of electron belong to the most famous. Gravitation is described by General Relativity by Einstein. As it can be seen from Table 1.1, it is much weaker than other interactions. Because of this and of the fact, that no satisfactory quantum gravity theory exists, this interaction is of no relevance in microscopic physics and, strictly speaking, is not a part of the Standard Model. Besides gravitation and electromagnetism there are also *weak* and *strong* interactions, which govern the phenomena observed not earlier than in the 20th century in laboratories of nuclear and particle physicists. The names of the last two are derived from their properties shown in Table 1.1.

Interaction	Relative strength	Lifetime [s]
Strong	1	$10^{-22} - 10^{-24}$
Electromagnetic	10^{-2}	$10^{-16} - 10^{-21}$
Weak	10^{-7}	$10^{-7} - 10^{-13}$
Gravity	10^{-39}	

Table 1.1.: Relative strength of the force between two protons in contact interacting by four fundamental forces and lifetimes of hadrons decaying by them. [43, 44]

The weak interaction is responsible e.g. for the β radiation (p $\rightarrow$ n + e$^+$ + ν_e and n $\rightarrow$ p + e$^-$ + $\bar{\nu}_e$, where ν_e is the electron neutrino, a very light particle undergoing only gravity and the weak interaction and $\bar{\nu}_e$ is its antiparticle), decays of pions and muons ($\pi^+ \rightarrow \mu^+ + \nu_\mu$, $\mu^+ \rightarrow$ e$^+ \nu_e + \bar{\nu}_\mu$) or numerous phenomena involving "strange" K-mesons. The weak force is of no relevance to the current work and will not be discussed any further.

The strong force governs the structure of atomic nuclei and their ingredients – hadrons (from Greek $\alpha\delta\rho o\varsigma$, "thick, stout", it is a common name for all particles sensitive to this force). It is described by a quantum field theory called Quantum Chromodynamics (QCD). Basic features of this theory are presented in the following sections.

The Standard Model introduces also classification of known elementary particles, shown in Fig. 1.1. Matter particles are *quarks* and *leptons* ($\lambda\epsilon\pi\tau o\varsigma$ – "thin, fine, small"). Quarks undergo all interactions, leptons do not the strong force, neutrinos are neutral with respect to electromagnetism. All these particles are *fermions* (have spin $s = \pm\frac{1}{2}$ and are subject to Fermi-Dirac quantum statistics) and are subdivided into *generations*, of which three are currently known. Interactions are mediated by *gauge bosons* (they are subject to Bose-Einstein quantum statistics): gluon for strong, photon for electromagnetic, W and Z bosons for weak. Higgs boson is a quantum of the field, coupling to which generates masses of all elementary particles. Its observation [45] is considered as a closure of experimental confirmations of the SM.
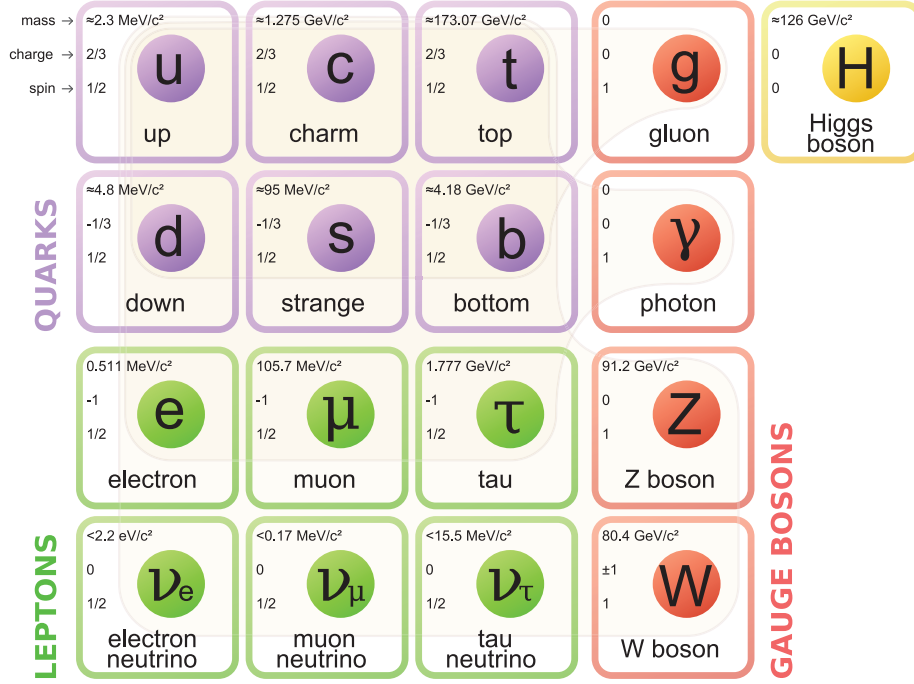
Figure 1.1.: Elementary particles and their basic properties. Note that the mass evaluations of certain particles are from 2008 and more recent can be found in [1]. Figure from `https://commons.wikimedia.org/wiki/File:Standard_Model_of_Elementary_Particles.svg` (accessed December 20th, 2016).

1.1 Quantum chromodynamics primer

It is on purpose, that the name of this theory makes an allusion to the Quantum Electrodynamics (QED). The latter emerges from the requirement, that quantum fields of matter particles are invariant under the phase transformation, that is under the multiplication by $e^{ie\Phi}$. Such transformations build up the $U(1)$ group and the phase invariance is called $U(1)$ symmetry. In the case, that the phase Φ is constant throughout the whole spacetime, the condition is fulfilled automatically, as all the measurable quantities involve the product of the field and its complex conjugate and the transformation multiplies them by $e^{-ie\Phi}e^{+ie\Phi}$. When one, however, allows Φ to vary in the spacetime, the only way to keep the theory invariant is to introduce a field $A(x)$, which transforms as a four-vector under the Lorentz transformation and undergoes the *gauge transformation* $A_\mu(x) \to A_\mu(x) - \partial_\mu\Phi(x)$ (μ here denotes a four-vector component) at the same time, when the matter field is multiplied by the phase factor with the phase $\Phi(x)$ (details can be found e.g. in [46]). Since this is the same as the gauge transformation, which is obeyed by the electromagnetic potentials according to the Maxwell equations, it is natural to identify components of A with electric and magnetic potentials and to understand the interaction with matter, which must be inevitably added to the theory together with the above phase and gauge transformations [1], as the electrodynamics. The constant $e \approx 1.602 \times 10^{-19}$ C, which was present in the phase factor, determines now the coupling of fields to each other and so the strength of their interaction. It is identified with the electric charge of the particle of interest (electron, muon, etc.)

---

[1] One has to redefine also a derivative to make it transform in the same way as the matter field. This must involve adding a new term, that is interpreted as the interaction.

1. Strongly interacting matter and its electromagnetic probes
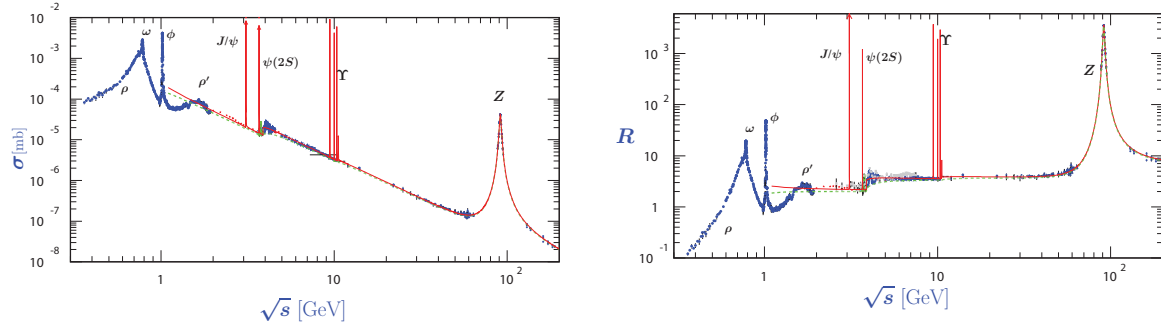
Figure 1.2.: Compilation of the world data for the $e^+e^- \to$ hadrons scattering cross-section as the function of center-of-mass energy $\sqrt{s}$ (left panel) and the ratio of this cross section to the $\sigma(e^+e^- \to \mu^+\mu^-)$ [1].

In the same way, as electromagnetism is a necessity, when the spacetime-dependent (*local*) $U(1)$ symmetry is required, QCD comes from the requirement to have local $SU(3)$ symmetry. Transformations of this group have the following form

$$g(x) = \exp(ig \sum_{a=1}^{8} T_a \Phi^a), \tag{1.1}$$

where $T_a = \lambda_a/2$ (λ are Gell-Mann matrices) are eight *generators* of the group, Φ^a are eight corresponding parameters, and g is the gauge coupling parameter analogous to the electric charge in QED. Since the transformation is a 3×3 matrix, there have to be 3 fields arranged in a column vector to be transformed by it. The 3 base vectors are labeled by "colors" ("red", "green" and "blue"), that are charges associated with the $SU(3)$ symmetry. There are also anti-charges ("anti-red", "anti-green" and "anti-blue") in the same way as there are two opposite charges in electromagnetism. This goes in line with the fact, that all observed hadrons are either bound states of three fields qqq, where each of them have different color charge, bound states of three fields of antiparticles $\bar{q}\bar{q}\bar{q}$ with different anti-colors or bound state of particle and antiparticle $q\bar{q}$, with corresponding colors ("red"-"anti-red", "green"-"anti-green" or "blue"-"anti-blue"). One can shortly say, that all hadrons are "white", i.e. color-neutral. In July 2015, the LHCb Collaboration reported a discovery of two pentaquark states consisting of $uudc\bar{c}$ [47]. Having the quark content of a baryon and a meson it is still "white"'.

The elementary fields q are called *quarks* and they are fermions of spin 1/2. Until now, six types (*flavors*) of them have been established. They are listed in Fig. 1.1. It is noticeable, that u and d quarks have very similar masses. The mass of s quark is also sufficiently close, that it is possible to define another $SU(3)$ group describing symmetry between different quark flavors. This symmetry is only approximate, but it has allowed to describe quite precisely spectra of hadrons containing u, d and s. This symmetry is global, so there are no gauge field associated with it. The quark model is corroborated by the cross section for $e^+e^- \to$ hadrons scattering, as shown in Fig. 1.2. The low energy range, up to about 1.5 GeV/c^2 is dominated by the resonant structures, which will be of interest later in this chapter. At higher energies one can observe steps in the continuum under the narrow resonant peaks. This steps can be understood already in the "naive quark model", that predicts

$$R = \frac{\sigma(e^+e^- \to \text{hadrons})}{\sigma(e^+e^- \to \mu^+\mu^-)} = N_c \sum_q e_q^2,$$

where N_c is the number of colors, e_q is the charge of the quark q in units of electron charge and sum ranges over the quark flavors, that can be produced at a particular energy. Then the steps indicate the thresholds for the production of $\bar{c}c$ pair (the one above the $\psi(2S)$ peak) and $\bar{b}b$ (above Υ).

Knowing all this, it is not surprising, that the Lagrangian density of QCD can be written in a very similar form as its QED counterpart:

$$\mathscr{L}_{\text{QCD}} = -\frac{1}{2}\text{tr}F_{\mu\nu}F^{\mu\nu} + \sum_{q=u,d,s} \bar{q}\left(i\gamma^{\mu}D_{\mu} - m_q\right)q, \text{ with } D_{\mu} = \partial_{\mu} - igA_{\mu}. \tag{1.2}$$

The objects denoted by individual symbols have of course much more complicated structure. The gauge field is now $A_{\mu} = \sum_{a=1}^{8} T_a A_{\mu}^a$. There are then eight independent *gluon* vector fields A_{μ}^a. When the matter fields transform according to (1.1), the gauge transformation of the gluon field takes the form:

$$A_{\mu}(x) \rightarrow g(x)\left(A_{\mu}(x) + \frac{i}{g}\partial_{\mu}\right)g^{\dagger}(x). \tag{1.3}$$

Main consequence of the matrix structure of the gauge field is the fact, that even though the *field-strength tensor* can be written as $F_{\mu\nu} = \frac{i}{g}\left[D_{\mu}, D_{\nu}\right]$ (which is also possible in QED), it takes more explicitly the form (for one color component):

$$F_{\mu\nu}^a = \partial_{\mu}A_{\nu}^a - \partial_{\nu}A_{\mu}^a + gf_{bc}^a A_{\mu}^b A_{\nu}^c, \tag{1.4}$$

where f_{bc}^a are *structure constants* of the $SU(3)$ group (for completeness: $[T_b, T_c] = f_{cb}^a T_a$). This means, that in the Lagrangian density there are terms describing interactions between gluons and gluons carry color charge (precisely, they are combinations of color and anti-color). These interactions can be visualized by vertices shown in Fig. 1.3. This all is in contrast to photons in QED. They are not charged, do not interact with each other and vertices analogous to those of Fig. 1.3 are not present. As the reason for gluon interactions is the presence of non-commuting generators (matrices), QCD is an example of *non-abelian gauge theory*.

Figure 1.3.: Gluon interaction vertices of Quantum Chromodynamics.

1.2 Running coupling constant and asymptotic freedom of QCD

In any quantum field theory, the *time-evolution operator*, involved in calculations of probabilities/cross-sections of any physical process, can be expressed as (see Ref. [48]):

$$U(t, t_0) = T\left\{\exp\left[-i\int_{t_0}^{t}dt'H_I(t')\right]\right\},$$

where $H_I(t) = e^{iH_0(t-t_0)}(H_{\text{int}})e^{-iH_0(t-t_0)}$ is the *interaction Hamiltonian* written in the *interaction picture*, where the full Hamiltonian can be split into parts describing free propagation of the fields and their interactions $H = H_0 + H_{\text{int}}$. The interaction part can be connected to the previously discussed Lagrangian density by the relation:

$$H_{\text{int}} = \int d^3x \mathscr{H}_{\text{int}}[\phi(x)] = -\int d^3x \mathscr{L}_{\text{int}}[\phi(x)].$$

Here $\mathscr{L}$ is again the part of the Lagrangian density responsible for the interaction. In the example of QED it is an interaction of a charged particle with a photon and has the form $-e\bar{\psi}\gamma^\mu\psi A_\mu$. $[\phi(x)]$ indicates a functional dependence on fields present in the theory, denoted generically as ϕ. In the expression for $U(t, t_0)$ the symbol T means the *time-ordering operation*. The operator rearranges each term in the Taylor expansion such, that the factors with later time argument appear to the left of the factors with earlier time.

The exponential form of the time-evolution operator means that the full calculation of any physical process has to take into account infinite number of Taylor series terms with increasing number of factors representing particles and their interaction points involved. Particles, that appear between vertices, are called *virtual*. Their masses differ from that of observed *real* particles (one says, they are *off-shell*) and they can be propagated only during the time for which the Heisenberg uncertainty principle allows for a violation of energy conservation that is caused by them. In the case of QED, when considering interactions of elementary particles or between electrons and low-Z atoms, higher-order terms include higher powers of the *fine-structure constant* $\alpha = e^2/4\pi\epsilon_0\hbar c \approx 1/137$ and will be small corrections to lower-order terms. This allows to develop *perturbation theory*, which restricts calculations only to the order that is necessary to obtain results with required precision.

It turns out, that considering higher-order (in first approximation only second-order) corrections to the process of the photon propagation leads to the modification of the coupling constant. At small distance it gets an effective value [48]:

$$\alpha_{\mathrm{eff}}(q^2) = \frac{\alpha}{1 - \frac{\alpha}{3\pi}\log\left(\frac{-q^2}{Am^2}\right)}, \qquad \text{(QED)}$$

where $A = \exp(5/3)$. One can set $q = 1/r$, where r is the distance to the charged particle. At very short distances (like $r_c \equiv \hbar/m_e c$) the coupling strongly rises. Putting aside the doubts, if virtual particles are anything more than just mathematical entities appearing in computations, one can interpret the *running coupling constant* in terms of *charge screening*. If a charged particle were inserted into a dielectric medium, the medium would be polarized in such a way, that the molecules would be turned towards the particle with their side charged oppositely to the particle's charge. If any other test particle were put to the medium at a large distance to the first one, it would interact with the superposition of the Coulomb field from the first particle and polarized molecules, which would seem smaller, than the field from the original particle only. The test particle would therefore effectively interact with a particle of smaller electric charge. If, however, the distance between embedded particles were smaller than the typical distances between molecules, the interaction would have the original, larger value.

According to the picture of virtual particles, pairs of electrons and positrons (and other charged particle-antiparticle pairs) are continuously created and annihilated around any charge. They get polarized and screen the charge from other test particles. Hence the notion of *vacuum polarization*. The electric charge, that we measure at large distances is the effect of this screening. Only so close to the measured charge, that one does not feel the effect of virtual pairs, the *bare* value of the charge can be accessed, the one, which is parameter in the Lagrangian and is different from the *physical* value measured in experiments (what is commonly referred to as *renormalization*).

Similar picture is valid in the case of QCD. The difference is that interactions between gluons lead to the lowering of the coupling with decreasing distance (*antiscreening*). The values of running coupling constant of QCD α_s as a function of energy scale Q, based on different measurements, is shown in Fig. 1.4 (left panel). The right panel of the same figure shows the three-jet event $e^+e^- \to Z^0 \to q\bar{q}g$ – a direct experimental evidence of the existence of gluon.

The fact, that α_s is small at high energy scale/small distance inspires the idea, that a new state of strongly interacting matter is formed, called *quark-gluon plasma* (QGP). At very high particle and energy densities first the volume available for each hadron will be of the order of hadron size and the hadrons start to overlap and lose their identity, making quarks not confined anymore, but instead free to crawl through the whole medium. In addition, for high momentum transfers, which translates to high energy

or particle densities, the coupling constant of QCD gets very small and this makes the gas nearly ideal. It is believed to have existed shortly after the Big Bang and be formed in the very high energy heavy ion-collisions at particle accelerators. Study of QGP and especially the phase transition between it and ordinary hadronic matter will give an insight into the reason, why in matter at normal conditions quark have to be confined in "white" hadrons and where do masses of hadrons, much larger than the masses of quarks that build them up, come from.

1.3 Broken symmetries of QCD

The existence of QCD, as discussed above, is one of most beautiful examples, that physics is all about symmetries. The QCD has further symmetries, which determine the phase structure of strongly inter-acting matter. The most important, center and chiral symmetries are presented briefly in the following, based on [7, 2].

1.3.1 Center symmetry and deconfinement

Thermodynamic properties of a many-body system can be derived from the grand canonical partition function:

$$Z = \operatorname{tr} \exp\left[-(H - \mu N)/T\right], \tag{1.5}$$

where H is the Hamiltonian, N - number of particles, μ - chemical potential, T - temperature (and $k_B = 1$). The derivation of the grand canonical ensemble does *not* require the system to be large, only to be in contact with energy and particle reservoir much larger than the system itself. Similarly as the transition amplitude or expectation values of observables, also the partition function can be represented in the path integral formulation:

$$Z \propto \int D\left[q, \bar{q}, A_\mu^a\right] \exp\left[-\int_0^{1/T} dt \int d^3x \left(\mathscr{L}_{\mathrm{QCD}}^{\mathrm{E}}\left[q, \bar{q}, A_\mu^a\right] - \frac{1}{3} i\mu q^\dagger q\right)\right]. \tag{1.6}$$

The factor in front of the second term in exponent takes into account, that the "baryon number" of quarks is $\frac{1}{3}$. The $\mathscr{L}_{\mathrm{QCD}}^{\mathrm{E}}$ denotes the Euclidean Lagrangian obtained from the ordinary one by change of
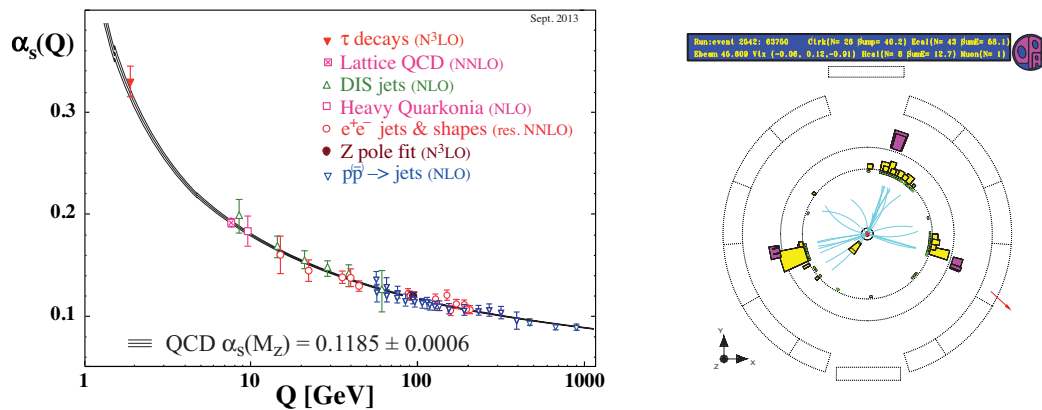
Figure 1.4.: Basic experimental checks of QCD. Left: summary of measurements of α_s as a function of energy scale Q [1]. Right: three-jet event recorded by the OPAL Collaboration.

variables $t = -ix_0$. This allows to exploit the formal similarity between e^{-iHt} encountered in field theory and $e^{-E/T}$ from statistical physics. This connection can be understood intuitively by noting that the time evolution of a single spin $\sigma = \pm 1$ described by e^{-iHt} has the same structure (series of randomly arranged $+1$'s and -1's) as a linear chain of such spins with temperature T having the energy distribution $e^{-E/T}$.

The integral over "imaginary time" extends then from 0 to $1/T$. Because the partition function was defined as the trace in Eq. (1.5), i.e. the sum of diagonal matrix elements in any complete set of states, the "time evolution" described by the exponent must bring the system back to the "initial" state. This leads to the requirement, that the gluon field is periodic in time (and quarks are anti-periodic):

$$A_\mu(t + 1/T, \vec{x}) = A_\mu(t, \vec{x}), \quad q(t + 1/T, \vec{x}) = -q(t, \vec{x}). \tag{1.7}$$

One can observe, that the periodic boundary condition on the gluon field restricts the gauge (1.1) to be periodic as well. Assuming in addition

$$g(t + 1/T, \vec{x}) = h g(t, \vec{x})$$

with the *twist matrix* $h \in SU(3)$, the gauge-transformed gluon field will have the property:

$$A_\mu^{\text{transf}}(t + 1/T, \vec{x}) = h A_\mu^{\text{transf}}(t, \vec{x}) h^\dagger.$$

But it still needs to be strictly periodic according to (1.7). This means, that h must belong to the *center* $Z(3)$ of the $SU(3)$, that is they must commute with all the elements of $SU(3)$. In other words, they must be proportional to the unit matrix:

$$h = z\mathbb{1}, \quad z = \exp(2\pi i n/3)$$

and $n \in \{1, 2, 3\}$ for the case of $SU(3)$. For quarks the twisted transformation gives:

$$q^{\text{transf}}(t + 1/T, \vec{x}) = g(t + 1/T, \vec{x}) q(t + 1/T, \vec{x}) = -zg(t, \vec{x}) q(t, \vec{x}) = -zq^{\text{transf}}(t, \vec{x}).$$

The anti-periodicity condition is fulfilled only if $z = 1$ and the center symmetry disappears. Thus the center symmetry is not a symmetry of the full QCD, but only of the theory, where quarks are neglected ("pure Yang-Mills $SU(3)$ theory").

This is a problem only for "dynamical" quarks, which are variables in the Lagrangian. One can consider the theory with static, i.e. infinitely heavy quarks, being nothing else than external sources of the color charge. To do this one defines a *Polyakov loop*:

$$L(x) = \text{tr}\mathscr{P} \exp\left[ig \int_0^{1/T} dt A_0(t, \vec{x})\right]$$

($\mathscr{P}$ enforces path ordering of the exponential and the term "loop" alludes to the integral along the line of imaginary time, where the integrand is periodic). It can be shown, that it corresponds to the infinitely heavy test quark in x. Namely, one can write the expectation value:

$$\left|\langle L(x)L^\dagger(0)\rangle\right| = \frac{1}{Z} \int D\left[A_\mu^a\right] L(x)L^\dagger(0) exp\left(-S_{\text{YM}}^{\text{E}}\right) = \exp\left(-F_Q(r, T)/T\right) \equiv \Gamma(r, T),$$

where S_{YM}^{E} is the action for gluons only (Yang-Mills theory) in Euclidean space (with imaginary time), r is the distance between quarks. The second expression is a ratio of partition functions that describe systems of gluons with and without heavy quark-antiquark pair inserted and thus is connected to the free energy of the pair (third expression). The free energy at $T = 0$ can be parametrized by the Coulomb-like

plus linear potential $F_Q(r, T = 0) = \sigma r - \alpha/r$. For $T > 0$, but below certain critical temperature T_c, it is expected to remain valid, but the parameters become functions of T. Especially, if the *string tension* $\sigma(T_c) = 0$, then it would be a signal of the deconfinement. However, heavy charge sources will polarize gluonic medium in their immediate surroundings. This mean, that even with deconfinement ($\sigma=0$) and at large distances ($r \to \infty$), $F_Q(r, T)$ has to be non-zero, because the polarized medium with quarks present will differ from the one without them. This leads to the introduction of the polarization term $Q(r, T)$, that vanish for $r \to 0$, because then the medium "sees" a color-neutral object. The free energy is then written as:

$$F_Q(r, T) = \sigma(T)r - \frac{\alpha(T)}{r} + 2Q(r, T).$$

Combining all this together and defining $\Gamma(T) = \lim_{r \to \infty} \Gamma(r, T)$ one can state, the the onset of deconfinement would be signalized by

$$\Gamma(T) = \begin{cases} 0 & \text{for } T \leq T_c \\ \exp(-2Q(T)/T) > 0 & \text{for } T > T_c. \end{cases}$$

The Polyakov loop plays then the role of the *order parameter*, quantity that vanishes in given thermodynamic conditions and is non-zero in other conditions, analogous to the total magnetization $m(T)$ of the Ising model (however this one is zero *below* the critical temperature). The presence of the order parameter and change of its value is the evidence for a phase transition. This behavior is shown schematically in Fig. 1.5 (left panel).
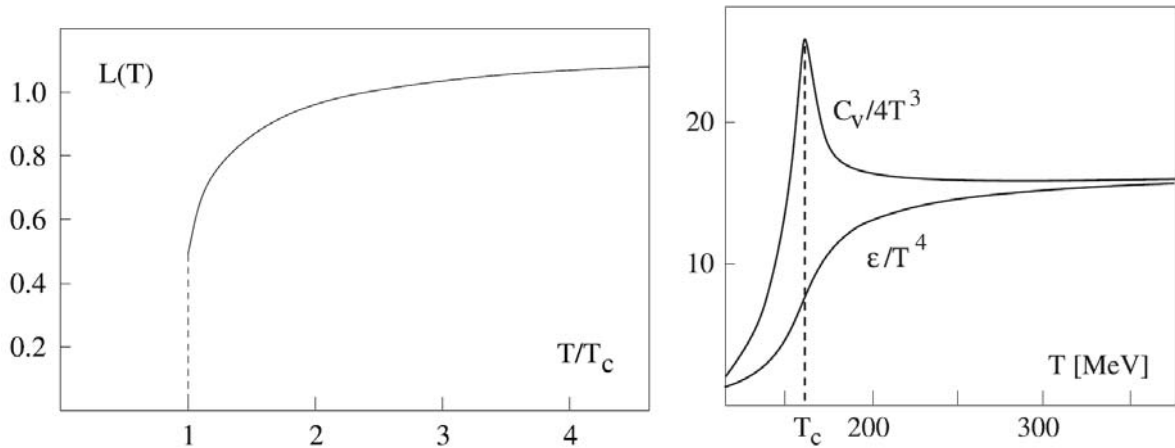
Figure 1.5.: Left: renormalized Polyakov loop in the pure SU(3) gauge theory. Right: energy density and specific heat of the full QCD. Plots are taken from [2].

As it was mentioned, the center symmetry is not a symmetry of the full QCD. Above a certain distance it is more favorable to create from vacuum a real quark-antiquark pair that binds to the heavy quarks and forms a pair of heavy mesons, like $D\bar{D}$ or $B\bar{B}$. Then the heavy quarks can be put apart without any further energy cost. Thus $F_Q(r, T)$ does not go anymore to infinity with $r \to \infty$ and Polyakov loop does not vanish.

The transition point can be defined naturally by considering the specific heat $C_V(T) = (\partial \epsilon/\partial T)_V$, where ϵ is the energy density. Both these quantities are shown in the right panel of Fig. 1.5 as obtained from the numeric calculation on a discrete space-time lattice for the case of two light and 1 heavy flavor and the ratio of masses $m_{\text{light}}/m_{\text{strange}} = 0.05$. The temperature of deconfinement obtained from the peak position in the $C_V/4T^3$ amounts to

$$T_c = 160 \pm 15 \text{ MeV}.$$

This is in remarkable agreement with the highest possible temperature, "a boiling point" of hadronic matter, estimated by Rolf Hagedorn to be $T_H = 160 \pm 10$ MeV [49].

1.3.2 Spontaneously broken chiral symmetry

In the limit of vanishing quark masses, QCD has further symmetry – *chiral symmetry* (also this limit is called *chiral*). This is an invariance of the Lagrangian under vector and axial-vector transformations:

$$\psi \to \exp\left(-i\alpha_V^i \frac{\lambda^i}{2}\right)\psi, \quad \psi \to \exp\left(-i\alpha_A^i \frac{\lambda^i}{2}\gamma_5\right)\psi,$$

that conserve Noether currents:

$$j_{V,i}^\mu = \bar\psi\gamma^\mu \frac{\lambda^i}{2}\psi, \quad j_{A,i}^\mu = \bar\psi\gamma^\mu\gamma_5 \frac{\lambda^i}{2}\psi$$

and conserved charges (3-space integrals of zeroth components of currents) commute with the Hamiltonian of QCD. One can decompose quark fields into left- and right-handed parts by defining

$$\psi_L = \frac{1}{2}(1 - \gamma_5)\psi, \quad \psi_R = \frac{1}{2}(1 + \gamma_5)\psi.$$

Then vector and axial-vector transformations get replaced by the following:

$$\psi_L \to \exp\left(-i\alpha_L^i \frac{\lambda^i}{2}\right)\psi_L, \quad \psi_R \to \exp\left(-i\alpha_R^i \frac{\lambda^i}{2}\right)\psi_R,$$

and related Noether currents are linear combinations of the vector and axial-vector ones: $j_{L,i}^\mu = \frac{1}{2}\left(j_{V,i}^\mu - j_{A,i}^\mu\right)$, $j_{R,i}^\mu = \frac{1}{2}\left(j_{V,i}^\mu + j_{A,i}^\mu\right)$.

In the physical vacuum expectation values of *quark condensate* $\langle\bar\psi\psi\rangle = \langle 0|\bar\psi_L\psi_R + \bar\psi_R\psi_R|0\rangle$ and *gluon condensate* $\langle G^2\rangle = -(\beta(g_s)/2g_s)\langle G_a^{\mu\nu}G_{\mu\nu}^a\rangle$ ($\beta(g_s)$ is the beta function from the renormalization group) do not vanish and the former one leads to the spontaneous breaking of the chiral symmetry. In general, one of consequences of spontaneous symmetry breaking is the existence of massless Goldstone bosons. For the chiral symmetry they would be pions for SU(2) and in addition kaons for SU(3). Their non-zero mass can be understood by taking into account, that in QCD chiral symmetry is only approximate, as up, down and strange quarks have very small, yet non-vanishing masses and they *explicitly break* the symmetry. Interestingly, the consequences of only approximate symmetry are still realized, even if also only approximately: masses of pions are clearly smaller than of all other hadrons ($m_\pi \approx 140$ MeV/c^2, $m_\rho \approx 770$ MeV/c^2, $m_p \approx 938$ MeV/c^2).

For massless fermions, eigenstates of helicity are at the same time eigenstates of parity. For unbroken symmetry there should then exist doublets of degenerate hadrons of opposite parity. That it is not the case (e.g. $m_{a_1} \approx 1260 \neq m_\rho$, $m_{f_1}(1260) \neq m_\omega \approx 782$ MeV/c^2, $m_{f_1}(1420) \neq m_\phi \approx 1020$ MeV/c^2), is another consequence of chiral symmetry breaking.

The strength of the breaking can be quantified by several order parameters. One of them is the quark condensate, which can be directly related to the pion decay constant $f_\pi = 93$ MeV by Gell-Mann-Oakes-Renner (GOR) formula [50]:

$$m_\pi^2 f_\pi^2 = -2\bar m_q \langle\bar q q\rangle.$$

Taking $\bar m_q = 6$ MeV/c^2 this yields $\langle\bar q q\rangle = -(240 \text{ MeV})^3/c^2 = -1.8$ fm$^{-3}\hbar^3 c$.

The connection between the breaking of chiral symmetry and hadronic spectra can also be understood in terms of Weinberg sum rules [51, 52]. They can be expressed in terms of the *electromagnetic spectral function*, defined as a Fourier transform of the retarded correlator of the electromagnetic current at different space-time points:

$$\Pi_{\text{em}}^{\mu\nu}(q_0, q) = -i \int d^4x\, e^{iqx}\, \theta(x_0) \langle\left[j_{\text{em}}^\mu(x), j_{\text{em}}^\nu(0)\right]\rangle \tag{1.8}$$
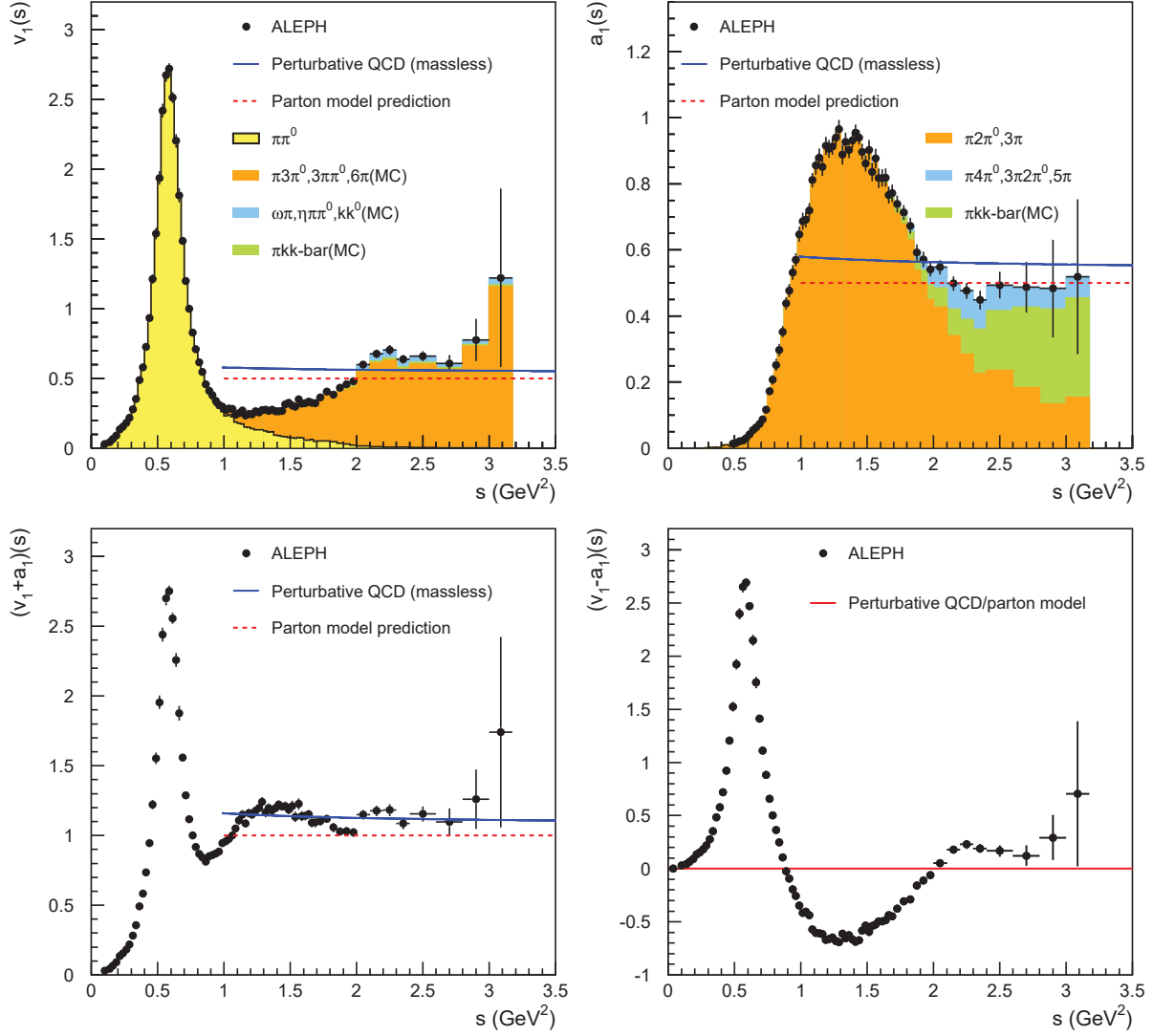
Figure 1.6.: Vector and axial-vector spectral functions, their sum and difference, as measured in τ decays by ALEPH [3, 4]. Shaded areas indicate exclusive decay channels and in case of "MC" in the labels, the shapes of the contributions are taken from Monte-Carlo simulation.

(angle bracket accounts is the quantum-mechanical expectation value). In vacuum the spectral function is related to the measurable quantities via:

$$R = \sigma(e^+e^- \to \text{hadrons})/\sigma(e^+e^- \to \mu^+\mu^-) = \frac{-12\pi}{s}\text{Im}\Pi^{\text{vac}}_{\text{em}}(s).$$

The sum rules connect order parameters of the chiral symmetry breaking with moments of the center-of-mass energy squared s, weighted by the difference between vector and axial-vector spectral function, namely:

$$f_n = -\int_0^\infty \frac{ds}{\pi} s^n \left(\text{Im}\Pi_V(x) - \text{Im}\Pi_A(x)\right).$$

In particular $f_{-2} = f_\pi^2\langle r_\pi^2\rangle/3 - F_A$ (r_π is the pion charge radius and F_A - coupling constant for $\pi^\pm \to \mu^\pm\nu_\mu\gamma$), $f_{-1} = f_\pi^2$, $f_0 = 0$. The vacuum vector and axial-vector spectral functions were measured by ALEPH [3, 4] and OPAL [53] collaborations in decays of τ produced in e^+e^- collisions at Large Electron-Positron collider, decaying into vector (even number of pions/kaons) and axial-vector (odd number of
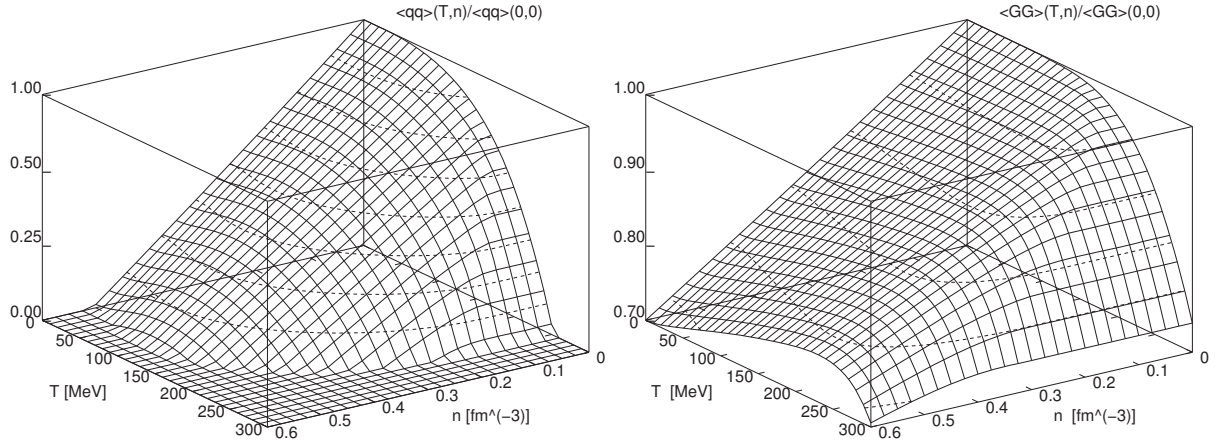
Figure 1.7.: Quark (left) and gluon (right) condensates as functions of temperature and density, normalized to the vacuum values [5]. See also [6].

pions/kaons) channels, see Fig. 1.6 which clearly displays the difference between spectral functions and thus the non-vanishing order parameter of chiral symmetry breaking.

1.3.3 Chiral symmetry restoration
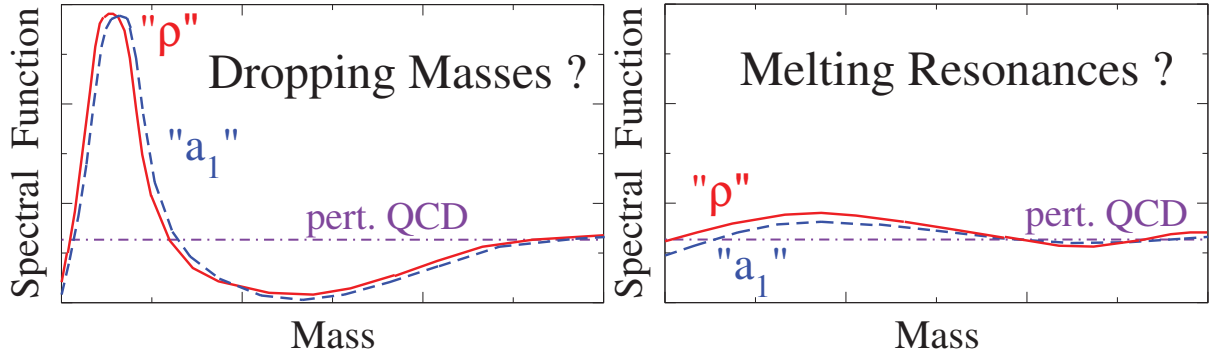
Figure 1.8.: Two scenarios for chiral restoration: dropping mass (left) and resonance melting (right). Plots taken from [7].

One can calculate the change of the chiral condensate using the low-density approximation, that assumes the thermal medium to be a gas of non-interacting hadrons: pions at finite T and small density, nucleons at finite ρ_N and small temperature. The result is (see [54]):

$$\frac{\langle\langle \bar{q}q\rangle\rangle(T,\mu_B)}{\langle \bar{q}q\rangle} \approx 1 - \frac{T^2}{8f_\pi^2} - \frac{1}{3}\frac{\rho_N}{\rho_0} - \dots,$$

where $\rho_0 \approx 0.16$ fm^{-3} is the normal nuclear matter density. According to this formula, already in normal nuclear matter the quark condensate drops by about 30% compared to its vacuum value.

Similar calculation can be done for the gluon condensate. Both condensates are plotted in Fig. 1.7. First suggestions about the connection between the quark condensate and spectral functions were made by Pisarski [55]. Brown and Rho [56, 57] predicted that the masses of hadrons, excitations of the QCD vacuum, will decrease monotonically with the order parameters. This "Brown-Rho scaling" is an example of "dropping mass" scenario: when the chiral symmetry gets restored, masses of chiral partners approach each other and at some point get degenerate. Certainly more sophisticated is the "resonance melting"

scenario, in which the degeneracy is realized by broadening of spectral functions of chiral partners and making them indistinguishable. This will be presented in more details in Sec. 1.4. Both scenarios are sketched schematically in Fig. 1.8.

1.4 Medium effects and chiral symmetry restoration

An alternative to the Brown-Rho-like ("dropping mass") description of the chiral symmetry restoration are hadronic many-body approaches. An example is based on effective Massive Yang-Mills Lagrangian. Here the "matter" field is the unitary field describing pions [58]:

$$U = \exp\left(i\sqrt{2}\phi/f_\pi\right), \ \phi = \phi_a \tau_a/\sqrt{2}.$$

Hadrons are gauge fields in this approach. As usual, their coupling to matter fields is realized by introducing covariant derivative, similar like when applying a "minimal coupling" to realize an interaction of non-relativistic quantum-mechanical particle with electromagnetic field:

$$D^\mu U = \partial^\mu - ig(A_L^\mu U - U A_R^\mu),$$

where A_L^μ and A_R^μ refer to the two circular polarizations of the gauge field. One can add kinetic and mass terms for hadrons and additional terms going beyond the minimal coupling, that are needed to get a right phenomenological behavior in vacuum. The resulting Lagrangian has the form:

$$\mathscr{L}_{\mathrm{MYM}} = \frac{1}{4} f_\pi^2 \mathrm{Tr}\left(D^\mu U D^\mu U^\dagger\right) - \frac{1}{2} \mathrm{Tr}\left[(F_L^{\mu\nu})^2 + (F_R^{\mu\nu})^2\right] + m_0^2 \mathrm{Tr}\left[(A_L^\mu)^2 + (A_R^\mu)^2\right]$$
$$- i\xi \mathrm{Tr}\left[D^\mu U D_\nu U^\dagger (F_L^{\mu\nu} + F_R^{\mu\nu})\right] + \sigma \mathrm{Tr}\left(F_L^{\mu\nu} U F_{R\mu\nu} U^\dagger\right).$$

Remembering, how left- and right-handed currents are related to the vector and axial-vector one, it is possible to define $\rho^\mu = V^\mu = A_R^\mu + A_L^\mu$ and $A^\mu = A_R^\mu - A_L^\mu$ and write the Lagrangian in the form (axial-vector field is redefined to remove the term $\partial^\mu \vec{\pi} A_\mu$, $g_{\rho\pi\pi}^2 = \frac{1}{2} g^2$ and, by convention, $V^\mu = \rho_a^\mu \tau_a/\sqrt{2}$):

$$\mathscr{L}_{\mathrm{MYM}} = \frac{1}{2} m_\rho^2 \vec{\rho}_\mu^2 + \frac{1}{2}\left(m_\rho^2 + g^2 f_\pi^2\right)\vec{a}_{1\mu}^2 + g^2 f_\pi \vec{\pi} \times \vec{\rho}^\mu \cdot \vec{a}_{1\mu}$$
$$+ g_{\rho\pi\pi}^2\left(\vec{\rho}_\mu^2 \vec{\pi}^2 - \vec{\rho}^\mu \cdot \vec{\pi} \ \vec{\rho}_\mu \cdot \vec{\pi}\right) + g_{\rho\pi\pi} \vec{\rho}_\mu \cdot (\vec{\pi} \times \partial^\mu \vec{\pi}) + \dots.$$

It is easy to spot the mass of a_1 meson: $m_{a_1}^2 = m_\rho^2 + g^2 f_\pi^2$, and figure out that the splitting of ρ^0 and a_1 masses is due to chiral symmetry breaking, as it involves the order parameter f_π. Electromagnetic interaction is introduced by the *Vector Meson Dominance* (VMD) model. In general this assumes, that the electromagnetic radiation is dominated or even entirely mediated by an excitation of intermediate vector meson. This is possible, because vector mesons have the same quantum numbers as photons ($J^{PC} = 1^{--}$), and comes from the fact, that for masses of the virtual photon $M_{\gamma^*} \lesssim 1 \ \mathrm{GeV}/c^2$ the spectrum is saturated by three lowest vector meson resonances: two-pion ($\rho(770)$), three-pion ($\omega(782)$) and kaon-antikanon ($\phi(1020)$) channels. The current can be then written as:

$$j_{\mathrm{em}}^\mu(M_{\gamma^*} \lesssim 1 \ \mathrm{GeV}/c^2) = \frac{m_\rho^2}{g_\rho} \rho^\mu + \frac{m_\omega^2}{g_\omega} \omega^\mu + \frac{m_\phi^2}{g_\phi} \phi^\mu.$$

In higher masses, the partonic description plays a dominant role:

$$j_{\mathrm{em}}^\mu(1.5 \ \mathrm{GeV}/c^2 \lesssim M_{\gamma^*} \lesssim 3 \ \mathrm{GeV}/c^2) = \sum_{q \in \{u,d,s\}} e^q \bar{q} \gamma^\mu q.$$

This can be seen in Fig. 1.2, keeping in mind, that e^+e^- scattering at given $\sqrt{s}$ is the inverse process to the dilepton production with the same value of M_{γ^*}. The spectra in Fig. 1.2 below $\sqrt{s} \approx 1 \div 1.5$ GeV are indeed dominated by resonant structures corresponding to vector mesons. Above this range the spectra are smooth, which corresponds to $\bar{q}q$ production with clear steps at energy thresholds for production of each heavy quark flavor. The charge-flavor part can be rearranged to reflect the quark content of the vector mesons ρ^0, ω and ϕ:

$$j^\mu_{\text{em}} = \frac{1}{\sqrt{2}} \bar{\psi} \gamma^\mu \psi \left(\frac{\bar{u}u - \bar{d}d}{\sqrt{2}} + \frac{1}{3} \frac{\bar{u}u + \bar{d}d}{\sqrt{2}} - \frac{\sqrt{2}}{3} \bar{s}s \right).$$

Inserting this into the correlator involved in the spectral function yields that the isospin coefficients are translating into relative weights:

$$\text{Im}\Pi_{\text{em}} \propto \left(\text{Im}D_\rho + \frac{1}{9} \text{Im}D_\omega + \frac{2}{9} \text{Im}D_\phi \right).$$

This means that in the spectral function of Vector Meson Dominance the most important is the propagator of the ρ^0 meson.

For the Massive Yang-Mills Lagrangian, all this is realized by adding the term (see Ref. [59]):

$$\mathcal{L}_{\gamma\rho} = \frac{em_\rho^2}{g_{\rho\pi\pi}} B_\mu \rho^3_\mu,$$

where B_μ is the photon field.

In the hot and dense medium properties of ρ^0 and a_1 mesons change by the possible excitations of virtual pairs of hadrons and mesons in similar way, as in electrodynamics vacuum polarization effects lead to modifications of coupling constants of particles relative to their "bare" values.

In the case of hadronic many-body theory one considers loop corrections shown in Fig. 1.9. Due to them, the longitudinal (L) and transverse (T) parts of the ρ^0 meson propagator have to be written as follows [8]:

$$D^{L,T}_\rho = \left[M^a - \left(m^{(0)}_\rho \right)^2 - \Sigma^{L,T}_{\rho\pi\pi} - \Sigma^{L,T}_{\rho M} - \Sigma^{L,T}_{\rho B} \right]^{-1}.$$

In this expression $\Sigma_{\rho\pi\pi}$ corresponds to the pion loop, which already in the vacuum makes the width of the ρ^0 finite as a consequence of the possible decay $\rho \to \pi\pi$. In the hadronic medium the lowest order modification will be given by dressing the pion propagator by hadronic resonance-hole pairs. This is shown as the first self-energy correction in the left part of Fig. 1.9. Analogous dressing will happen to the ρ^0 propagator itself, as represented by the second self-energy in the same Feynman diagram. The corresponding terms in the propagator are $\Sigma_{\rho B}$ for baryon and $\Sigma_{\rho M}$ for meson resonances. As the physical mass of the particle is in the pole of the propagator, the relation of medium effects to the modification of the vector meson spectral function is evident.
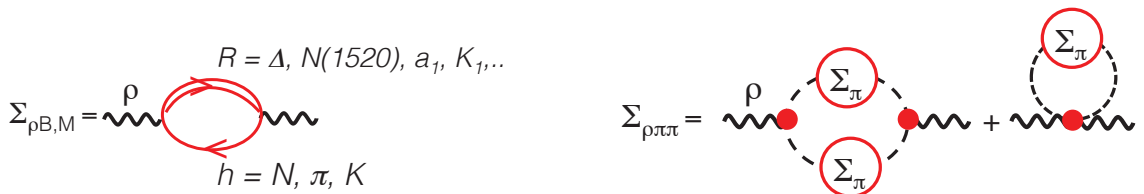
Figure 1.9.: Feynman diagrams for ρ^0 meson propagator in hot and dense medium. Left: excitation of baryon or meson resonances, right: formation of pion loops.

Cutting the diagram in the left part of Fig. 1.9 through the bubble representing baryonic resonance excitation, one can obtain the diagram like in the right panel of the figure. It represents a decay of

the resonance with ρ^0 excitation according to VMD. This has important consequences for low-energy heavy-ion collisions. In this regime the production of *thermal* pions is too small to excite many $\pi\pi$ resonances. However, ρ^0 can be excited in the pion cloud of baryons and its properties, modified by strongly interacting medium, will give a contribution to the spectra of virtual photons. Moreover, this brings a possibility to constrain ρN couplings and their dependence on the density of cold nuclear matter by studying the production of the vector meson in πN and πA reactions [60].

Alternatively, one can adopt the scattering amplitude approach, like the one presented in [9]. There the amplitude $f_{\rho a}^{c.m.}$ to scatter the ρ^0 meson from a particle a is calculated as a sum over resonances given by Breit-Wigner distributions and the term describing smooth underlying background. The spectral function can then be obtained as:

$$\Pi_{\rho a}(E, p) = -4\pi \int \frac{d^3 k}{(2\pi)^3} n_a(\omega) \frac{\sqrt{s}}{\omega} f_{\rho a}^{c.m.},$$

with E and p being the energy and momentum of the ρ^0 meson, $\omega^2 = m_a^2 + k^2$ and n_a is the occupation number from Bose-Einstein or Fermi-Dirac distribution, depending if a is boson or fermion.
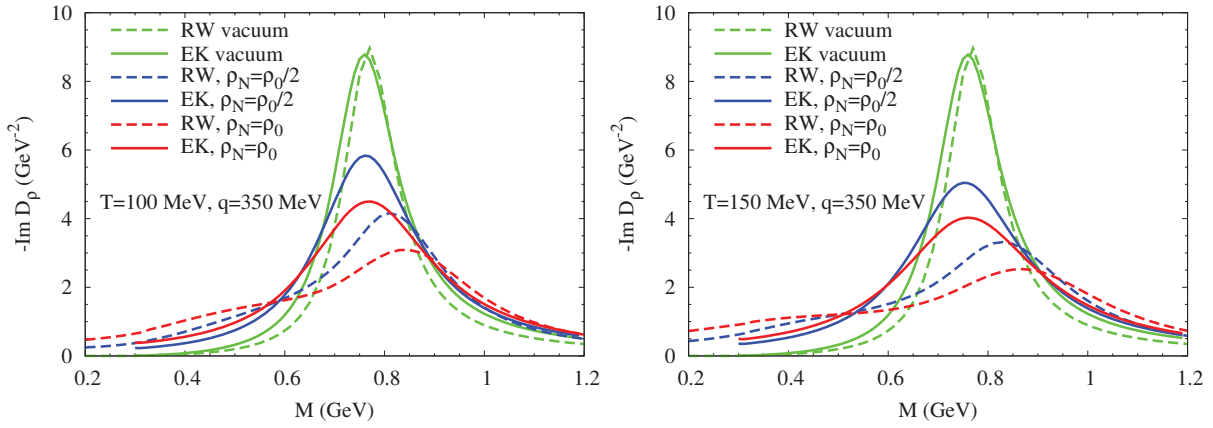
Figure 1.10.: Imaginary parts of the ρ^0 meson propagators for different conditions of the hot and dense medium, calculated in [8] (RW) and [9] (EK).

Fig. 1.10 shows the calculations of D_ρ in hot and dense hadronic medium under different conditions using both approaches outlined above. Both predict "resonance melting", which is stronger in the many-body theory. In addition, with a good will, one can observe a shift of the maximum towards smaller masses in the scattering amplitude approach. In the many-body theory the maximum moves rather to higher masses.

The calculation of QCD and Weinberg sum rules at finite temperature, presented in [61] confirm that the melting of the ρ^0 meson spectral function, observed in dilepton experiments (cf. Section 1.7), is indeed compatible with chiral symmetry restoration.

1.5 Phase diagram of QCD

The existence of order parameters that change with thermodynamic properties of strongly interacting medium, modify the symmetry pattern of the theory, and even influence how important different degrees of freedom (hadrons, quarks) are, leads to an idea that strongly interacting matter can exist in different phases.

Phase structure of matter can be more complex than expected at the first glimpse. This is the case even for the substance the most familiar from everyday observation: H_2O. The number of different crystalline forms of ice is now referred to as "many" (but it is at least 18) and there are three amorphous phases [62].
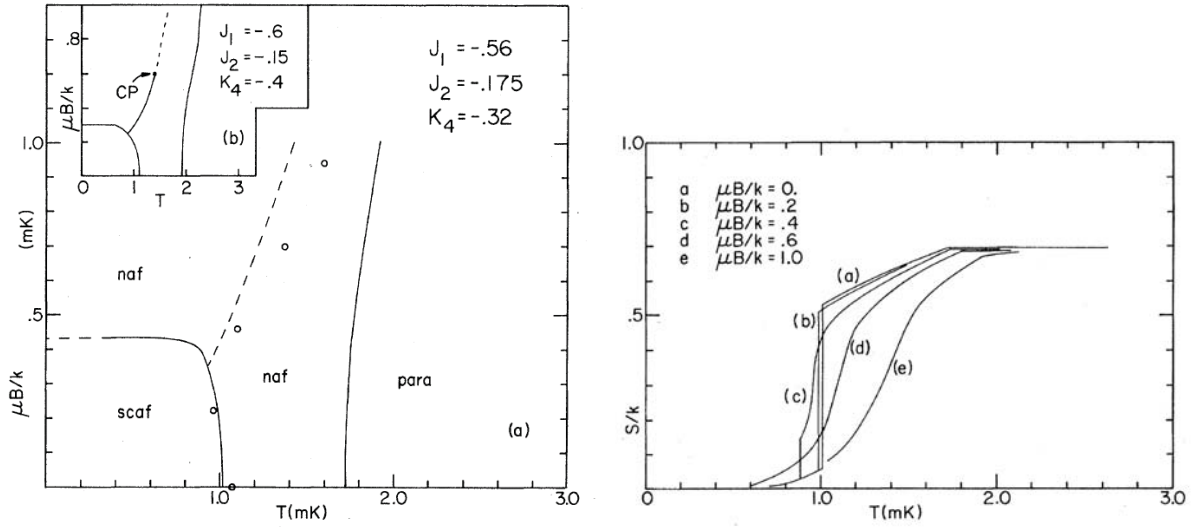
Figure 1.11.: Left: phase diagram of bcc ^{3}He, calculated in [10], inset shows the result of slight variation of the parameters of Hamiltonian out of the optimal fit to high-temperature experiments. Right: entropy as a function of temperature for different values of the magnetic field.

Also body-centered cubic (bcc) ^{3}He has phases which differ by their magnetic behavior. Among the others, two antiferromagnetic ones can be observed. In the normal antiferromagnetic (naf) state two simple cubic sublattices of the bcc structure are magnetic. In the simple cubic antiferromagnetic (scaf) phase, simple cubic sublattices are themselves antiferromagnetic and spins of both of them are rotated with respect to each other by 90° around the $\vec{B}$ field in order to minimize the energy. Left panel of Fig. 1.11 shows the low-temperature region of ^{3}He phase diagram, resulting from a mean-field calculation of the appropriate Hamiltonian with parameters listed also in the figure, obtained from fit to various high-T experiments [10]. Right panel shows the entropy as a function of temperature for several values of the magnetic field. There is a first-order phase transition (indicated by solid line) between naf and scaf phases and smooth cross-over (dashed-line) between low- and high-entropy regions of the naf phase. It is worth noting, that slight adjustment of the Hamiltonian parameters outside the optimal fit causes the emergence of the first-order transition with a critical end-point (CP), as shown in the inset of the left panel of Fig. 1.11.

It is expected that the phase diagram of strongly interacting matter has also a very rich structure (see Fig. 1.12 for one example). Most often discussed are the hadronic matter and gas of faintly interacting quarks and gluons (*quark-gluon plasma*, QGP). The vital question is about the nature of the phase transition between the hadronic and quark-gluon phase. In contrast to phase diagrams of water or bcc ^{3}He, QCD phase boundaries have not been established experimentally and are yet subject to various theoretical predictions providing quite different results on the existence and location of the critical point. Here the first-order phase transition is expected up to a certain temperature and above it the phase boundary is supposed to be a smooth cross-over. The location of the critical point (and even number of them) is being a topic of extensive theoretical and experimental studies.

Besides the possible deconfinement, the phase diagram has many more interesting features. Examples are different kinds of *color superconductor* (CSC phases). This is the strong-force analogue of superconducting metals described by the Bardeen-Cooper-Schrieffer (BCS) theory. Already within the cold hadronic matter, as density increases, the gas-like behavior should convert into liquid-like and this is expected to happen through the first-order phase transition with a critical end-point. Low-energy heavy-ion collision experiments place the critical point at chemical potential of normal nuclear matter and temperature of $T = 15 - 20$ MeV [63]. At finite chemical potential, hadronic phase can be separated from QGP by states with inhomogenous spontaneous breaking of chiral symmetry or quarkyonic matter. The former arise from the idea, that quark condensate or similar quantity would be spatially modulated.
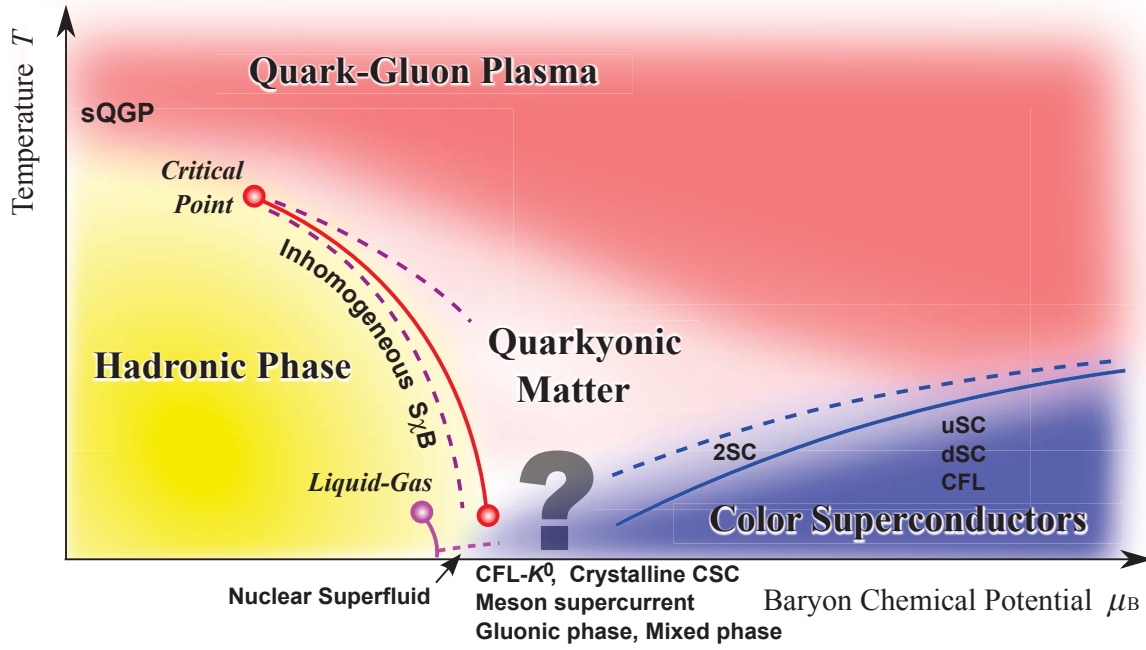
Figure 1.12.: One of many expected QCD phase diagrams [11, 12]. Not that first-order transition line with critical point can exist only in thermodynamic limit $N \to \infty$. In addition, quite diverse predictions can be made about the order of the chiral phase transition, as μ_B increases, including the possibility, that the first order region of the $m_{u/d} - m_s$ plane shrinks in the direction of vanishing quark masses (it is already below physical masses for $\mu_B = 0$ and this is the reason for the cross-over nature of the transition here), see for example [13, 14].

The latter is a confined phase with weakly interacting quarks deep below the Fermi surface and baryons close to it, within the shell of the thickness roughly Λ_{QCD}. Thus the excitations are still hadrons, but bulk thermodynamic properties of the matter are governed by partonic degrees of freedom. It is not clear, how such predictions, valid for QCD with very large number of colors, hold in reality with $N_c = 3$.

There are only few possibilities, when extreme states of matter, occupying points of the phase diagram far from the normal atomic nuclei, could exist. First of all, few microseconds after the Big Bang, the matter should have been extremely hot and without baryons, so the early Universe evolved down close to the Y axis of the phase diagram. The cores of neutron stars are predicted to be extremely dense, but not too hot, which are the conditions necessary to form color superconductors. In relativistic collisions of heavy ions, nuclear matter can reach finite temperature and density and make a journey through different areas of the phase diagram, depending on sizes of the ions and their initial kinetic energies. Finally, in neutron star mergers temperatures as high as 100 MeV/k_B may occur [64], in which case they would be the systems with very high density and moderately high temperature, where the thermodynamic limit would be undoubtedly applicable.

1.6 Evolution of a heavy-ion collision system

Before the collision, ions have normal nuclear matter properties. When they meet, the density increases and the initial kinetic energy becomes the energy of chaotic thermal motion of nucleons, and then in the end shards of the collision fly away, reaching finally zero temperature and density. Therefore, the colliding system has to pass a trajectory through the phase diagram undergoing possibly several phase transitions if the total energy of colliding ions is large enough.

More detailed picture is shown in terms of a cartoon scheme in Fig. 1.13. Initial stage is governed by nucleon-nucleon processes, like *Bremsstrahlung* or, at energies high enough, *Drell-Yan processes* (hard
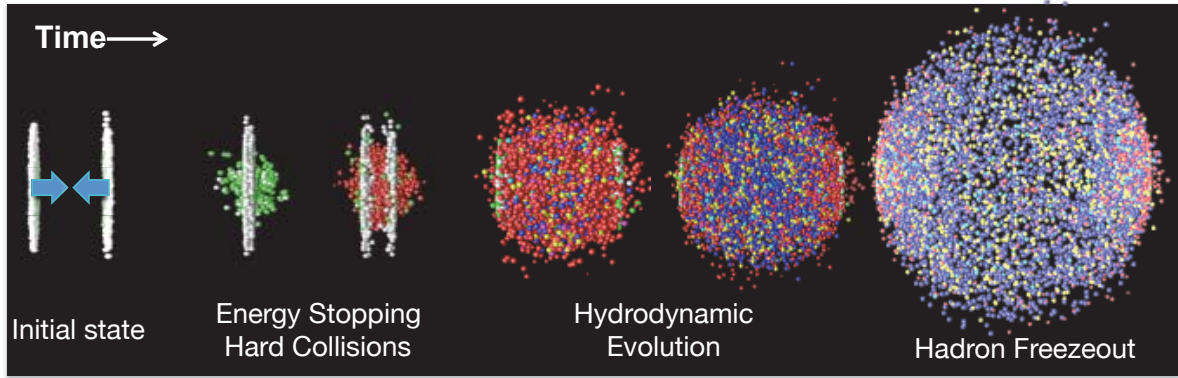
Figure 1.13.: Schematic evolution of a heavy-ion collision for high-energy case, where intermediate evolution can be described by equations of hydrodynamics.

scattering, in which quark from one hadron annihilates with antiquark from another one into virtual photon or weak Z boson, that then decays into a l^+l^- pair, $l = e, \mu$). Then the system compresses and gets heated, possibly forming the QGP. The existence of a sizable collective flow of particles (see e.g. [65] for RHIC results) indicates a generally rapid thermalization of the medium: if it happens before the initial spatial anisotropy of non-central collisions is smeared out, pressure gradients with different values in different directions are built up, and this makes the medium to expand stronger in these directions, where the gradients are larger.

Further evolution can be described by microscopic transport calculations like UrQMD (Ultra-relativistic Quantum Molecular Dynamics, [66]), GiBUU (Gießen Boltzmann-Uehling-Uhlenbeck, [67]) or HSD (Hadron-String Dynamics, [68]) and at low energies this accounts for the whole evolution of the fireball. At higher energies, the success of hydrodynamic description of particles collective flow parameters at high energies, at least at low transverse momenta, where there is no contribution from hard processes [69, 70], gave rise to the conjecture that the medium evolves as a, possibly slightly viscous, fluid. These two approaches are merged together in hybrid models (see e.g. [71, 72]), where the hydrodynamic calculation describes intermediate stage of the system's evolution, while the transport simulation is used for the early stage, before the system reaches thermal equilibrium (providing an initial condition for the hydrodynamics) and in the late one, when the particle picture is more appropriate.

Moreover, the scaling of the flow parameters with number of constituent quarks in hadrons (see left panel of Fig. 1.14), observed at RHIC, may be considered as one of the most prominent signatures of the quark-gluon plasma formation and hadron production through quark coalescence mechanism. However, deviations from such scaling have been later observed at LHC [73].

If thermodynamic conditions allowed to form the QGP, the system has to transit back to the hadronic phase. Then, as the cross sections for inelastic scattering are clearly smaller than for elastic ones, the former cease earlier. The identities of hadrons do not change anymore and this moment is called *chemical freeze-out*. Using grand canonical partition functions with different empirical modifications (so called *Statistical Hadronization Model*, [74, 75, 76]), one can extract from particle ratios T and μ_B of the system at this moment. For different $\sqrt{s_{NN}}$ the points accumulate around a single curve on the phase diagram, called the *chemical freeze-out line*, see right panel of Fig. 1.14.

At the end also elastic collisions cease and thermal spectra of the particles get fixed (giving a chance to extract temperature as an inverse slope of the Boltzmann distribution). This last stage of the evolution of the system is called *thermal freeze-out*.
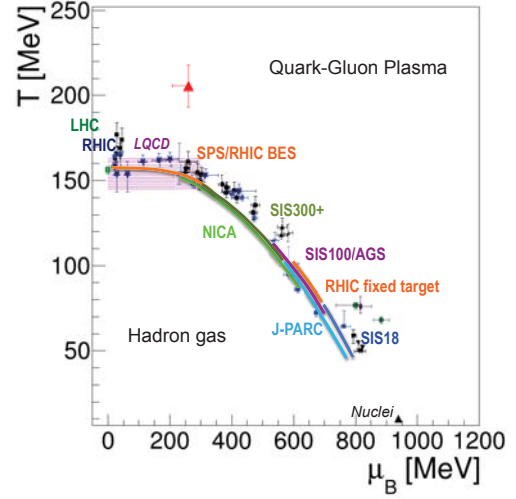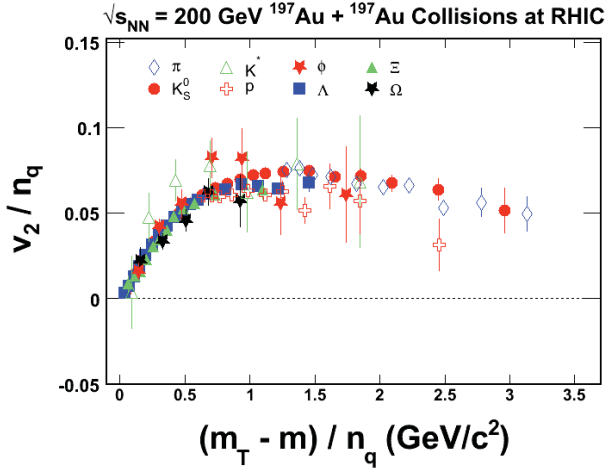
Figure 1.14.: Left: scaling of the elliptic flow measured at RHIC as a function of transverse mass with the number of constituent quarks [15]. Right: chemical freeze-out points on the $T - \mu_B$ plane. Black squares and dark blue stars: [16], black solid symbols (squares, circles, triangles): [17], green square: [18], green solid circles: [19], lila diamond: [20]. Red triangle is thermal fit to dilepton spectra from [21].

1.7 Probing QCD matter with photons

Flow observables provide information about an early stage of heavy-ion collision and formation of equilibrium, hadrons distributions are settled only at the end of the system's evolution. However, to probe hot and dense state of QCD matter directly, photons, real γ and virtual γ^*, are needed. The latter decay into lepton pairs $l^+ l^-$ practically immediately, so lepton pairs and virtual photons are often notionally identified and referred to as *dileptons*. They are not subject to the strong force and their electromagnetic interaction probability is suppressed by α^2 ($\alpha \approx 1/137$ – fine structure constant) and is negligible on the distance needed for such *electromagnetic probes* to leave the medium. This means, that they do not undergo practically any rescatterings and bring undistorted information about the process in which they were created.

Furthermore, they are emitted in different processes during the whole nuclear collision. More specifically, the sources of radiation can be summarized as in Fig. 1.15, for case of ultrarelativistic collisions. It shows the conjectured distribution of dileptons' invariant mass:

$$M = \sqrt{(E_1 + e_2)^2 - (\vec{p}_1 + \vec{p}_2)^2} \approx 2\sqrt{|\vec{p}_1||\vec{p}_2|} \sin \frac{\Theta_{12}}{2}.$$

The last approximation is valid for particles with masses much smaller than their momenta and involves the opening angle Θ_{12} between leptons. It is not needed technically, because one can always easily perform full calculation, but it often facilitates an understanding of the kinematics.

It turns out, that different parts of the distribution are populated by processes dominating at different stages of the collision. Before the nuclei meet, electromagnetic radiation is emitted through the Bremsstrahlung process. In the initial stage of the collision, before the nuclear matter gets equilibrated, dileptons from Drell-Yan annihilations can be radiated. This source requires very large collision energy and occupies correspondingly high mass region of the spectrum. If the energy is sufficient to reach temperature and density of deconfinement phase transition and if QGP has enough time to get equilibrated, thermal dilepton spectrum from perturbative quark-antiquark annihilation will be populated. It should be best visible in the *intermediate mass region* (IMR) of 1.5 GeV/$c^2 \lesssim M_{ll} \lesssim 3$ GeV/c^2, when subtracting the background of *semileptonic decays* (decays of a hadron with producing only one lepton) of correlated

charmed baryon pairs $D\bar{D}$. Then QGP cools down and expands, vector mesons are produced, either through resonant $\pi\pi$ or KK annihilations, dominant at high energies, or through off-shell pion annihilation at low energies. As the vector mesons couple directly to the l^+l^-, the dilepton spectroscopy in the *low mass region* (LMR, $M_{ll} \lesssim 1.5$ GeV/c^2), reflects immediately the modifications of ρ^0, ω and ϕ spectral functions and gives an insight into the pattern of the chiral symmetry restoration. To extract this information, one has to subtract contribution of sources radiating mainly after the freeze-out: decays of hadronic resonances, and π^0, η and ω in Dalitz (i.e. three-body) channels. The picture is closed with the late decays of charmonia J/Ψ or Ψ'. Their production is related to the deconfinement pattern and absorption in nuclear matter.

Rates of the dileptons from decays of vector mesons are directly related to their spectral function, provided that the Vector Meson Dominance is still valid in the medium. The relation is as follows:

$$\frac{\mathrm{d}N_{ll}}{\mathrm{d}^4x\mathrm{d}^4q} = -\frac{\alpha_{\mathrm{em}}^2}{\pi^3M^2}f^B(q_0,T)\tfrac{1}{3}g_{\mu\nu}\mathrm{Im}\Pi_{\mathrm{em}}^{\mu\nu}(M,q;\mu_B,T), \tag{1.9}$$

which is correct only to the first order in α_{em} on the side of the electromagnetic interaction, but exact in the strong interaction. In this expression f^B is the thermal Boltzmann factor dependent on energy component of the four-momentum q_0 and the temperature. To make a connection with the experiment, which typically measures $\mathrm{d}N_{ll}/\mathrm{d}M_{ll}$ with M_{ll} being the invariant mass of the l^+l^- pair, an appropriate integral over phase-space evolution has to be performed and this requests an input from models constrained by the experiment.

The opportunity to directly access the properties of hot and dense strongly interacting matter with photons and dileptons has been exploited since decades with different sizes of colliding systems and at energies from around $1A$ GeV to several TeV. At relatively high energies, dilepton spectra were measured by the CERES Collaboration at the Super Proton Synchrotron (SPS) in CERN. While e^+e^- production in p+Be and p+Au collisions at $450A$ GeV could be described by a sum *cocktail* of simulated hadronic e^+e^- sources (see left and middle panel of Fig. 1.16), in S+Au collisions at $200A$ GeV a clear enhancement over the cocktail has been observed (right panel of Fig. 1.16). In the measurement of Pb+Au at $158A$ GeV it was possible to subtract the hadronic cocktail and compare the resulting ρ^0 spectrum
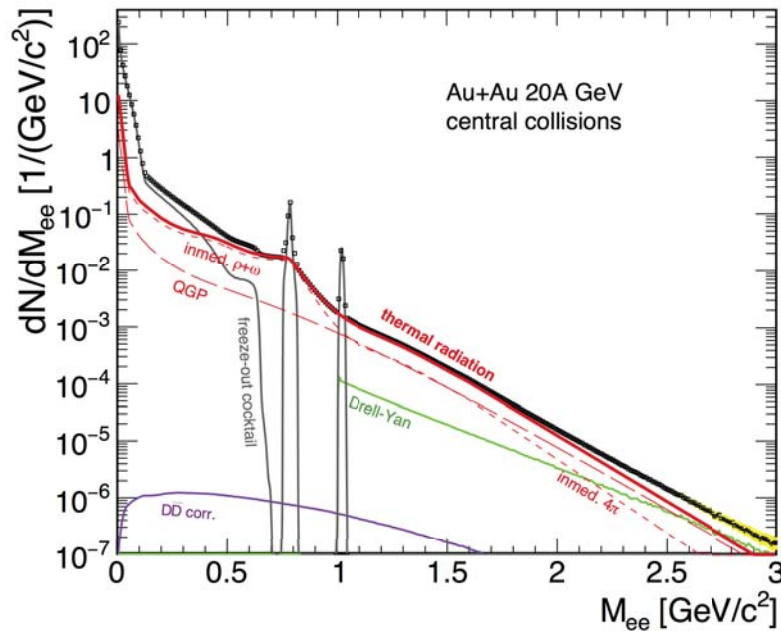
Figure 1.15.: Expected spectrum of dilepton invariant mass in ultrarelativistic heavy-ion collisions with particular sources marked. Figure taken from [22].
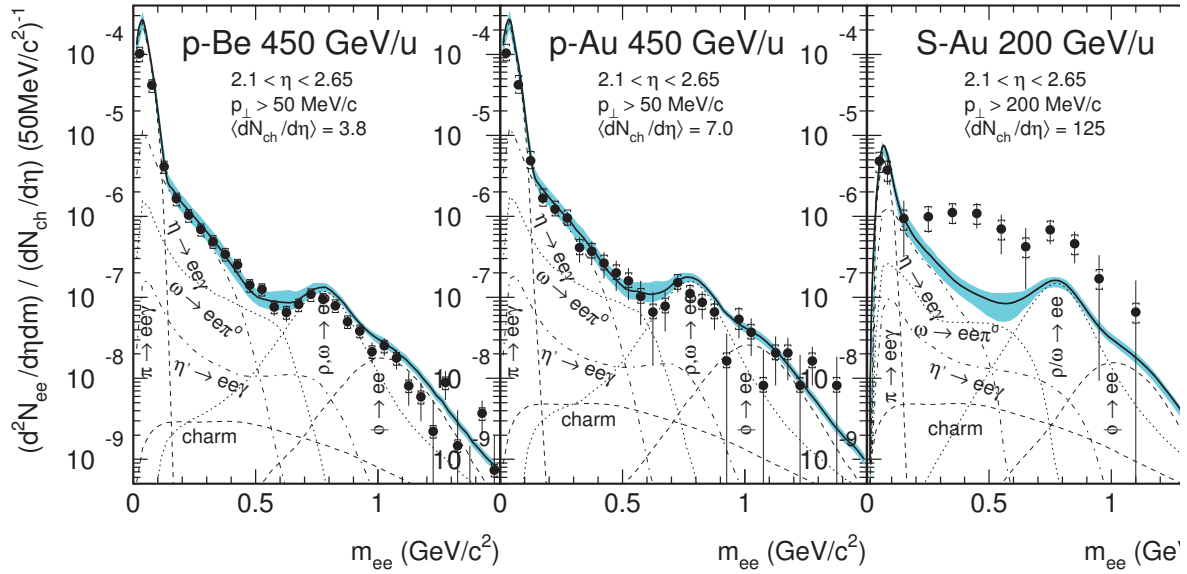
Figure 1.16.: Inclusive e^+e^- invariant mass spectra from proton-nucleon and nucleon-nucleon collisions, measured by the CERES Collaboration[23]. Curves show contributions from different hadron decays, expected based on proton-proton collisions. Thick line with the shaded area represents the sum and its systematic error. Higher transverse momentum (here denoted by $p_\perp$) cut results in the decrease of the yield from π^0-Dalitz decay in S+Au.

with two in-medium scenarios [56, 77], discussed in Section 1.4. This comparison clearly favors the in-medium hadronic many-body effects. At the same accelerator the NA60 Collaboration measured $\mu^+\mu^-$
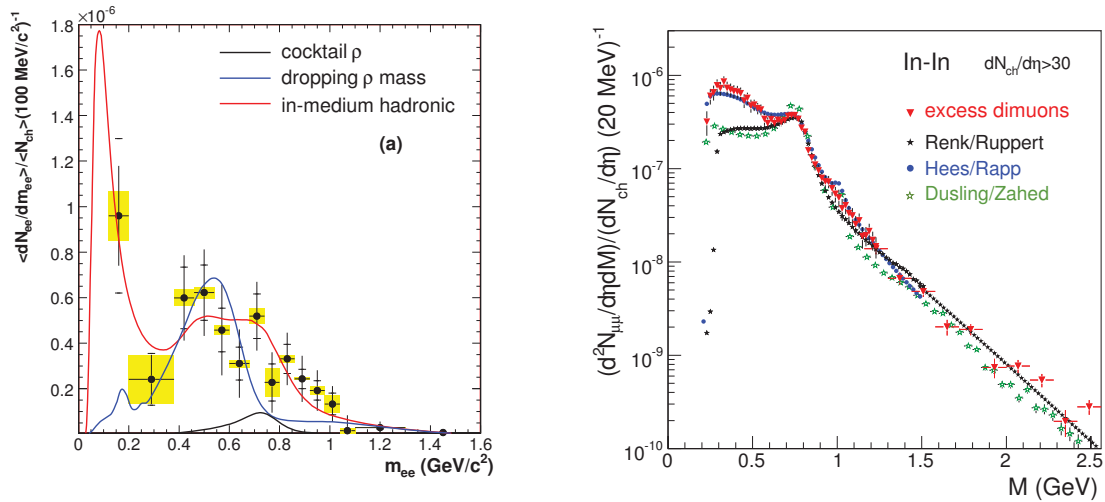
Figure 1.17.: Left: invariant mass spectrum of dileptons measured in Pb+Au at $158A$ GeV beam kinetic energy by the CERES Collaboration [24], together with model calculations of the ρ^0 spectral function. Right: invariant mass of excess dimuons measured at the same energy in In+In by the NA60 Collaboration [21] compared to the model calculations of Ruppert *et al.* [25], van Hees and Rapp [26] and Dusling and Zahed [27].

in In+In at $158A$ GeV energy [78, 21]. In the dimuon channel it was affordable to achieve an excellent data quality thanks to the absence of the main uncorrelated background source in e^+e^- – the external photon conversion in detector material. In Fig. 1.17 (right panel), comparison of the excess dimuons

to theoretical models is displayed. Good agreement of the many-body calculation of [26] with data is clearly visible. It is also possible to fit the function $dN/dM \propto M^{3/2} \exp(-M/T)$ to the IMR of the spectrum after subtracting Drell-Yan and $D\overline{D}$ contributions. The advantage over fitting to the spectra of transverse momenta or related quantities is that invariant mass, by definition, is a Lorentz invariant and is insensitive to the motion of the source emitting the radiation. The inverse slope parameter T can then be interpreted as a true temperature, not shaded by the collective expansion. In case of $\mu^+\mu^-$ measurement by NA60, the value extracted from the fit in the range $1.2 < M < 2.0\,\mathrm{GeV}/c^2$ was $T = 205 \pm 12\,\mathrm{MeV}$ [21]. The obtained value is an average over space-time evolution of the source of the dileptons in the fit range. Even though the source is supposed to be dominated by the quark-gluon plasma and this constraints the spread of temperature values around the average, this result still shows, that the temperatures reached in hot and dense stage of heavy-ion collisions are by far higher than those of chemical freeze-out in the same nuclear reactions.

Electromagnetic probes are also used at much higher energies available at Large Hadron Collider (LHC) in CERN. Here the result from direct real photons (photons not coming from decays of particles, but from thermal source) measured by the ALICE Collaboration in Pb+Pb at $2.76A$ GeV [28] are difficult to interpret. On the one hand, extremely high temperature extracted from the fit to the transverse momentum spectrum of photons, $T = 304 \pm 51\,\mathrm{MeV}/k_B$, see left panel of Fig. 1.18, indicates that they are radiated mostly in rather early stage of the collision. On the other hand, a sizable elliptic flow parameter v_2, see right panel of the Fig. 1.18, comparable to the one of hadrons, speaks for later emission, when the flow is already established. Similar measurements have been made by PHENIX at
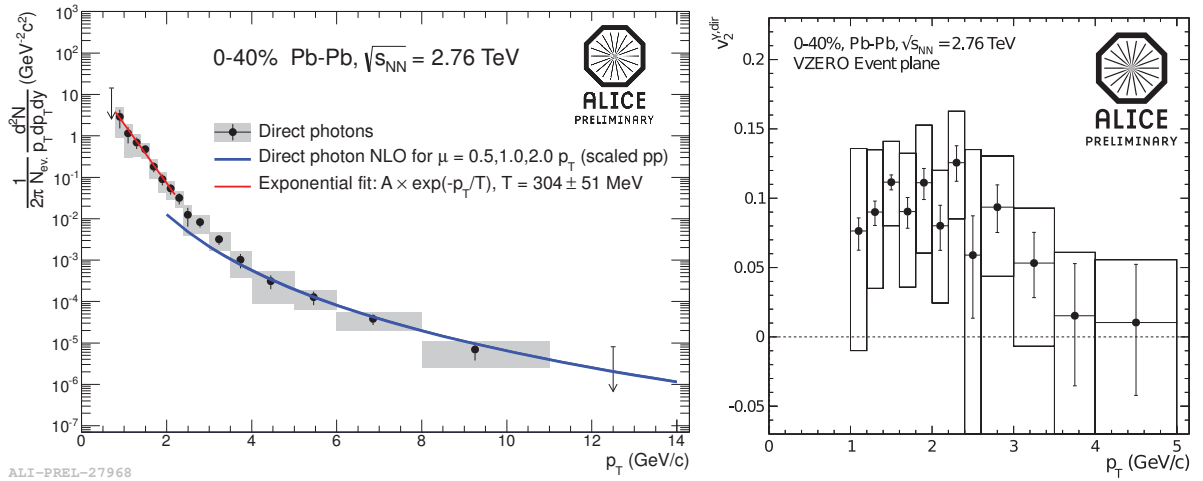
Figure 1.18.: Direct photons measured by the ALICE Collaboration in 40% most central Pb+Pb at $2.76A$ GeV beam kinetic energy [28]. Left: transverse momentum spectrum, right: elliptic flow coefficient v_2 as a function of transverse momentum.

RHIC [79] with the slope $T = 321 \pm 19(\mathrm{stat}) \pm 19(\mathrm{syst})\,\mathrm{MeV}/k_B$ for 0-20% most central Au+Au collisions. Even though it can be argued, that part of the high value inverse slope parameter can be explained by the blue-shift of the expanding fireball, large yield of direct photons itself indicates early emission with high temperature and the precise statement of the so-called "direct photon puzzle" is that theoretical models have difficulties in simultaneous of p_T and v_2 distributions [80]. For example, in refs. [81, 82] calculations that agree with ALICE and PHENIX data within systematic uncertainties were presented, but later ref. [80] provided higher precision data, with which the calculations are no longer fully consistent.

The connection between high and low energy regime is brought by the Beam Energy Scan at Relativistic Heavy Ion Collider (RHIC) in Brookhaven National Laboratory (BNL) in Upton, NY, US. Initial results on the size of the low-mass dielectron excess over hadronic sources, normalized to the number of pions, as a function of $\sqrt{s_{NN}}$ is shown in Fig. 1.19.
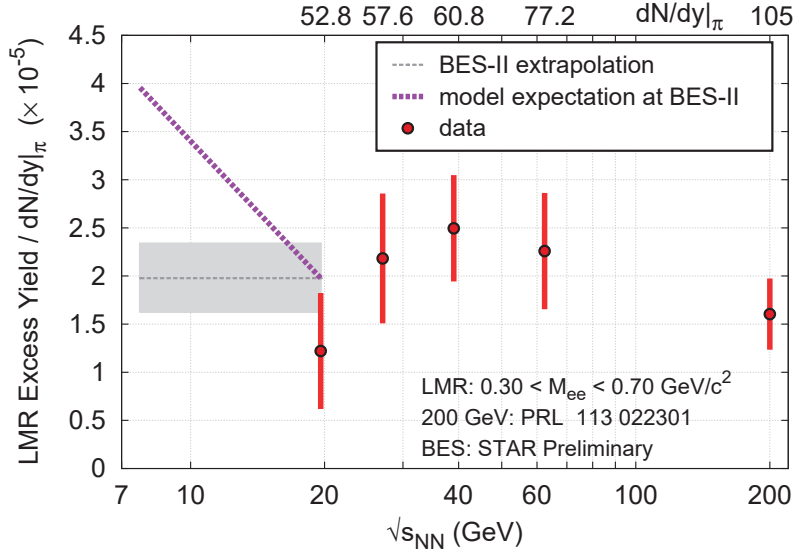
Figure 1.19.: Dielectron excess as a function of beam energy, measured by STAR at RHIC [29].

At low energies of the order of 1A GeV, first measurements of several collision systems were performed by the DLS Collaboration at Bevalac in BNL [31]. The difficulties to explain the data with the models used for higher energies collisions became famous in the history of the field as the "DLS puzzle". Eventual doubts about the correctness of the data were resolved by the HADES measurement at SIS18 (*Schwerionen-Synchrotron*, 18 stands for magnetic rigidity in T·m) in Darmstadt, Germany [30]. The results are in great agreement, as can be seen in Fig. 1.20. The right panel of this figure shows, that the excess yield scales with the beam kinetic energy in the same way as π^0. This leads to the conjecture, that at low energies significant contribution are Dalitz decays of baryonic resonances, the source of much less relative importance in high-energy experiments. The comparison with later measured $p + p$ and $n + p$ (quasi-free neutron from deuterium) showed, that dilepton production in C+C is nothing else, than just a sum of contributions of individual nucleon-nucleon collisions. Together with the fact that the excess yield in C+C, scaled to the number of produced pions, is independent of collision energy, this provides a convenient reference for collisions of heavier systems [83].

First such measurement was Ar+KCl at bombarding energy of 1.76A GeV [38]. In this case the excess yield is much larger, as can be seen in Fig. 1.21. It shows, that the yield in C+C is indeed just a superposition of elementary collisions, while in Ar+KCl it is enhanced in the region above the π^0 mass. The scaling of the excess with the number of nucleons participating in the collision was found to follow the power law $N_{\text{exc}} \propto A_{\text{part}}^{\alpha}$ with $\alpha = 1.41^{+0.19}_{-0.27}$. Corresponding exponents for pion production amount to $\alpha \approx 0.85$ and for η to $\alpha \approx 1.2$ at 1A GeV and $\alpha \approx 0.8$ at 2A GeV [84]. The transverse mass ($m_\perp = \sqrt{M_{ee}^2 + p_\perp^2}$) distribution $1/m_\perp^{3/2} \, dN/dm_\perp \propto \exp(-m_\perp/T_{\text{eff}})$ was also extracted from this data and is shown in the right panel of Fig. 1.21 for different invariant mass bins. This allows to extract slope parameter T_{eff}. The fits are also indicated in the figure. The parameter stays close to the value 80 MeV for lower masses, but gets as high as 130 MeV in the region dominated by decays of vector mesons. This reflects increase of the T_{eff} as mass grows, according to the relation $T_{\text{eff}} = T + \frac{1}{2}m\beta_T^2$, where T is the true temperature of the emittng source and β_T is the radial expansion velocity (see. e.g. [85, 86]).

The spectra can be well reproduced by a coarse-graining approach within the framework of microscopic transport calculations [87]. The idea is to extract thermodynamic properties of the hadronic medium in small space-time cells from the transport simulation and use the formula 1.9 to calculate the modifications of vector meson spectral functions. The results are shown in Fig. 1.22. The right panel proves the inevitable necessity of including baryonic effects to the spectral functions.
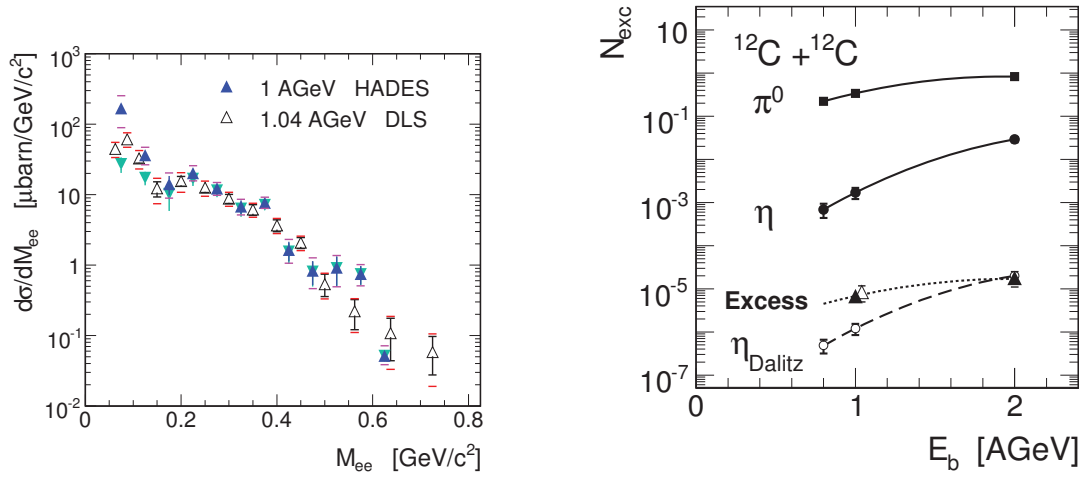
Figure 1.20.: Left: dielectron production in C+C collisions measured at $1A$ GeV by HADES [30] and at $1.04A$ GeV by DLS [31]. Both data sets are within the DLS acceptance. Right: scaling of the excess e^+e^- yield with the beam kinetic energy. In this plot full triangles represent HADES excess, open triangles - DLS, full squares - inclusive π^0 yield in C+C, full circles - inclusive η, open circles - η-Dalitz contribution. Dotted and dashed lines are scaled-down lines from total π^0 and η yield, respectively, for better comparison with the excess yield.

1.8 The aim of this work

To push forward the understanding of the strongly interacting matter at relatively low temperatures but high densities, studies of heavy-ion collisions at low energies but large systems are necessary. This
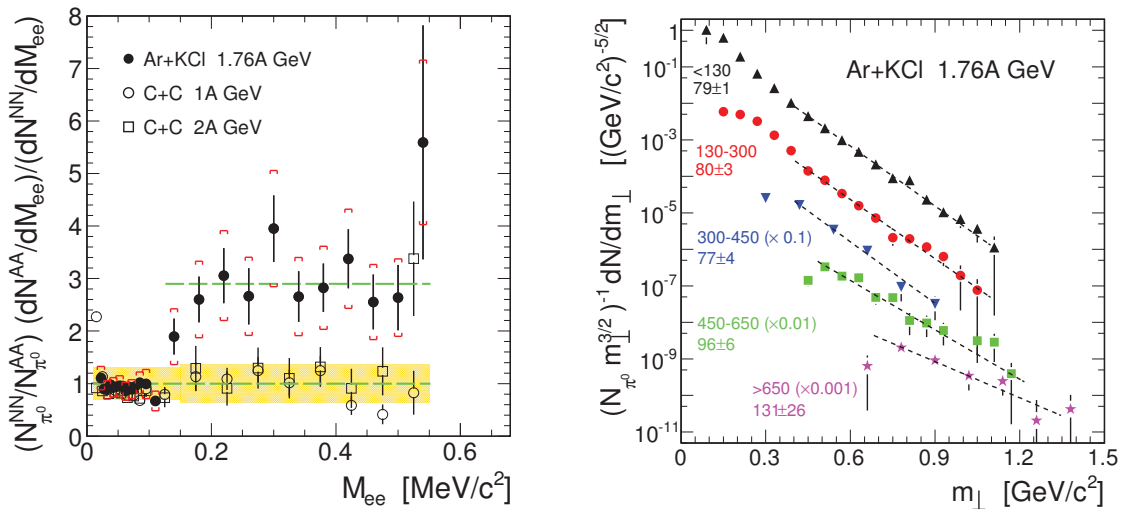
Figure 1.21.: Left: spectra of dilepton invariant mass, measured by HADES in C+C and Ar+KCl collisions, normalized to the respective numbers of produced pions and divided by average yield in $p+p$ and $n+p$ collisions. Right: transverse mass distribution in different invariant mass bins, as measured by HADES in Ar+KCl reactions at $1.76A$ GeV. Scaling factors added for visibility and extracted inverse slope parameters are indicated.
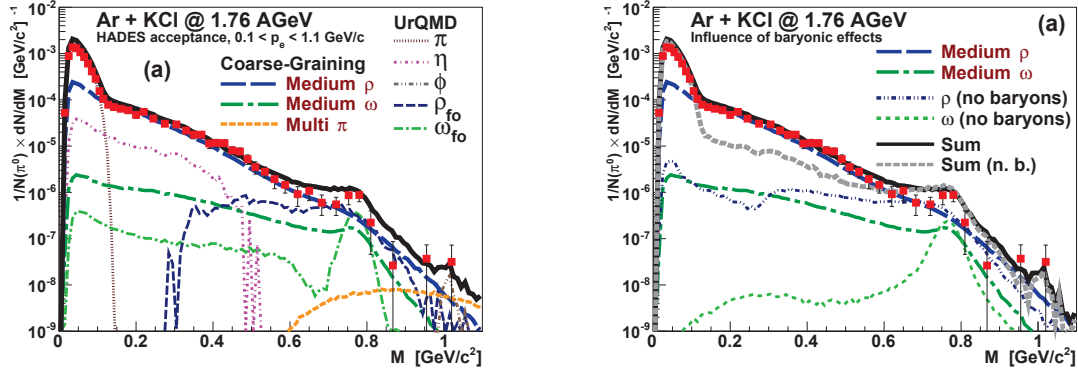
Figure 1.22.: Invariant mass spectra obtained from microscopic transport approach with coarse-grained modifications of vector meson spectral functions compared to the measurement done by HADES. Left panel shows different cocktail components, right – the importance of inclusion baryonic effects in the spectral function self-energies.

was the inspiration of the heavy-ion program in HADES. It started with the mid-sized system Ar+KCl at $1.76A$ GeV beam kinetic energy and continued with Au+Au at $1.23A$ GeV – the largest system possible with this energy at SIS18. Fig. 1.23 shows the evolution of the most central cell of the Au+Au collision as obtained in the coarse-graining approach, similar in spirit to the one discussed above [88, 89]. While at SPS energies the system reaches much higher densities than in the SIS18 and SIS100 regime, it remains in this state only for a very short time. In contrast, at lower energies the lifetime of the hot and dense fireball is much longer – up to 30 fm/c. It can be argued, that the contemporary phase diagram of
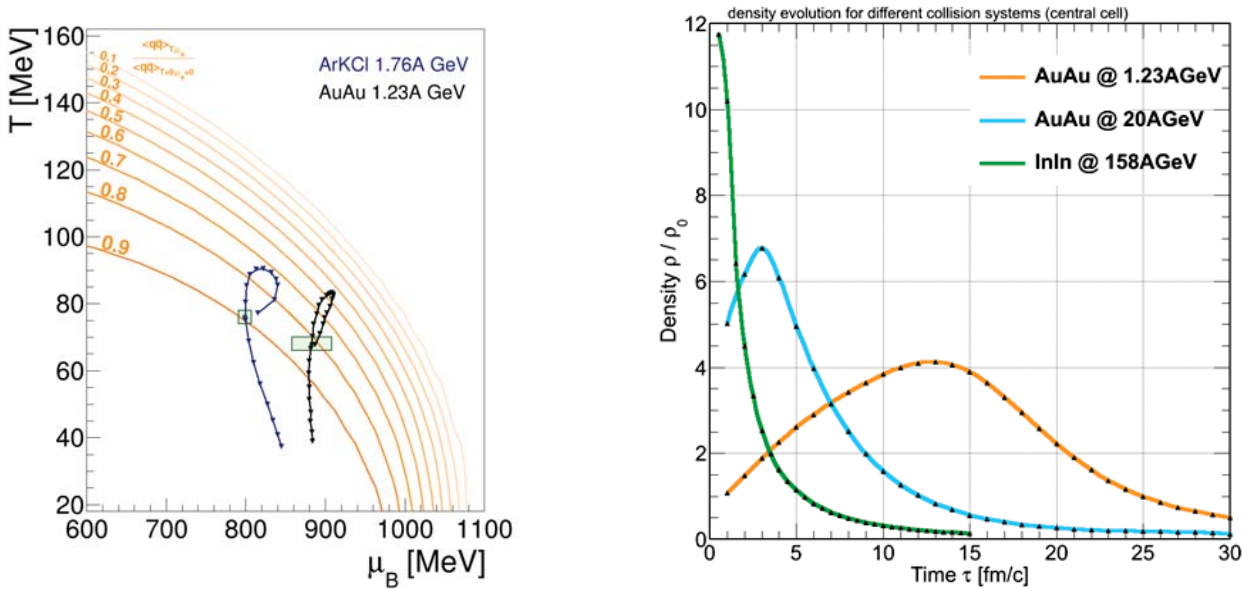
Figure 1.23.: Left: evolution of the central cell of Au+Au at $1.23A$ GeV and Ar+KCL at $1.76A$ GeV collisions in the plane of temperature and baryochemical potential. each point is plotted after a step of 2 fm/c, so their distances reflect the velocity of the evolution. In orange, the lines of constant ratio of the quark condensate to its vacuum value are indicated. They show, that at high T and μ_B the chiral symmetry is fully restored, but the onset of the restoration should be observed already at SIS18 energies.
Right: density as a function of time for different reactions.

strongly interacting matter is often plotted very carefully without any scale on axes and it is hard to state exactly where the central cell really travels in it and if the hadronic transport is still valid there. One can even doubt, if it is allowed at all to extract thermal properties of for systems at such low energy, but results on particle rates [90] and dilepton production [38, 87] in ArKCl show surprisingly good description. Thus Au+Au reactions at low energies may explore the *terra incognita* of the diagram. Similar like in other systems and energies, dileptons are one of the most promising senses to be used in this exploration. The aim of this work is thus to extract possibly the highest quality spectra from Au+Au at 1.23A GeV measured by HADES and hopefully to give the theory as a gift a new inspiring motivation!

2 The HADES apparatus
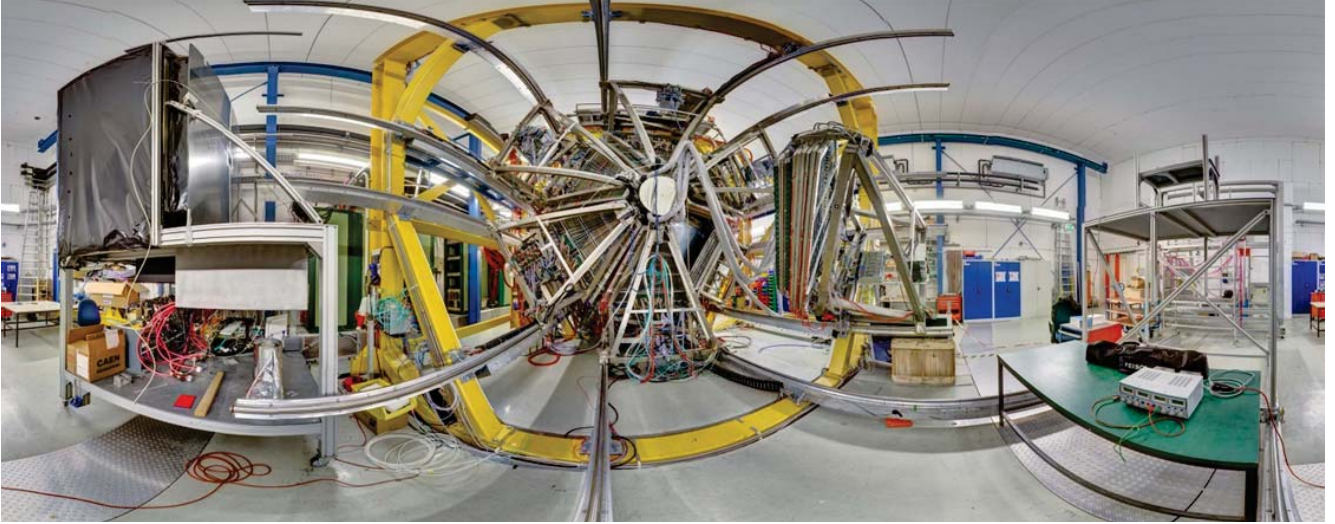
Figure 2.1.: A "fish-eye" view of HADES inside its cave. Photograph by A. Rost.

The experimental system particularly suitable for measuring properties of virtual photons radiated from heavy-ion collisions at low beam energies is the High Acceptance Di-Electron Spectrometer (HADES) operating at SIS18 accelerator in GSI Helmholtzzentrum für Schwerionenforschung in Darmstadt, Germany. The accelerator facility is able to provide a variety of beams ranging from protons to Uranium ions, of the maximum kinetic energy per nucleon depending on accelerated species, i.e. $\sim$4.5 GeV and $\sim$1.5 AGeV, respectively. Experiments using proton (on H_2 and Nb targets), deuteron (on H_2), C (on C), Ar (on KCl) and Au (on Au) have been performed by HADES. The opportunity to use a secondary π^- beam was taken recently by HADES in the summer 2014 campaign.

The HADES is essentially a magnetic spectrometer. It consists of a tracking system composed of two pairs of Multiwire Drift Chambers (MDC), located in front of and behind the magnetic field. A hadron-blind Ring Imaging CHerenkov (RICH) detector, placed in the magnetic field free region, is supported by an electromagnetic Pre-Shower detector to serve lepton identification. Velocity of a particle is measured by the time-of-flight wall detectors. The whole system is arranged in six identically designed parts (*sectors*), each of them covering 60° of the azimuth angle around the beam axis and 18-80° polar angle, cf. Figures 2.1 and 2.2 (left panel).

Precise measurements of dilepton spectra are fulfilled by the following features of the detector design:

1. A large geometrical acceptance allows to effectively register rare dielectron decays, i.e. about 40% of decay pairs with large opening angle (like $\omega \rightarrow e^+ + e^-$) can be measured and about 10% of close pairs (like from π^0-Dalitz decay).

2. A high trigger rate of the order of 10-40 kHz sufficient for collection of statistics necessary to study rare dielectron decays. With this respect, HADES is very competitive to all existing (and many of planned) heavy-ion experiments studying hadronic matter characterized by large baryon chemical potential.

3. Excellent invariant mass resolution (of the order of few %), necessary to study in-medium modifications of vector mesons.
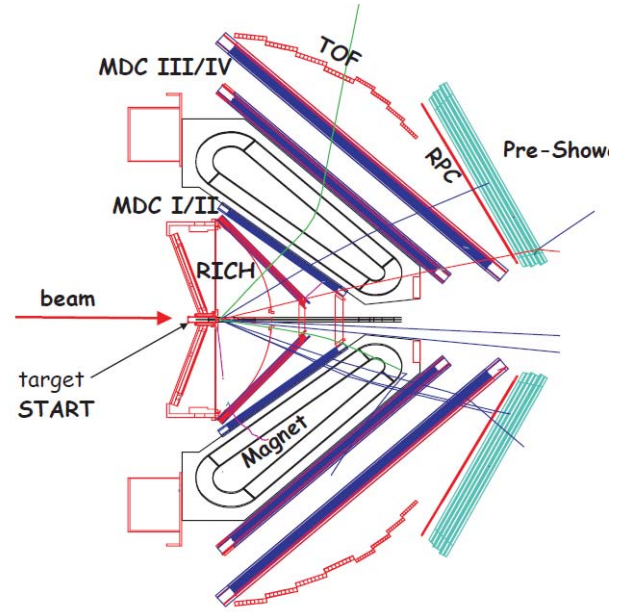
Figure 2.2: A schematic view of a cross section through two opposite sectors of HADES.

4. Low material budget ($X/X_0 \sim 2 \cdot 10^{-3}$ for tracking chambers [91]) to reduce background from secondary particles produced in detector material, especially from e^+e^- products of γ conversion, as well as multiple scattering of particles.

5. An excellent hadron discrimination makes it possible to obtain a clear e^+/e^- sample in the experimental conditions, where up to 200 charged particles in an event are crossing the acceptance of the spectrometer (for Au+Au at 1.23 AGeV), but the interesting dilepton signal is of the order of 10^{-4}.

The detector system is capable for the reconstruction of rare strangeness production like Ξ, Λ, ϕ and K^+/K^-, as well as global properties of nuclear reaction. The full description of the spectrometer is given in [92]. The following sections provide an overview of the features most relevant for the physics analysis being the topic of the current work.

2.1 Ring Imaging CHerenkov

2.1.1 Cherenkov radiation

When a charged particle passes through a medium, its electric field causes a polarization of the medium close to particle's trajectory [33]. Afterwards, the medium relaxes to its initial state, but the momentary polarization produces a small electromagnetic perturbation propagating with the speed of light. As shown on the left panel side of Fig. 2.3, if the velocity of the particle is smaller than the speed of light in the medium $v < c/n$ with n - refractive index of the medium, contributions from perturbations at different points of the trajectory will cancel out at large distances. If, however, $v > c/n$, these contributions will add up coherently to form a conical wavefront. Its propagation can also be represented in terms of rays of light, one of them is also shown in the Fig. 2.3. From the geometry shown there, one can immediately obtain the angle at which the rays are emitted:

$$\Theta_C = \arccos\left(\frac{c}{v \cdot n}\right), \tag{2.1}$$
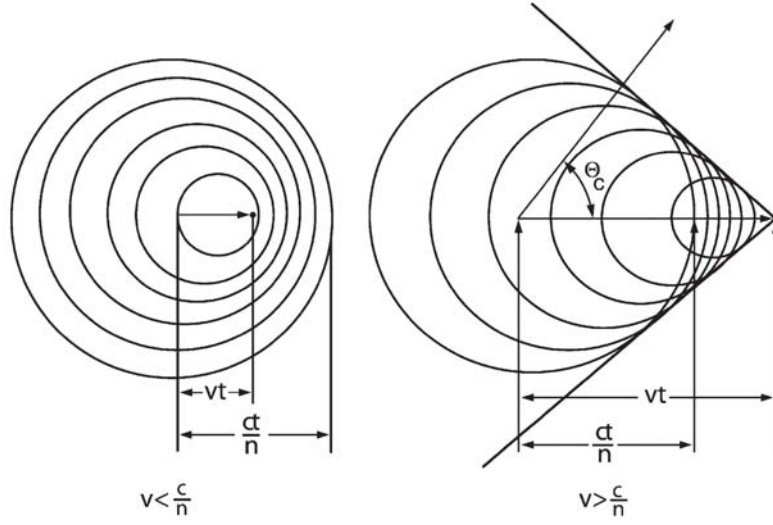
Figure 2.3.: Propagation of the electromagnetic perturbation caused by a particle traversing a medium with the velocity lower (left) and higher (right) than the speed of light in the medium. Figure taken from [33]
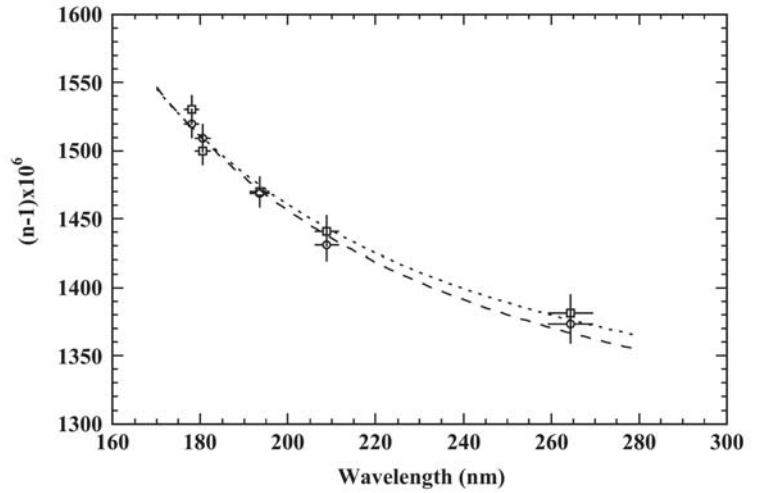
Figure 2.4: Refractive index of C_4F_{10} measured [34] as a function of the wavelength with the help of Fabry-Perot interferometer. Lines are fits of the Sellmeier formula Eq. 2.2.

where c is the speed of light, v is particle's velocity and n is the refractive index of the medium. The wavelength dependence of the refractive index is governed by the empirical Sellmeier formula:

$$(n(\lambda) - 1) = \frac{10^{-6} p_1}{p_2^{-2} - \lambda^{-2}}, \tag{2.2}$$

where λ is the wavelength and p_1 and p_2 are free parameters. The dependence, measured using Fabry-Perot interferometer [34], is shown in Fig. 2.4. From this one can see, that the condition $v > c/n(\lambda) \Rightarrow n > \beta^{-1}$ imposes an upper limit on the wavelength. Together with the fact, that the spectrum in general grows monotonically with the energy [93] and that the sensitivity of the human eye is peaked at the green light, this allows to understand, why Cherenkov radiation is often observed as a blue light.

2.1.2 RICH detectors

From Eq. 2.1 the opening angle of Cherenkov cone depends directly on the momentum of a particle of a specific type. Measuring the angle can thus be used for particle identification with Ring Imaging
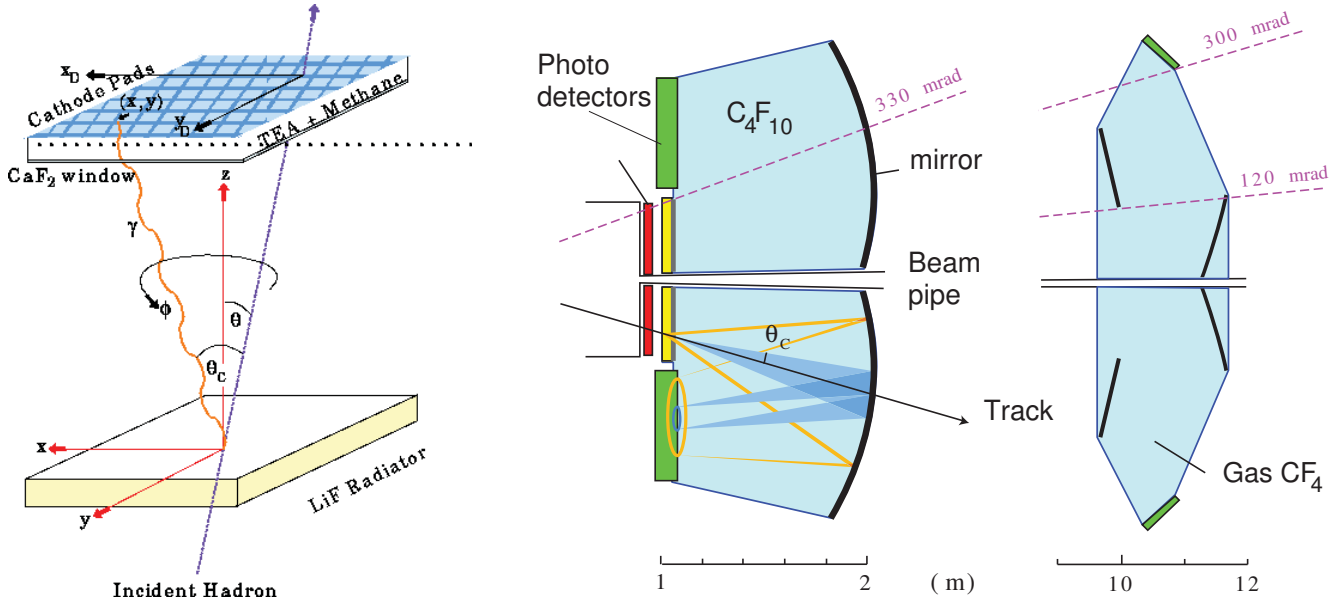
Figure 2.5.: Schematic view of RICH detectors in CLEO III (left, figure taken from [35]) and LHCb (right).

Cherenkov (RICH) detectors. One of the simplest possible applications of this idea is the RICH detector of the CLEO experiment [94], shown schematically in Fig. 2.5 (left panel). Cherenkov light is emitted, when a hadron goes through a thin LiF radiator. A small gap between it and the Multi-Wire Proportional Chamber (MWPC) serving as photon detector lets the cone open such, that photons emitted at specific opening angle hit those pads of the MWPC, which are located on the circle of a radius corresponding to the opening angle.

A disadvantage of such a simple setup is a short path of the particle through the radiator and thus a small number of Cherenkov photons. However, introducing thicker radiator while still letting the photons hit the photon detector directly would lead to appearance of a "donut" instead of a circle on the pad plane (sum of circles of different radii from different points of the path) and again make the determination of the cone opening angle impossible. Another problem is that installing the photon detector on the way of charged particles will lead to a number of difficulties (e.g. many direct hits of particles, which both make fake signals and damage the detector), especially in heavy-ion collision experiments.

Both issues can be solved by introducing a spherical mirror reflecting Cherenkov light in such a way, that photons emitted along the whole path of a particle hit a single circle on the detection surface (in this case located backwards), as shown in case of both RICH detectors of LHCb experiment [95], shown in Fig. 2.5 (right panel), and HADES RICH in Fig. 2.6.

2.1.3 HADES RICH

In case of HADES' RICH detector, shown in Fig. 2.6 (left), opening angle of the Cherenkov cone is not measured. For the C_4F_{10} radiator gas, the threshold value of the Lorentz factor $\gamma = \sqrt{\frac{1}{1-1/n^2}}$ is 18. Fig. 2.7 shows, that in the momentum region available for particles emitted from Au+Au at 1.23 AGeV only electrons and positrons can have γ high enough to radiate Cherenkov light. The respective momentum threshold is 10 MeV/c, while for next heavier particles, muons and pions, it is roughly 1.9 and 2.4 GeV/c, respectively. The criterion for electron identification is then just the existence of the ring.

The photon detector is an MWPC with CsI photocathode segmented such, that ring diameter in terms of segments (*pads*) is almost constant over the whole detector (7-8 pads). This allows for application of efficient ring finding algorithms. The counter gas of MWPC is CH_4.

The two volumes of HADES RICH are separated by a CaF_2 window to avoid mixing of gases. The material of the window was chosen to obtain sufficient transmittance. The data on transmittances and
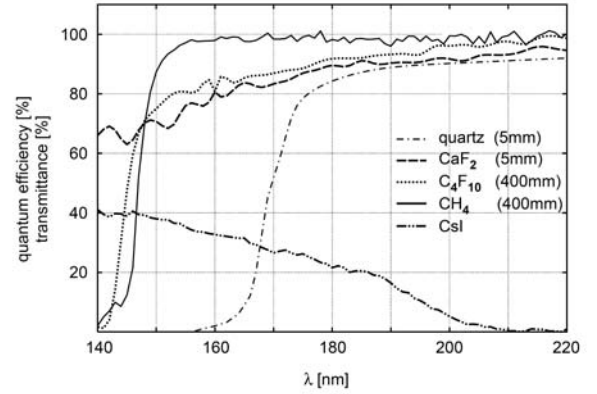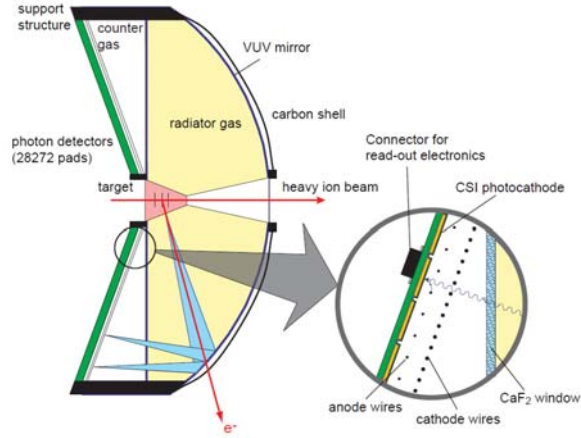
Figure 2.6.: Left: schematic view of the HADES RICH and its photon detector plane. Electron track is indicated in red, rays of Cherenkov light in blue. Right: Optical parameters of the components of HADES RICH detector. [36]

quantum efficiencies of materials used to build the HADES RICH detector are shown in Fig. 2.6 (right). One may note rather low quantum efficiency of the CsI, which might even have decrease due to the known effect of aging. This led to an idea of replacing the MWPC by an array of Photo-Multiplier Tubes (PMTs), which will be performed in HADES from 2019 on.
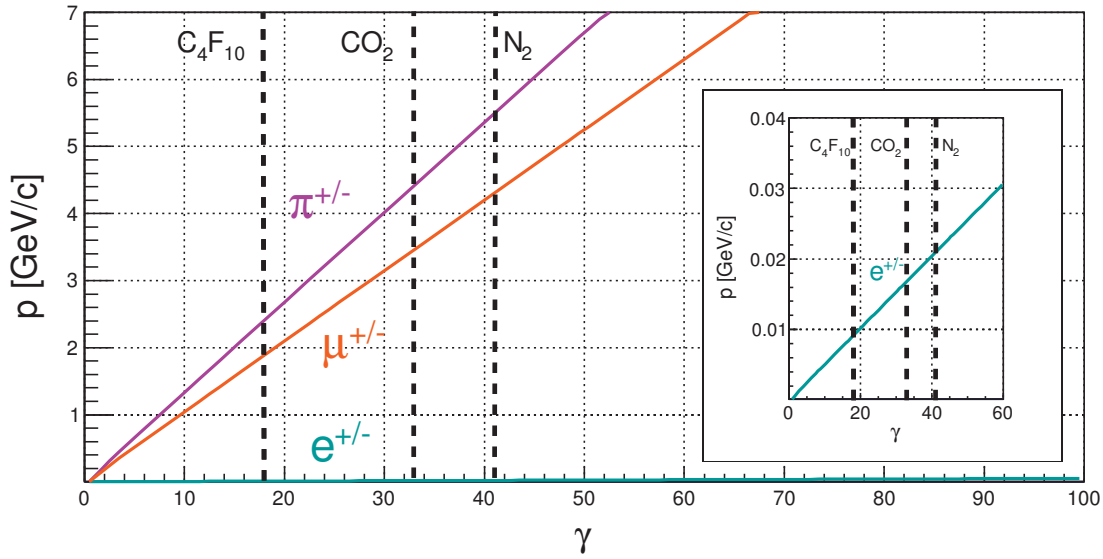
Figure 2.7.: Lorentz factor γ dependence of the momentum of electrons muons and pions. Dashed lines indicate threshold values of γ for emission of Cherenkov light in the C_4F_{10} used in HADES RICH, as well as in CO_2 and N_2, also often considered as radiator gases in RICH detectors.

2.2 Target

In the April 2012 experiment the Au target consisting of 15 segments, shown in Fig. 2.8, was used. The reason for taking the segmented target was to reduce photon conversion probability (by increasing the chance, that photon leaves the target region without interacting with other Au nucleus).

2.3 Tracking system

The main design guidelines for the tracking system were invariant mass resolution of 1-2% for electron-positron pairs from decays of vector mesons, e.g. $\rho(770)$, $\omega(782)$, $\phi(1020)$ (corresponding to about 2% momentum resolution of single leptons) and low material budget to reduce the probability of γ conversion and multiple scattering of charged particles. It should also be able to handle large charged particle multiplicities with a high event rate, what is necessary to investigate electromagnetic decays of vector mesons in Au+Au collisions.

To fulfill these requirements, the tracking system of HADES consists of a compact superconducting magnet and four sets of multiwire drift chambers, two traversed by a charged particle before its trajectory is bent by the magnetic field and two traversed after that.

2.3.1 Magnet

Six coils of the IronLess Superconducting Electron (ILSE) magnet are mounted around the circular support structure. The coils generate field of a nearly toroidal shape and strength of 3.6 T inside the coils and below 0.8 T between them, when operating with the highest current of 3500 A, see Fig. 2.9. During the Au+Au run the current was set to 2500 A. The chosen shape of the field assures, that it vanishes in the region, where MDCs and RICH are located. Coils of the magnet are cooled by a single phase liquid helium at $p = 2.8$ bar and $T = 4.7$ K.

Figure 2.8.: Gold target used in the April 2012 experiment.
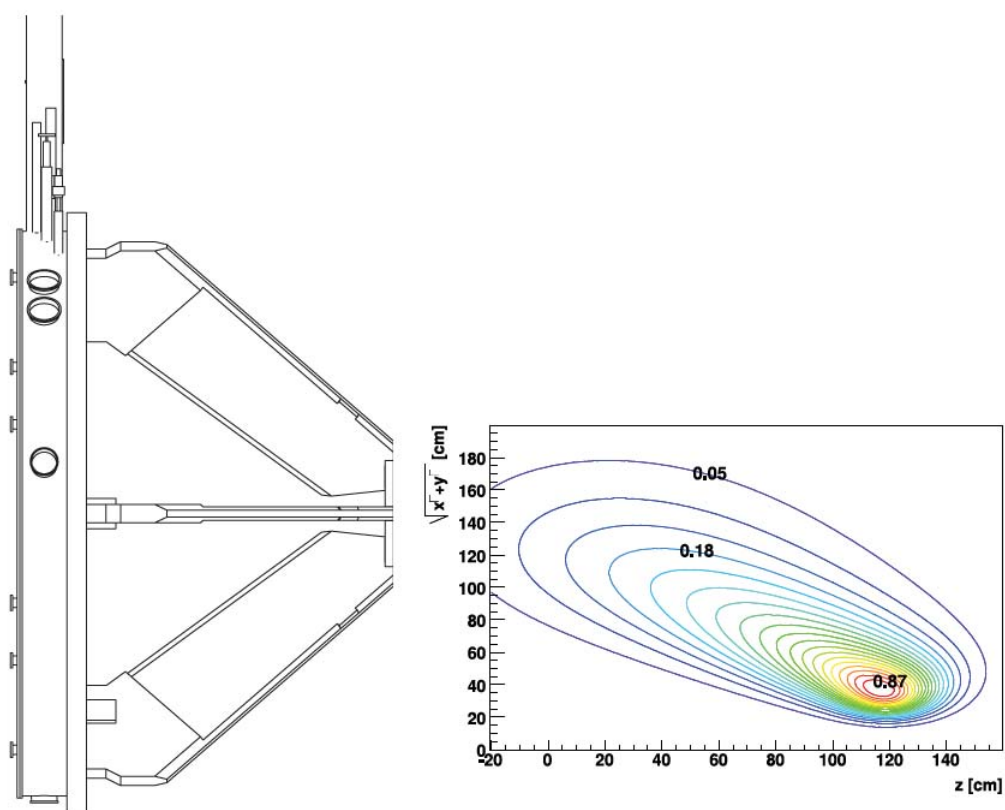
Figure 2.9.: Left: side view of HADES magnet coils. Right: map of the magnetic field between the coils.

2.3.2 Multiwire Drift Chambers

The smallest unit of the Multiwire Drift Chambers (or Mini Drift Chambers, in all cases abbreviated as MDC) of HADES is a cell consisting of a sense wire together with two potential wires located in the same plane and with two surrounding planes of cathode wires, as shown in the left panel Fig. 2.10. Each of 24 chambers (6 sectors×4 modules) contains 6 layers of such cells which are orientated as explained in the right panel Fig. 2.10 in order to get high spatial resolution of the order of 60-100 μm in polar and 120-200 μm in azimuth direction.

Particle's trajectory and momentum has to be reconstructed from only two points before and two after the magnetic field, what is already challenging. First, fired cells in all layers of each single chamber are projected to a common plane to find a maximum representing a crossing point of fired wires, corresponding to a point traversed by a particle. This is illustrated in Fig. 2.11. Two such points in the inner and the outer pair of chambers define *inner* and *outer track segments*, which are then matched to obtain a *track candidate*.

Momentum is calculated with a *Runge-Kutta* algorithm, which is used to solve numerically the equation of motion of a particle in known magnetic field (defined by a 3-dimensional field map). It is applied iteratively and the quality of the trajectory reconstruction is quantified by the result of the χ^2 test.

Moreover, the readout electronics of drift chambers is able to extract width of measured signal defined as time-over-threshold. This can be translated by a non-linear transformation into specific energy loss dE/dx_{MDC} of a particle. As Fig. 2.12 shows, it is not really a quantity allowing to discriminate between electrons and pions, but at least it can be used to reject of protons in a multi-parameter analysis.
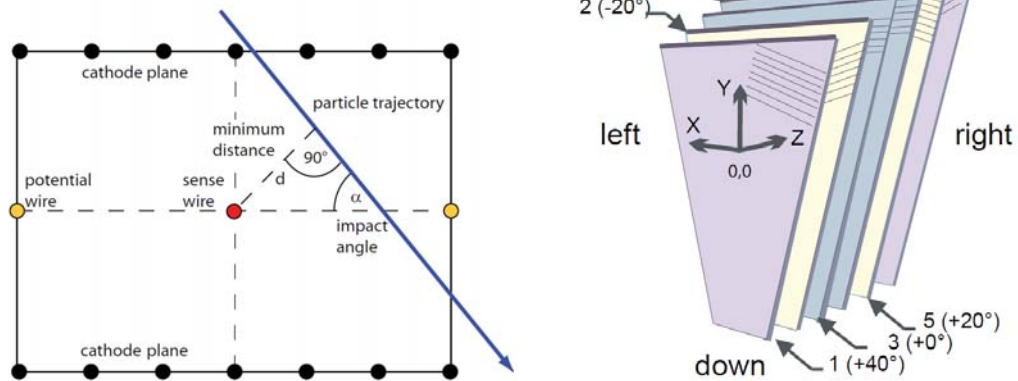
Figure 2.10.: Left: a single cell of MDC showing the arrangement of different wires. The minimum distance of a charge particle track (indicated as a blue arrow) to the sense wire is also defined. Right: orientation of wires in different layers of HADES MDCs.
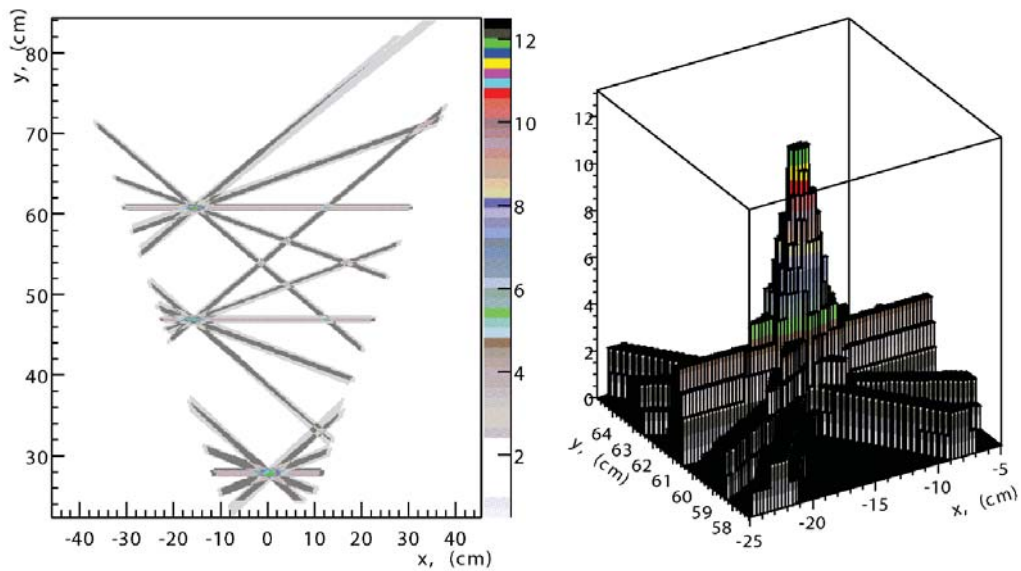
Figure 2.11.: Finding a point passed by a charged particle in MDCs as a crossing of several fired wires.
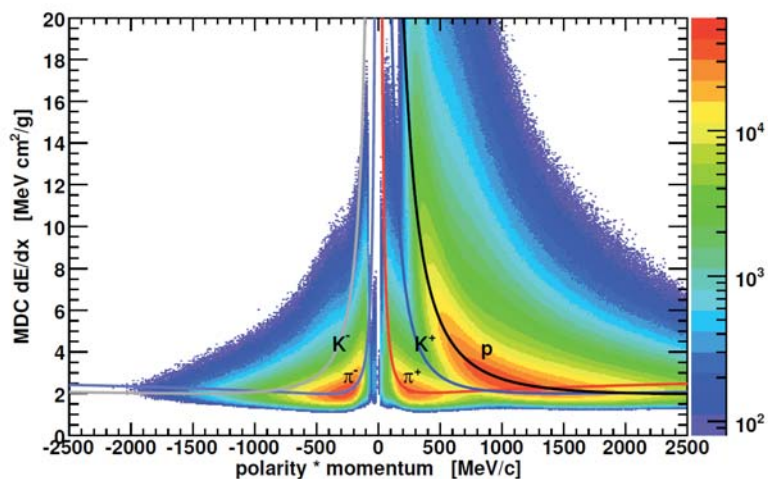
Figure 2.12: Momentum dependence of the specific energy loss dE/dx in HADES Multiwire Drift Chambers. Colored solid lines indicate values expected for different particle species as calculated using usual Bethe-Bloch formula.

2.4 META detectors

At the end of the way of a charged particle through the HADES detector system, three META (Multiplicity Electron Trigger Array) detectors are placed. Polar angles above roughly 45° are covered by the TOF scintillator wall to measure time-of-flight. The same task is performed in polar angle region below 45° by the wall of Resistive Plate Chambers (RPC). Behind the RPC, electromagnetic Pre-Shower detector supports the electron identification in the region of high occupancy.

2.4.1 TOF wall

It consists of 8 modules, each containing 8 scintillator strips (of the cross section varying from 2×2 cm^2 to 3×3 cm^2 and length from 1475 to 2365 cm) in every HADES sector (see Fig. 2.13) with photomultiplier tubes (PMT) attached on both sides. From the times, when light arrives to both PMTs one can easily extract time as well as the position of the hit. After the proper offline calibration, the time resolution was found to be $\sigma = 150$ ps [96]. Additional information useful for particle identification is the specific energy loss dE/dx_{TOF} calculated from the signal amplitude.

For the Au+Au at 1.23 AGeV collisions and central events, i.e. with impact parameter from 0 to 3 fm (4% most central collisions) the probability, that more than one particle crosses the same TOF cell is about 4%.

2.4.2 RPC wall

During the detector upgrade in 2010 Resistive Plate Chambers have been installed in place of the old TOFino scintillator wall. It was necessary to handle high particle multiplicities in the Au+Au experiment.

In each sector of HADES the RPC wall consists of two layers [97], each subdivided into three columns containing 31 strip-like cells (cf. Fig. 2.14). This design allows both for a very high time resolution and a granularity sufficient for the high multiplicity regime. Two layers of RPC increase reconstruction efficiency and acceptance. Widths of cells range from 12 to 52 cm, heights from 2.2 to 5 cm. The resistive material in cells are two glass electrodes, three aluminum electrodes serve as the conductor, see Fig. 2.15. High voltage is applied to the middle of the aluminum electrodes, while the upper and the lower one are grounded. Signal is read out from these electrodes as well, through the soldered connectors visible in the central part of the photograph in Fig. 2.15.

Cells are flushed with the mixture of $C_2H_2F_4$ (90%) and SF_4 (10%) [98]. Each single cell is contained in an individual shielding in order to reduce crosstalk effect and keep clusters created by charged parti-
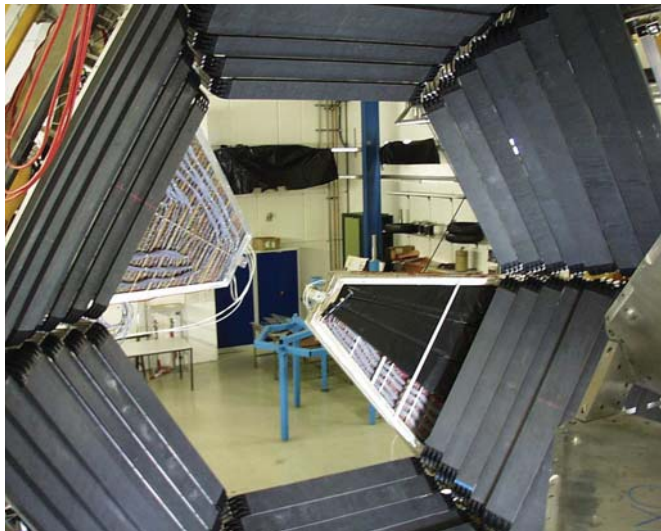
Figure 2.13: TOF during installation on the HADES mechanical frame. In the central part two sectors of Pre-Shower can be also seen.
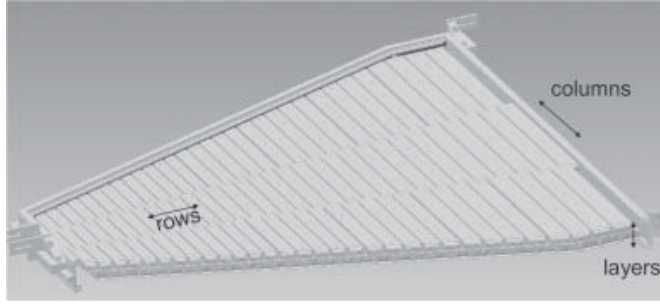
Figure 2.14: Arrangement of cells in a one sector of the RPC wall.
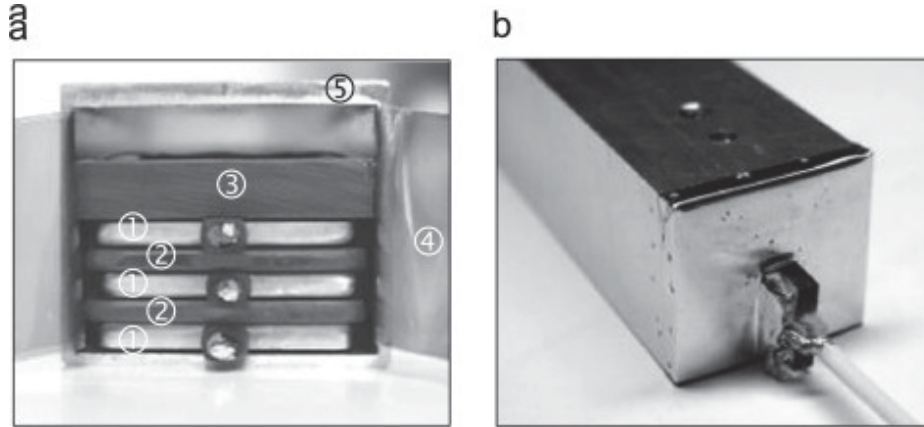
Figure 2.15.: (a) Cross-section through a single RPC cell: 1-aluminum electrodes, 2-glass electrodes, 3-PVC pressure plate, 4-kapton insulation, 5-aluminum shielding. (b) Outside view of a cell with shielding, end cap and HV cable.

cles small. Since mechanical uniformity may influence the time resolution, cells are compressed by three springs applying a controlled force on a PVC plate, which in turn distributes it over the whole cell.

It has bean found [99], that during the Au+Au experiment the intrinsic efficiency of the HADES RPC was about 95%, the intrinsic time resolution below $\sigma = 70$ ps (stable over the whole beam-time, as shown in Fig. 2.16) and the measured time resolution for electrons (including contributions from the Start detector and tracking) amounted to $\sigma = 81$ ps.

For the Au+Au at 1.23 AGeV collisions and central events the probability, that more than one particle crosses the same RPC cell is about 5%.

2.4.3 Pre-Shower detector

When a fast, light particle passes through heavy material (like Pb) it gets decelerated and emits electromagnetic radiation (*bremsstrahlung*). Radiated photons may convert in the same material into e^+e^- pairs, which in turn may emit further bremsstrahlung photons. This leads to development of a cascade (or *shower*) of charged particles. Because of much larger masses of other particles, like protons or pions, emission of bremsstrahlung is strongly suppressed. Therefore this phenomenon can be used for electron and positron identification.

The Pre-Shower detector consists of three gas chambers separated by two layers of lead. In each chamber signal is read by a planar electrode divided in 32 rows of pads. Each row contains from 20 to 32 pads, as shown in Fig. 2.17. If an electromagnetic cascade is induced, the number of charged particles traversing some region of the third (*Post II*) chamber should be larger, then in the second one (*Post I*) and this should be larger than in the first one (*Pre*). For the given pad geometry, the signal integrated over 3×3 pads around the local maximum found in Pre chamber is in average larger in Post I and Post II than in Pre (see Fig. 2.18). This is not the case for hadrons which fly through the detector without
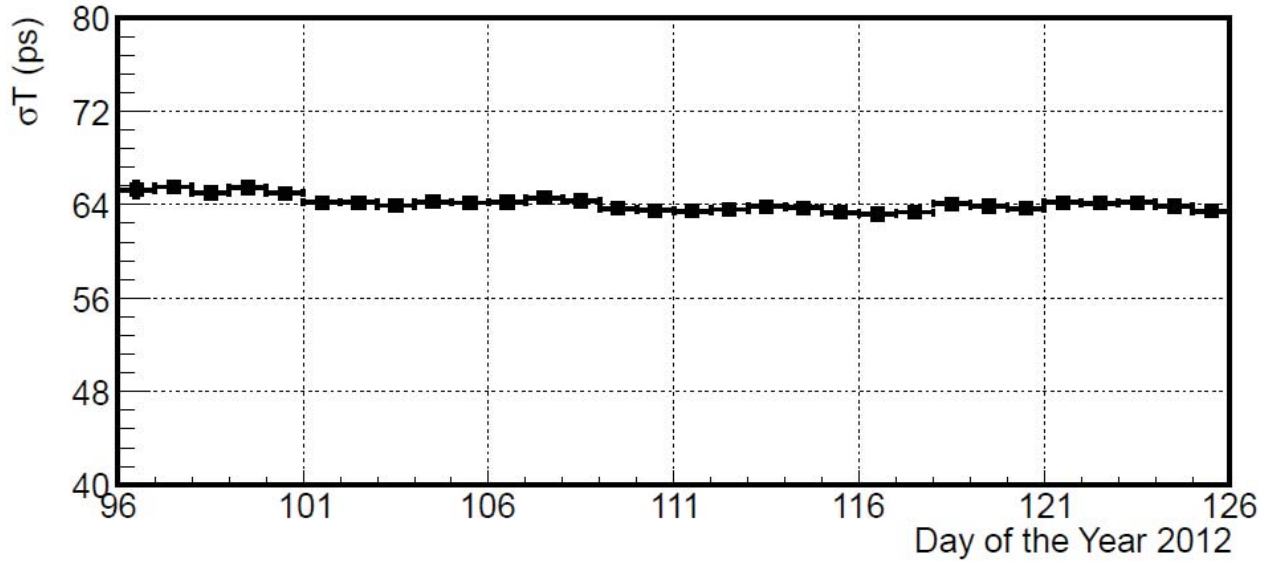
Figure 2.16.: Time resolution of the RPC determined separately for each day of the Au+Au run, showing performance of the detector stable in time.
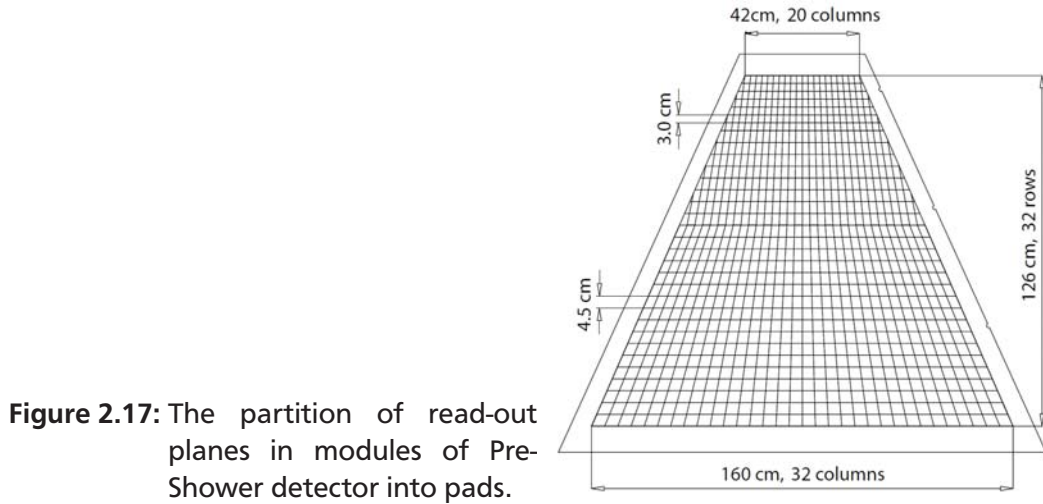
Figure 2.17: The partition of read-out planes in modules of Pre-Shower detector into pads.

generating additional particles, except few percent cases when hadronic showers are generated, or even get stopped in one of lead layers. This allows to define the quantity:

$$\Delta Q = \sum_{\text{Post I}} Q + \sum_{\text{Post II}} Q - \sum_{\text{Pre}} Q \qquad (2.3)$$

as a quantity discriminating between electrons (or positrons) and hadrons. A careful calibration of the detector, allows to remove inhomogenities in detector's response due to different behavior of readout electronics and gas amplification and thus to cut on the above quantity in a consistent way for the whole detector. It is described in the Appendix A.

2.4.4 Beam detectors

The beam detector Start, shown in the Fig. 2.19, is used to provide start time with a high resolution, crucial for time-of-flight measurements and also to monitor beam structure and focusing. It is a 70 μm
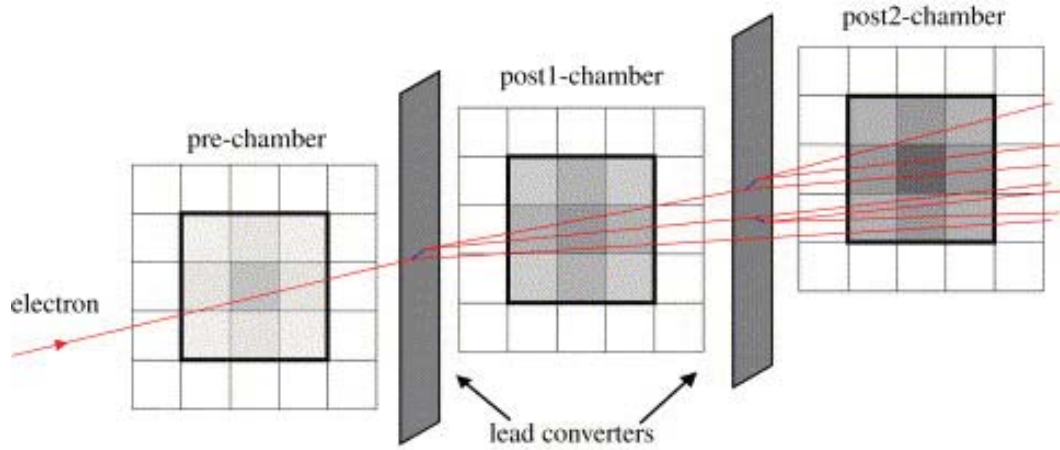
Figure 2.18.: A schematic view of the Pre-Shower hit reconstruction algorithm. In three modules charge induced on 3×3 corresponding pads around the maximum in the first module is integrated. If an electromagnetic shower was formed, the charge in the second and third module should be larger, than in the first one.
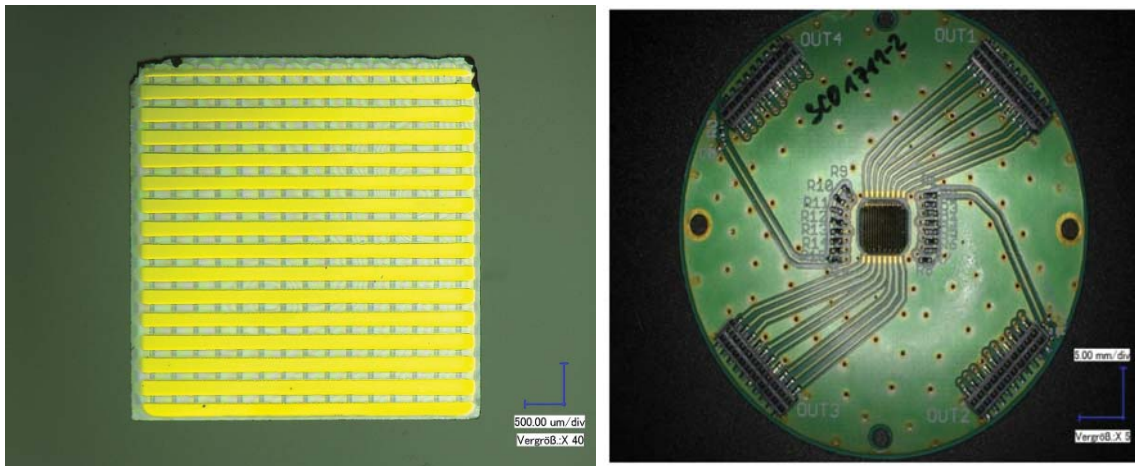
Figure 2.19.: Photographs of the Start detector used in the Au+Au run. Left: metalization. Right: detector mounted in the PCB.

thick single-crystal Chemical Vapour Deposition (scCVD) diamond detector [100, 101]. On both sides of the diamond there is a 50 nm Cr layer and 150 nm Au layer split in 16 strips of 200 μm width oriented in x and y direction and thus providing position information. Intrinsic time resolution of the Start detector was about 60 ps and efficiency was 90%.

During the Au+Au run also the VETO detector and Forward Wall hodoscope were installed in the HADES cave along the beam line behind the START counter. The former one was introduced to reject coincidences between signals in Start and TOF detectors, which were not caused by a nuclear reaction in the target. The latter one serves for reaction plane reconstruction. Information obtained from them is not relevant for the current work and then they are not described here.

Schematic view of the trigger generation in HADES during the Au+Au beam-time is shown in Fig. 2.20. Very precise digital signals from Start and time-of-flight detectors are sampled with 800 MHz clock, equivalent time span is 1.25 ns (yellow area in the figure). Then only the first signal is taken (red area). Signal from Start is delayed by ~270 ns (purple area). Signals from time-of-flight detectors are stretched to have the length of 50 ns (light green rectangles) needed to collect signals from all particles from an event and build the analog multiplicity signal which is used by the trigger (see below). Finally, the coincidence between signals is requested (dark blue rectangles), and after additional conditions of technical nature (data acquisition is not busy, there is no other trigger e.g. calibration, pulser etc.) an event is triggered with the reference time being the result of operations described. The reference time is sent to all TDC boards digitizing TOF detectors. PT2 and PT3 stand for Physical Trigger and correspond to conditions on minimal particle multiplicity. This is defined in terms of hit multiplicity in the TOF detector (in fact the number of signals from photomultipliers being two times the requested number of hits): 6 for PT2, 20 for PT3. Downscaling means, that only every eighth event of PT2 class is really triggered and stored. There is no second level trigger, defining an event with a lepton candidate, used in the past experiments (see e.g. [30, 38]), because in high multiplicity events a lepton candidate is now expected to be found in practically every event.
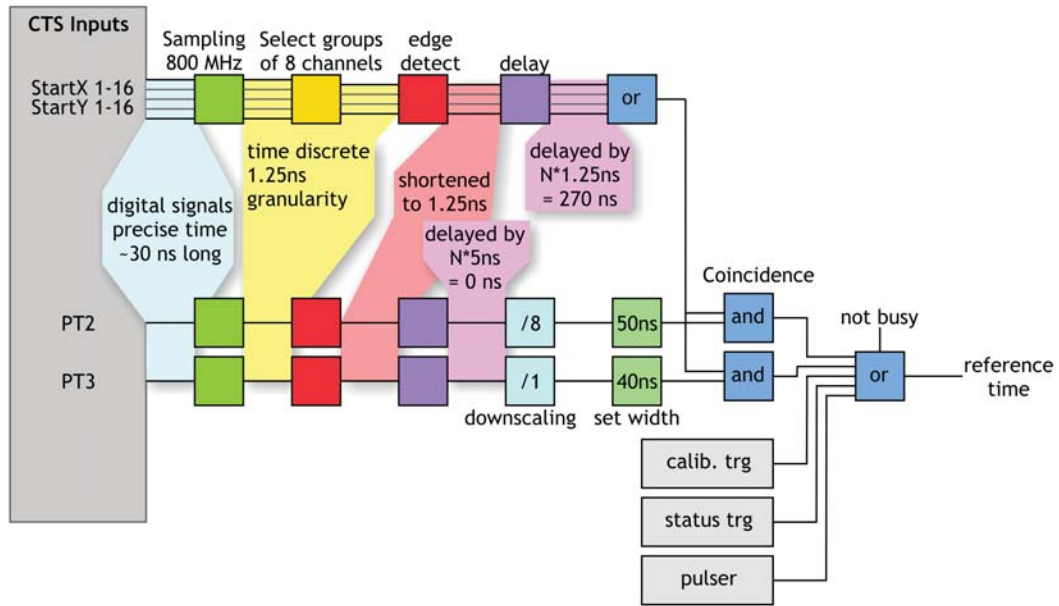
Figure 2.20.: An overview of the HADES trigger system in the Au+Au experiment.

Data acquisition system, upgraded for the April 2012 experiment, is based on Trigger and Read-out Boards developed especially for HADES (TRB [102]) using versatile Field-Programmable Gate Arrays (FPGA) with dedicated add-on boards for different subsystems (containing ADC, TDC, hubs etc.) and optical links for serial data transmission, using a special protocol called TRBnet. This provided a very high performance allowing for 8 kHz trigger rate and 200 MB/s data rate. The total volume of collected raw data in comparison to previous runs is shown in the left panel of Fig. 2.21. In the right panel, interaction rate in HADES is compared to other facilities. In HADES it is the highest out of the currently existing experiments.
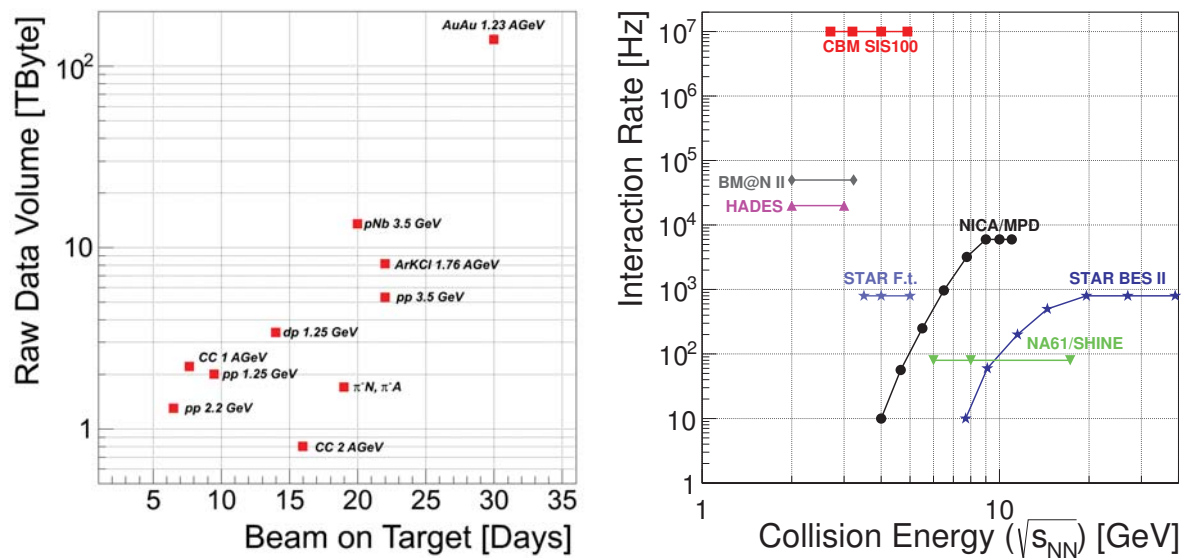
Figure 2.21.: Left: total amount of collected raw data in Au+Au and other HADES runs. Right: interaction rate in HADES compared to other existing and future experiments.

2. The HADES apparatus

3 Data analysis tools and techniques

3.1 Particle reconstruction in HADES

Data acquisition system writes *Hades List Data (HLD)* files. They contain raw data obtained from read-out electronics of various detectors: ADC or TDC values together with hardware addresses allowing to identify single module of the corresponding detector. To get the data useful for physics analysis one has to produce *Data Summary Tape (DST)* files containing, among the others, physical quantities characterizing reconstructed particles. This part of the analysis is standard and the same for all the physics cases (production of virtual and real photons, pions, strange hadrons etc.) and is performed once (although is repeated, when algorithms performing one of steps listed below are improved) and the resulting files are used by each person interested in a particular physics question. This is possible, because most of the software used in HADES is build over Hades sYstem for Data Reduction and Analysis (HYDRA) toolkit, based in turn on the ROOT Object-Oriented Data Analysis Framework.

The production of such data consist of the following steps:

1. **Unpacking** Every component of the read-out electronics is designed in such a way, that it sends the data in the form as compact as possible, especially encoding different pieces of information in a single data word (example for Pre-Shower: sector, module, row and column, where a single pad electrode is located and ADC value are encoded in a single 4-byte integer). This information has to be decoded in order to be processed further.

2. **Calibration** Values obtained from electronics modules (like ADC values) have to be converted into physical quantities (like charges), even when they are expressed in arbitrary units. This allows also to remove variations emerging from not perfectly identical modules of electronics or response of detector modules.

3. **Hit reconstruction** In this step calibrated read-outs are put together in order to reconstruct a response of charged particle trajectory with the given detector. This involves e.g. reconstruction of RICH rings, determination of crossing points in drift chambers, finding maxima and calculating integrated charges in Pre-Shower, calculating position and time-of-flight in TOF and RPC.

4. **MDC track reconstruction** From hits in drift chambers straight-line *segments* are combined separately in two chambers located "before" the magnetic field (*inner* segment) and in two chambers "after" the field (*outer* segment). One tries then to match inner and outer segments using a Runge-Kutta method. The measure of how well two particular segments fit together is quantified by the χ^2, which takes into account reconstruction errors. Requiring it to be below a specific limit allows to keep only well matched segments belonging with a high probability to the track of a single real particle. An output of the computation is a vector of particle's momentum.

5. **Full track reconstruction** To get the full information needed to identify a charged particle passing through the spectrometer, the track reconstructed in MDC has to be matched with a hit in one of time-of-flight detectors and, in case of leptons, also with a RICH ring. From all the rings found in the event the one is taken, for which the quantity [1]:

$$d_{\text{track-ring}} = \sqrt{\left(\Delta\theta_{\text{track-ring}}\right)^2 + \left(\Delta\phi_{\text{track-ring}} \cdot \sin\theta_{\text{track}}\right)^2}. \tag{3.1}$$

---

[1]   The multiplication (and not division) by factor $\sin\theta$ may be not intuitive, but at least can be understood mathematically by inserting transformation to spherical coordinates into the infinitesimal path length: $(ds)^2 = (dx)^2 + (dy)^2 + (dz)^2 = (dr)^2 + r^2(d\theta)^2 + r^2(\sin\theta)^2(d\phi)^2$ and setting $r = 1$, $dr = 0$ for a sphere.

Figure 3.1: Distribution of reconstructed reaction vertices for all events with reconstructed Start hit. 15 slices of segmented gold target are clearly visible. Logarithmic intensity axis was used in order to indicate Au+C reactions on the diamond Start detector.
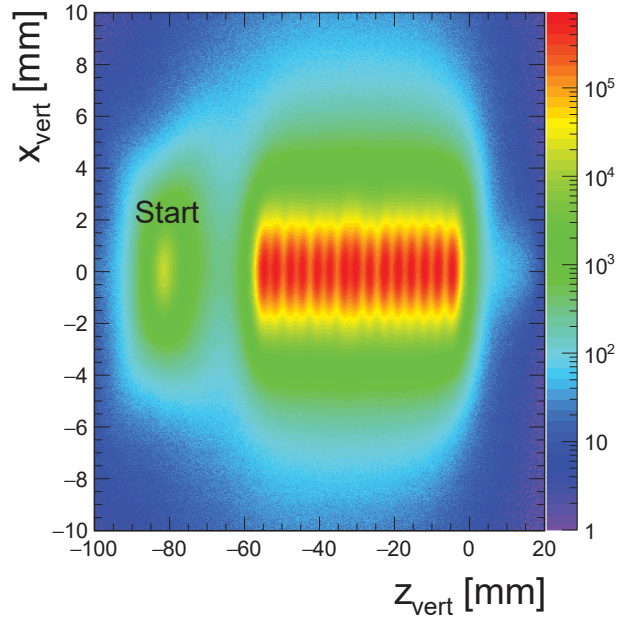
called RICH matching quality is the smallest. Then the properties of this ring are associated with the track. If however there is no ring within the window $|\Delta\theta_{\text{track-ring}}| < 8°$, $|\Delta\phi_{\text{track-ring}} \cdot \sin\theta_{\text{track}}| < 8°$, then no ring information is attached to the track. Similarly, the best matched, if any, hit in TOF, RPC and Pre-Shower is matched to the track together with the detector-specific information (e.g. ToF, dE/dx, ionization charge etc.)

All these steps are performed by dedicated classes included in HYDRA. The output has a form of a tree data structure as implemented within ROOT. The most important branches are those containing global properties of the event (trigger, multiplicities of tracks, TOF and RPC hits etc.) and properties of single tracks (velocity, momentum, properties of RICH ring matched to the track etc.) They can be read in user's program (also here HYDRA provides major facilitation).

3.2 Event selection

As mentioned in the part devoted to the data acquisition system, during the Au+Au beam time HADES was running with two physical triggers (see Section 2.4.5) and among them the one denoted as PT3 selects high-multiplicity events. Further conditions allow to get a high quality data sample. They are evaluated during the data reconstruction procedure and stored in binary flags that can be read during the data analysis. In the current work the following flags are used:

- Physical high multiplicity trigger PT3 (`kGoodTRIGGER`).

- Correct hit in the START detector (`kGoodSTART`), which is needed for particle time-of-flight calculation. For a better resolution, correlated signals from both detector layers are requested.

- Since in high multiplicity events one can very precisely reconstruct event vertex by fitting the points, where all reconstructed tracks are pointing back. Selecting only events with the vertex position within the target allows to reject Au+C reactions in the Start detector and (in principle) collisions of an Au ion with the beam pipe, as it can be seen from the vertex distribution shown in Fig. 3.1. The flag `kGoodVertexCand` requests that the Z position of the vertex calculated from fully reconstructed particle candidates is larger than -65 mm.

It is possible, that particles from more than one nuclear reaction are registered within the time window settled for the data acquisition. Such overlapping or *pile-up* events have to be removed since they lead to wrong estimation of reaction centrality and other event characteristics. The conditions to reject pile-up events are [103]:

- Reconstructed START hit object exists and has no second cluster (`kNoPileUpSTART`).

- No VETO hit within ±15 ns from the START time (`kNoVETO`).

- Exclusion of events, where a later START hit was found within the range 15-350 ns, that has no correlated VETO hit in the window ±2 ns (`kGoodSTARTVETO`).

- Exclusion of events, where a later START hit was found within the range 80-350 ns, that is correlated to more than four META hits inside the time window of 7±5 ns. The offset of 7 ns corresponds to the fastest particles (`kGoodSTARTMETA`).

Fig. 3.4 shows the numbers of events after applying each selection condition.

During the data acquisition it occurred from time to time, that one or more gas chambers (MDC modules or RICH MWPC) suffered from trips. The affected detector gets then inefficient for a certain time. Moreover, in the case of MDC this inefficiency depends on the type of the particle and its velocity: it will be larger for minimum ionizing particles and smaller for highly ionizing ones. The MDC sector 2 (azimuth angle $\phi \in (240° - 300°)$) remained inactive during the most of the beam-time. This issues can hardly be handled in the analysis, if problematic sectors are not removed from the data sample. Since the usual time needed to fully recover MDC's from trips was of the order of few minutes, it was decided to remove problematic sectors for each separate run (typically 2-3 minutes). In order to quantify loses, for each sector the number of reconstructed charged pions and RICH rings has been plotted as a function of time-ordered runs. Then for runs, when any of the numbers is much away from its the average (3σ), the corresponding sector is marked as useless for hadron (number of pions) or lepton (number of rings) analysis. Examples of time trends of both quantities are given in Fig. 3.2. In the upper panel, showing the number of pions, one can see attempts to maintain the high voltage of MDC sector 2 on. For details see [104].

Missing sectors change the geometrical acceptance of the spectrometer. This is a problem, when spectra are going to be compared with the model or reference from elementary reactions. Even apart from that, the spectra from Au+Au should be presented in a unified acceptance. This can be achieved either by analyzing only runs, in which five sectors were active (besides sector 2), or by taking into account also runs with smaller number of sectors and correcting them for the relative loss in the acceptance, as it will be discussed in Section 4.6. It is also discussed there, that it makes no sense to include in the analysis runs with three or less active sectors. Hence in the Fig. 3.4 numbers of events with at least four and at least five sectors are plotted. It can be inferred, that the events with less than four sectors useful for lepton analysis are roughly 10% of selected events, what corresponds on average to 3 days of the beam-time. Events with less than five sectors are 42%, what corresponds to 13 days. Only in 8.5% of selected events (2.5 days) all 6 sectors were available.

3.3 Centrality selection

In order to study system-size dependence of the results, centrality selection of the events, based on the Glauber Monte Carlo simulation is used in HADES (see B. Kardan [105]). The mean value of the number of charged particles produced in a collision N_{ch} is assumed to be directly proportional to number of nucleons participating in the interaction N_{part}: $N_{ch}^{mean} = \mu N_{part}$ with fluctuations given by the Gaussian distribution of the width $\sigma = k \sqrt{N_{ch}^{mean}}$. The minimization procedure is used to fit the generated distribution of N_{ch} to the experimentally measured distribution of the number of tracks in MDC N_{track} or of hits in TOF and RPC N_{hits} in order to extract values of the free parameters μ and k. This allows to relate
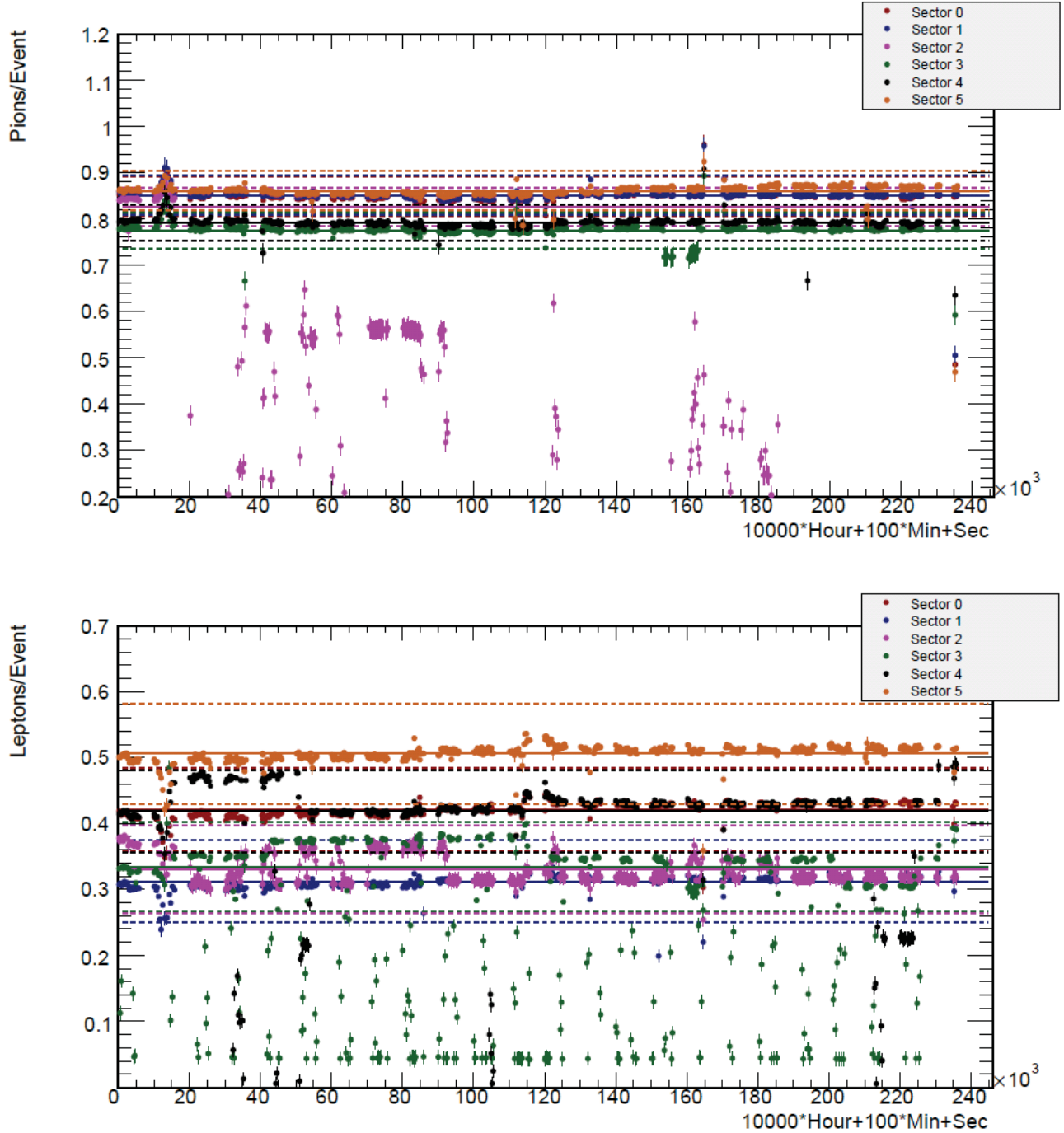
Figure 3.2.: Number of charged pions (upper panel) and RICH rings (lower panel) reconstructed per event in each sector of HADES, during a one day of the beam-time. Lines indicate 3σ deviations from corresponding mean values in the given sector. In particular runs, sectors (indicated in the legend) with the number of pions outside the window are marked as recommended to be skipped for hadron analysis. For leptons both quantities have to be taken into account. Note, that the X axis is arranged in such a way, that 10000 units correspond to one hour and 100 units correspond to one minute of the beam-time, so 40% of every interval is empty by construction and this does not indicate any break in beam delivery of break down of the detection system.
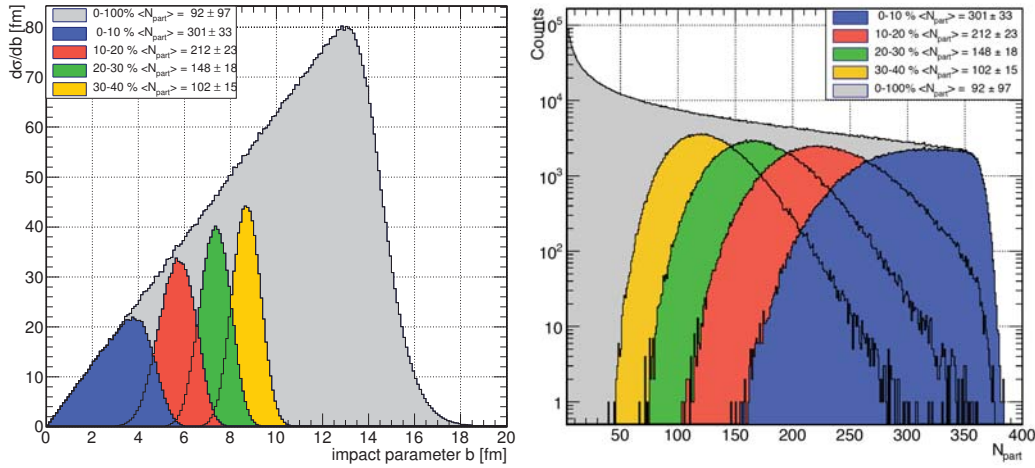
Figure 3.3.: Impact parameter (left panel) and number of participants (right panel) distributions in HADES corresponding to the selected centrality bins of constant width (10%). Note that in the legends widths of the number of participant distributions are given and not systematic uncertainties of the mean.

Class	$\langle N_{\text{part}}^{\text{data}} \rangle$	b [fm]	$N_{\text{low}}^{\text{META,cut}}$	$N_{\text{high}}^{\text{META,cut}}$	bin in Fig. 3.4
0-10%	301.1 ± 11.2	0.00-4.60	≥ 160	< 250	mult bin 4
10-20%	211.8 ± 10.1	4.60-6.50	≥ 121	< 160	mult bin 3
20-30%	148.5 ± 7.8	6.50-7.95	≥ 88	< 121	mult bin 2
30-40%	101.7 ± 6.3	7.95-9.18	≥ 60	< 88	mult bin 1
0-40%	190.9 ± 8.7	0.00-9.18	≥ 60	< 250	

Table 3.1.: HADES centrality classes defined by numbers of hits in TOF and RPC.

event classes defined in terms of N_{track} or N_{hits} to the corresponding average impact parameter $\langle b \rangle$ or number of participants $\langle N_{\text{part}} \rangle$ as shown in Fig. 3.3 and in Table 3.1.

In the experimental data, the definitions of the centrality classes are based on the total number of META hits within $t < 35$ ns for TOF and $t < 25$ ns for RPC. Using number of META hits instead of MDC tracks to estimate the centrality is much more robust, as it is not influenced by transient inefficiencies of gas chambers. Simulated UrQMD events can be distributed into centrality classes defined directly by the event impact parameter b. At the time of completing this part of work, the number of META hits in simulation was by roughly 20% higher in simulation than in experiment. This was due to usage of GHEISHA hadronic interaction model in GEANT, which is not optimized for low-energy experiments. Therefore, the centrality classes derived from the Glauber fit to experimental data were not applicable to the simulation and the selection based on the impact parameter was prefered in this case. Later, change to the GCALOR model resulted in an agreement better than few percent. The centrality classes are summarized in Table 3.1.

Here $\langle N_{\text{part}}^{\text{data}} \rangle$ denotes an average number of participants, $\langle b \rangle$ is the impact parameter, $N_{\text{low}}^{\text{META,cut}}$ and $N_{\text{high}}^{\text{META,cut}}$ are minimum and maximum numbers of META hits in a particular centrality class.

Numbers of events after each selection condition discussed above and within all centrality bins are shown in Fig. 3.4. The total number of selected events is around $2.9 \cdot 10^9$.
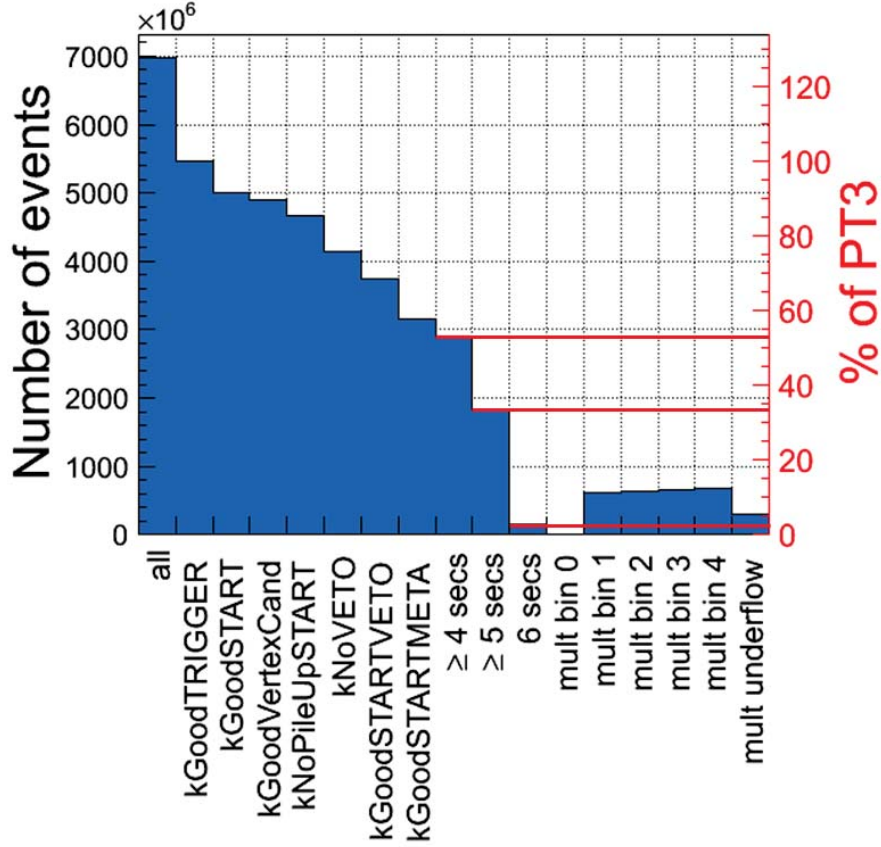
Figure 3.4.: Number of events after each subsequent event selection condition separated into the multiplicity classes. mult bin 0 denotes an overflow bin, i.e. events with 140 or more particle candidates. Multiplicity underflow contains events with less than 17 candidates.

3.4 Track pre-selection and sorting

In the output of the DST production many combinations of the same track segments and RICH and META hits are contained. In the analysis to each track maximum one RICH ring can be attached and up to 3 hits in each of META detectors. However, RICH rings and META hits can be shared between in principle unlimited number of tracks. Also joining inner and outer track segments produces a number of combinations and a particular segment is shared among many track candidates. This however increases combinatorics which must be reduced. Ideally, only one pair of inner and outer segment, one cluster of hits in any of the time-of-flight detectors and possibly one RICH ring and one Pre-Shower hit should correspond to one electron. Moreover the ring and hits in META detectors should be used exclusively by this particle. Exceptions could be very close pairs of particles (two particles produced together in a decay with a very small opening angle), which may produce overlapping RICH rings and inner tracks segments, which cannot be resolved and only one segment/ring is reconstructed. Also, if two particles hit the same cell of one of time-of-flight detectors, only one hit will be detected and reconstructed (time and position information will correspond to the faster particle). There is in fact no good way, to handle this exceptional situations, however they are anyway very seldom compared to wrong combinations. And this main issue is solved by *track sorting*.

Track sorting is an algorithm, which loops over all track candidates in a given event. If it finds several tracks sharing the same component (track segment, detector hit...) values of a parameter quantifying their quality are compared among them. Possible quality parameters are the product of the χ^2_{RK} of the Runge-Kutta fitting and the distance between the track extrapolated to the plane of a META detector and
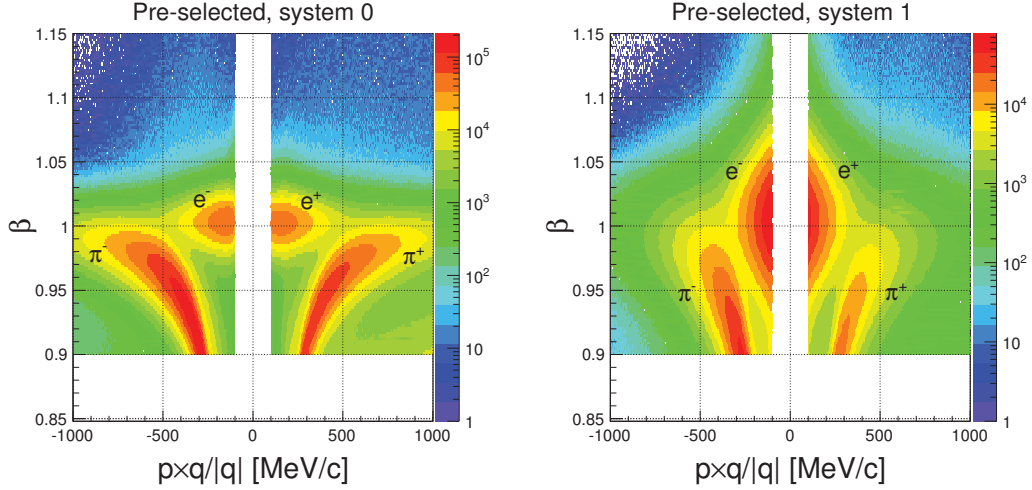
Figure 3.5.: Velocity of the particle vs. its momentum times charge for the two HADES sub-systems separately for pre-selected particles after the track sorting. **System 0** denotes the particles with time-of-flight measurement derived from the RPC detector, **system 1** - from the TOF scintillator wall.

the reconstructed hit position (in mm): $\chi^2_{\text{RK}} \times d_{\text{track-META}}$ or just the χ^2_{RK}. The analysis discussed in [106] shows, that there is no significant difference between final results obtained using either of the two and in the current analysis χ^2_{RK} is used. Only the track candidate with the smallest χ^2_{RK} is then marked to be used in the further analysis.

In general, one expects, that electron tracks have worse quality parameter than protons or pions, because of their on average smaller momentum which induces more multiple scattering and are stronger bent in the magnetic field. If they share e.g. the same hit in one of META detectors, then the electron will be removed from the data sample. To minimize the probability of such a situation, one may request certain preconditions before the track sorting. This means, that only those tracks, for which the conditions are fulfilled are considered by the sorter and only sharing track segments or detector hits between them is taken into account. This leads to an idea of including in these preconditions loose identification cuts and minimum quality requirements. The conditions used in the current analysis are as follows:

1. Quality requirements:

   - Track is not marked as a *fake* by the track finding procedure.
   - Track has been constructed from fitted track segments and the outer segment matches to a hit in any META detector, Runge-Kutta fit converged.
   - $\chi^2_{\text{RK}} < 500$.
   - META hit is within the cell pointed by the track.
   - The distance between the track and META hit in the direction along the META cell is smaller than 3σ.

2. Loose identification cuts for electrons:

   - Track has matched RICH ring ($|\Delta\theta_{\text{track-ring}}| < 8°$, $|\Delta\phi_{\text{track-ring}} \cdot \sin\theta_{\text{track}}| < 8°$).
   - $\beta > 0.9$.
   - $p > 100$ MeV/c and $p < 1000$ MeV/c.

There are two types of *fake* tracks [107]. One are those containing a track segment that shares fired wires (at least 4) with another segment. In this case the segment that has less shared wires, or smaller

χ^2 from segment fitting if the number of not shared wires is equal, is taken as not being *fake*. The second type are tracks containing a segment being a combination of wires fired by other tracks.

The distributions of particle's velocity vs. momentum times charge for pre-selected particles after the sorting procedure are shown in Fig. 3.5. Here and further in this work the following definitions of the HADES detector sub-systems, originating from the convention in analysis software, will be used:

- **system 0** consists of RPC and Pre-Shower detectors and particles that fall into any of the two are associated with this system.

- **system 1** consists is the TOF detector and particles that fall into it are associated with this system.

3.5 Single lepton identification with hard cuts

To start with a more comprehensible case and to provide a reference, to which the multivariate analysis can be compared, single lepton identification is performed with a set of *hard cuts* defined on some relevant quantities. These are $d_{\text{track-ring}}$ (see Eq. 3.1), $m^2_{\text{eff}} = p^2(1-\beta^2)/\beta^2$ vs. $p \times q/|q|$ and $\Delta Q_{\text{Pre-Shower}}$ vs. $p \times q/|q|$. The first one, $d_{\text{track-ring}} < 1°$, is taken the same as in the multivariate analysis, as discussed later in Section 3.7.5.

3.5.1 Cut on Pre-Shower observable

The cut on the Pre-Shower observable is optimized as follows: First, in order to get a good separation between electrons and hadrons, cuts on $d_{\text{track-ring}}$ and m^2_{eff} are applied. Then, in each 100 MeV/c wide bin of momentum, in each 25 units wide bin of $\Delta Q_{\text{Pre-Shower}}$ and for both polarities separately, a second order polynomial + Gaussian distribution is fitted to the $\Delta\theta_{\text{track-ring}}$ (as shown in Fig. 3.6) in order to describe signal from electrons correlated to rings and background of randomly matched hadrons. Integrals of the Gaussian part are then plotted as a function of $\Delta Q_{\text{Pre-Shower}}$ for all momentum bins separately. This is shown in Fig. 3.7 for few examples. Finally, a histogram of cut values as a function of momentum is created in such a way, that for $p < 300$ MeV/c a negative constant is taken (equivalent to no cut on the Pre-Shower observable, due to the fact that low momenta leptons do not produce sufficiently large electromagnetic cascades), for $300 < p < 600$ MeV/c the cut is defined as a value for which 20% of the signal is removed. Finally, the function $\Delta Q_{\text{Pre-Shower}}(p) = \frac{a}{p+b} + c$ with free parameters a, b and c is then fitted to the resulting histogram. The distribution of $\Delta Q_{\text{Pre-Shower}}$ vs. momentum times charge with the cut marked as a black line is shown in Fig. 3.8. As expected, there is no cut below roughly 300 MeV/c. Above this value a nearly straight line removes hadrons, which pass through the detector without producing the cascade and inducing almost the same charge in all the Pre-Shower modules.
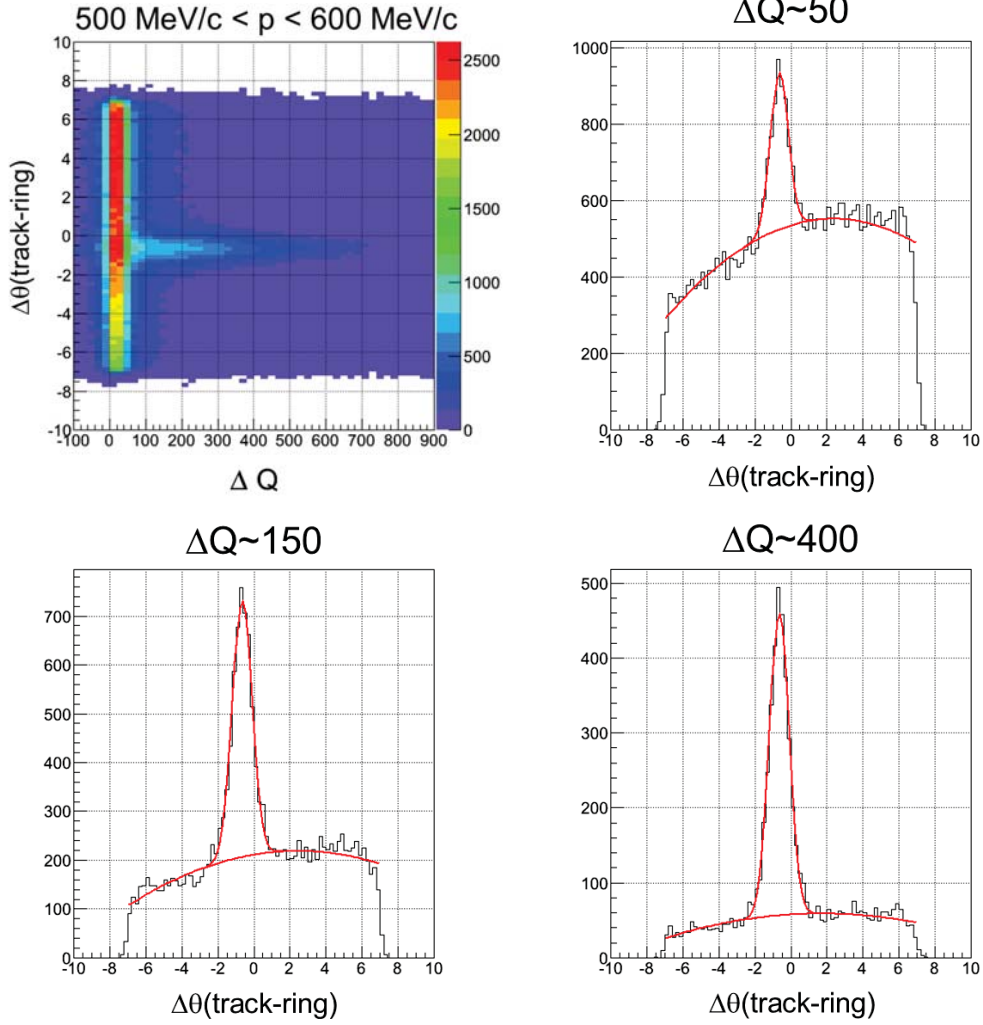
Figure 3.6.: Matching between a track and a RICH ring in the θ angle vs. Pre-Shower $\Delta Q_{\text{Pre-Shower}}$ observable for a selected momentum bin and projections of $\Delta\theta$ in several narrow bins of ΔQ. In the projections, fits of polynomial + Gaussian distributions are indicated with red curves. The shift of the maximum position from 0 is due to RICH misalignment for which a correction was introduced later.
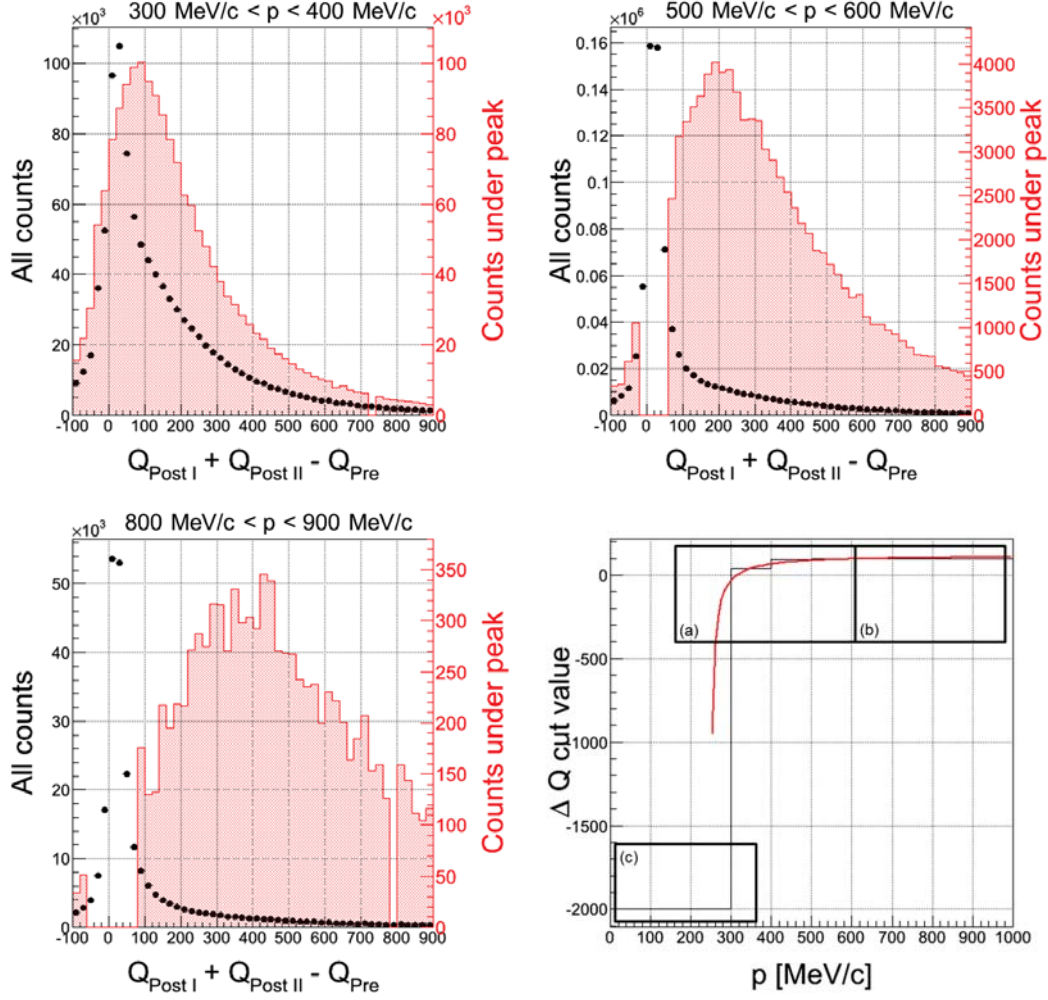
Figure 3.7.: Integrals of the whole distributions (black) and the Gaussian part (red) of the fits from Fig. 3.6, plotted as a function of the Pre-Shower observable $\Delta Q_{\text{Pre-Shower}} = Q_{\text{Post I}} + Q_{\text{Post II}} - Q_{\text{Pre}}$ for a few momentum bins. Bottom right: the construction of the $\Delta Q_{\text{Pre-Shower}}$ vs. momentum cut: In the momentum range denoted by (a) the cut value corresponding to removal of 20% of the signal is marked. In the area (b), a constant value $\Delta Q = 100$ is taken, in (c) it is a large negative value. To the resulting histogram the function $\Delta Q(p) = \frac{a}{p+b} + c$ is fitted.
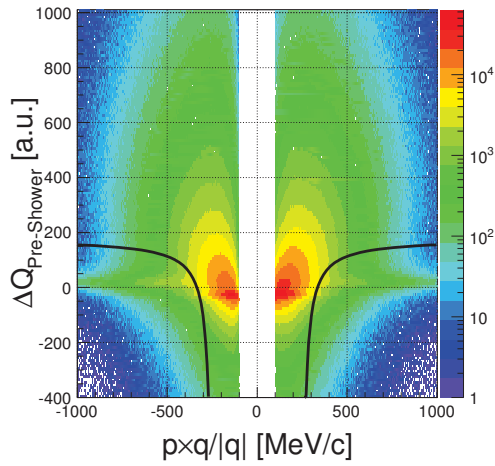
Figure 3.8: $\Delta Q_{\text{Pre-Shower}}$ as a function of particle's momentum for two polarities separately. The cut on the observable is indicated by the black curve. Entries above the curve are accepted, below are rejected. For better visibility, distribution is made after applying cuts on $d_{\text{track-ring}}$ and m_{eff}^2.

3. Data analysis tools and techniques

The final cut on m^2_{eff} is optimized in such a way, that in 100 MeV/c wide momentum bins a distribution of two Gaussians (for electrons and pions peaks) + fourth order polynomial (for other components of underlying background) is fitted to the m^2_{eff}. A few examples of the fit are shown in Fig. 3.9 (for negatively charged particles). Then the cut is defined as $\overline{m}_{\text{electron}} + 4\sigma_{\text{electron}}$ based on the mean $\overline{m}_{\text{electron}}$
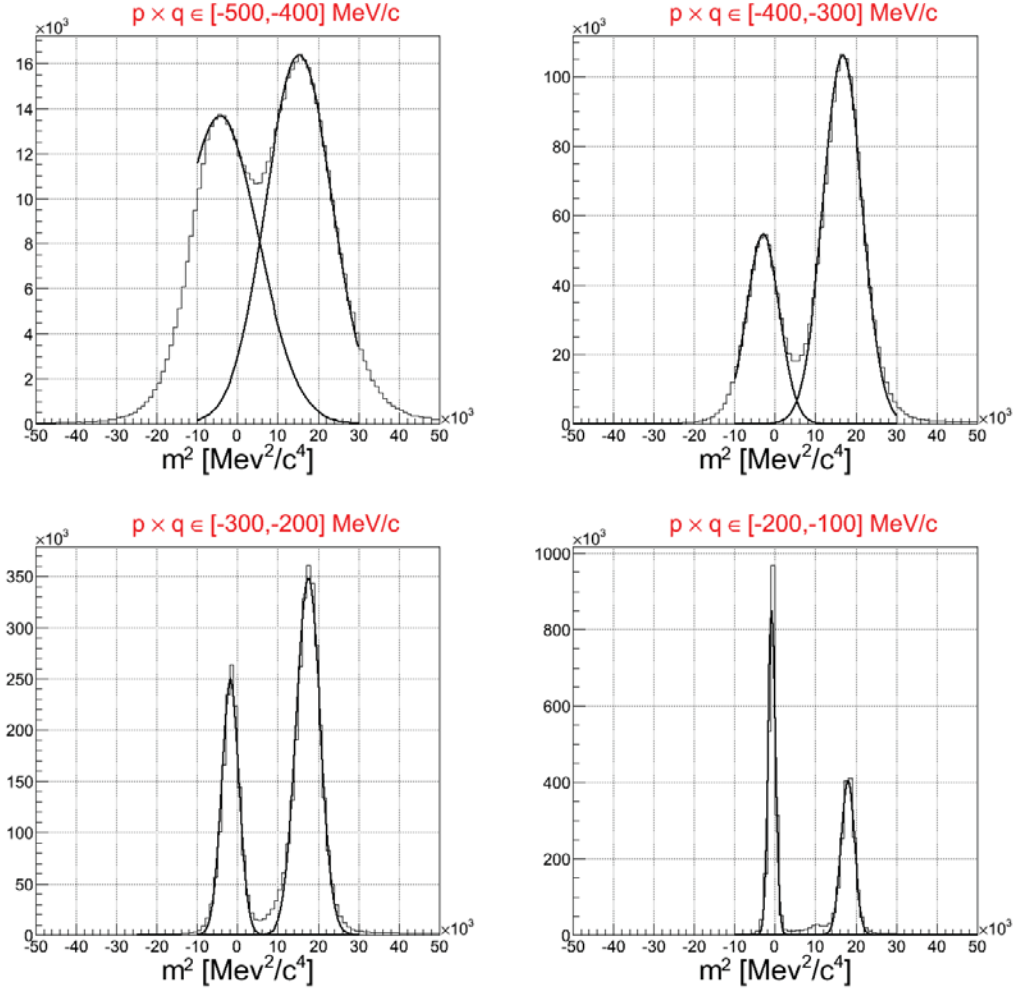
Figure 3.9.: Effective mass distributions of particles for a few selected momentum bins. Out of the polynomial + two Gaussians function fitted to the distributions, both Gaussian parts are plotted. It should be noted, that for the momentum high enough, the two peaks overlaps and, consequently, there is no good separation anymore. For this region the constant value of the cut is chosen, as shown in Fig. 3.10.

and with the width σ_{electron} of the Gaussian part fitted to the electrons' peak or the cut value fixd to $m^2_{\text{eff}} = 10000$ MeV^2/c^4 ($m_{\text{eff}} = 100$ MeV/c^2) at higher momentum, where one cannot resolve between electrons' and pions' peaks. The resulting cut is shown in Fig. 3.10. Final distributions of velocity vs. momentum for identified particles are shown in Fig. 3.11 and projections on the momentum after applying subsequent identification cuts in Fig. 3.12.
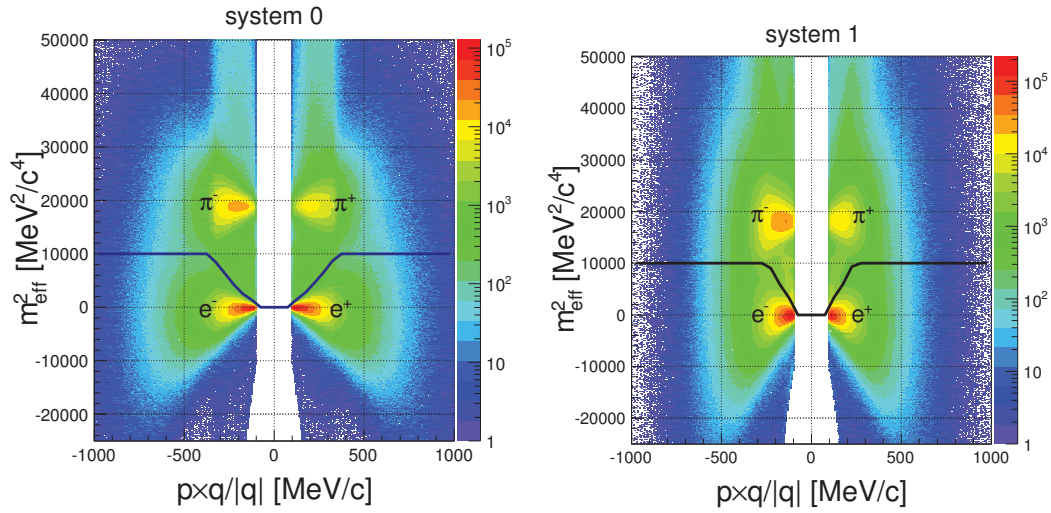
Figure 3.10.: Effective mass of the particle vs. its momentum times charge for the two systems separately. Momentum-dependent cut on the mass is indicated with the black curve. For better visibility, the distribution is plotted after applying cuts on $d_{\text{track-ring}}$ and $\Delta Q_{\text{Pre-Shower}}$, as explained before, but no cut on β.
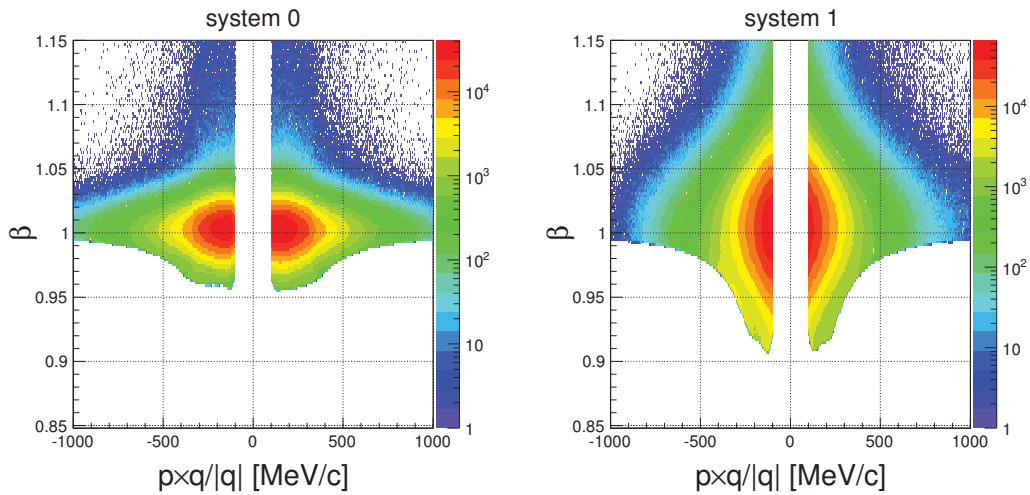
Figure 3.11.: Velocity of the particle vs. its momentum times charge for two systems separately for leptons identified with the hard cut method.

3. Data analysis tools and techniques
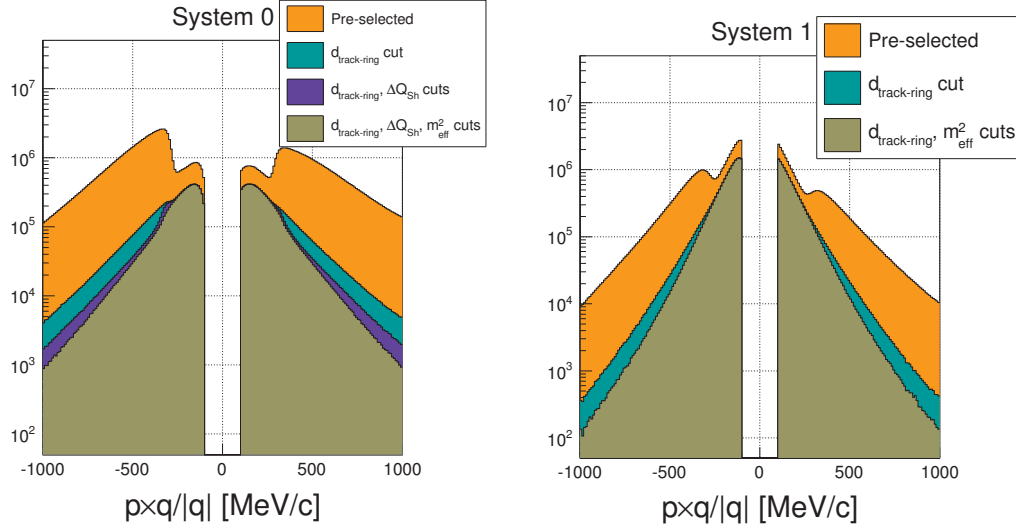
Figure 3.12.: Momentum distributions of leptons candidates after each subsequent hard identification cuts.

3.6 Multilayer perceptrons

Feed-forward multilayer perceptron (MLP) is a type of an artificial neural network and an example of techniques of multivariate analysis (MVA). It allows to make a single decision based on values of a number of quantities. The key advantage is, that all the quantities and correlations between them are taken into account at the same time, which allows for the most careful and the fairest possible discrimination of underlying events. For example, when considering all discriminating quantities separately, a particular event can be rejected if one of quantities lies just below the threshold for it, even though all the other quantities are well above respective thresholds. Similarly, an event might be accepted, even when it should be rejected when taking into account all the quantities at the same time.

Mathematically, MLP is nothing else than a function $y : \mathbb{R}^n \rightarrow [0,1]$. Applying a condition $y(x_1, ..., x_n) = \text{const}$ defines an $(n-1)$-dimensional surface in the n-dimensional space of input quantities $x_1, ..., x_n$ (one may compare it to a surface of total energy conservation $E = \text{const}$ in a phase space of many bodies, however in the case of neural networks the surface usually will not be closed). Points in the space, simultaneous measurements of all the quantities for single events, will be located on an
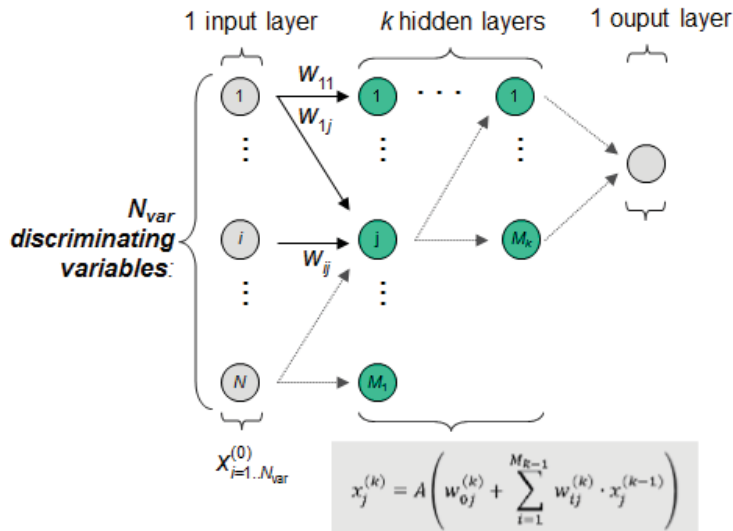
Figure 3.13: An example scheme of multi-layer perceptron.

either side of the surface and this will allow to discriminate them. The condition $y(x_1, ..., x_n) = c$, for c between 0 and 1, will then define the surface which divides the space into points to be accepted (with $y(x_1, ..., x_n) > c$) or rejected (with $y(x_1, ..., x_n) < c$).
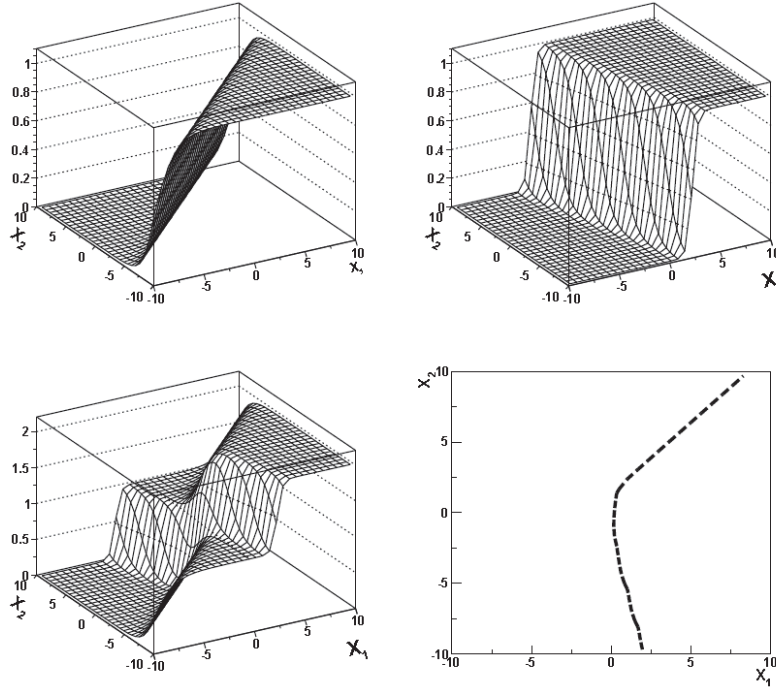
Figure 3.14.: The simplest non-trivial MLP. It has two input variables x_1 and x_2. Two top panels represent two nodes in the single hidden layer. They calculate sigmoid of different linear combinations of the input variables. Bottom left panel is the output node which adds the sigmoids up. Computing the activation function of the last sum is skipped and bottom right panel shows just the decision boundary for a particular value of the output variable.

The mathematical form of the function makes it possible to obtain a very flexible discriminating surface. It consists of *layers* containing *nodes* (see Fig. 3.13). The minimum number of layers is two: one contains input quantities $x_1, ..., x_n$, the other one - calculated output. It is possible to define arbitrary number of additional "hidden" layers with arbitrary number of nodes, performing intermediate steps of calculation. Each node in every layer (besides the input one) is connected to all nodes in the preceding layer and only to them. This means, that the value at a particular node is calculated based only on values at nodes, to which it is connected, according to the formula:

$$x_j^{(k)} = A\left(w_{0j}^{(k)} + \sum_{i=1}^{M_{k-1}} w_{ij}^{(k)} \cdot x_i^{(k-1)} \right). \tag{3.2}$$

Here, (k) or $(k-1)$ in the superscript denote the layer and j or i in the subscript denote the node in the layer. Summation runs over all nodes in the preceding layer, $w_{ij}^{(k)}$ are parameters (*weights*) to be fitted. A is called *activation function*. The simplest choice would be a step function, but the sharp threshold can be also smeared by using e.g. hyperbolic tangent function $tanh$ or sigmoid function $A(x) = \frac{1}{1+e^{-x}}$ (which is a Fermi function flipped around the y axis: $x \rightarrow -x$). The weights $w_{0j}^{(k)}$ corresponds to the so-called *bias node*. As it can be read off the Eq. 3.2, this is an additional node of each layer, having always the value 1 at the input. When the activation function $A(x)$ is the step function, all the other weights define the shape of the hypersurface in the $\mathbb{R}^{M_{k-1}}$ space of the neuron's inputs, above which the neuron responds. The weight associated with the bias node shifts the surface with respect to 0. This might be crucial for

the convergence of the neural network optimization procedure. Similar interpretation is valid in case of a more complicated activation function, only the surface becomes a thicker o thinner skin.

Perceptron or *feed-forward network* is a neural network in which output from a one node is sent only to nodes in the following layer.

It is instructive to examine, how a complicated decision boundary is built up. Fig. 3.14 shows the simplest non-trivial MLP with two input quantities and one hidden layer. Two top panels are sigmoid functions at two nodes of the hidden layer: $1/(1 + \exp(-x_1 + x_2))$ and $1/(1 + \exp(-4x_1 - x_2))$. Bottom left panel shows a sum of the two, which would be calculated in the output node with both weights equal 1. The step of calculating sigmoid of this sum is here skipped, thus the output value ranges from 0 to 2 and not to 1. Then bottom right panel shows the decision boundary for the value $y(x_1, x_2) = 1.2$.

Finding optimal values of weights $w_{ij}^{(k)}$, often called *training* or *learning*, is a minimization problem. One prepares a sample of events, which certainly should be accepted and of those, which certainly should be rejected. Having in mind an application of the MLP in physics, one can call them *signal* and *background* samples. Then a loss function is defined, which describes a performance of the perceptron on the training data. Usually the cross-entropy function is taken:

$$L(\mathbf{w}) = \sum_i^{\text{events}} \left[y^{(i)} \ln\left(y\left(\mathbf{x}^{(i)}, \mathbf{w}\right)\right) + \left(1 - y^{(i)}\right) \ln\left(1 - y\left(\mathbf{x}^{(i)}, \mathbf{w}\right)\right) \right],$$

where $y\left(\mathbf{x}^{(i)}, \mathbf{w}\right)$ is the response of the MLP to the training event $\mathbf{x}^{(i)}$ with weights $\mathbf{w}$, $y^{(i)}$ is 1 for signal events and 0 for background. One can start with random weights and search for the minimum of the loss function iteratively by calculating gradients of it with respect to weights and tuning them to get lower value of $L(\mathbf{w})$.

3.7 Application of MLP for lepton identification

In the present work MLP was used to identify single e^+/e^- tracks present in the large background of hadrons. The implementation used was the one included in the Toolkit for Multivariate Data Analysis (TMVA [108]), which is currently fully integrated into the ROOT Object Oriented Data Analysis Framework - a base for almost all the software used in HADES data analysis. One argument for choosing this implementation was thus its availability and possibility to easily and clean merge it with all programs used. Another reason was the existing in the working group experience from using this implementation in previous experiments.

3.7.1 Training sample

In order to find optimal definitions of signal and background samples, the following possibilities were compared:

1. Tracks from real data, selected based on $d_{\text{track-ring}}$, Eq. 3.1,

2. Simulated tracks selected based on $d_{\text{track-ring}}$,

3. Simulated tracks selected based on the identity information propagated from the event generator.

Potentially the purest way of defining signal and background sample for training of MLP would be using a Monte Carlo simulation. There it can be checked, which tracks are leptons and which hadrons. However, this is not optimal for particle identification in the real data if all the characteristics of particle tracks are not perfectly reproduced in simulation. Then the second best possibility is to select from data lepton sample as little as possible contaminated by hadrons and treat it as signal and possibly
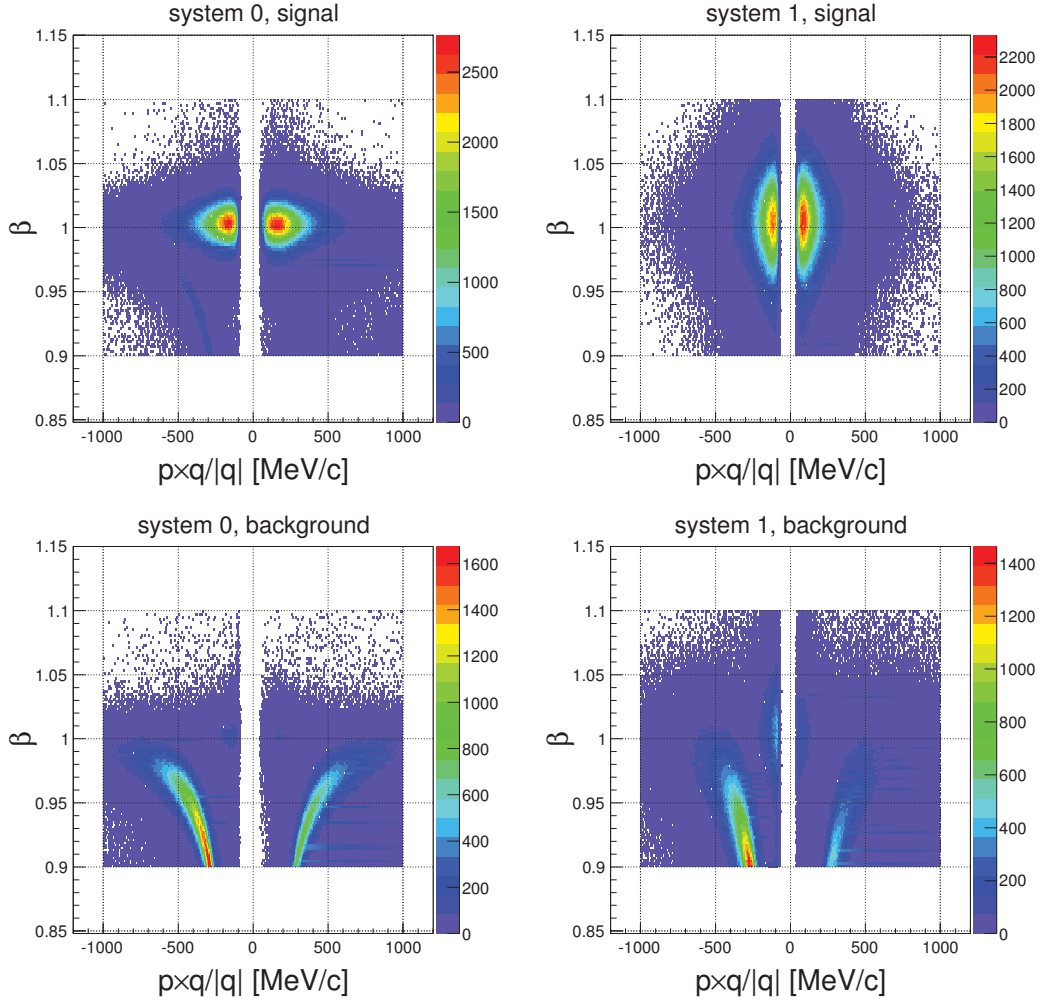
Figure 3.15.: PID plots of signal and background models for the MLP training, defined by the RICH matching quality cut in real data, in two systems separately.

clean hadron sample as background. In HADES lepton analysis this selection can be done based on the RICH ring-track matching quality 3.1. Fig. 3.25 in Section 3.9.1 shows the difference of the azimuth angle $\Delta\phi$ between lepton candidate track and closest matched RICH ring. From the discussion there, it can be easily concluded, that applying a very tight condition on the angular correlation does not eliminate hadron contribution fully, but at least minimizes it. Conversely, requiring the angle difference to be larger then a certain value, will eliminate almost fully true correlations and leave only chance coincidences. Definition of signal and background sample is then as follows:

$$d_{\text{track-ring}} < 0.5° \text{ for signal,}$$
$$d_{\text{track-ring}} > 7° \text{ for background.}$$

Velocity vs. momentum distributions (*PID plots*) for signal and background sample defined in this way are shown in Fig. 3.15.

Training on simulated tracks with signal and background defined based on $d_{\text{track-ring}}$ serves as an intermediate step for comparison with the two other possibilities.

The quantities, which are used to define signal and background sample cannot be used as an input to the MLP. Otherwise, the network training algorithm would find them to perfectly discriminate between signal and background and the largest weights would be associated with them. All the other quantities would have weights close to 0. As a consequence, the identification would be performed based only on the quantities and cuts defining training sample and there would be no profit from the multivariate analysis.

Different sets of input variables were checked and compared. Some of the variables are available only in the *system 0* (that is for tracks entering the RPC and the Pre-Shower detectors) or in the *system 1* (for tracks entering TOF). Because of this and because of the different time resolution of TOF and RPC detectors, the training of MLP and single leptons identification is done for both systems separately. The input variables used the final analysis in both systems are as follows:

1. Particle's velocity in units of the speed of light, β (`beta`).

2. Quantities characterizing RICH ring attached to the track:

    a) Number of fired pads of the photon detector (`ringNP`).

    b) Total charge of the ring signal divided by the number of pads (`ringAC`).

    c) Result of matching the signal from a certain area of the RICH detector with the ring pattern (*ring pattern matrix*, `ringPM`).

3. Energy loss dE/dx in MDC (`mdcdEdx`).

4. Polar angle of the emission θ (`theta`).

5. Distance in number of standard deviations of the track to the matched hit in one of META detectors (*META matching quality*, `metaQa`).

6. Particle's momentum (`mom`).

The result of the Hough-like transformation (`ringHT`) [109] is not included, because it is strongly correlated with `ringPM` and brings no additional information.

In addition there are specific variables for ($\Delta Q_{\text{Pre-Shower}}$.`showerDq`) and for system 1 (dE/dx in TOF).

Figure 3.16 shows the summary of input variables and training sample definitions for all the neural network parametrizations that have been checked and compared in the initial stage of the analysis. Their performance is summarized in Fig. 3.26 later in this chapter, which shows that differences between efficiency and purity of different variants are very small. Therefore only the weights numbered 1, containing the most comprehensive set of input variables, are used in further analysis.

Figures 3.17 and 3.18 show distributions of several input variables for signal (blue histograms) and background (red histograms) training samples obtained from the real data defined on the basis of the RICH matching quality. Even though most of the variables individually provide very poor separation between signal and background, they all influence the shape of multi-dimensional decision boundary, which separates signal from background much more effectively (although it cannot be visualized). Fig. 3.19 shows the shape of the neural network indicating also the values of the fitted weights. There is no fundamental difference between positive and negative weights. For a positive input value, a negative weight tends to "switch off" the neuron. However, due to the multi-layer structure of the neural network, that accounts for correlations between input variables, no strong conclusions can be made about the influence of each variable on the network output. This can be seen from the Fig. 3.19, where certain nodes have both positive and negative outgoing connections.

weights no.	ringNP	ringAC	ringHT	ringPM	metaQa	richQa	beta	theta	mom	mdcdEdx	tofdEdx	showerDq	trained on
0	green	green	red	green	green	red	green	green	blue	green	green	green	EXP, RICH QA
1	green	green	green	red	green	red	green	green	blue	green	green	green	EXP, RICH QA
2	green	green	green	red	green	green	green	green	blue	green	green	green	EXP, RICH QA
3	green	green	red	red	green	green	green	green	blue	green	green	green	EXP, RICH QA
4	green	green	red	red	green	green	green	red	blue	green	green	green	EXP, RICH QA
5	green	green	red	green	red	green	green	green	blue	green	green	green	EXP, RICH QA
6	green	green	red	green	red	green	green	red	blue	green	green	green	EXP, RICH QA
7	green	green	red	green	red	green	green	red	blue	green	red	green	EXP, RICH QA
8	green	green	red	green	red	green	green	red	blue	green	green	green	EXP, RICH QA
9	green	green	red	green	red	green	green	red	blue	green	green	green	EXP, RICH QA
10	green	green	red	green	red	green	green	red	blue	green	green	green	SIM, GEANT PID
11	green	green	red	green	red	red	green	red	blue	green	green	green	SIM, GEANT PID
12	green	green	red	green	red	red	green	red	blue	green	green	green	SIM, RICH QA

Input variables span the columns ringNP through showerDq. Weight set 1 is marked with a thick outline.

Figure 3.16.: Different sets of input variables and definitions of signal and background sample used in the neural network training. Green color means that a variable is used in a particular training instance, red that it is not used. Blue in the column corresponding to the momentum of particle indicates that this variable is used in the neural network input only in system 0. Thick outlines indicate the weights, that are chosen to be used in the pair analysis. The most right column describes signal and background definitions for the training. "EXP" means that the network was trained on the experimental data, "SIM" - on simulation. "RICH QA" indicates the standard definitions based on the RICH matching quality, "GEAND PID" means, that signal and background samples were selected based on the particle's type information transported from the GEANT analysis level.
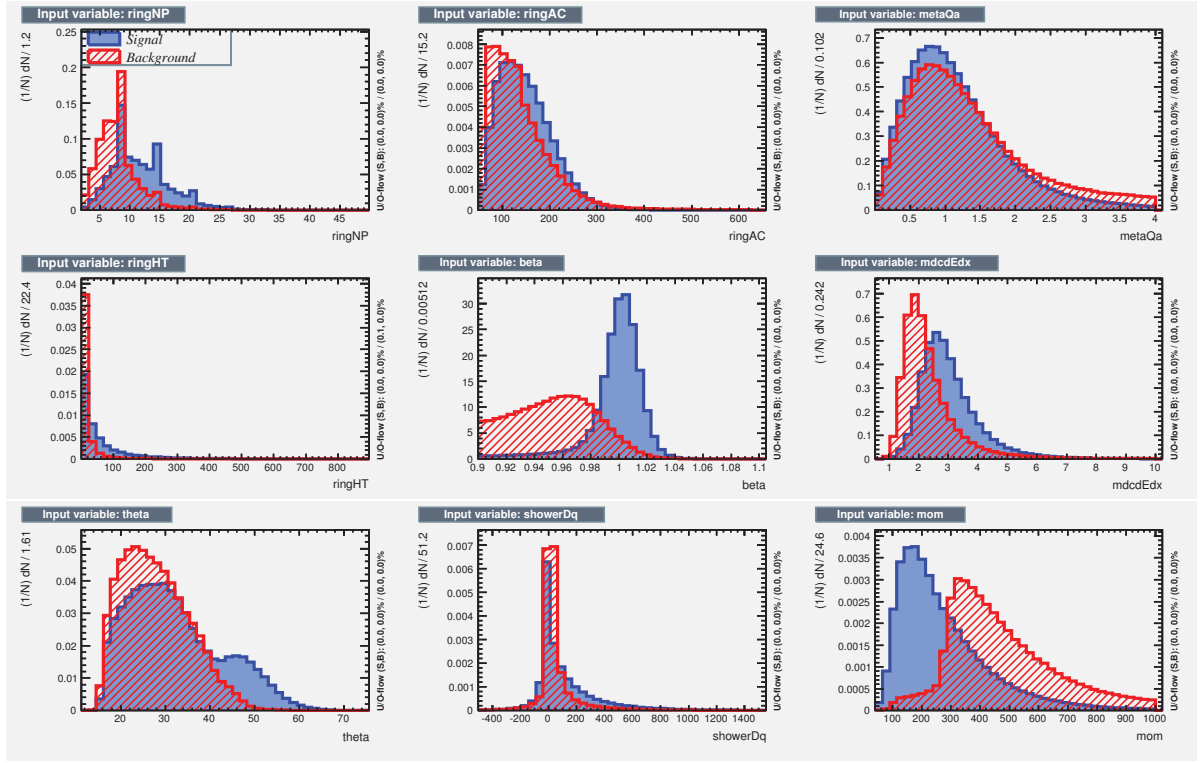
Figure 3.17.: Distributions of all input variables in **system 0** for signal (blue histograms) and background (red histograms).
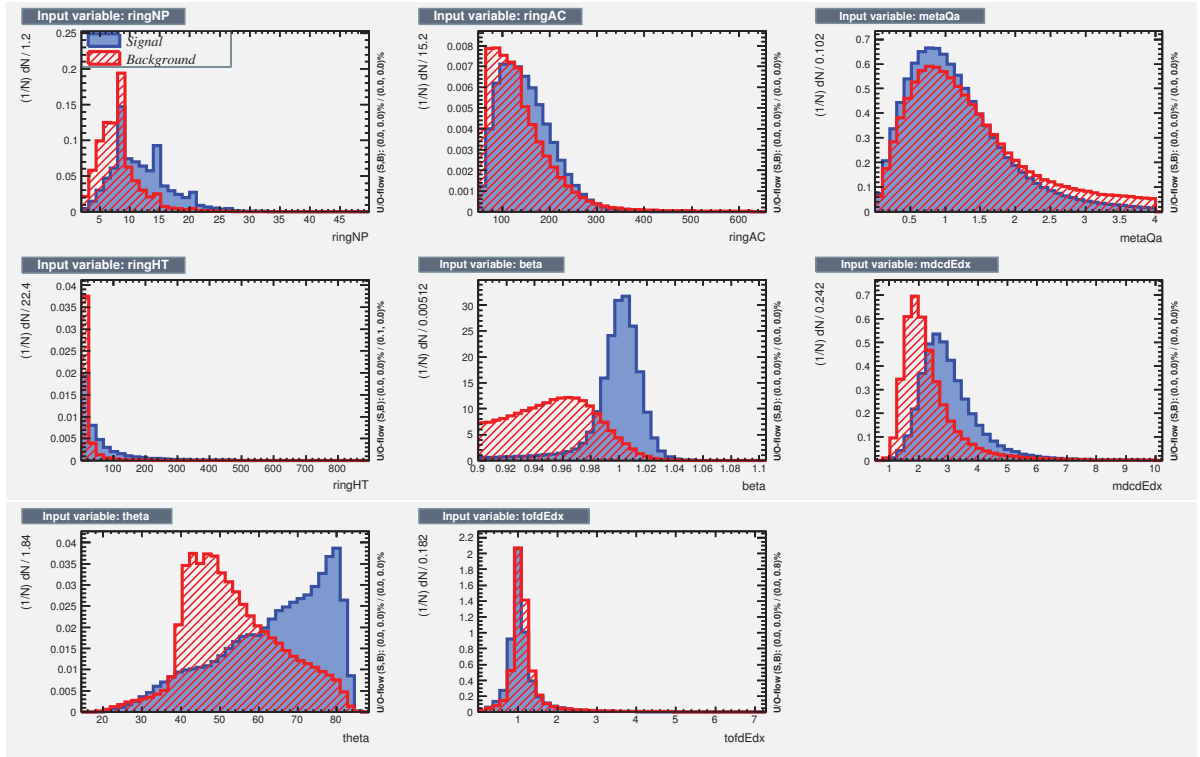
Figure 3.18.: Distributions of all input variables in **system 1** for signal and background.

3.7.3 Training procedure

It is a commonly accepted, that details of the neural network architecture do not have big influence on the results, at least in nuclear and particle physics applications. Therefore, the choice here is to keep the default configuration of the TMVA's MLP training: with 2 hidden layers and $N + 1$ and N nodes in them, where N is the number of input variables. The activation function is sigmoid, $A(x) = \frac{1}{1+e^{-x}}$. The default number of 500 training cycles was preserved, as a loss function cross-entropy was used, training was done with the standard back-propagation method, where updating of weights starts from the output and proceeds towards the input layer. There were roughly 10^6 training tracks both for signal and background in both systems.
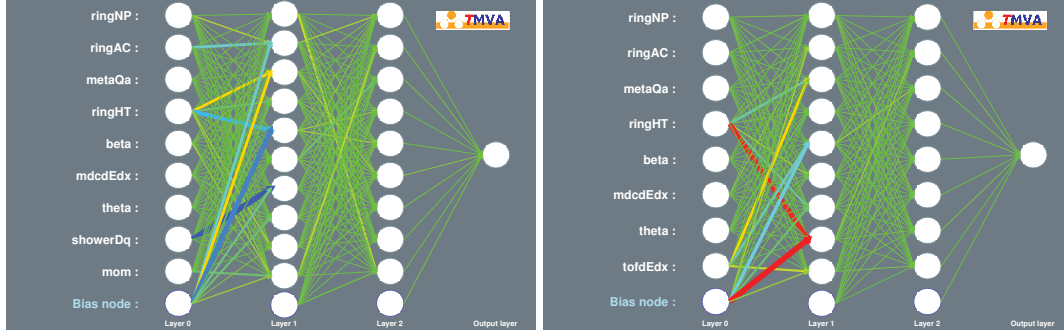
Figure 3.19.: Architecture of the MLP used in system 0 (left) and system 1 (right). Thickness of each line is proportional to the absolute value of the associated weight. Color corresponds to the value with sign: red means large positive, blue large negative, green is close to 0.

3.7.4 Condition on $y(\mathbf{x})$
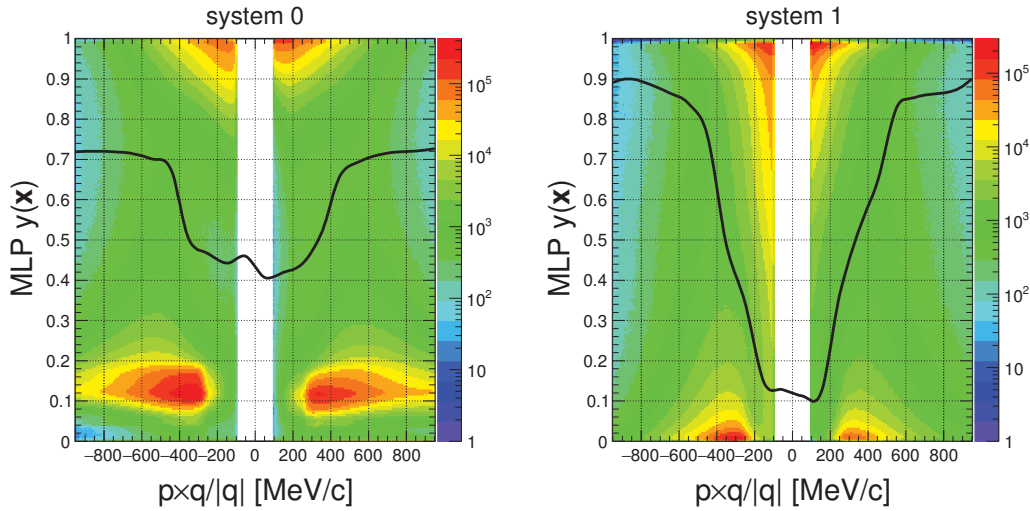
Figure 3.20.: Distributions of the quantity $y(\mathbf{x})$ as a function of particle's momentum times charge (q is the charge of the particle, so $q/|q|$ is the sign of the charge that is charge). Entries with $y(\mathbf{x})$ close to 1 correspond to signal, those close to 0 are background.

Fig. 3.20 shows the output value $y(\mathbf{x})$ of the MLP for system 0 and 1 for weights number 6, drawn versus momentum times charge of a particle. The separation between signal- and background-like tracks is clearly visible. The shape of the spectrum encourages to define the decision boundary momentum

3. Data analysis tools and techniques

dependent. One can see, that at low momentum the sample is strongly dominated by leptons and their distribution stretches towards the values of $y(\mathbf{x})$ as low as 0.2. This is not the case at higher momentum values, where the number of pions and protons is larger and they become predominant at lower $y(\mathbf{x})$. To make use of this property of the distribution and make the cut well defined, the sample was divided into 100 MeV/c wide momentum bins (separately for both systems and for positive and negative particles). In each bin a high order polynomial was fitted to the $y(\mathbf{x})$ distribution in order to make it easier to find its minimum. In the analysis, the value of the cut on $y(\mathbf{x})$ for a particular momentum is found as a linear interpolation between locations of minima in two nearest bins. The resulting lines of cuts are also shown in Fig. 3.20 and of β vs. momentum×charge after this cut in Fig .3.21. The resulting β vs. momentum×charge distributions obtained after this cut are shown in Fig .3.21.
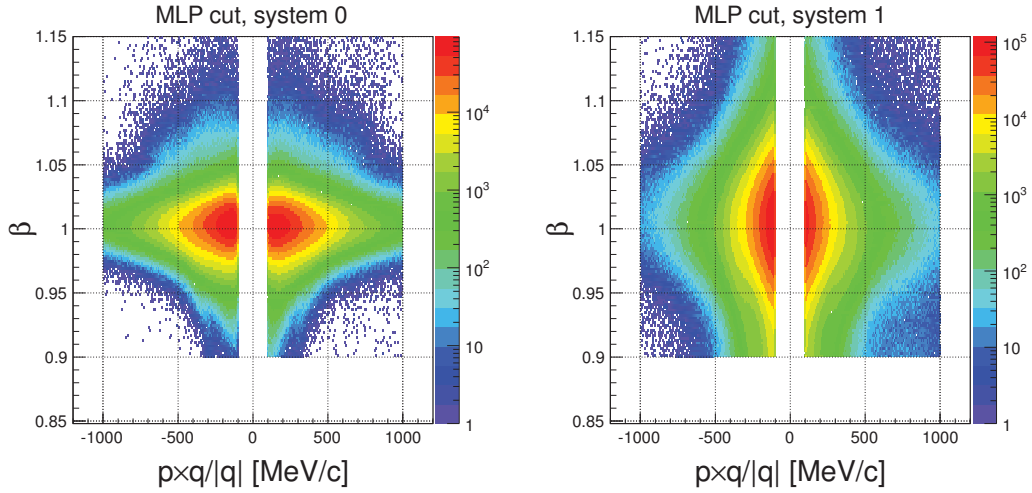
Figure 3.21.: Resulting distributions of particle's velocity versus momentum times charge (PID plots) after applying the cut on $y(\mathbf{x})$.

3.7.5 Additional cut on $d_{\text{track-ring}}$

The quantity $d_{\text{track-ring}}$ (Eq. 3.1), used to define signal and background training samples for MLP cannot be used as an input variable. Nothing prevents however from cutting on it additionally to the cut on $y(\mathbf{x})$. The precise definition of the cut is again a matter of discussion. As can be seen from Fig. 3.25 in Sec. 3.9.1, the signal, which would remain after subtracting background of randomly matched hadrons, at low momenta has broad tails under a narrow peak. There is a variety of phenomena, which contribute to this effect. One of them comes from e^+e^- pairs with relatively small opening angle. Because of the low efficiency of the RICH detector, it is possible, that the ring created by a particular lepton will not be found and the nearest matched ring will be the one created by the partner lepton. Another possibility are so called *corona rings*. It may happen, that the ring created by a lepton will not be found, but another ring will be reconstructed from a few pads of the original one and some pad(s) fired nearby due to noise or a direct hit of a particle or photon on the detector. Matching quality $d_{\text{track-ring}}$ for such a ring might be up to about 8 degree (twice the typical radius of a ring), but still might be a good signature, that the track of interest was lepton.

Both cases, together with the shape of the $d_{\text{track-ring}}$ vs. momentum distribution, shown in Fig. 3.22, suggest that the best decision would be a momentum-dependent graphical cut on $d_{\text{track-ring}}$, wide at low and strict at higher momenta. However, it turns out, that the narrow cut, independent of the momentum, works better with respect to the combinatorial background suppression. This is due to the fact, that the efficiency for lepton reconstruction and identification is rather low and clearly lower than 50%. This means, that in most cases only one lepton from a particular pair will be identified. If there is a lepton
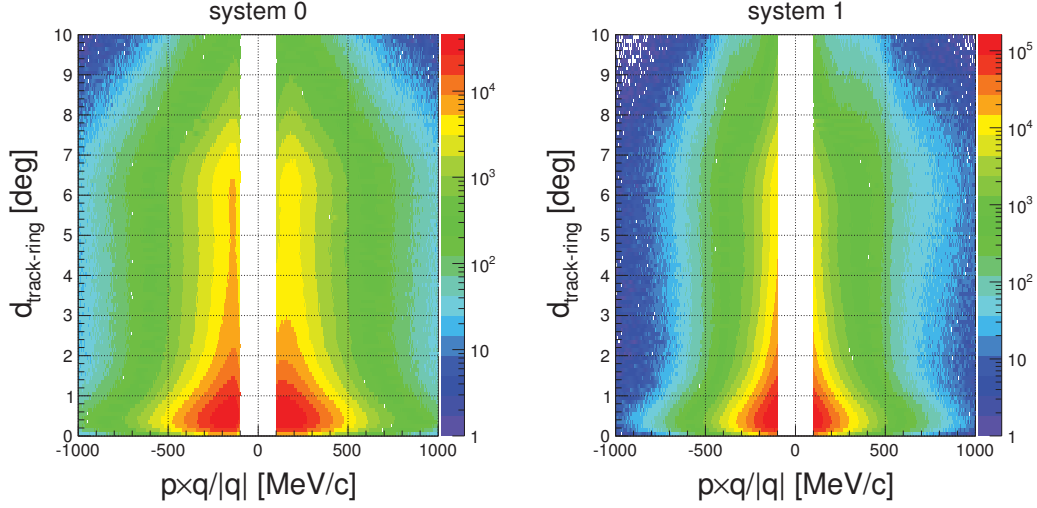
Figure 3.22.: Matching of the track to the ring as a function of particle's momentum times charge after applying the cut on the MLP response.
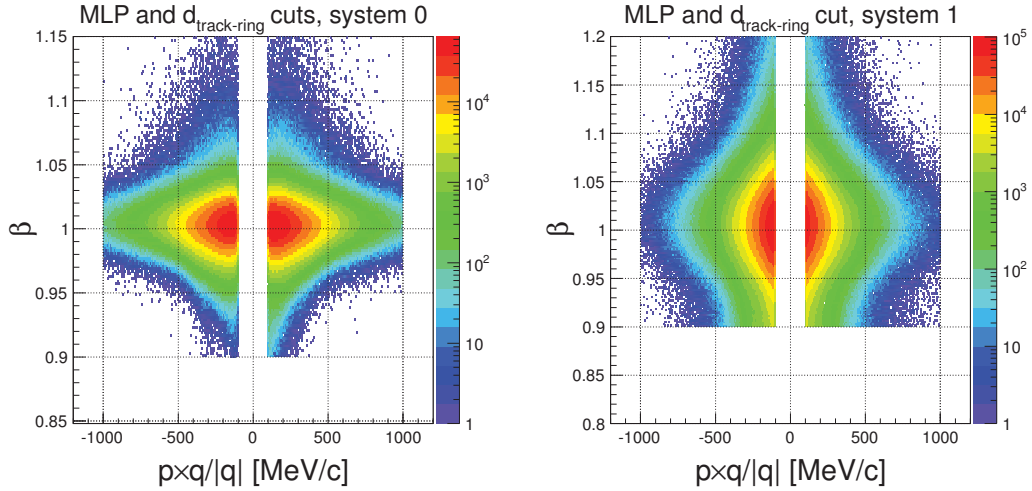
Figure 3.23.: PID plots after applying the cuts on $y(\mathbf{x})$ and on $d_{\text{track-ring}}$

found with low momentum and a high $d_{\text{track-ring}}$ value, its partner from a small opening angle pair is most probably not reconstructed. The found lepton can be therefore safely rejected. The cut was chosen to be $d_{\text{track-ring}} < 1°$ and this was validated by the study presented in Section 3.9.3 (Fig. 3.27).

Distributions of β versus $p \times q/|q|$ for the identified lepton sample after applying both cuts are presented in Fig. 3.23 and momentum distributions after each subsequent cut in Fig. 3.24.

3.8 Cut on the angle to nearest neighbor track candidate α_{CP}

Similar like in previous experiments, a cut to lepton's nearest neighbor is applied also in this analysis. The purpose of this cut is to reduce combinatorial background rather than to improve lepton identification. However, this cut is made for every single lepton and also it enters the calculation of efficiency matrices presented in the next chapter. Therefore the cut is discussed here.

In previous experiments the analysis was based on quantities, which is also currently available in the data set: *angle to nearest segment fitted* and *angle to nearest segment non-fitted*. The *segments* are the inner segments of MDC tracks, *fitted* means that the inner segment could be matched to an outer segment. In
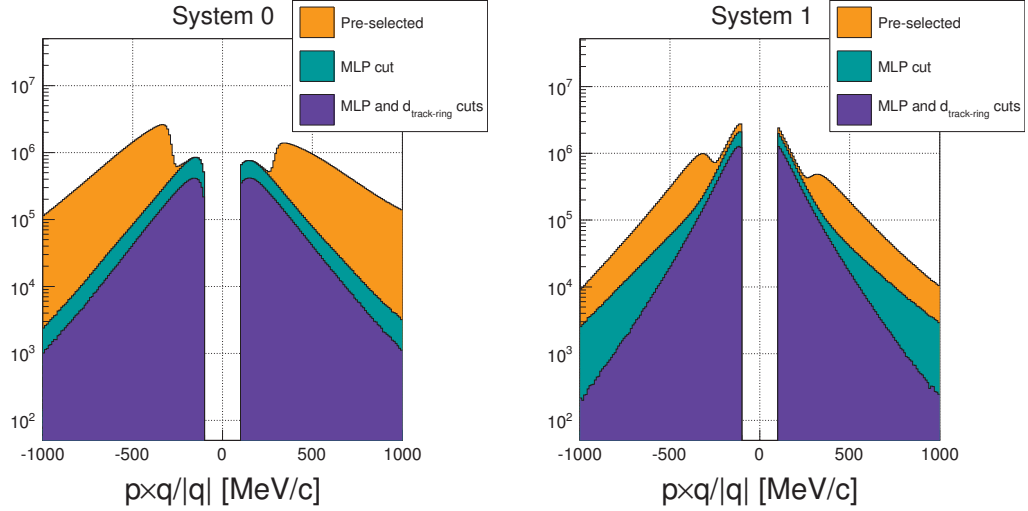
Figure 3.24.: Distributions of $p \times q/|q|$ for lepton candidates sample after pre-selection and subsequent identification cuts.

the Au+Au analysis, non-fitted segments are not relevant, because almost all segments can find a match due to large track multiplicity.

These two quantities try to assign a possible lepton identity to the found nearest segments. If the nearest neighbor is predicted not to be lepton, then the opening angle to the reference track is multiplied by -1 and the negative angle is stored in the data set for the primary track. However, the prediction is based only on the matching to a RICH ring. If tight matching is requested for the reference lepton track, then the nearest neighbor segment will probably be matched to the same ring, given high track density in Au+Au.

To improve the situation, in this analysis, the nearest neighbor is sought manually and the opening angle is multiplied by -1 if no ring was matched to the neighbor or it's $\frac{dE}{dx}(\text{MDC}) > 3$. Then the reference tracks for which angle to the nearest neighbor lie between 0 and a certain cut value are removed. In Section 3.9.3 results of the two cut values are compared in terms of invariant mass signal, signal-to-background ratio and significance to provide an ultimate benchmark.

3.9 Evaluation of the signal purity

3.9.1 Rotated RICH technique

One of the factors that has to be taken into account when comparing different lepton identification techniques is the purity of the obtained sample. Misidentified particles of other types present in the sample after all identification cuts must be treated as a background which should be considered. Their relative contribution can be estimated based on the Monte Carlo simulation using the information about particle's true identity obtained from the event generator. The results yielded by this method are however far from being realistic as long as particle distributions and detector responses are not in a very good agreement with the data.

An alternative approach is fully based on experimental data and exploits the sixfold symmetry of the HADES acceptance with respect to rotations by azimuth angle ϕ. Since wrongly identified leptons are those particles, which are only by chance matched to RICH rings, one can statistically reproduce the contribution of such mismatched tracks. This is done by adding 60° to azimuth positions of the reconstructed rings and then running the usual track-ring matching algorithm. In this way, rings are virtually moved to the neighboring sector and it is impossible to match track and ring left in the detector
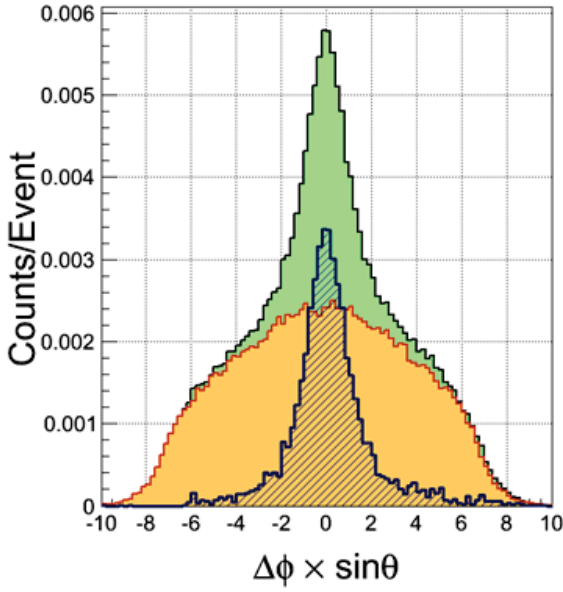
Figure 3.25: The principle of the rotating RICH technique. The green distribution is one of the components of the RICH matching quality (Eq. 3.1) for original data. The orange one is the distribution from data with RICH rings moved to the neighboring sector. Dashed area is the signal resulting from the difference of those two. In order to make the background better visible in this plot, no lepton identification cuts were applied.

by the same real lepton. Thus the procedure yields only accidental matches and the assumption is, that the number of them will be the same, as when the matching procedure is applied to the original data, without rotated RICH rings. The data prepared in such a way can then be analyzed in order to estimate, how many of mismatched tracks remain after identification cuts.

As it can be seen from Fig. 3.25, data with rotated RICH reproduces very well the background lying under the signal of lepton tracks correlated to RICH rings and this technique can be used to estimated the purity of the final lepton sample or at least to decide, which of the compared identification methods provides the best purity.

3.9.2 Comparison between hard cut and multivariate analyses

The most decisive criteria when comparing two ways of identifying particles is to evaluate efficiency and purity. Efficiency is the ratio of particles of interest, which survive identification cuts, purity quantifies the contamination from misidentified particles: it is a ratio of those correctly identified to all identified. One can compare efficiency values relatively between two methods just by comparing two particle yields, while purity values can be calculated using RICH rotating technique.

Comparison of integrated yields and average purity values for all tested considered ways of neural network training and for hard cut analysis is shown in Fig. 3.26 for both systems separately. There is no big difference between all the types of the neural network. The hard cut analysis provides slightly lower yield (i.e. lower efficiency) together with the purity comparable to the one obtained with the multivariate analysis. For the further analysis, weights 1 were chosen.

3.9.3 Comparison of pair spectra

Fig. 3.27 shows dilepton pair signal (S), signal-to-background ratio (S/B) and significance ($\text{Sgn} = \frac{S}{\sqrt{S+B}}$) for different cuts on $y(\mathbf{x})$ and on $d_{\text{track-ring}}$. For the case when the cut on $d_{\text{track-ring}}$ was momentum-dependent (*graphical cut*), it was designed to keep the purity constant as a function of momentum. Two different values of the cut on angle to nearest neighbor are tested in Fig. 3.28. They show that the best combination concerning signal-to-background ratio and significance is momentum-dependent cut on $y(\mathbf{x})$, $d_{\text{track-ring}} < 1°$ and $\alpha_{\text{CP}} > 4°$ and it is used in the subsequent analysis. Details on the subtraction
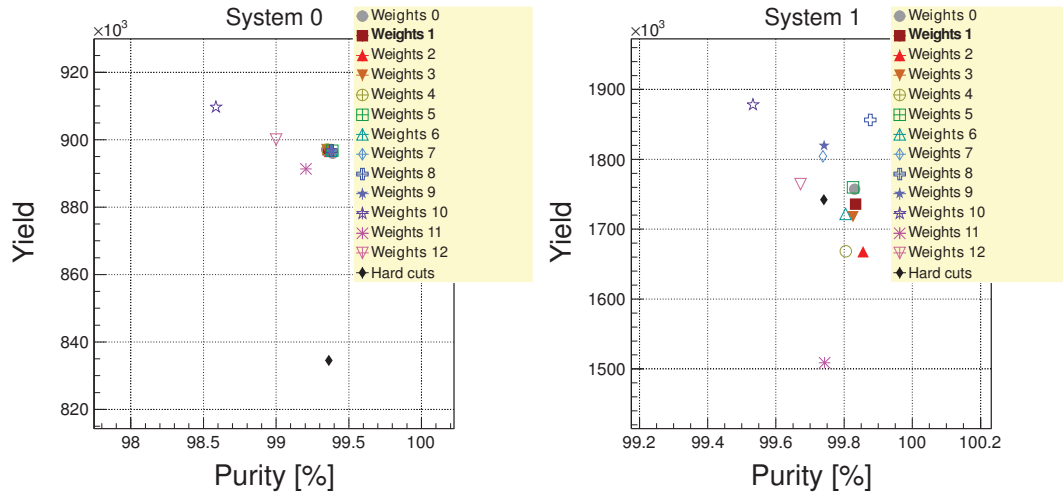
Figure 3.26.: Integrated yield and average purity in the momentum range $p \in (400 - 500)$ [MeV/c] obtained from multivariate analyses with different sets of input variables and definitions of signal and background models as well as from hard cut analysis. Numbering of weights is according to Fig. 3.16.

of the combinatorial background and signal extraction are given in Chapter 5.

Numbers of events with given electrons and positrons multiplicities are shown in Fig. 3.29 for the case of only particle identification applied (left panel) and after applying in addition close pair rejection cuts discussed above. In both cases only events with at least two leptons (i.e. the events which contribute to the pair spectra) are plotted for better visibility. Plots of this type have to be carefully interpreted. One could for example argue, that if they are not symmetric about the diagonal, this indicates the presence of hadron contamination (in fact in the present analysis the distributions are reasonably symmetric, especially after close pair cuts). It has been however checked with the Monte Carlo simulation, that this is just an effect of different acceptance and efficiency for e^+ and e^-, this is also confirmed by Fig. 5.5. Similarly, one could expect, that after close pair cuts the distribution would become more concentrated about the diagonal (i.e. have higher correlation coefficient) as on average more background (represented by like-sign pairs – off-diagonal) should be removed than the signal (represented by the opposite-sign pairs, close to diagonal). This is in fact not the case in the current analysis. This comes from the construction of the close pair rejection procedure – it is the cut on the opening angle between two *well reconstructed unlike-sign leptons*, which are identified as converted photon. Removing them reduces number of events at the diagonal. The signal-to-background ratio *averaged over the whole dilepton invariant mass range* is indeed reduced because pairs of very small opening angle, where the signal-to-background ratio is very high, are removed. Nevertheless, his brings a gain in the higher invariant mass range. Plots of the type as in Fig. 3.29 do not contain this information.
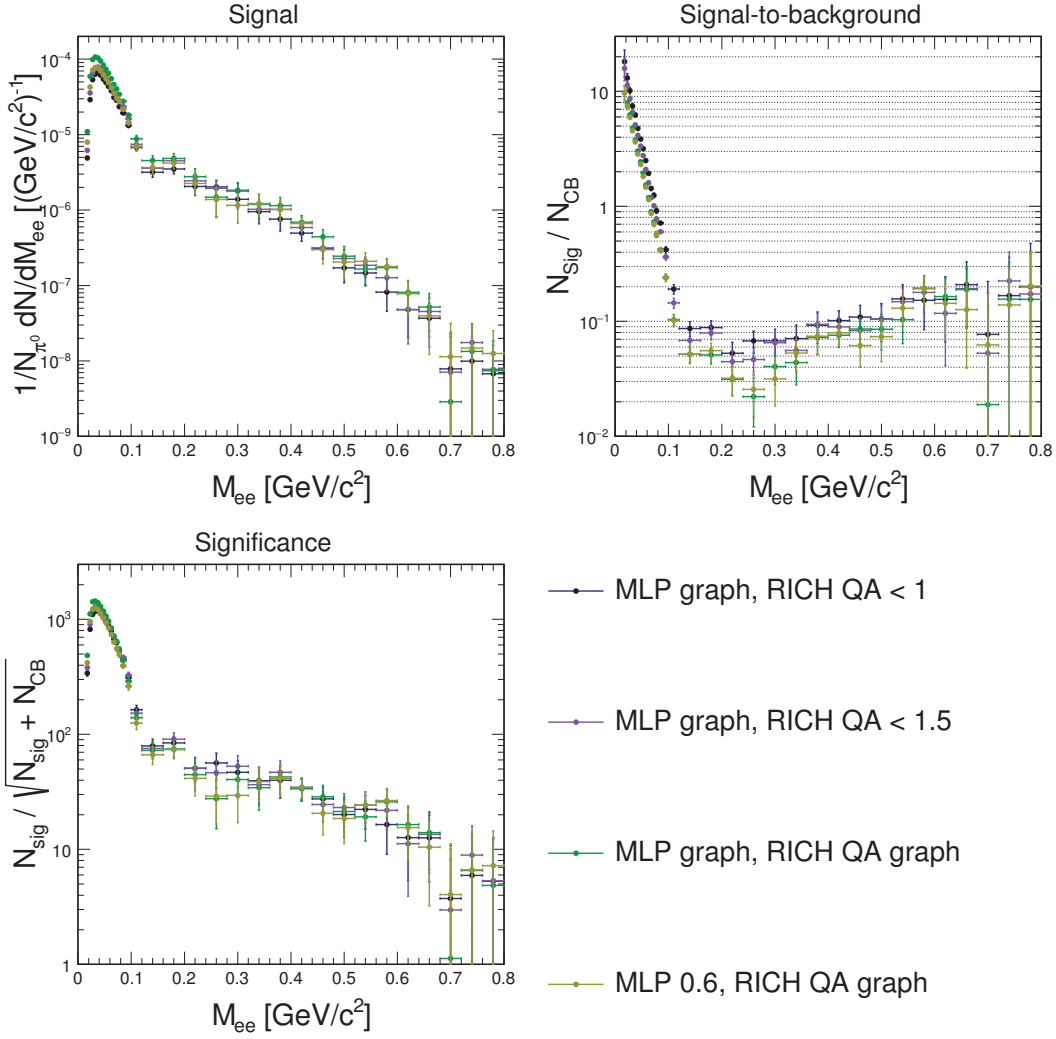
Figure 3.27.: From left to right: signal, signal-to-background ratio and significance $\mathrm{Sgn} = \frac{S}{\sqrt{S+B}}$ obtained for different cuts on $d_{\text{track-ring}}$ (denoted here as RICH QA) and $y(\mathbf{x})$ (denoted MLP).
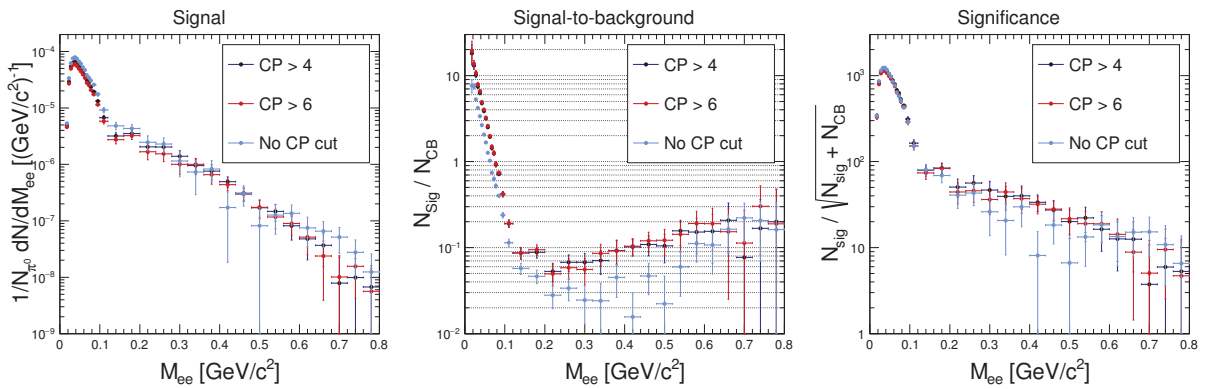
Figure 3.28.: From left to right: signal, signal-to-background ratio and significance $\mathrm{Sgn} = \frac{S}{\sqrt{S+B}}$ obtained for different cuts on the angle to the nearest neighbor of lepton track.
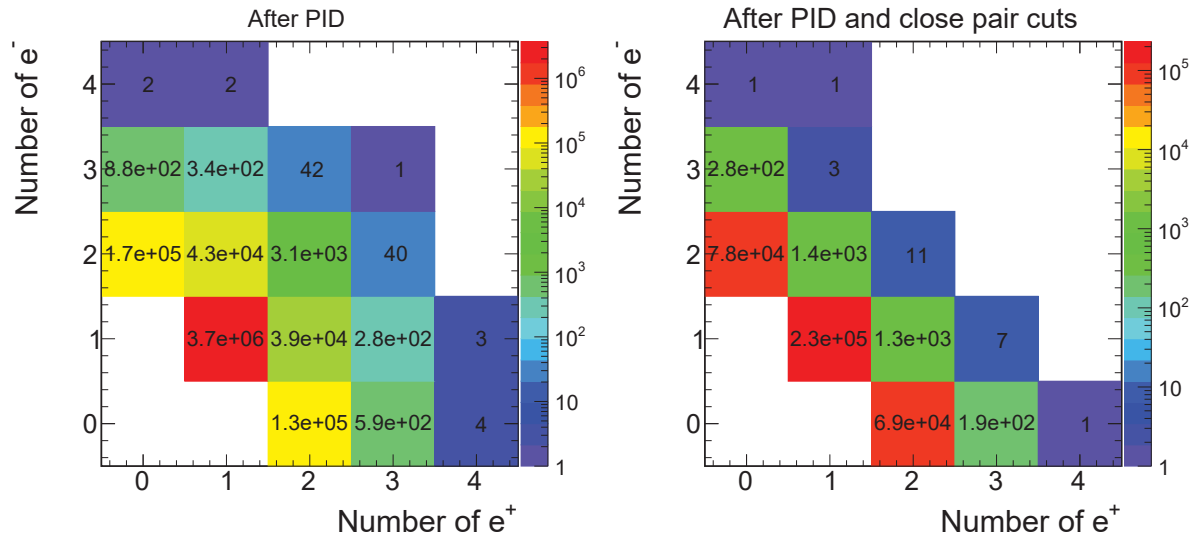
Figure 3.29.: Numbers of events with given electron and positron multiplicity after PID selection (left) and additionally after cuts removing close pairs (right).

4 Efficiency corrections

All the processes, that lead to particle's detection, whether it is ionization of atoms in a gas or excitation of them in a scintillator, ejection of an electron from a photocathode or production of an electron-hole pair in a semiconductor, have a stochastic character. As a consequence, the probability, that a charged particle will produce a measurable signal is always different from the unity. Moreover, tracking and matching algorithms may fail to reconstruct a certain particle and it is more likely, when more of them are passing through a single piece of detection system, as it is often the case in heavy-ion experiments. In addition, distributions of measured quantities have finite widths, due to finite resolution of detectors. When cuts on these distributions are used to select particles of requested type, those of them that populate tails of distributions will be almost inevitably removed from the sample. All such losses are described with a common name of *inefficiencies*. Physics spectra can only be compared to theory predictions and results from other experiments, thus interpreted, if they are free from inefficiency effects or *corrected for efficiency*.

One possibility is to multiply the final spectra by a (usually non-constant) factor that heals the losses due to inefficiency. This method comes with the risk that the factor will be model-dependent, i.e. that the corrected spectra will not really show the features of real physical distributions, but rather those of the model used to calculate the correction. The source of this problem is following: Assume that the emission of an interesting particle depends on two kinematic variables, say transverse momentum p_t and rapidity y, and one wishes to make a distribution of one of them, e.g. of rapidity. If in a selected bin of rapidity, transverse momentum is distributed differently in reality and in the model (what is not known *a priori*), and if the efficiency itself depends on p_t, then the correction factor for this y bin will be dominated by the efficiency value in the range of p_t that is strongly populated in the model and possibly different from the value in the range populated in the real data. This will make the factor simply wrong. A solution would be to make a multi-differential distribution in all kinematic variables, on which particle emission may depend, calculate the correction factor in this multi-dimensional space, correct in each cell of the space separately and only then project on the axis that is of interest.

This solution is impractical for the dilepton analysis. In principle, the emission of the electron-positron pair and efficiency of its reconstruction depend on its full kinematics. The kinematics of two particles is described by two four momenta, i.e. eight variables. Since the rest mass of e^+/e^- is fixed, $8 - 2 = 6$ independent variables remain. It is possible to find such that fully characterize the pair: besides those relevant for physics considerations (invariant mass, transverse momentum, helicity[1]), this could be azimuth and polar direction of the pair and its orientation. However, it would be very difficult to calculate the correction factor in the space of all these variables with a reasonably fine cell sizes.

Another approach is to treat both particles that build up the pair separately. Their kinematics are then described by three variables each, e.g. momentum value, and azimuth ϕ and polar θ angles of the emission. For a pair this gives again six degrees of freedom. The correction factor has then to be calculated only in three-dimensional cells and this is much easier. The main difference compared to the method discussed previously is that the correction has to be applied event-by-event. The pair spectra have to be filled with weights corresponding to the values of the correction factors for both particles that belong to the pair. This cannot be, however, regarded as a disadvantage of this method.

A typical way to calculate the correction factor is to use a Monte Carlo simulations, that describes rescattering processes of particles in the detectors and electronic signal generation. Such simulated signals can in principle be processed by the same algorithms that serve to track reconstruction and

---

[1]   Angle between the direction of the virtual photon in the rest frame of the mother particle and the direction of electron (or equivalently positron) in the rest frame of the virtual photon

particle identification in the analysis of measured data. An important assumption is that interactions of particles and generation of signals in the simulation reflect the reality to high precision. This requires a thorough study of existing detectors. One of problems of calculating the correction factor in a highly-dimensional space is that it would require an enormous number of events to be simulated in order to fill all the cells with sufficient statistics.

In the current analysis the efficiency correction is calculated based on the Monte Carlo method. In the first step the correction factor is calculated for single simulated electrons and positrons as a function of their total momentum p as well as θ and ϕ angles (Section 5.2.1). It turns out, that the number of identified leptons in a single event (and thus the efficiency) decreased in the course of the beam-time and this has to be taken into account by an overall empirical factor (Section 4.2). In addition, the presence of another nearby lepton (what is very likely, because e^+/e^- pair have mostly small opening angles) influences the reconstruction of the first one. This is regarded as a residual effect due to correlation in the reconstruction with respect to the full efficiency description and therefore is represented by a factor that depends only on the opening angle of the pair (Section 4.4). Finally to the efficiency correction contribute also the losses due to the fact, that no leptons could be reconstructed in specific parts of the spectrometer in certain periods of time. As there are no simply tracks that could be weighted by any correction factor, these losses are accounted for by a factor dependent on the pair kinematics, in a similar way, as discussed in the beginning of this chapter. It is done, however, only in two-dimensional space to minimize the problem of statistics and the variables are selected such to minimize model dependence. Since these are not the same variables, as one would like to plot from the point of view of physics discussion, this correction cannot be applied on the final spectra, but event-by-event (Section 4.6).

4.1 Determination of single lepton efficiency

In the first step, the detector response on single electrons and positrons is to be computed. To do this, electrons and positrons with homogeneous spectra of momentum (from 0 to 1000 MeV/c), θ and ϕ are simulated using the Pluto event generator [110]. They are then processed using the GEANT-3 Detector Description and Simulation Tool to simulate the particle interactions within the detector system and to generate secondary particles. This also gives an information, which detector volumes were crossed by the particle. Then appropriate digitizers contained in the HYDRA package can be used to simulate electronic response of the individual detectors. The example of the Pre-Shower digitizer and tuning of its parameters, performed by the author, is discussed in the Appendix A.

The output of the digitizers can already be subject to the usual hit/cluster finding, tracking and matching procedures, that are used for the experimental data. But to make sure, that the result will approximately correspond to the effect of lepton reconstruction in the data, the background of all other particles produced in the reaction has to be introduced. This can be done by combining simulated e^+/e^- with full events, either measured in experiment (established expression: *embedding to data*) or simulated with some model, like UrQMD (*embedding to UrQMD*) in our case. In both cases, one e^+ (and separately one e^-) per event is embedded in each sector of the HADES spectrometer. This allows to increase the number of simulated leptons keeping the computing time and disk space approximately the same (as they are governed by much more abundant background particles). On the other hand, this should bring no bias on the results, since the reconstruction in different sectors should be completely independent. In the current analysis embedding to UrQMD is used to calculate efficiency matrices and embedding to data is used then to estimate systematic uncertainty.

Reconstructed events with embedded leptons are analyzed in the way, that closely follows the full analysis of the real data. In parallel to the three-dimensional distributions of $N(p, \theta, \phi)$ for reconstructed and identified e^+ and e^-, analogous distributions are filled for particles that crossed the HADES acceptance, based on the geometric information transported from the GEANT calculation. **Both types of distributions are build as functions of original ("ideal") values of p, θ and ϕ, with which the particles were simulated.** The condition for the latter ones is that in each of the MDC modules at least four
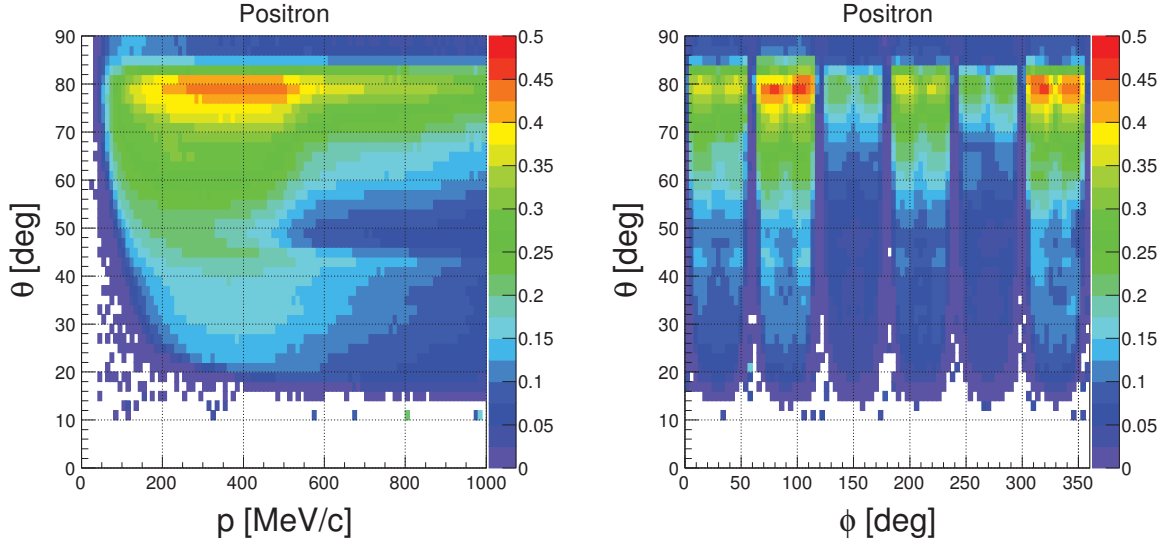
Figure 4.1.: Two-dimensional representations of the efficiency of positron reconstruction and identification. The values are averaged over the variable which is not shown (ϕ in the left panel, momentum in the right one).
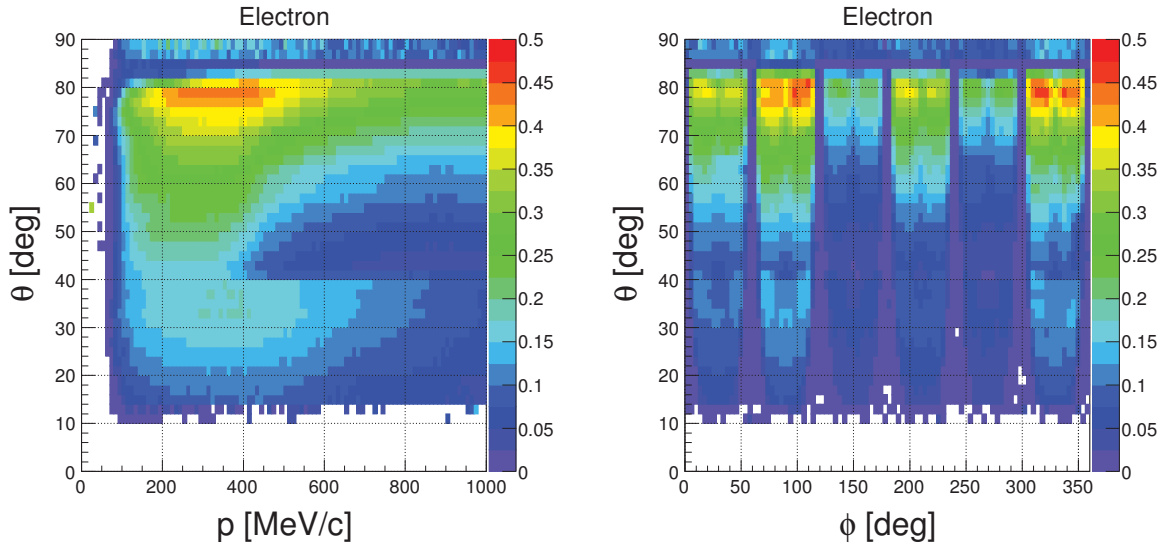
Figure 4.2.: Two-dimensional representations of the efficiency of electron reconstruction and identification. The values are averaged over the variable which is not shown (ϕ in the left panel, momentum in the right one).

layers of wires should be crossed by the lepton's trajectory. This provides a reasonably safe definition of the particle, that fall into HADES acceptance and should be reconstructed if the efficiency would be 100%. The iterations over reconstructed tracks and particles transported from the GEANT stage are done independently and corresponding distributions are also filled independently. However, in the iteration on the reconstructed tracks there is an explicit check, that the GEANT particle associated with the track, is the one, that has been embedded. Efficiency is defined as the ratio of the $N(p, \theta, \phi)$ distribution for the reconstructed leptons to the one for leptons crossing the HADES acceptance:

$$\mathrm{Eff}(p, \theta, \phi) = \frac{N_{\mathrm{reco}}(p, \theta, \phi)}{N_{\mathrm{acc}}(p, \theta, \phi)}. \tag{4.1}$$
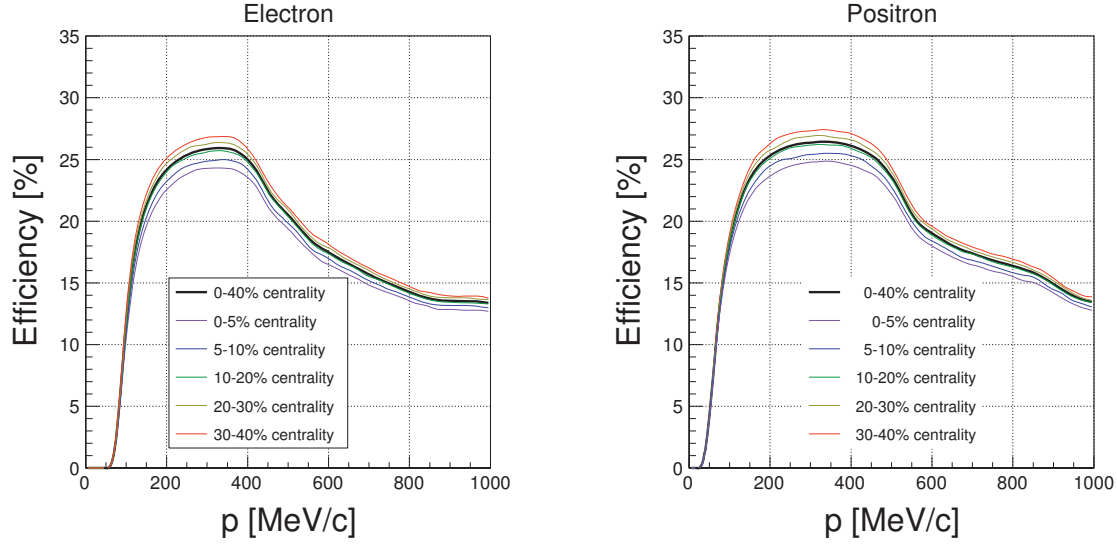
Figure 4.3.: One-dimensional representations of the efficiency for electron (left panel) and positron (right panel) reconstruction and identification in different centrality bins, averaged over θ and ϕ.

The calculation were done with 10^7 events for electrons and the same number for positrons in case of embedding to UrQMD and $4.9 \cdot 10^7$ events for both lepton signs in case of embedding to the data. Besides the efficiency matrix calculated from all the available events together (that corresponds to PT3 in real data), there are also ones calculated separately for different centrality classes as defined in Section 3.3.
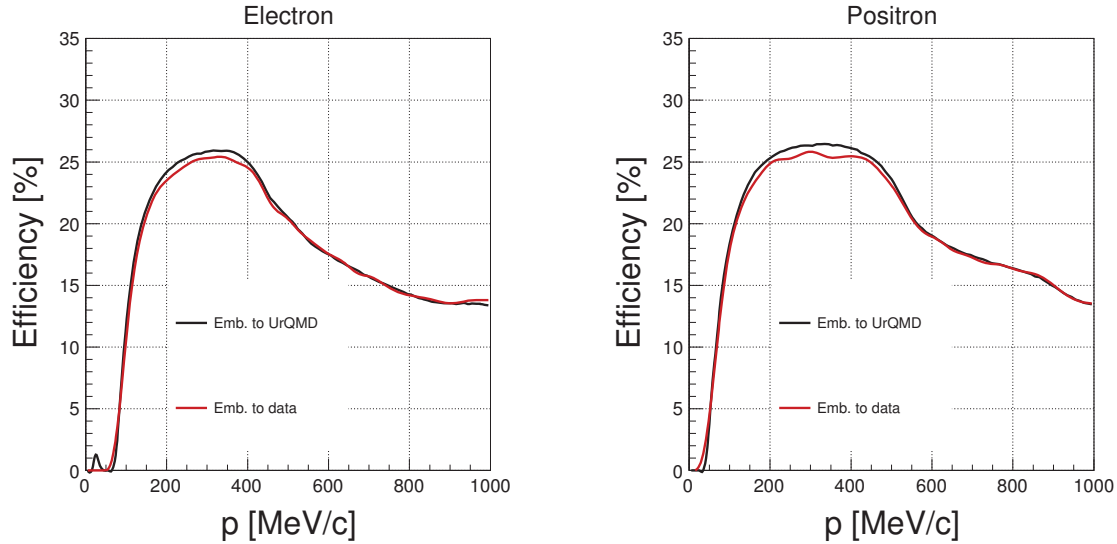
Figure 4.4.: One-dimensional representations of the efficiency for electron (left panel) and positron (right panel) obtained from embedding single leptons to real events (red curve) and to UrQMD (black curve), both for 0-40% centrality.

Making a projection of a matrix, which is a ratio of two distributions, from three to two dimensions requires a special care and will never be accurate if the statistics is not constant in the dimension, that is integrated-out. Therefore, more understandable information is carried by the matrices that are calculated from the beginning in two dimensions, just to present the main features of the real, three-dimensional ones. Such 2D representations are shown in Figs. 4.1 and 4.2.

Efficiencies in different centrality bins are plotted in one-dimensional representation in Fig. 4.3. The main point is that the efficiency drops with increasing centrality because of higher occupancy of the involved detectors, that disturb the reconstruction of the embedded leptons.

Similar comparison, but for embedding to events measured experimentally and simulated with UrQMD is shown in Fig. 4.4. The latter is systematically higher by few percent. It comes from different description of the background present in the event. This means that the background description provided by Monte Carlo is not fully accurate.

In the further analysis efficiency matrices calculated with embedding to UrQMD are used in order to enable self-consistency checks with simulated dilepton sources, which at the moment are available only embedded to UrQMD. As a consequence, the deviation between the two descriptions of the event background has to be taken into account as systematic uncertainty. To study this uncertainty in grater detail, one-dimensional efficiency corrections as a function of pair observables have been calculated using the method desribed in Section 4.5 for embedding to real data and to UrQMD. Example results are shown in Fig. 4.5. The relative deviation is again of the order of few percent.
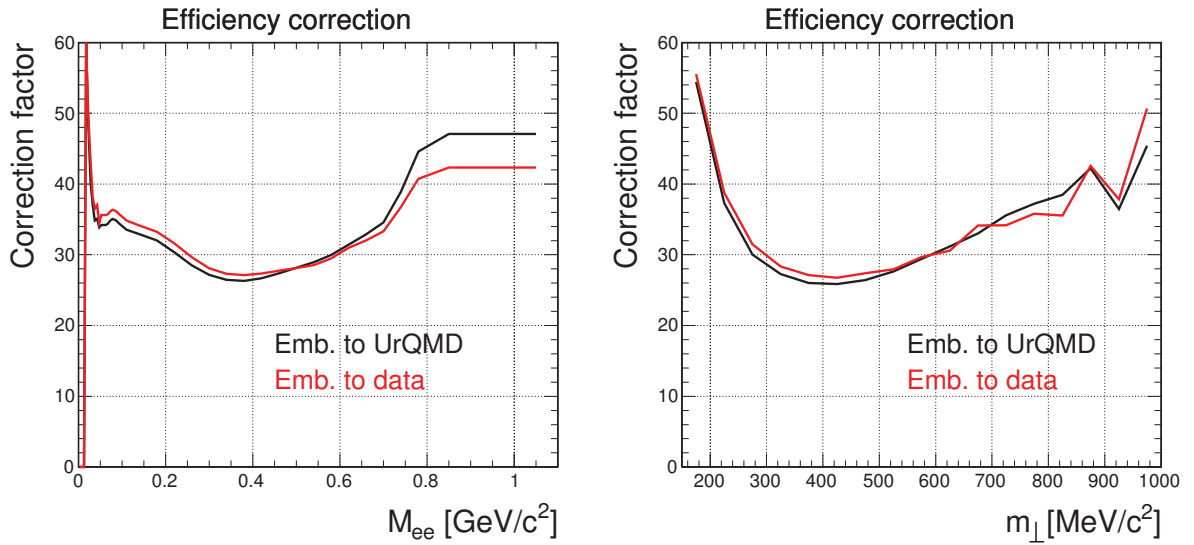
Figure 4.5.: Efficiency correction as a function of dilepton invariant mass (left panel) and transverse mass (for invariant mass $0.15 M_{ee} < 0.55 \, [\text{GeV}/c^2]$, right panel) obtained from single lepton efficiency matrices calculated with embedding leptons to UrQMD events (black line) or to real data (red line).

The contribution to systematic uncertainty, resulting from Fig. 4.5, is included in the presentation of final results.

4.2 Efficiency drop in the course of the beam-time

Plotting the number of identified electrons or positrons per event as a function of time one can observe clear decreasing trend during the beam-time, see Fig. 4.6. There is no reason to expect decreasing radiation of leptons, so the trend has to be assigned to the degradation of the reconstruction efficiency and has to be taken into account empirically, when the data is corrected for inefficiency. To account for this effect, the linear fit to the trend is done in the sectors 0, 1, 4 and 5. In sector 3 fluctuations do not allow to fit the linear function, but just the inspection suggest constant efficiency in this sector (sector 2 is ignored in the analysis). The factor obtained from evaluating the fit function at the time of a particular event is then used as an additional weight when filling the spectra. The question emerges,
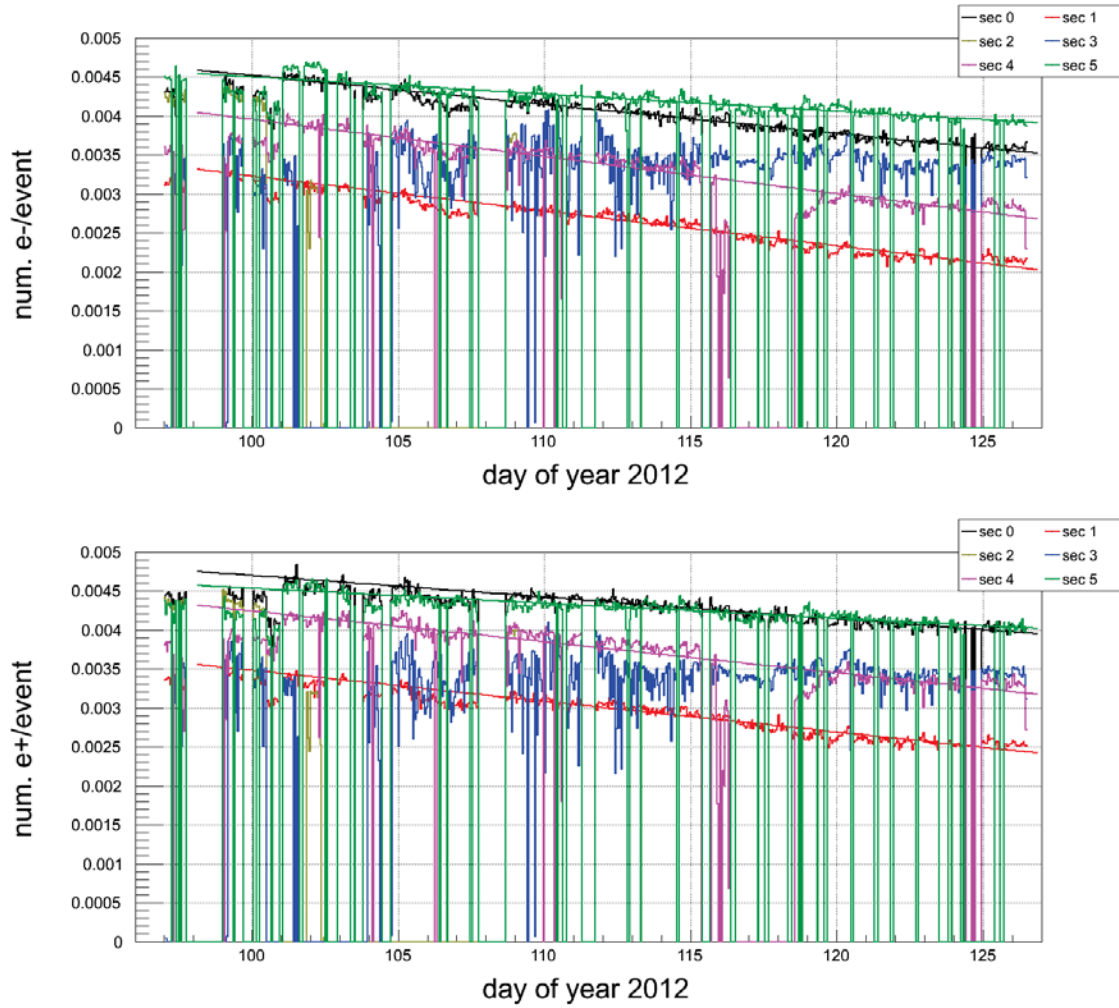
Figure 4.6.: The truncated (in order to get rid of large fluctuations) average number of identified electrons (upper panel) and positrons (lower panel) in a single event as a function of the time during the data acquisition. For the sectors, for which it was possible to make a linear fit to the trend, it is shown as well.

how the factor should be normalized, that is, at which time should it have the value of unity. To answer this, one can compare the trend for average numbers of reconstructed tracks per sector and per event with the numbers of leptons, as shown in Fig. 4.8. The drop of efficiency is not visible for all tracks and it has to be addressed to the detector specific for lepton identification i.e. to RICH. The parameters of the RICH in simulation are tuned based on the measurements with single-photon UV lamp, performed several months after the experiment. Therefore if the fall of the efficiency is associated with the damage of the detector (or its readout), the simulation reflects the state at the end of the beam-time and at this moment the time-dependent factor should be fixed to 1 [111, 112].

The effect of applying the factor can be seen in Fig. 4.7. As one would expect, the trends become constant on average. The cross-check can be done, by plotting the number of reconstructed π^0-Dalitz pairs[2]. With the linear drop of the single track efficiency, pair reconstruction should decrease non-linearly. Nevertheless, applying the time-dependent factor should make even pair trends constant. This is indeed true, as shown in Fig. 4.9.

---

[2] $M_{\mathrm{inv}} < 150$ MeV/c^2, $\Theta_{\mathrm{ee}} > 9$ deg, dilepton pair reconstruction will be discussed in more detail in following chapters.
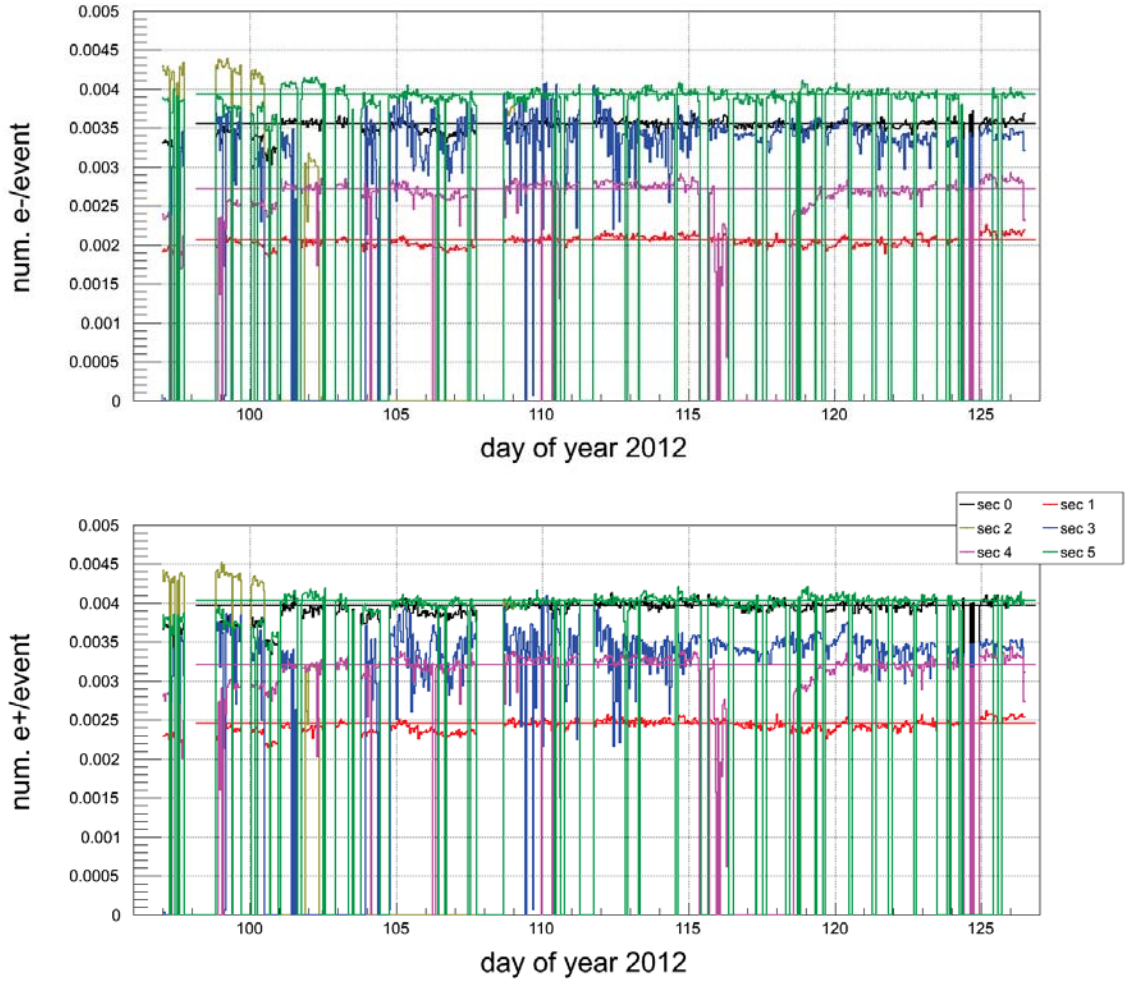
Figure 4.7.: The truncated average number of identified electrons (upper panel) and positrons (lower panel) per event as a function of the time during the data acquisition. The time-dependent factor taking into account the degradation of efficiency has been applied.
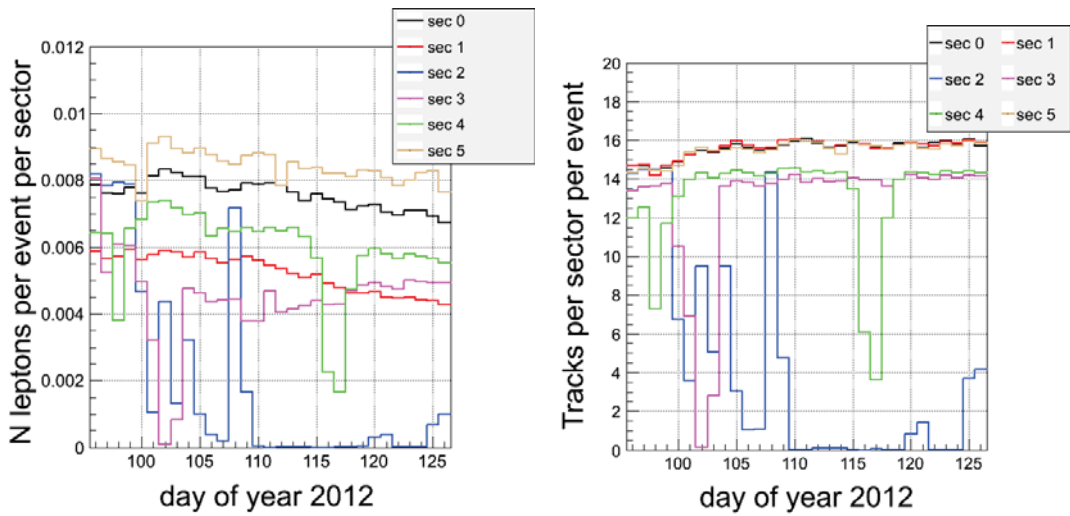
Figure 4.8.: Average number of leptons(left panel) and all tracks (right panel) reconstructed per sector and per event.
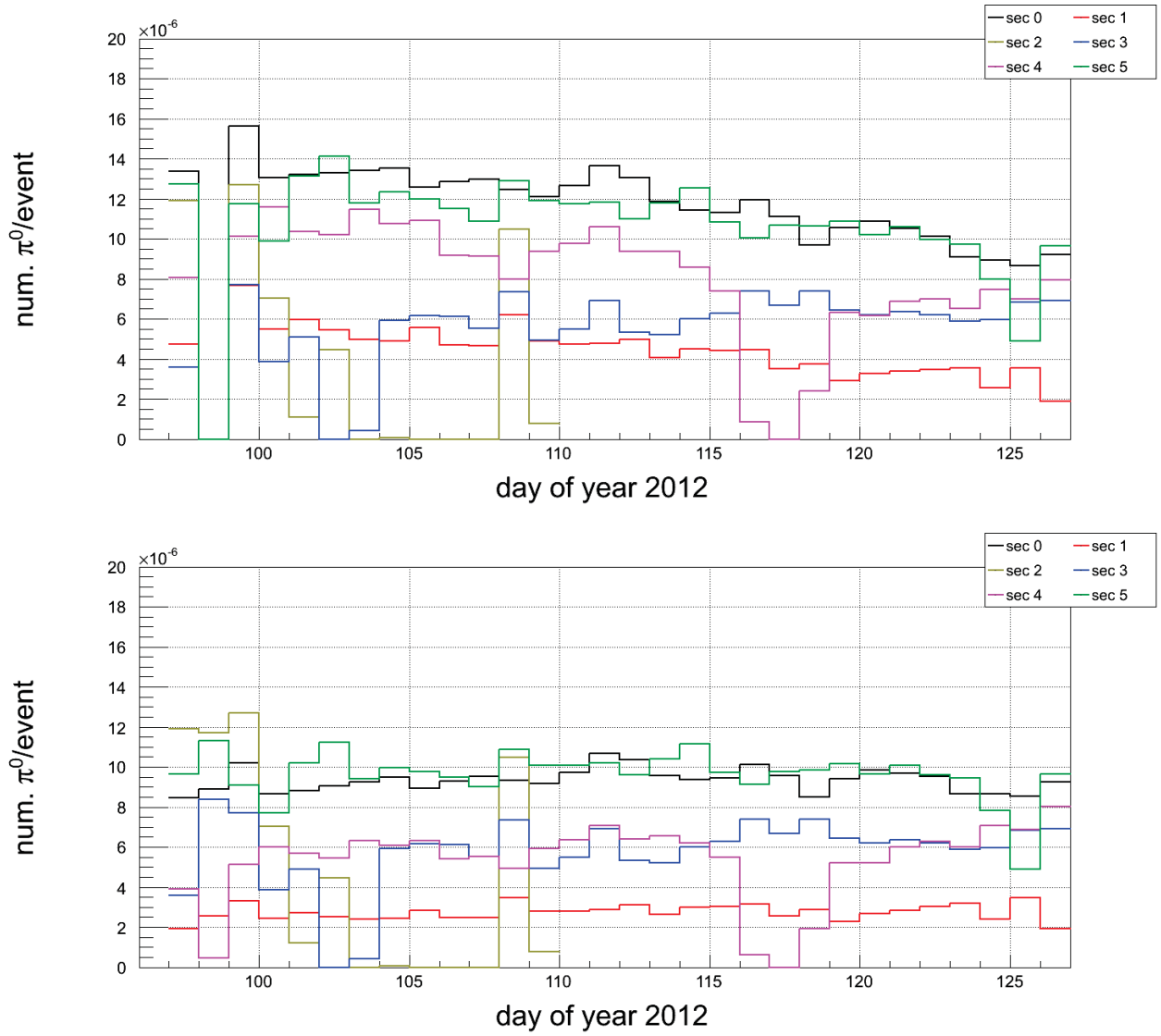
Figure 4.9.: The truncated average number of reconstructed π^0-Dalitz pairs in a single event as a function of the time during the data acquisition. The upper plot shows the trends without applying the time-dependent factor for reconstruction of single leptons and the lower plot shows them after applying such factor.
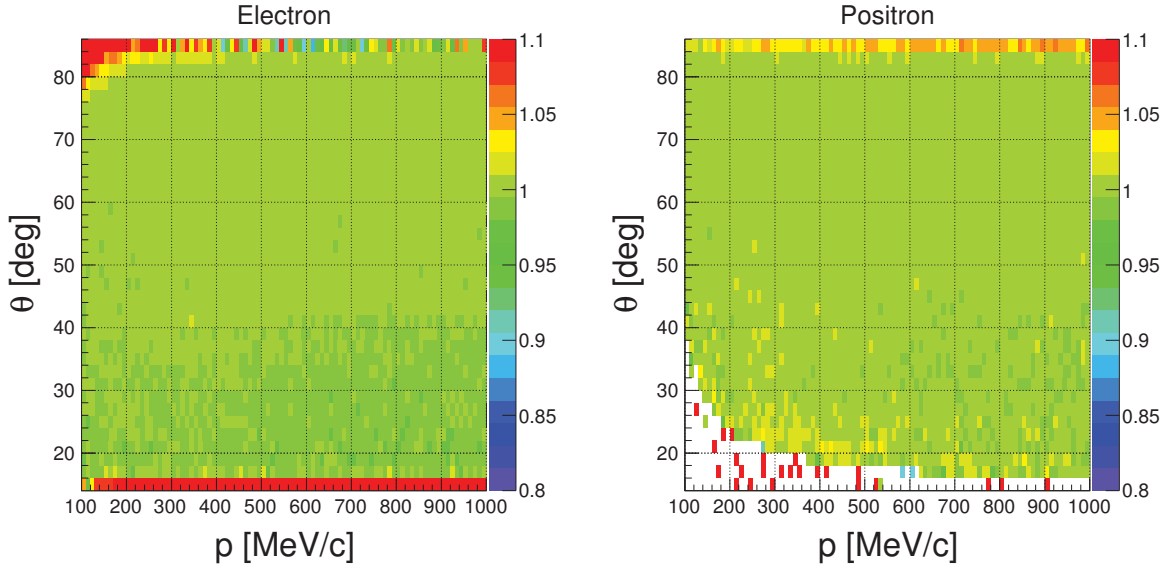
Figure 4.10.: Ratio of the number of the reconstructed tracks corrected for efficiency to the number of the particles inside the HADES acceptance, calculated for the same data sample, as used to generate the efficiency correction, separately for electron and positrons.

The minimum requirement on the consistency of the efficiency correction is that applying it for tracks reconstructed in simulation should allow to reproduce distributions of particles within the acceptance of the detector system. Preferably, this should be the case also if the code used to check this is maintained separately and follows a slightly different approach to the analysis, than the code used to generate efficiency correction matrices.

The method was based on the iteration over reconstructed tracks nested in the loop over simulated particles, transported from the GEANT level. Since the information about the simulated particle, used to generate signals, from which the track has been reconstructed, is included in the track object, the matching of those two is possible in the nested loop.

In the first step, the check is done in the trivial case of the same input data, as used to generate the correction. The result, being effectively the ratio [3]

$$\frac{\int f_{\mathrm{corr}}(p,\theta,\phi) \cdot N_{\mathrm{reco}}(p,\theta,\phi) \mathrm{d}\phi}{N_{\mathrm{acc}}(p,\theta)}$$

of the distributions of reconstructed tracks corrected for efficiency to the distribution of particles inside the HADES acceptance as a function of the polar emission angle and the momentum, is shown in Fig. 4.10 for electrons and positrons. The values very close to unity indicate a very good agreement. Since in the computation of the efficiency matrices and in the self-consistency check two alternative algorithms are used in looping over the data and matching a reconstructed track to a simulated particle, the agreement proves also, that the choice of the algorithm does not introduce any significant systematic error.

The next step is to perform check using event generator with particle decays. This can be done by simulating production and decays of dilepton sources in Pluto, embedding the daughter particles to data or simulated events and perform the self-consistency test. Here, 10^7 events of each π^0-Dalitz and η-Dalitz were simulated and embedded to UrQMD. Fig. 4.11 shows the result for positrons coming from

---

[3] $f_{\mathrm{corr}}(p,\theta,\phi) = 1/\mathrm{Eff}(p,\theta,\phi)$, see Eq. 4.1.
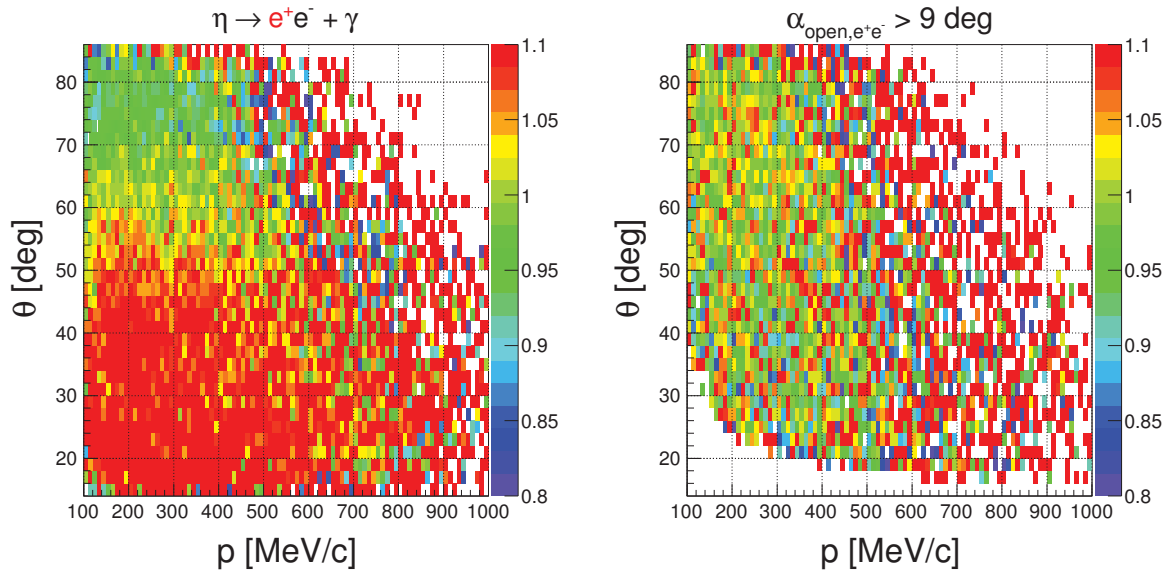
Figure 4.11.: Ratio of the number of the reconstructed tracks corrected for efficiency to the number of the particles inside the HADES acceptance, calculated for positrons produced in η-Dalitz decays, taking into account all decay events (left) and only those with lepton pair opening angle above $9°$ (right).

the η-Dalitz decay. In the left panel the ratio for all reconstructed events is shown, the agreement is rather poor. However, when selecting only events with e^+e^- pair opening angle larger than $9°$, the result of comparison is satisfactory, taking into account limited statistics. This points towards correlation effects in the reconstruction of lepton pairs when two tracks are close to each other. This cannot be taken into account assuming pair efficiency as a product of the two single leg efficiencies calculated independently and is the matter of pair correction and will be discussed in the next section.

4.4 close pair effects

The influence of one lepton track on the reconstruction of another one is expected to be a residual effect, small compared to the value of efficiency itself. Also the full dependence of efficiency on the pair kinematics has been already taken into account by the single track correction. Therefore, even if lepton close pair effects have to be corrected on the pair level, it is not necessary to calculate the correction in six-dimensional space, as it was discussed in the introduction to this chapter. One expects, that one-dimensional correction should be sufficient. The most obvious quantity, on which the correction factor should depend, is the opening angle of the pair.

The procedure is then to use again simulated Dalitz decays of π^0 and η embedded to UrQMD events and build the distributions of the dilepton opening angle for pairs inside the HADES acceptance and of the pairs of reconstructed tracks corrected for efficiency. The ratio can be used as an additional correction factor. It is shown in the left panel of Fig. 4.12. It has been checked, that the ratio is the same for both π^0 and η, so both data sets were merged together to get more statistics.

The rise of the ratio towards very small opening angles means that efficiency correction calculated for single tracks overestimates the true one in this region. The reason is that even if one track could not produce enough Cherenkov light in the RICH detector to be identified as a lepton, it can still be matched to the ring produced by the second lepton if the opening angle is small enough. Furthermore, Cherenkov light produced by both particles can contribute together to a ring of better quality. This is confirmed by the correspondence between the width of the rising peak in Fig. 4.12 and the cut on the $d_{\text{track-ring}}$ quantity. It can also be shown, that for wider cuts the width of the rising region gets larger as well.
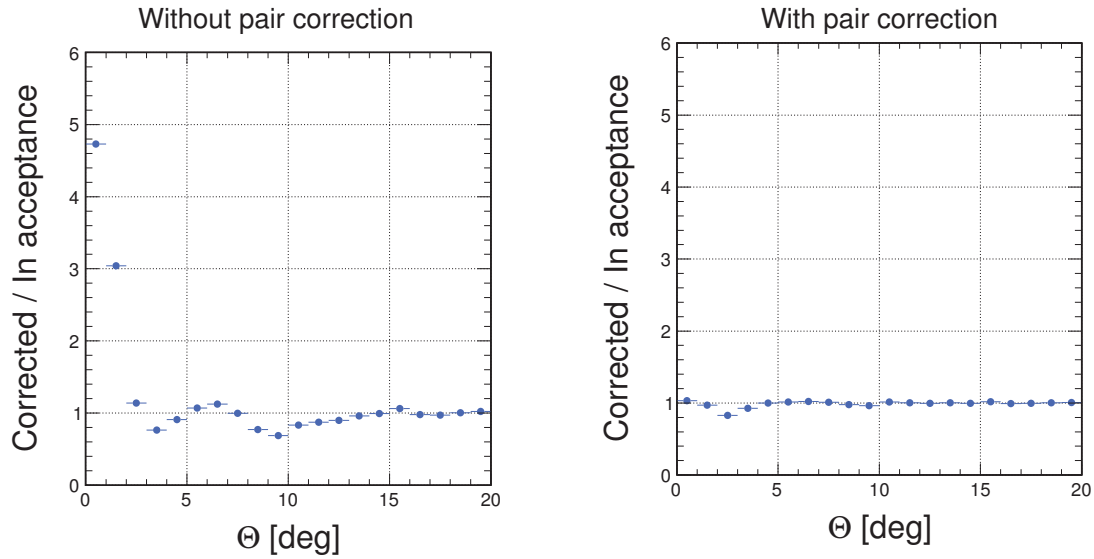
Figure 4.12.: Left: ratio of the opening angle distributions of e^+e^- pairs from π^0 and η Dalitz decays for tracks reconstructed and corrected for efficiency to the pairs in the HADES acceptance. Right: the same after applying the correction emerging from the ratio in the left panel.

In the range of about $1.5-6°$ the ratio drops dramatically. This is due to the sorting procedure, which does not allow two reconstructed tracks to share common outer MDC segment or META hit. In such case only the one, that has best (lower) Runge-Kutta χ^2 is used in the further analysis. In the first order this allows to reject clone/ghost/fake tracks, but the secondary effect is the drop of efficiency of close lepton pairs.

The ratio from the left panel of Fig. 4.12 can be used as a correction applied on the pair level in the event-by-event manner. The first test is to check the same ratio after applying this corrections. It is shown in the right panel of the Fig. 4.12. The ratio is now compatible with the unity within statistical uncertainties and the differences from various PID methods became even smaller than before. Small discrepancy from the unity is still present between $1.5°$ and $3°$. This is the remnant of the large drop in the range $1.5-6°$ in the left panel. The possible explanation is that due to a very low efficiency there is insufficient number of reconstructed pairs that could be weighted by the correction factor and the agreement with the distribution of pairs within the geometric acceptance cannot be reached.

As the next step the effect of the correction on a distribution of a variable, that is of more physical interest has been checked. Fig. 4.13 shows the ratio of invariant mass distributions for the reconstructed pairs corrected by the product of single track efficiency values and for the pairs inside the HADES acceptance. In the left panel it is shown without any additional correction and reflects similar features as the same ratio drawn as a function of opening angle (since the invariant mass is a monotonic function of the opening angle). Their ratio in the right panel is made again after applying the correction factor from the left panel of Fig. 4.12. In this case the ratio is also compatible with the unity within error bars and the small discrepancy visible in the opening angle representation is washed out in the invariant mass.

The right panel of Fig. 4.13 allows to estimate the systematic error introduced by the correction for inefficiency for pairs. It reflects namely the difference between the reconstructed distributions after applying all the corrections and the original spectra. Since the ratio deviates from 1 by 0.1 at maximum, **a contribution of 10% to the systematic uncertainty** is assumed.
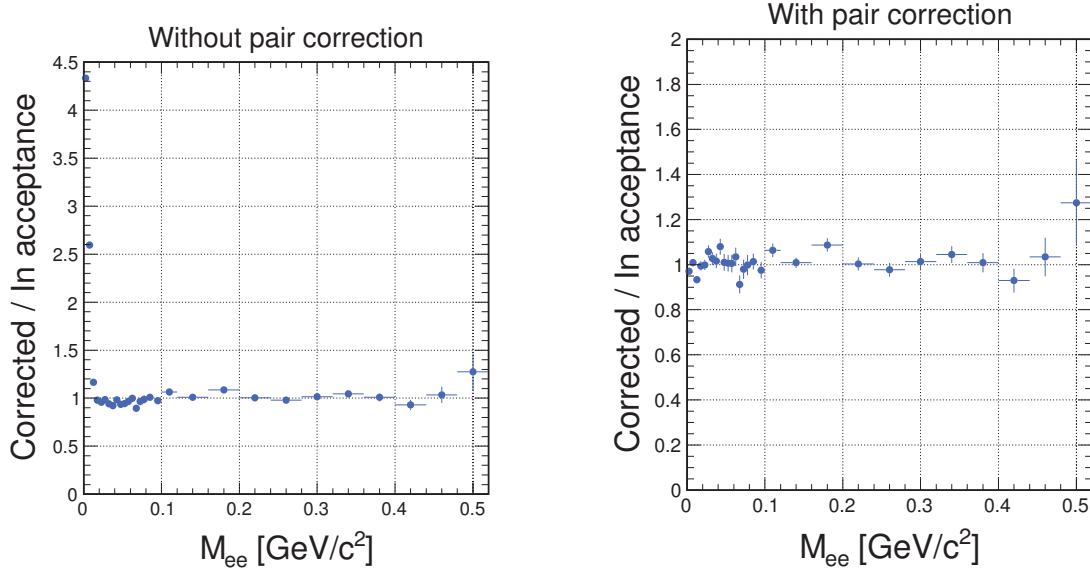
Figure 4.13.: Left: ratio of the invariant mass distributions of e^+e^- pairs from π^0 and η Dalitz decays for tracks reconstructed and corrected for efficiency to particles in the HADES acceptance. Right: the same after applying the correction emerging from the ratio in the left panel of Fig. 4.12.

4.5 One-dimensional efficiency correction for pairs

In the previous sections the validity of the single-leg event-by-event approach to the efficiency correction and the way to calculate such correction was discussed. In practice, applying this correction does not provide satisfactory results. The issue is illustrated in the left panel of Fig. 4.14. It shows the invariant
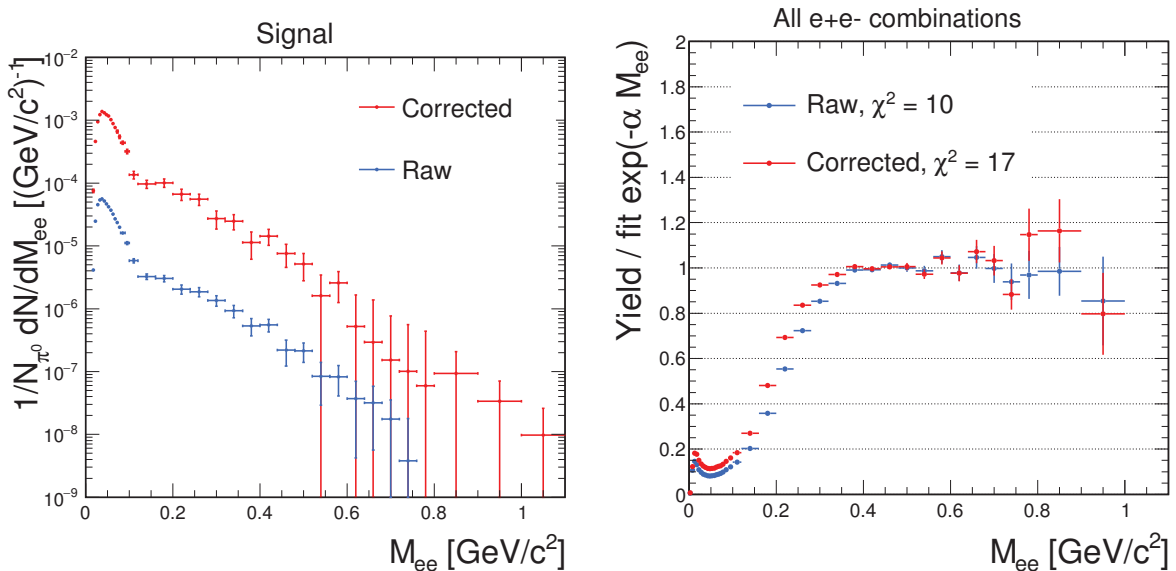
Figure 4.14.: Left: invariant mass distribution of e^+e^- signal without efficiency correction and after applying the single-leg correction. Right: distributions of all e^+e^- combinations divided by the exponential functions fitted separately to both of them.

mass distributions of the signal pairs both without efficiency correction (blue circles) and after the single-

leg correction applied (red circles). It is evident that the corrected spectrum has larger point-to-point fluctuations.

Point-to-point fluctuations appear not only in the signal spectrum, but they are present already in the distribution of all e^+e^- as well as like-sign pairs. This cannot be easily seen, because all such distributions drop rapidly, exponentially in the first approximation, with increasing invariant mass. The difference in value between two adjoining points coming from this trend is therefore larger than the fluctuation. Yet the fluctuation can be observed when the function $f(M_{ee}) = a \exp(b M_{ee})$ is fitted to the distribution and then the distribution is divided by the fit result. This is shown in the right panel of Fig. 4.14, where the fluctuations are clearly visible. It can also be noticed, that they are enhanced after applying efficiency correction. The origin of the latter effect is not yet fully understood. A possible interpretation involves not fully independent probabilities to detect two leptons of not necessarily small opening angle, when they fire the same MDC wire or hit the same time-of-flight module. Nevertheless, after subtracting combinatorial background the fluctuations grow, while the dropping trend is reduced, because signal has its mass dependence weaker than exponential.

Remarkable is also increase of the size of statistical error bars relative to the positions of the points after correcting for efficiency. One does not expect the correction to enhance statistical uncertainty, it should grow proportionally to the value of the points and in the plot made in logarithmic scale the lines should appear to have roughly the same length. The errors are correctly propagated in the histograms of all unlike-sign and like-sign combinations even if they are filled with weights representing corrections for both legs. However, the formalism for combinatorial background estimation and subtraction, discussed in the next chapter, operates essentially on numbers of reconstructed pairs and does not take into account correction weights. This may lead to incorrect subtraction which in turn may be reflected in overestimated statistical errors of the signal. This can also contribute to artificially enhanced point-to-point fluctuations discussed above.

To reduce these effects, efficiency is calculated as a function of dilepton pair properties, based on single-leg matrices computed in the first place, using simulated pairs from various sources. First, uncorrected signal is extracted and only then it is multiplied by the correction function. In order to avoid model dependence it would be desirable to represent the correction in multidimensional space, using as many degrees of freedom as possible, preferably all six. Even though it would (in principle) be possible to populate such a phase space in simulation by generating enough events, it is impossible with real data. In fact, measured events provide enough statistics only for one-dimensional distributions. Subtraction of the combinatorial background in the situation of empty bins in two-dimensional representations leads to many difficulties and partially incorrect results, as it is elucidated in the next chapter. Therefore the only viable procedure is to subtract background and correct it for efficiency in one dimension using each time a factor calculated as a function of the same variable as the spectrum under study. When the correction is obtained from the pair cocktail not very far from reality, the introduced error due to model dependence should not be very large.

4.5.1 Simulating the cocktail

The correction functions are calculated based on a cocktail of dilepton sources simulated with Pluto [110]. The two leptons in each event are first filtered by the HADES acceptance. This is done using single leg acceptance matrices, dependent on p, θ and ϕ. While filtering by the acceptance matrices, a random number is generated from the flat distribution between 0 and 1. If the random number is smaller, than the respective value in the acceptance matrix, the particle is regarded as being accepted. If this is the case for both particles in the pair, this pair is used to fill all the required distributions of pairs inside the HADES acceptance. In order to mimic the distributions of reconstructed pairs, efficiency values are read for both leptons in accepted pairs from the respective single-particle matrices. Additional factor, which takes into account correlation effects on pair reconstruction, is taken from the distribution shown in the left panel of Fig. 4.12. Then the second set of distributions is filled, this time with weights being products of the

three factors. This is the main advantage of this method over the full simulation and reconstruction chain (besides highly reduced computing resources): the spectra that represent reconstructed pairs contain the same number of counts as the spectra of pairs in the acceptance (only the weights are different). Concerning the efficiency values shown later on, the spectra of pairs from full reconstruction chain of simulated data have roughly 30 times less counts than the spectra only weighted with reconstruction efficiency. This influences statistical errors and fluctuations of the simulated spectra.

As suggested by [87, 88, 89] and will be further discussed in Chapter 7, the dominant source of dilepton pairs above $M_{ee} = 150$ MeV/c^2 is the decay $\rho^0 \rightarrow e^+e^-$, where the spectral function of ρ^0 has been calculated within the coarse-graining approach. This is also the second largest contribution below 150 MeV/c^2, the first one being the π^0 Dalitz decay. Therefore these two contributions constitute a cocktail sufficient for pair efficiency calculation, that should not introduce too large model bias. They can be also accompanied by $\omega \rightarrow e^+e^-$ in order to populate masses above 700 MeV/c^2, where the ρ^0 contribution starts to die out. The η-Dalitz is included just for the sake of formality.

The parameters of the sources are following: π^0 is generated thermally with two temperature components: 49 MeV/k_B and 89 MeV/k_B, the fraction of the former one being 98%, these parameters are obtained from the charged pion analysis, described in Section 7.1.1. η is generated from the thermal source of the temperature 50 MeV/k_B (the same as for pions, neglecting the second component) and ω with the assumption of 60 MeV/k_B. ρ^0 is taken from [89]. Decays to respective channels are simulated directly in Pluto with branching ratio of unity. Roughly 10^7 pairs from each source were generated.
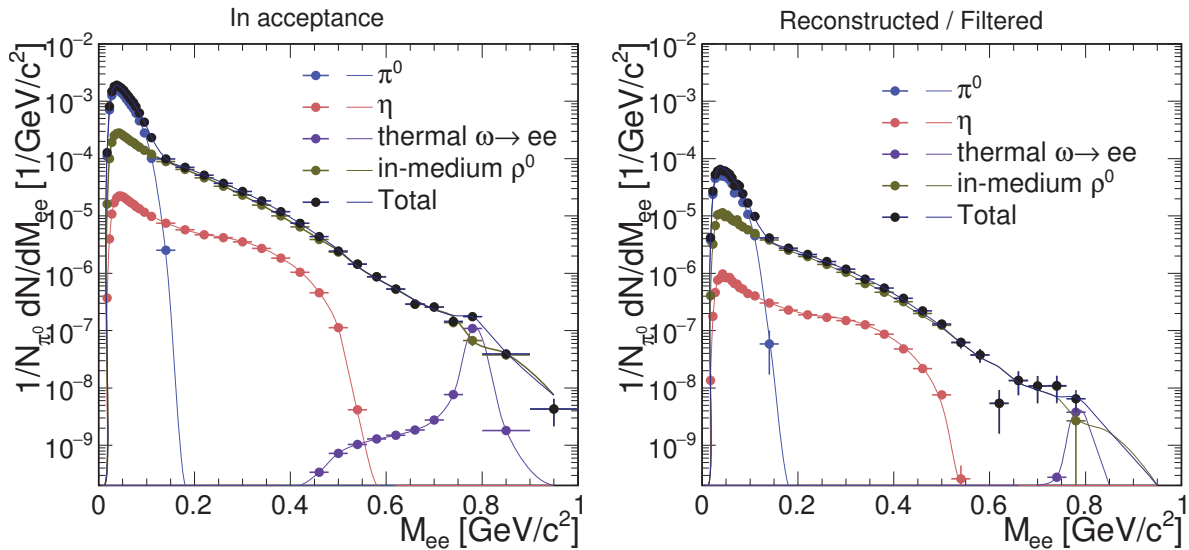
Figure 4.15.: Invariant mass distributions of the simulated cocktail used for the pair efficiency correction. Left: pairs filtered by single-leg acceptance matrices (**lines**) and pairs processed through GEANT and analyzed requiring the standard acceptance condition (**points**), Right: pairs filtered by single-leg acceptance matrices and weighted by single-leg efficiency matrices (**lines**) and pairs processed through full analysis chain (**points**). The fact, that values measured in experiment are different due to particle scattering and momentum resolution of the detector are addressed in Section 4.5.3.

All the contributions are properly scaled in the same way as the measured spectra, as explained below. The latter are normalized to the number of analyzed events and to the average number of neutral pions produced in the reaction, also the cocktail components are scaled down to the number of simulated pairs and to the number of π^0. The branching ratios to respective channels [1]: $1.174 \cdot 10^{-2}$ for π^0-Dalitz, $6.9 \cdot 10^{-3}$ for η-Dalitz, $7.28 \cdot 10^{-5}$ for $\omega \rightarrow ee$ are taken into account as well. The final multiplicative factor is the production rate per event in 40% most central events, which is taken as 0.107 for η, based

on the direct reconstruction with the conversion method, as discussed in Ref. [41] and outlined in Section 7.2. and 0.003 for ω as it comes from the Statistical Hadronization Model fit to the data. Special case with respect to the normalization is ρ^0, where the multiplicity×branching ratio can be estimated as $1.55 \cdot 10^{-2}$ based on the coarse-graining calculation. The calculation was done, however, for impact parameter $b = 0$, so to make it consistent with other cocktail ingredients, a scaling like $A_{\text{part}}^{1.4}$ [38] is assumed.

4.5.2 Consistency check of the cocktail

In order to verify, that the used methods describes pair reconstruction efficiency, the cocktail filtered by acceptance and weighted down by efficiency is compared to the result of full analysis of the same sources. The signal sources are embedded to UrQMD events and processed through the GEANT and DST procedures in the same way, as single leptons used to compute efficiency matrices. The simulation data are then analyzed in the same way as the experimental ones, with the only difference that in the former case only true leptons coming from the appropriate source are taken into account, what is obviously not possible with the measured data.

In Fig. 4.15 invariant mass distribution of cocktail components from the full chain analysis and from the filtering method are compared. Left panel shows the spectra in the HADES acceptance, right panel the reconstructed spectra and corresponding ones filtered by acceptance and scaled down by efficiency. In both cases the agreement is of the order of 1 %.

4.5.3 Momentum smearing

All the plots concerning efficiency discussed until now involved "ideal" kinematics of the particles, i.e. with which they were generated. They are different from the reconstructed values. Examples of original vs. reconstructed momentum distributions of e^- in two selected polar angle ranges are shown in Fig. 4.16. One effect that can be seen is the resolution of reconstructed momentum. It is expected to get
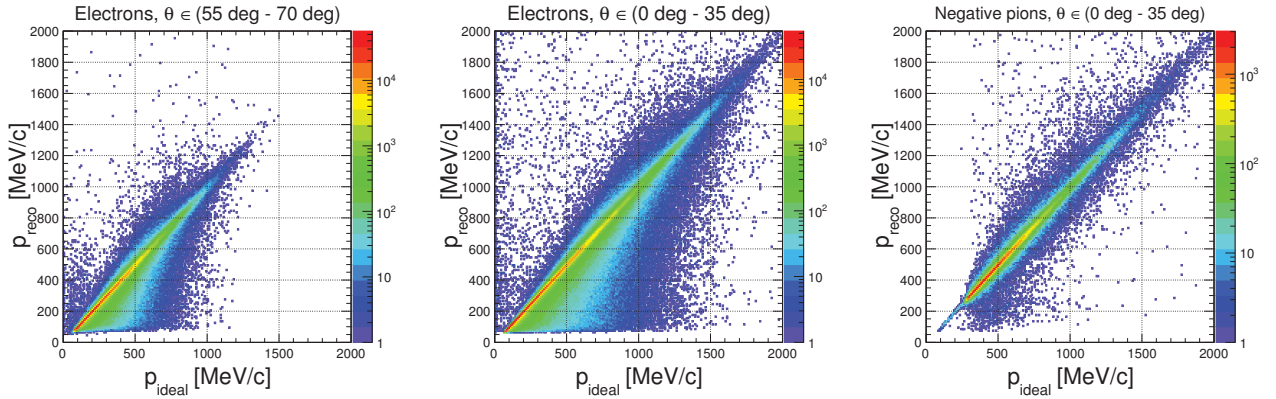
Figure 4.16.: Distributions of original vs. reconstructed momentum of electrons in two selected θ bins, based on a combined π^0-Dalitz and η-Dalitz simulation. For comparison, π^- from UrQMD (fulfilling track quality criteria as for leptons) are shown in one bin of polar angle.

worse towards larger values, because of smaller curvature of particle's track in the magnetic field. This effect is symmetric: it makes the reconstructed value of the momentum larger or smaller than the ideal one with equal probability. Another effect is energy loss, most prominent at low momenta. This acts only in one direction, i.e. the reconstructed value is lower than the original one. It can be observed, that a particle may lose its momentum almost entirely. This, together with the fact, that the effect is not visible for pions (also shown in Fig. 4.16) indicates, that the main energy loss mechanism is bremsstrahlung and it must happen mostly in the target, where heavy atomic nuclei are present.

It can be argued how these effects should be taken into account, when correcting measured data for efficiency. The assessment of this issue is as follows. It is always easier to destroy an information, than to try to recover it afterwards. Both approaches involve a probabilistic factor. Given an ideal value of momentum, only a probability distribution of reconstructed values is known. Conversely, given a reconstructed values, only a probability distribution of real values can be known. But recovering ideal momentum from the reconstructed one requires matrix inversion (deconvolution, unfolding, "de-smearing"), which is the source of uncertainty due to numeric issues but not only. This is where the shape of the original momentum distribution of particles used to fill the smearing matrix plays a role. At a single value of reconstructed momentum two different values of ideal momentum will contribute differently depending if the original distribution is flat or falls off exponentially. This influences the distribution of ideal momentum for a given reconstructed value, obtained after inverting the matrix. In contrast, the distribution of reconstructed momentum for a given ideal value comes from direct, not inverted matrix and is independent of the distributions for other values and thus independent of the shape of the original distribution. **This speaks for smearing the momentum in the simulation, which has been used to calculate the efficiency correction, instead of attempting to de-smear experimentally measured values.**

In this analysis it was not possible to reach the level of self-consistency of efficiency correction as shown in Sections 4.3 and 4.4, when reconstructed values were used in the numerator of the single-leg matrices, Eq. 4.1. Therefore both numerator and denominator were filled with ideal values and these values consequently used to read the efficiency and to calculate kinematic quantities (like pair invariant mass) up to the level of all the distributions in Fig. 4.15. In this approach efficiency matrices still contain energy loss effects, the fact if particle was reconstructed or not depends on its momentum after rescattering. Original momentum is used only to do accounting in a consistent way. One can say, that the probability of particle's detection depends on the momentum, with which it was emitted, because it influences the momentum value after rescattering and this determines if the particle could be detected or not. From this point of view, ideal values can readily be used when reading from the matrix efficiency values in the filtering procedure. To build the filtered spectra compatible with those measured in experiment, the smeared values should be used in calculating invariant mass and other pair observables as well as in reproducing the cuts that are applied in experimental data, like $p > 100$ MeV/c. The factor that is introduced to the invariant mass distribution due to the smearing can be seen in Fig. 4.17. In addition, Fig. 4.24 shows raw data points compared to the cocktail with and without the smearing.

Fig. 4.18 shows efficiency and acceptance corrections as a function of invariant mass for different centrality bins. The centrality dependence is as expected: in most central events efficiency is lower due to higher track density and thus the correction is larger. Acceptance correction was calculated together with the efficiency as the ratio of the yield in the full solid angle to the yield in the acceptance. In this case small differences between centrality bins come from the fact, that also minimum single-leg efficiency of 5% is required to consider a particle being accepted.

4.5.4 Model dependence of the correction factors

In order to estimate the systematics due to the theoretical model used in the calculation of efficiency and acceptance correction for pairs, alternative models have also been used to calculate the corrections and compare them. It can be expected, that using for such a purpose a cocktail containing only freeze-out sources is not adequate. Such a cocktail ignores in-medium radiation, which should have a dominant role in the mass range above π^0. This would lead to overestimation of the systematic uncertainty. Furthermore, with freeze-out sources only, it is practically impossible to populate the mass range between η and ω masses with statistics large enought to compute the corrections. Therefore the followingalternative models have been used in the present analysis:

1. Hadron-String Dynamics [113]

Total cocktail
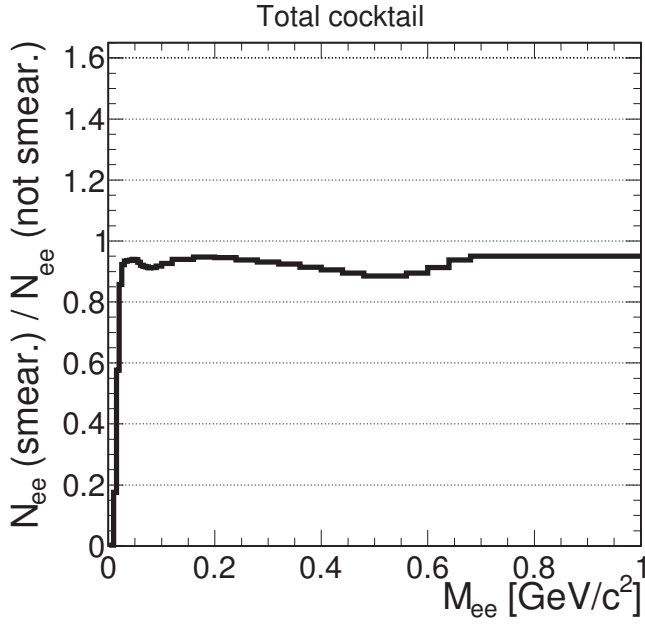
Figure 4.17: Ratio of the invariant mass distributions of the full Pluto cocktail filtered by acceptance and weighted by efficiency, before and after performing the momentum smearing procedure for calculation of the invariant mass. As discussed in text, efficiency values are in both cases obtained for ideal values of momentum.
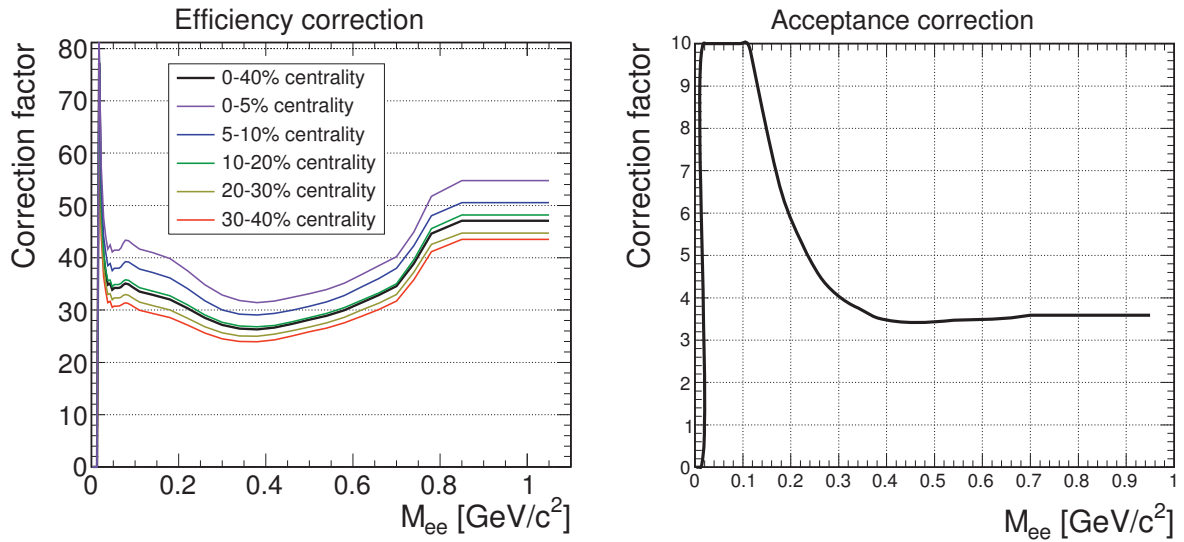
Figure 4.18.: Efficiency (left) and acceptance corrections (right) as a function of pair invariant mass for various centrality bins.

2. Cocktail as in Section 4.5.1, but with in-medium ρ^0 contribution replaced with thermal $\rho^0 \longrightarrow e^+e^-$, with temperature of 55 MeV/k_B, with factor $1/M_{ee}^3$ coming from Vector Meson Dominance and without the threshold of two pion mass.

The comparison of the efficiency and efficiency×acceptance correction factors from the three models is shown in Fig. 4.19 as an example for invariant mass and transverse mass in the region above π^0 and below η mass.

To quantify the spread, mean and standard deviation of the three corrections has been calculated bin-by-bin. It is shown in Fig. 4.20. Positions of the points indicate the mean and error bars indicate the standard deviation. It can be seen, that the relative spread is rather small. For this reason, **the mean correction has been used for all the final spectra**.
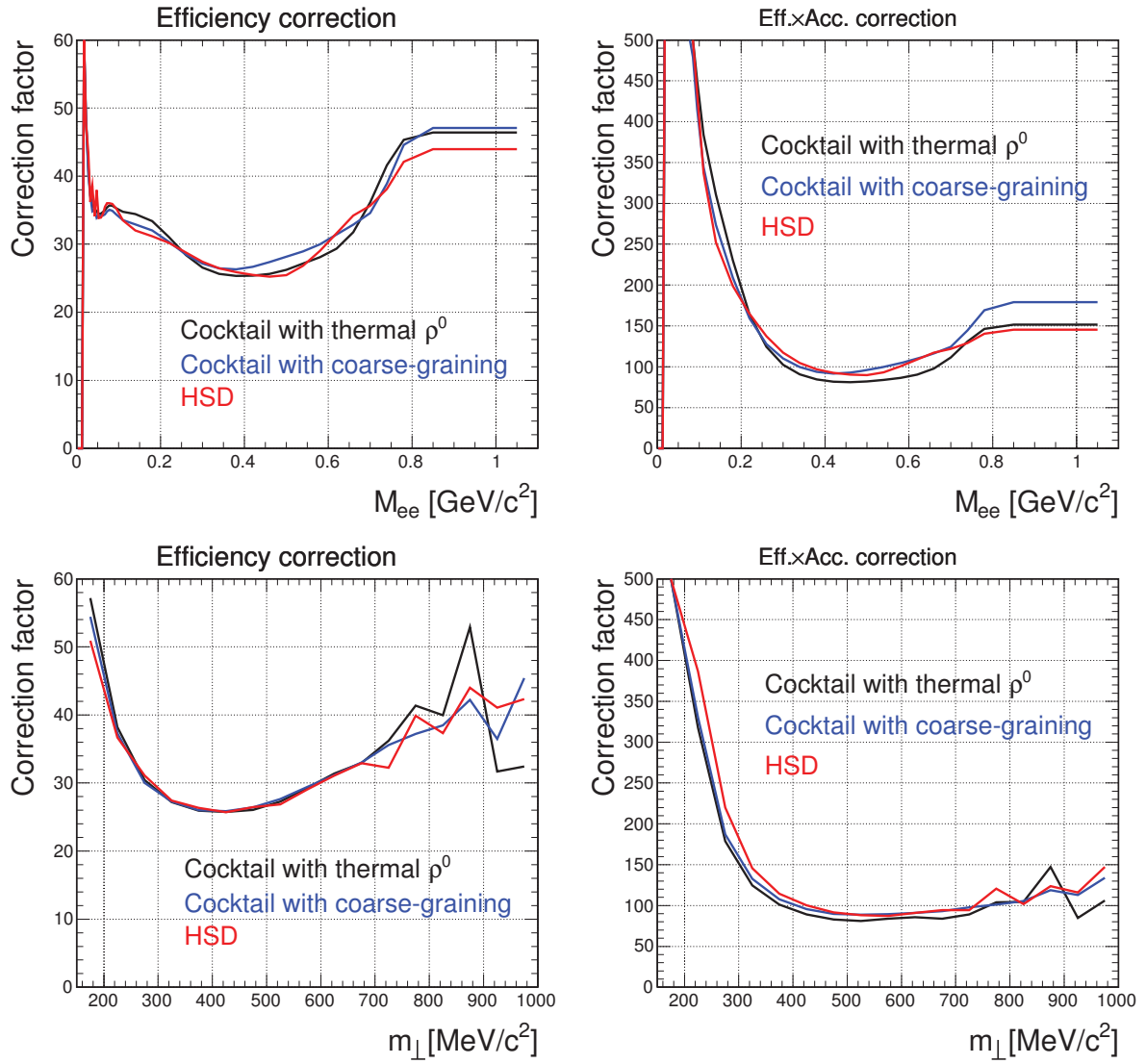
Figure 4.19.: Efficiency (left) and efficiency×acceptance corrections (right) as a function of pair invariant mass (top) and transverse mass (in the range $0.15 < M_{ee} < 0.55$ [MeV/c^2], bottom) calculated with three different models.

In the presentation of final results, the relative deviation (standard deviation divided by mean), as in Fig. 4.20, is added to the total systematic uncertainty. For spectra corrected for efficiency, the relative deviation of efficiency correction factors is taken. For spectra corrected for acceptance, it is the deviation of efficiency×acceptance correction factors. This takes into account *possible* cancellation of the deviations of that come from the efficiency and acceptance corrections separately.
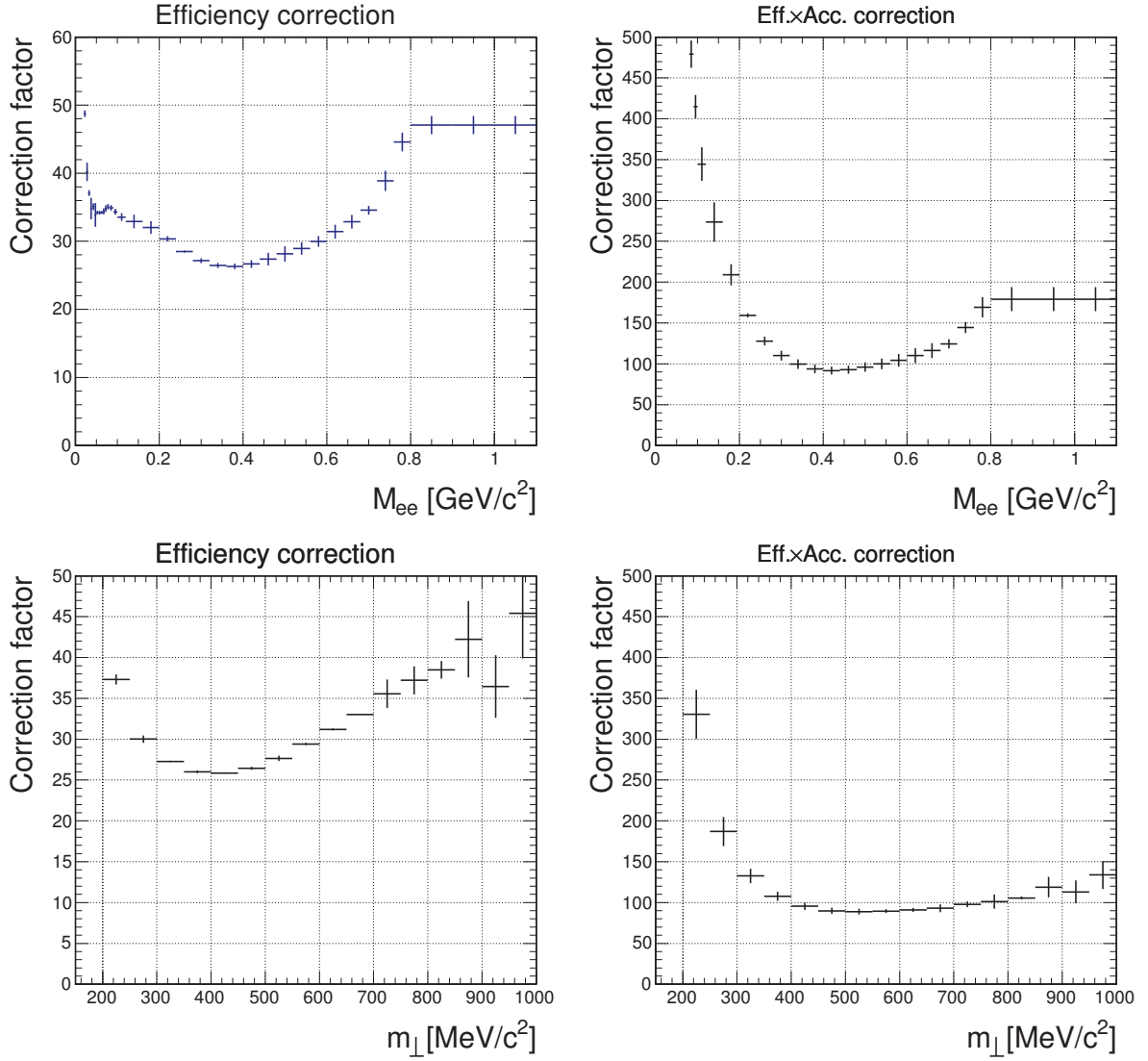
Figure 4.20.: Mean efficiency (left) and efficiency×acceptance corrections (right) as a function of pair invariant mass (top) and transverse mass (in the range $0.15 < M_{ee} < 0.55\,[\text{MeV}/c^2]$, bottom) calculated with three different models. Mean is represented by positions of the points and standard deviation by the error bars.

4.6 Relative acceptance correction for missing sectors

As discussed in Section 3.2, in particular periods of the beam-time certain HADES sectors were not operational and they are completely removed from the affected events to avoid difficulties related to corrections for effects that triggered the partial operation of the particular sector. Thus HADES operated in these events effectively with different acceptance. This prohibits to analyze the complete data set as a whole and to compare the results with previous experiments running where all six sectors were operational. Events with all 6 sectors operating in the Au+Au experiment are available only for only small (2%) part of the total statistics. Therefore, corrections for the missing acceptance due to not operational sectors with respect to configuration with six sectors have to be calculated. Fig. 3.4 shows, that the number of events with only four sectors is almost the same as with five, hence independent corrections have to provided for these two cases. Acceptance correction in general depends on the model but in this case it will be shown, that model dependence is large only in the phase-space regions, that are weakly populated by dileptons.
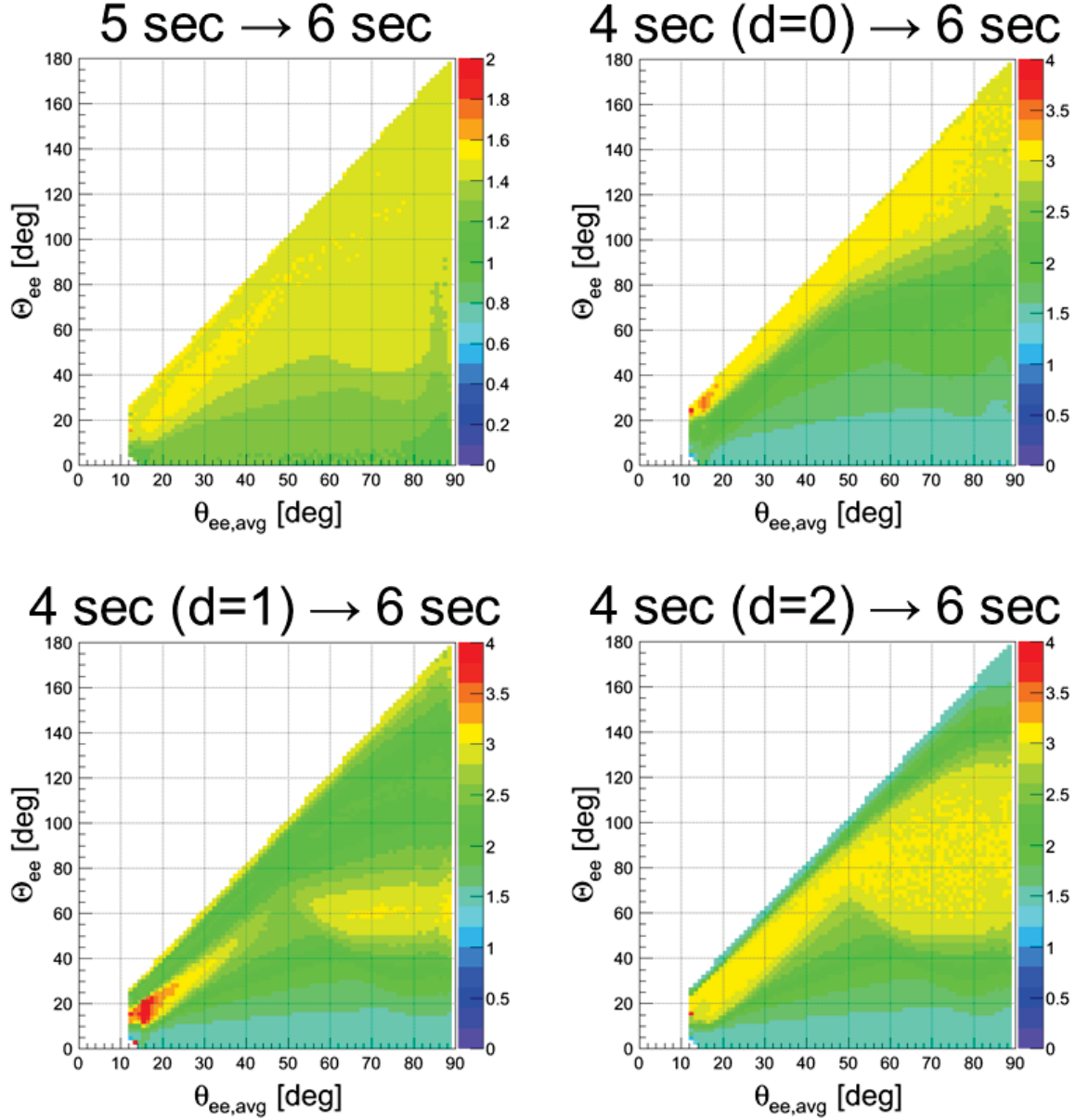
Figure 4.21.: The correction acceptance losses due to one or two missing sectors. $\theta_{ee,avg}$ is the average polar angle of two leptons and Θ_{ee} is the opening angle of the pair.

The correction can be calculated as a ratio of the distribution obtained with one or two sectors switched off to the one with all sectors present. This cannot be done on the single particle level, as a function of quantities that characterize single particles, p, θ and ϕ. A sector removed from the analysis means, that there are no tracks in a certain range of the ϕ angle and there is nothing that could be weighted by a correction factor. Various pair observables have been studied to reduce model dependency. Finally, it has been found that a two-dimensional function of $\Theta_{ee} - \theta_{ee,avg}$, where Θ_{ee} is the opening angle and $\theta_{ee,avg}$ is the average polar angle of two leptons building up the pair is best suited for this purpose.

As an input, the sample of pairs, that are homogeneously distributed in invariant mass, rapidity and transverse momentum is simulated in Pluto. This correction is purely geometric and to be applied under the assumption, that all the tracks are already corrected for efficiency. Therefore in this calculation it is not necessary to do the GEANT analysis and track reconstruction. Instead, in the calculations both leptons of the pair are filtered by a single particle acceptance matrix, introduced in Section 4.5.1, in
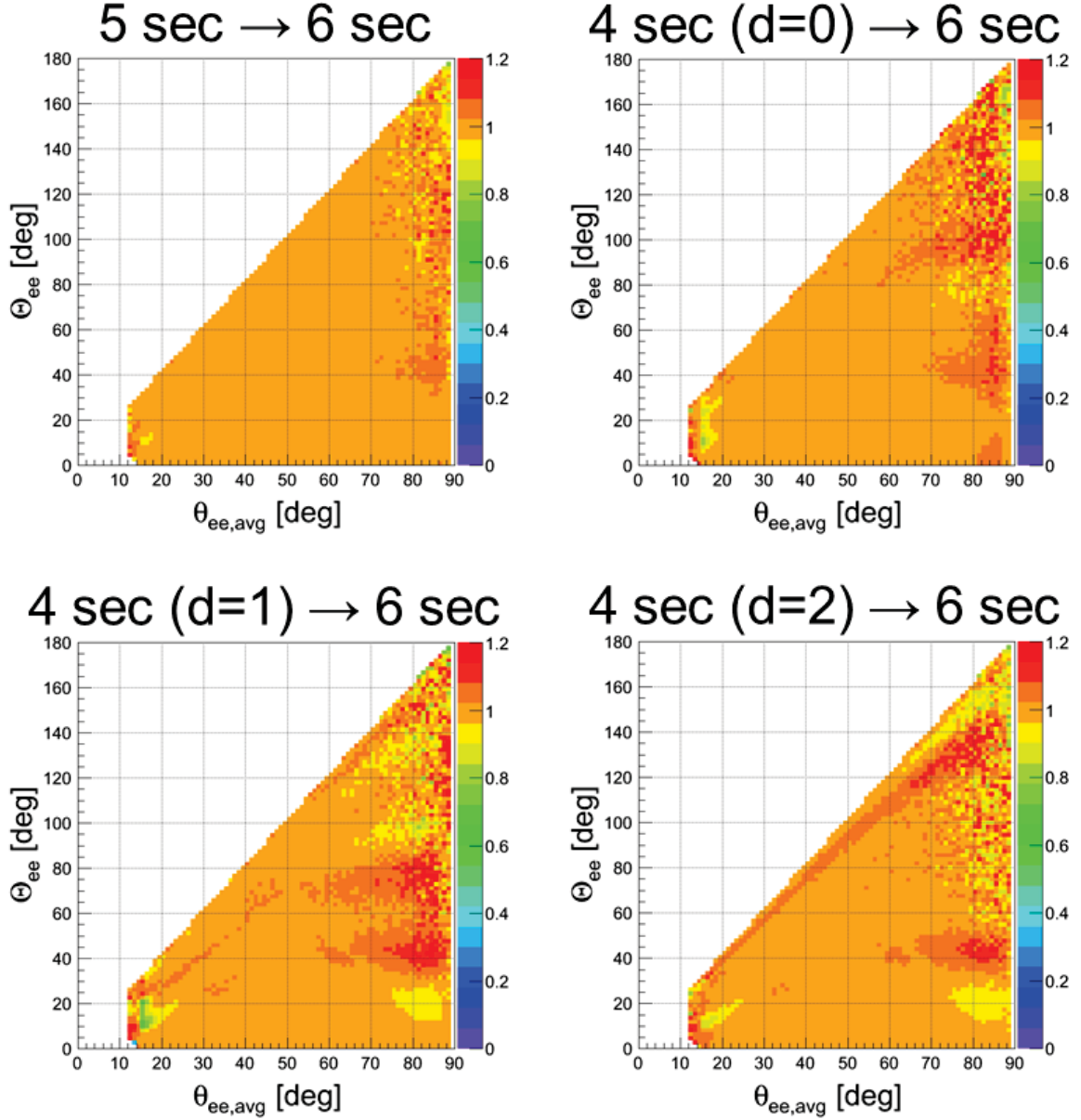
Figure 4.22.: Ratios of the correction factors like in Fig. 4.21 calculated from η-Dalitz decay pairs to the ones obtained with lepton pairs homogeneous in p, θ and ϕ.

order to obtain the distribution of pairs inside the acceptance. On the top of it, sectors are removed by applying cuts on the ϕ angle. Because of the assumption, that the data are already corrected for efficiency, the data set is symmetric under six-fold rotation around the Z axis. Consequently, only the following conditions are sufficient to account for loses present in the data:

- Remove $\phi \in (0° - 60°)$ to cover all the cases, with one sector missing.

- Remove $\phi \in (0° - 120°)$ to cover all cases with two adjacent sectors missing (**d=0**).

- Remove $\phi \in (0° - 60°) \cup (120° - 180°)$ to cover all cases with two sectors missing, separated by one working sector (**d=1**).

- Remove $\phi \in (0° - 60°) \cup (180° - 240°)$ to cover all cases with two opposite sectors missing (**d=2**).
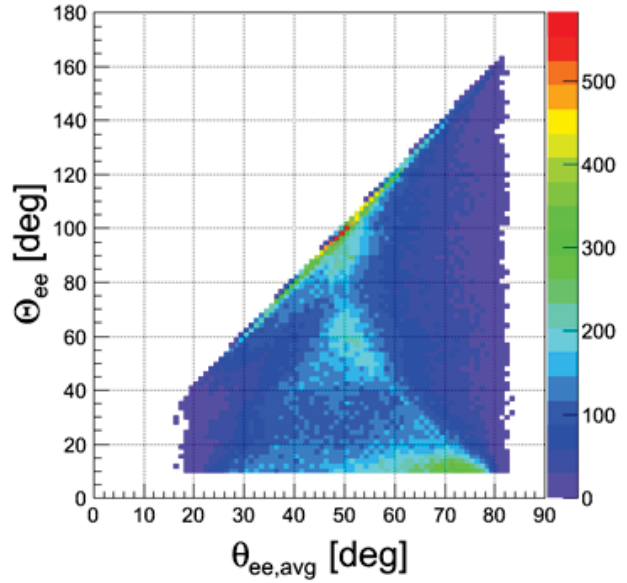
Figure 4.23: Distribution of the opening angle vs. average polar angle of the two particle in the pair, for all e^+e^- combinations reconstructed in the experimental data.

The shapes of the resulting corrections are shown in Fig. 4.21. The factors are quite sizable in certain regions, reaching the value of about 4. This strengthens the argument to skip events with three or less working sectors – in this case the correction would be even larger. The cut-off along the diagonal has its origin in the kinematics. Low average polar angle implies that both particles are close to each other and this limits possible values of the opening angle. If average θ is large, the opening angle can take any value, depending on the difference of the azimuth angles.

In order to validate the model dependence of the missing sector correction, it has been computed in the same way, but for pairs with kinematics of π^0 and η Dalitz decays. The ratios of the correction factors calculated with η-Dalitz pairs to those computed from homogeneous pairs are shown in Fig. 4.22. The differences are of the order of 5-10%. Comparison with the distribution of opening angle vs. average polar angle, obtained from experimental data and shown in Fig. 4.23, confirms, that significant deviations from the unity are present mainly in those regions of the phase space, which are not strongly populated in the data. This corroborates the validity of the correction.

In order to not underestimate systematic uncertainty contribution originating from this correction, it was assumed to be of **10%** i.e. the largest deviation from unity visible in Fig. 4.22 in regions, where statistics is non-zero according to Fig. 4.23.

4.7 Validation of the efficiency correction methods

Both the cocktail used in the calculation of the pair correction and experimental spectra are normalized to the π^0 multiplicity. The efficiency correction is the ratio of the cocktail filtered by acceptance to the one weighted additionally by single-lepton efficiencies. In order to validate the method used to correct spectra for efficiency, one can go other way around and compare raw data with the cocktail filtered and weighted with single track efficiency values. If the procedure is applied in a right way, distributions should agree in the π^0 region, allowing for some tolerance due to in-medium ρ^0 contribution to the cocktail. This can be seen in Fig. 4.24 for cases when ideal momentum values were used in the cocktail and when momentum smearing was done as described in Section 4.5.3. The data points are corrected for missing sectors, because this is the only correction, that has to be applied on the event-by-event basis, as discussed in Section 4.6. Momentum smearing brings the agreement to the very good level. Additionally, one can observe the effect of the smearing on the spectral shape of cocktail components, especially of ω.
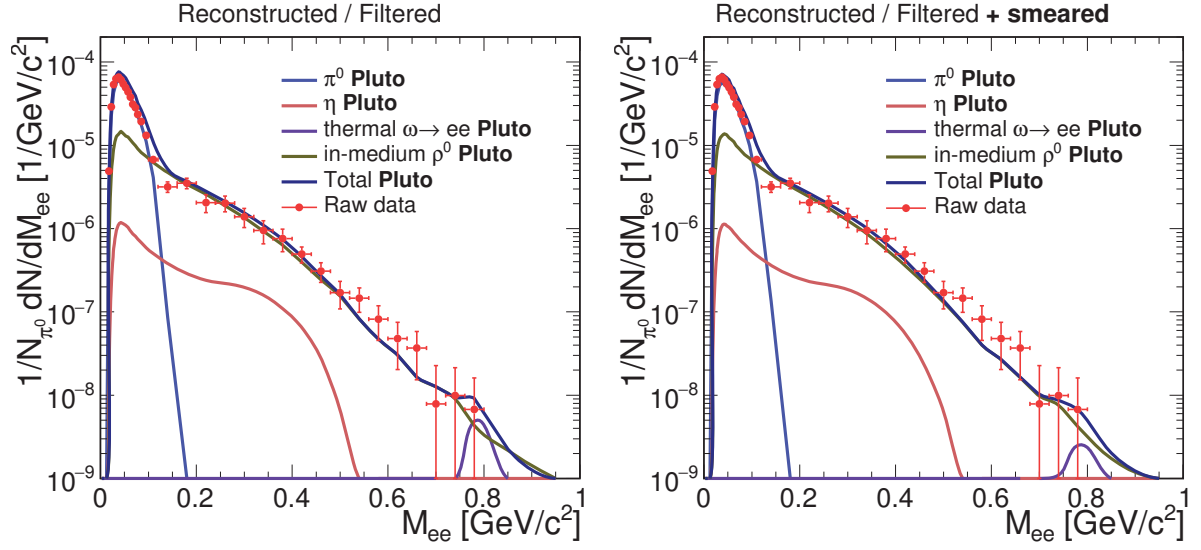
Figure 4.24.: Comparison of the cocktail used to calculate pair efficiency correction, filtered by acceptance and weighted by single-lepton efficiency with data points, corrected only by the relative acceptance of missing sectors. In the left panel ideal values were used in the cocktail. In the right panel momentum was smeared to calculate invariant mass and to cut on $p > 100$ MeV/c, analogous to what is done in experiment.

5 Subtraction of the combinatorial background

In heavy-ion collision several particles decaying to leptons can be produced. The dominant source are neutral pions, that decay predominantly into 2γ channel (with probability of 98.8%) or into Dalitz channel $e^+e^-\gamma$ (probability 1.2%) [1]. The average number of π^0 produced in PT3 Au+Au collisions in HADES is of the order of 10 (see Section 7.1.1). The probability to create an e^+e^- pair from γ conversion in the target region of the HADES is relatively high – enough to make it possible to reconstruct observable signal of π^0 (and also η) in events, where both photons converted into dileptons [41]. Putting all this together it is natural to expect, that in a single event leptons from different sources may be present.

On the other hand, there is no possibility, to identify electrons and positrons from the same decay vertex. The only way out is to build all combinations in an event and estimate, what is the contribution of wrong pairings to final spectra. This contribution is called *combinatorial background*. The spectrum obtained after subtracting combinatorial background from all possible pairings is equivalent to the spectrum of true pairs only, as it will be discussed in the next section.

Two cases are usually distinguished. *Uncorrelated background* consists of pairs of e^+ and e^- produced in decays of different particles. In case of two-photon or Dalitz decays of π^0 and η (with subsequent γ conversions) it is also possible to pair leptons having different parent particles, but common grandparent. Such pairs are correlated to some extent in the phase-space and therefore this contribution to the background is referred to as *correlated background*. These cases are shown schematically in Fig. 5.1.
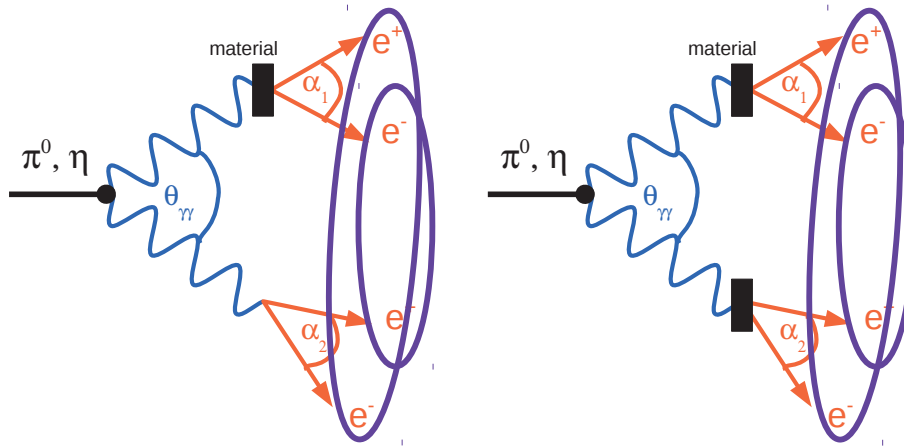
Figure 5.1.: Schematic view of correlated background pairs in Dalitz decay of neutral mesons (left) and in decay to two photons with subsequent conversion. Background pairs are marked with ellipses.

5.1 Calculation of the combinatorial background

5.1.1 Like-sign geometric background

It is rather intuitive, that combinatorial background can be estimated by spectra of lepton pairs of *the same sign*: in the full phase-space (that is, leaving aside the acceptance and efficiency of the detection system) there is no difference between electrons and positions and therefore the probability to build a combinatorial e^+e^- pair should be the same as to build e^+e^+ or e^-e^- pairs that are always of combinatorial origin. This argument does not change in the case of correlated background. The intuition does not give an answer if for combinatorial background estimation one should take e^+e^+, e^-e^-, some combination of them and which type of combination. This was studied in [114, 115, 116], where the result

$$\langle BG_{+-} \rangle = 2\sqrt{\langle FG_{++} \rangle \langle FG_{--} \rangle}.$$

was obtained, where BG_{+-} is the combinatorial background contribution in the yield of opposite-sign pairs and FG_{++}, FG_{--} are yields of like-sign pairs. The result was obtained for muons from charmed mesons decays in the intermediate mass region. In particular, the derivations of the above formula make use of the assumptions that (a) the numbers $N_{+/-}$ of mesons have Poisson distributions, (b) $\text{cov}(N_+, N_-) = 0$. These assumptions are not applicable to dileptons from hadron decays populating invariant masses below 1 GeV/c^2. Such dileptons are always produced in pairs (correlated). Moreover, statistical distributions of the multiplicity of their parent particles cannot be assumed.

The derivation that can be applied in the case, when signal pairs are *correlated* is given in [117]. It assumes, that e^+ and e^- are always produced in pairs, due to charge conservation. Then it considers the probability of registering n_p out of N initially produced pairs given by the binomial distribution $B(n_p, N, \epsilon_p)$. Out of the not registered pairs, single tracks can be still detected and the probability is given by the multinomial distribution with three possible outcomes: no track, one e^+ detected, one e^- detected:

$$\begin{aligned} \omega(n_+, n_-) &\overset{\text{def}}{=} M(n_+, n_-; N - n_p, \epsilon_+, \epsilon_-) \\ &\overset{\text{def}}{=} \frac{(N - n_p)!}{n_+! n_-! (N - n_p - n_+ - n_-)!} \epsilon_+^{n_+} \epsilon_-^{n_-} (1 - \epsilon_+ - \epsilon_-)^{N - n_p - n_+ - n_-}, \end{aligned} \tag{5.1}$$

where ϵ_+ and ϵ_- are the probabilities to detect a single track (from a not fully reconstructed pair). Summing over values of n_+ (or n_-) up to the total number of not reconstructed pairs $N - n_p$ one gets the probability distributions for n_- (or n_+, respectively):

$$\begin{aligned} \omega(n_+) &\overset{\text{def}}{=} \sum_{n_-=1}^{N-n_p} M(n_+, n_-; N - n_p, \epsilon_+, \epsilon_-), \\ \omega(n_-) &\overset{\text{def}}{=} \sum_{n_+=1}^{N-n_p} M(n_+, n_-; N - n_p, \epsilon_+, \epsilon_-). \end{aligned} \tag{5.2}$$

Then the number of all unlike-sign combinations of reconstructed leptons is given by:

$$\langle n_{+-} \rangle = n_p^2 + n_p \sum_{n_+=1}^{N-n_p} n_+ \omega(n_+) + n_p \sum_{n_-=1}^{N-n_p} n_- \omega(n_-) + \sum_{n_+=1}^{N-n_p} \sum_{n_-=1}^{N-n_p} n_+ n_- \omega(n_+, n_-) \tag{5.3}$$

For like-sign combinations it is:

$$\langle n_{++} \rangle = \sum_{n_+=1}^{N-n_p} \frac{(n_p + n_+)(n_p + n_+ - 1)}{2} \omega(n_+) \tag{5.4}$$

and similarly for $\langle n_{--} \rangle$. The expected number of reconstructed pairs for given N is obtained by averaging over n_p:

$$\langle N_{+-} \rangle = \sum_{n_p} \langle n_{+-} \rangle B(n_p, N, \epsilon_p) = [\epsilon_p + \epsilon_+(1-\epsilon_p)][\epsilon_p + \epsilon_-(1-\epsilon_p)](N^2 - N) + \epsilon_p N,$$

$$\langle N_{++} \rangle = \sum_{n_p} \langle n_{++} \rangle B(n_p, N, \epsilon_p) = \frac{1}{2}[\epsilon_p + \epsilon_+(1-\epsilon_p)]^2 (N^2 - N), \tag{5.5}$$

$$\langle N_{--} \rangle = \sum_{n_p} \langle n_{--} \rangle B(n_p, N, \epsilon_p) = \frac{1}{2}[\epsilon_p + \epsilon_-(1-\epsilon_p)]^2 (N^2 - N).$$

Then averaging over N yields the total number of "foreground" pairs (detailed explicit calculation makes use of properties of binomial and multinomial distributions and is outlined in the reference [117]):

$$\langle FG_{+-} \rangle = \sum_N \langle N_{+-} \rangle P(N) = [\epsilon_p + \epsilon_+(1-\epsilon_p)][\epsilon_p + \epsilon_-(1-\epsilon_p)](\langle N^2 \rangle - \langle N \rangle) + \epsilon_p \langle N \rangle = \langle BG_{+-} \rangle + \langle S \rangle. \tag{5.6}$$

Identifying $\epsilon_p \langle N \rangle$ with the signal leads to the conclusion that the unlike-sign foreground separates into signal and background. In case of like-sign pairs only background is present:

$$\langle FG_{++} \rangle = \sum_N \langle N_{++} \rangle P(N) = \frac{1}{2}[\epsilon_p + \epsilon_+(1-\epsilon_p)]^2 (\langle N^2 \rangle - \langle N \rangle) = \langle BG_{++} \rangle,$$

$$\langle FG_{--} \rangle = \sum_N \langle N_{--} \rangle P(N) = \frac{1}{2}[\epsilon_p + \epsilon_-(1-\epsilon_p)]^2 (\langle N^2 \rangle - \langle N \rangle) = \langle BG_{--} \rangle. \tag{5.7}$$

Comparing the expressions for background of different signs allows to express the unlike-sign combinatorial background through yields of like-sign pairs:

$$\langle BG_{+-} \rangle = 2\sqrt{\langle BG_{++} \rangle \langle BG_{--} \rangle} = 2\sqrt{\langle FG_{++} \rangle \langle FG_{--} \rangle}. \tag{5.8}$$

The above calculations were done assuming silently, that the reconstruction probability does not depend on the sign of the pair: $\epsilon_{+-} = \epsilon_{++} = \epsilon_{--} = \epsilon_p$. This assumption can be withdrawn in order to generalize the approach of [117]. The result will be then:

$$\langle BG_{+-} \rangle = \frac{[\epsilon_{+-} + \epsilon_+(1-\epsilon_{+-})][\epsilon_{+-} + \epsilon_-(1-\epsilon_{+-})]}{[\epsilon_{++} + \epsilon_+(1-\epsilon_{++})][\epsilon_{--} + \epsilon_-(1-\epsilon_{--})]} 2\sqrt{\langle FG_{++} \rangle \langle FG_{--} \rangle}. \tag{5.9}$$

This expression is clearly different from the often quoted (see e.g. [116, 118]):

$$\langle BG_{+-} \rangle = \frac{\epsilon_{+-}}{\sqrt{\epsilon_{++} \epsilon_{--}}} 2\sqrt{\langle FG_{++} \rangle \langle FG_{--} \rangle}$$

Nevertheless, the steps described below are valid also for the latter expression.

The quotient in Eq. 5.9 could in principle be calculated directly using Monte Carlo methods. However, all the systematic uncertainties from modeling of efficiency in simulation would be amplified. Moreover, the risk of biasing the data by the model dependence would appear. A possible way to avoid these problems is to generate a data sample *without signal*. For such a sample unlike-sign foreground is equal to background and the above equation can be written as (lower-case letters are used to distinguish from the original data sample):

$$\langle fg_{+-} \rangle = \frac{[\epsilon_{+-} + \epsilon_+(1-\epsilon_{+-})][\epsilon_{+-} + \epsilon_-(1-\epsilon_{+-})]}{[\epsilon_{++} + \epsilon_+(1-\epsilon_{++})][\epsilon_{--} + \epsilon_-(1-\epsilon_{--})]} 2\sqrt{\langle fg_{++} \rangle \langle fg_{--} \rangle}. \tag{5.10}$$

Together it gives:

$$\langle BG_{+-}\rangle = \frac{\langle f g_{+-}\rangle}{2\sqrt{\langle f g_{++}\rangle\langle f g_{--}\rangle}}2\sqrt{\langle FG_{++}\rangle\langle FG_{--}\rangle} \equiv k2\sqrt{\langle FG_{++}\rangle\langle FG_{--}\rangle}. \qquad (5.11)$$

The signal-free data could be simulated, but the problems of systematic and model dependence would still be present. Instead, particles from different measured events can be combined into pairs (*event mixing*). Such pairs do not contain correlated signal by definition, all the efficiency values are true and single track distributions are identical as in data. Possible difficulty emerge in case of pairs with opening angle so small, that the presence of one particle influences the detection of another one. This effect plays a role only for same-event pairs and leads to a difference between pair efficiency in real data sample and in event mixing. Nevertheless, this is not a problem if a cut on minimal opening angle is applied, what is the case in a typical dilepton analysis (see Fig. 4.12). In addition, small opening angles are weakly populated by background pairs in any case.

The probability $P(N)$ in Eqs. 5.6 and 5.7 serves only for proper averaging of terms with N from Eq. 5.5 and there is **no assumption about the underlying probability distribution, in particular Poisson distribution, at this point**. In other words, $\langle f(N)\rangle = \sum_N f(N)P(N)$, no matter how $P(N)$ is distributed. In this context, the only distinctive property of the pair production according to the Poisson distribution is the fact, that background would then be equal to the product of average single electron and positron multiplicities, as it is discussed in [117].

The formula to estimate combinatorial background as a *geometric* mean of yields of like-sign pairs is exact (provided that all used assumptions are justified). For quick checks it can be approximated by *arithmetic* mean, which can be calculated by simple additions and subtractions of histogram without taking care of calculating square roots of bin entries and correct error propagation. Assuming namely, that N_p **and** N_n **are both larger than their difference**, one can write e.g. $N_{nn} = N_{pp} + \varepsilon$ and

$$\sqrt{N_{pp}\cdot N_{nn}} = N_{pp}\cdot\sqrt{1+\frac{\varepsilon}{N_{pp}}} \approx N_{pp}\cdot\left(1+\frac{1}{2}\frac{\varepsilon}{N_{pp}}\right) = N_{pp}+\frac{\varepsilon}{2} = \frac{1}{2}(N_{pp}+N_{nn}). \qquad (5.12)$$

It is a general fact, that arithmetic mean is always larger than geometric, because $\frac{1}{2}\left(N_{pp}+N_{nn}\right) - \sqrt{N_{pp}\cdot N_{nn}} = \frac{1}{2}\left(\sqrt{N_{pp}}-\sqrt{N_{nn}}\right)^2$ is always a positive number.

5.2 Correction for pair reconstruction asymmetry

The k-factor used in this analysis was calculated with mixed event for each centrality class separately. The event mixing procedure was the same as for determining the shape of the combinatorial background at higher masses, as discussed in Section 5.3.

The shape of the k-factor as a function of dilepton invariant mass and its effect on the combinatorial background shape and on the signal obtained after background subtraction from all e^+e^- combinations are shown in Fig. 5.2. When the asymmetry factor is ignored, an accumulation of the signal develops above π^0-Dalitz with the maximum around 0.15 GeV/c^2. It corresponds precisely to the invariant mass value, for which the k-factor reaches the maximum of around 1.05. This shows that the accumulation is an unphysical artifact due to the asymmetry between reconstruction of like- and unlike-sign pairs in HADES. Similar observations have been made also in PHENIX [117], STAR [119] and ALICE [120, 121] analyses.

Below 0.1 GeV/c^2 the asymmetry factor deviates strongly from the unity and this is where it has the largest influence on the background value. On the other hand, as it can be seen e.g. from the right panel of Fig. 5.2 or from Fig. 3.27, the background in this region is clearly lower than the signal and the latter is barely affected by the k-factor.
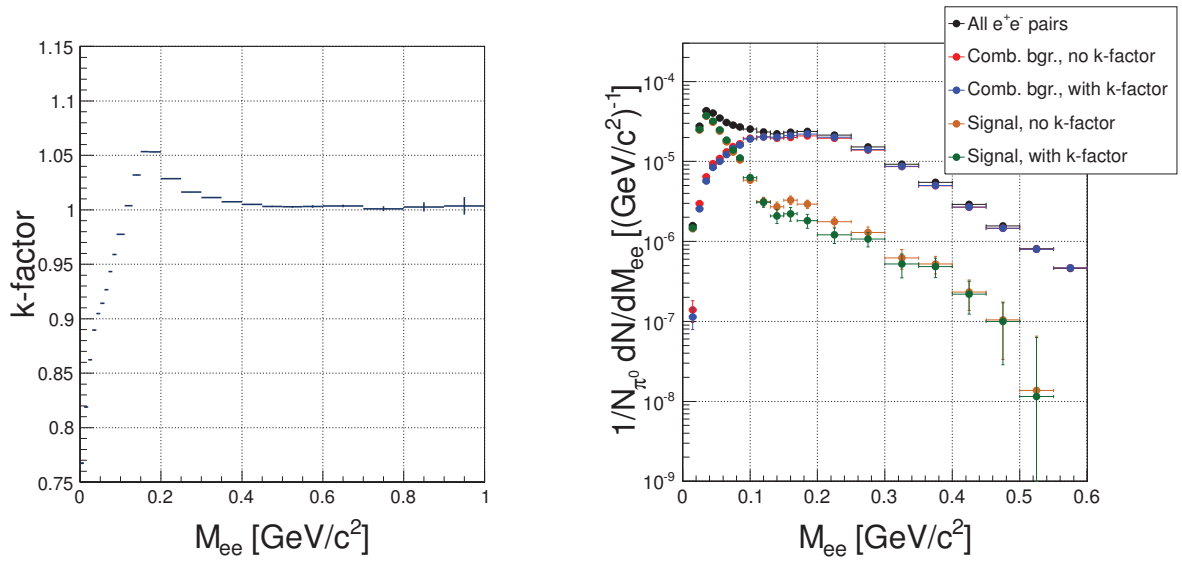
Figure 5.2.: Left: shape of the k-factor as a function of dilepton invariant mass. Right: Invariant mass of all e^+e^- combinations (black), like-sign combinatorial background not multiplied (red) and multiplied (blue) by the detection asymmetry factor, and signal obtained after subtraction of both background spectra from all e^+e^- pairs (orange and green respectively). No single-track efficiency corrections were applied to these spectra.

5.2.1 Influence of the track reconstruction on the k-factor

In order to better understand the origin of the asymmetry, which is corrected for with the k-factor, it has been calculated with various approaches, as shown in Fig. 5.3. All were based on the event mixing. In the first one, experimental events were mixed and object used to build pairs were reconstructed tracks (black points in the figure). In the three other cases, UrQMD events were mixed. In one of these cases, pairs of reconstructed tracks were mixed in the full analogy to experimental data (red points). In another one, pairs were build from original simulated particles, after filtering them through the acceptance (blue points). The last case was identical with the exception, that the spectra were weighted by products of single particle reconstruction efficiencies, described in Section (green points). The error bands represent statistical uncertainty of each analysis.

The figure shows that the k-factors calculated with reconstructed tracks in experimental data and in simulation are fully consistent. This is a manifestation of detector efficiency reproduced with excellent accuracy in HADES Monte Carlo simulation. Filtering by the geometric acceptance only gives very different results, while adding weights from single particle efficiencies makes the k-factor again close to the one calculated with reconstructed tracks. This implies, that the effects corrected for by the k-factor cannot be fully explained by geometrical acceptance of the detector, but reconstruction efficiency plays an important role.

5.2.2 k-factor applied in one or many dimensions

Concerning the practical application of the detection asymmetry factor, it can be discussed, whether it should be applied on the event-by-event basis, as an appropriate weight for each like-sign background pair, or only the final background distribution should be multiplied by it. The former case would have the advantage, that the factor could be calculated in many variables, on which pair kinematics may depend (invariant mass, transverse momentum, rapidity, polar angle of both leptons) and afterwards applied directly to other distributions, even of quantities, in which k-factor was not calculated explicitly (e.g.
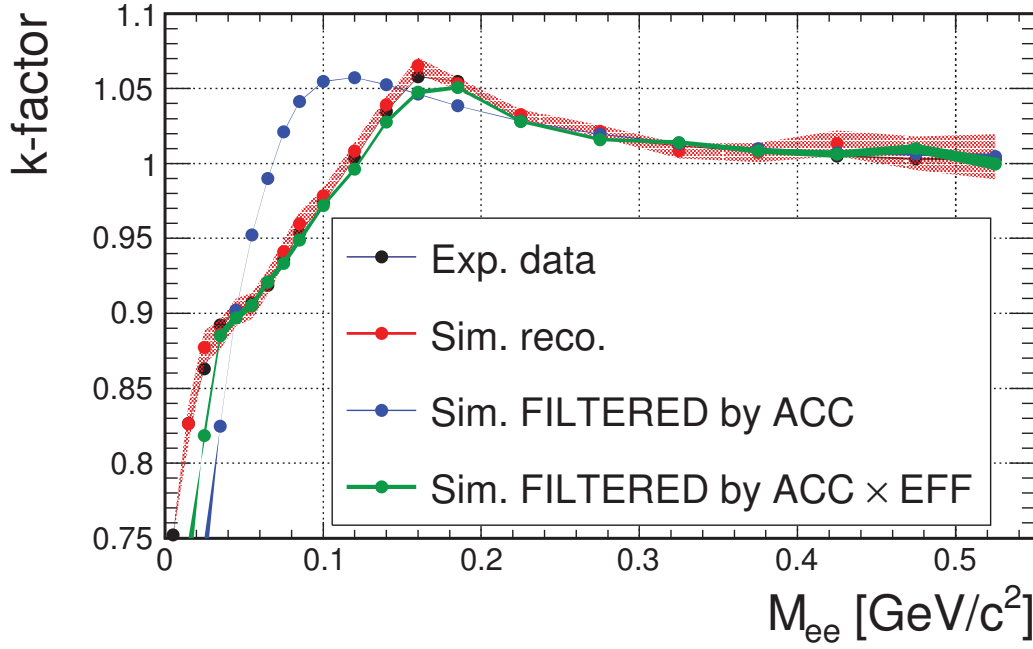
Figure 5.3.: The k-factor as a function of dilepton invariant mass calculated with different approaches. Details are in the text.

opening angle or transverse mass). However, this is not the right approach. Assuming for simplicity, that the asymmetry factor was calculated only as a function of invariant mass and transverse momentum, the yield of like-sign pairs in a particular mass bin is equal to:

$$N_{++}^k(M) = \sum_{p_t} N_{++}(M, p_t) k(M, p_t),$$

$$N_{--}^k(M) = \sum_{p_t} N_{--}(M, p_t) k(M, p_t).$$

Then calculating like-sign combinatorial background as the geometric mean gives the result:

$$N_{\mathrm{CB}}(M) = 2\sqrt{N_{++}^k(M) \cdot N_{++}^k(M)} = 2\sqrt{\left(\sum_{p_t} N_{++}(M, p_t) k(M, p_t)\right) \cdot \left(\sum_{p_t} N_{++}(M, p_t) k(M, p_t)\right)}$$

$$\neq k(M) \cdot 2\sqrt{N_{++}(M) \cdot N_{++}(M)},$$

because the k-factor cannot be moved from under the square root sign. This point is illustrated in Fig. 5.4. Correction for detection asymmetry on the event-by-event basis leads to strong overestimation of the combinatorial background so that it gets much higher than the amount of all e^+e^- combinations. The situation does not change significantly, when the set of variables, in which k-factor is calculated, varies.

Therefore only final background distribution can be multiplied by the detection asymmetry factor. It may be done in many dimensions in order to keep a possible multi-variable dependence. In the end the background distribution is integrated over the variables other than the one that is of interest in a particular moment. There is however a hazard of not populating certain bins with enough counts. In the case of rare probes detected with small efficiency, even the statistics that can be obtained with event mixing is not completely unlimited, as it is often assumed. This is even bigger problem for same-event spectra. If a particular bin of e^+e^+ or e^-e^- distribution is empty, then the geometric mean used to calculate same-event like-sign background or the k-factor in event mixing gets zero and this leads to rather unphysical situations of no background or infinite k-factor. Then the second-to-best solution is to
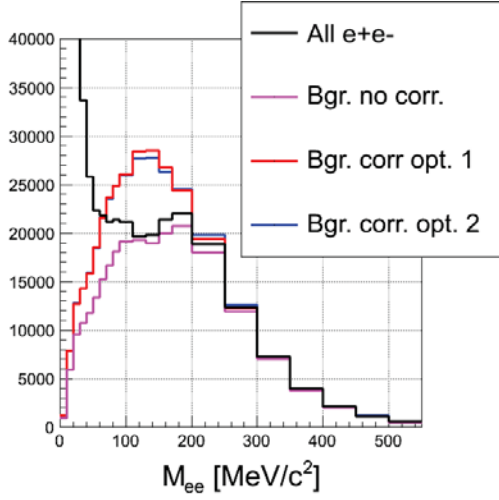
Figure 5.4: Comparison of the invariant mass distributions (numbers of counts) of all e^+e^- combinations (black), like-sign combinatorial background without a correction for the k-factor (magenta) and with k-factor correction applied on the event-by-event basis in two ways (red and blue). In option 1, k-factor is a matrix in invariant mass, transverse momentum and rapidity of a lepton pair. In option 2 such matrices are calculated for four polar angle bins of both leptons (in total 16 matrices) separately.

replace the geometric average with arithmetic one, which in case of one component being zero means taking just the second one. But this leads to discontinuity between bins, where geometric and arithmetic means are used, because the arithmetic one is actually a good approximation of the geometric only if the difference between two components is much smaller then each of them, see Eq. 5.12. It is just opposite to the situation, when one component is zero.

Similar situation takes place at edges of acceptance and this case is better for the illustration of the problem. Fig. 5.5 shows distributions of invariant mass vs. transverse momentum of pairs of various signs, obtained in event mixing. They are strongly suppressed at low M and p_t but the value of the transverse mass $m_t = \sqrt{M^2 + p_t^2}$ where it happens is different for all signs[1]. This has a strong effect on the distribution of average between e^+e^+ and e^-e^-. Very low values of m_t are not populated by e^+e^+ and the yield of e^-e^-, rather large in this region, is used in place of geometric mean. For slightly higher m_t, e^+e^+ is populated only very weakly and geometric mean takes low values, that increase again with increasing e^+e^+, as m_t grows further.
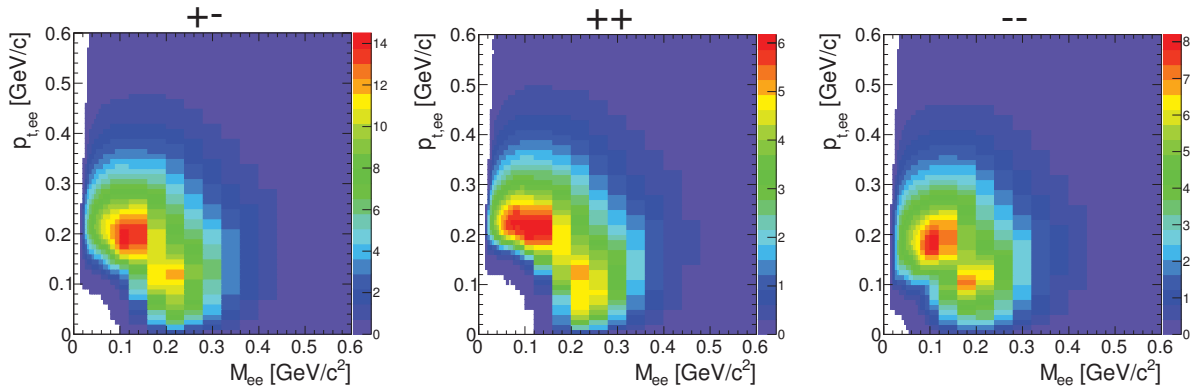
Figure 5.5.: Invariant mass vs. transverse momentum distributions for lepton pairs of different signs obtained with event mixing.

A possible solution is to set a condition on minimal value of the ratio $r = \frac{\min\{N_{++}, N_{--}\}}{\max\{N_{++}, N_{--}\}}$, below which arithmetic mean is used instead of geometric one. As displayed in Fig. 5.6 (left panel), this makes

---

[1] m_t is the radial coordinate in the $M - p_t$ plane and the minimum radius at which non-zero yield appears depends on the sign of the pair.

the distribution of the mean smoother. Nevertheless such a description of background or calculation of the k-factor are still mathematically incorrect. and better solution is to avoid empty bins, possibly by multiplying background with k-factor only in one dimension. It is therefore necessary to check if the results from different multi-dimensional calculations are consistent with the one-dimensional ones.

Fig. 5.6 (right panel) shows comparisons of signal obtained by subtracting background corrected with one-dimensional k-factor and different variants of two-dimensional ones. In the left panel it is done in the $M - p_t$ plane, with several values of the ratio $r = \frac{\min\{N_{++}, N_{--}\}}{\max\{N_{++}, N_{--}\}}$. While without using this ratio signal is fully removed in the range 80-140 MeV/c^2, increasing it makes two-dimensional approach consistent with one-dimensional up to 0.4 GeV/c^2. The right panel compares one-dimensional application of k-factor with two-dimensional, done in the mass vs. opening angle representation. Those two are fully consistent up to 0.4 GeV/c^2, even without the ratio r. In both representations, the deviations above 0.4 GeV/c^2 come from statistics in same-event like-sign background, which is quite sparse in this region and has many bins empty or with very few counts. The agreement between the case, when k-factor is applied in one-dimensional representation M and the cases. when it is done in two-dimensional $M - p_t$ or $M - \theta$ shows, that there is no need to consider a three-dimensional $M - p_t - \theta$.
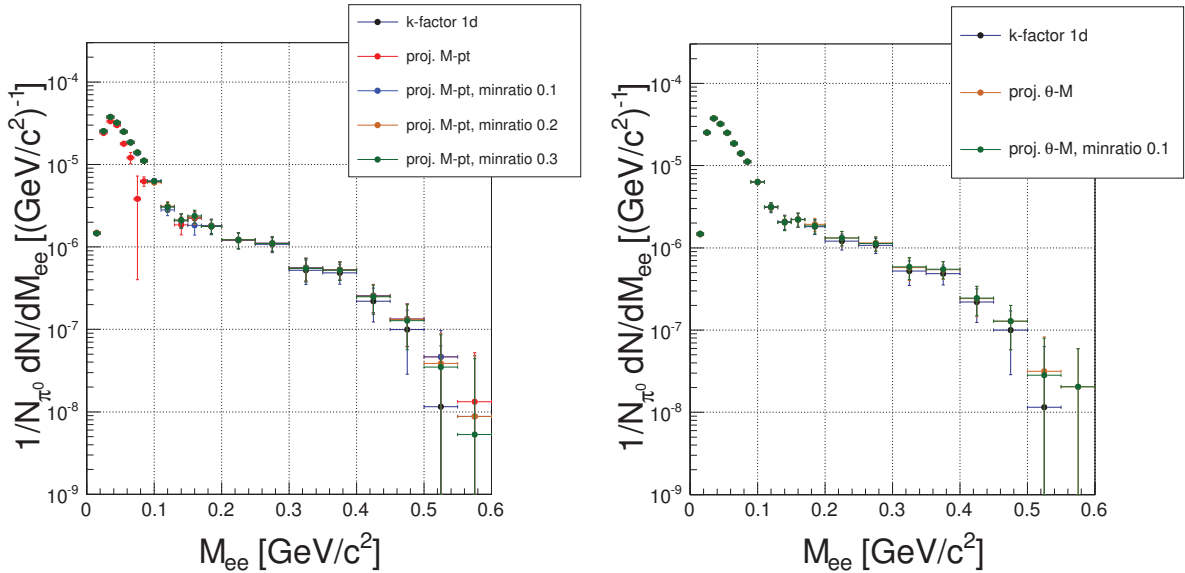
Figure 5.6.: Comparison of signal obtained after correcting background with k-factor in one or two dimensions. Left: one-dimensional mass-dependent correction and two-dimensional, dependent on mass and p_t, with several values of minimal ratio $r = \frac{\min\{N_{++}, N_{--}\}}{\max\{N_{++}, N_{--}\}}$ (denoted as *minratio*), below which geometric mean is replaced by arithmetic one. Right: one-dimensional and two-dimensional, dependent on mass and opening angle, with two values of minimal r.

This paragraph can be concluded by the statement, that one-dimensional application of k-factor agrees with two-dimensional in the regions, where statistics is sufficient and deviations appear, when the two-dimensional suffers from empty bins. Therefore doing the correction in one dimension is the correct approach.

5.3 Mixed-event combinatorial background

At sufficiently high values of invariant mass no significant contribution of correlated combinatorial background is expected and this makes the mixed-event spectrum a good approximation of the combinatorial background. Thanks to this, the issue of small statistics in this mass region can be resolved at least partially. The statistics in event mixing is almost unlimited and only the spectrum of all $e^+ e^-$ combinations

contributes to statistical uncertainties and fluctuations. As a result, they get better by factor of about 2 for signal.
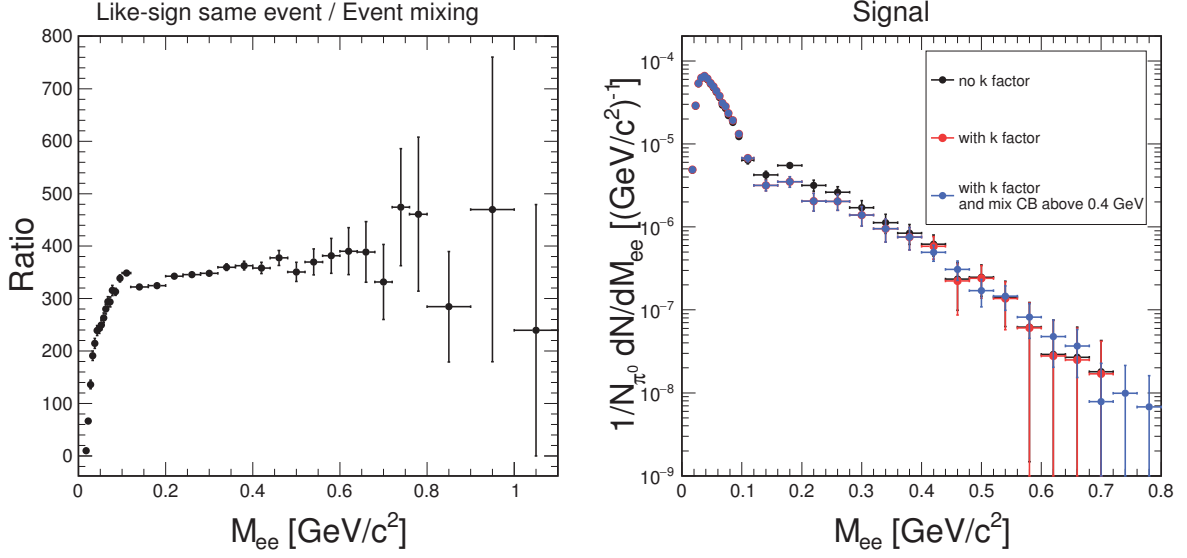
Figure 5.7.: Left: ratio of the same-event like-sign distribution to the mixed-event opposite-sign. Right: signal after subtracting combinatorial background calculated in three different ways.

Various aspects of the event mixing procedure have been tested. In order to avoid combining leptons from events of very different characteristics, events were divided into pools. These are 10% centrality classes, 5 bins of z position of the event vertex and four bins of the reaction plane azimuthal angle (see [105]) – in total 80 event pools. In each pool an event buffer of length 80 was stored and leptons from every single event were combined with those coming from 80 previous events of the same class. With this event partition and buffer size it was possible to obtain the mixed-event background spectrum that is in agreement with the same-event like-sign background and also to avoid the situation when events of the types that occur seldom or in which leptons are particularly rare, would be never mixed.

It is, however necessary to verify, that the slopes of same-event like-sign spectrum and mixed-event e^+e^- are the same. An example can be seen in the left panel of Fig. 5.7. It shows the ratio of the two mentioned distributions as a function of the invariant mass. The error bars are statistical and they are governed by the uncertainty of same-event. All what can be said is that the ratio is consistent with constant within errors above $M_{ee} = 0.4\,\text{GeV}/c^2$. In the same way the slopes are consistent in this range.

Next question is the proper normalization of the mixed-event spectrum. It has of course much more counts than same-event. On the other hand, if any type of weighting that takes into account the frequency of different event classes is used, then the bin contents in the histogram from event mixing are typically very low. The simplest way to handle this is to scale the mixed-event distribution by the ratio of its integral to the integral of same-event like-sign, both computed in an appropriate range. In this analysis, the integrals are calculated in the same mass range in which mixed event is applied to describe the background. It is $M_{ee} > 0.4\,\text{GeV}/c^2$.

In the right panel of Fig. 5.7 one can see the comparison of signal spectra obtained in different approaches. Black circles show the same-event like-sign background, calculated without the k-factor (black points), second with it (red points). One can see, that the k-factor reduces an unphysical enhancement of the signal just above the π^0 mass. The third spectrum comes from using mixed event to describe the background above $M_{ee} = 0.4\,\text{GeV}/c^2$ (blue points). This choice is based on the results from Fig. 5.7. Right panel shows, that in this region both estimators of combinatorial background have exponential shape with the same slope. This is also confirmed by the left panel, where the ratio is above $M_{ee} = 0.4\,\text{GeV}/c^2$ consistent with the constant value. Extending the region, where mixed event is used,

further below $M_{ee} = 0.4$ GeV/c^2 is not necessary, because same event like-sign backround has sufficient statistics there. The normalization of mixed-event is as discussed above. This approach is consistent with the second one, but reduces statistical error and fluctuations between points. This is therefore the final approach to calculate combinatorial background as a function of the mass.

5.4 Systematic uncertainty of the combinatorial background

Like-sign combinatorial background is well justified mathematically and the k-factor allows to account for difference in reconstruction probability of like- and unlike-sign pairs as a function of pair kinematic properties. It has still to be checked that it describes combinatorial background accurately, that is if the like-sign spectrum is equal the spectrum of wrong unlike-sign pairings. Such check can be carried out only in simulation. In this work, such attempt was made using 10^8 UrQMD events, generated for efficiency calculations in HADES. UrQMD produces, among other particles, π^0, η and photons. When the UrQMD output is processed through GEANT, the particles decay with known branching ratios and photons have a chance to convert in detector materials. These generates a sample of dileptons. The decay and conversion is calculated independently, with different random number generator seed, every time, when the GEANT simulation is performed separately for UrQMD events with particles of every species embedded to them. [2] Even though the events are reused, so π^0, η and γ have the same kinematics, different of them will decay into Dalitz channel or convert in each run. The dileptons are thus well randomized. For this reason, four data samples [3] were added together to get larger statistics of UrQMD combinatorial background lepton pairs. It has been also checked, that the results of the present considerations obtained with every of these data sets separately, vary in general by less than 10% with respect to each other and that the variation is smaller than the statistical error. The combined sample contains $4 \cdot 10^8$ events, the true combinatorial background cocktail from this sample is shown in the left panel of Fig. 5.8. The background is dominated by uncorrelated pairs from different sources. Important contribution comes also from correlated background. The third type of the background is due
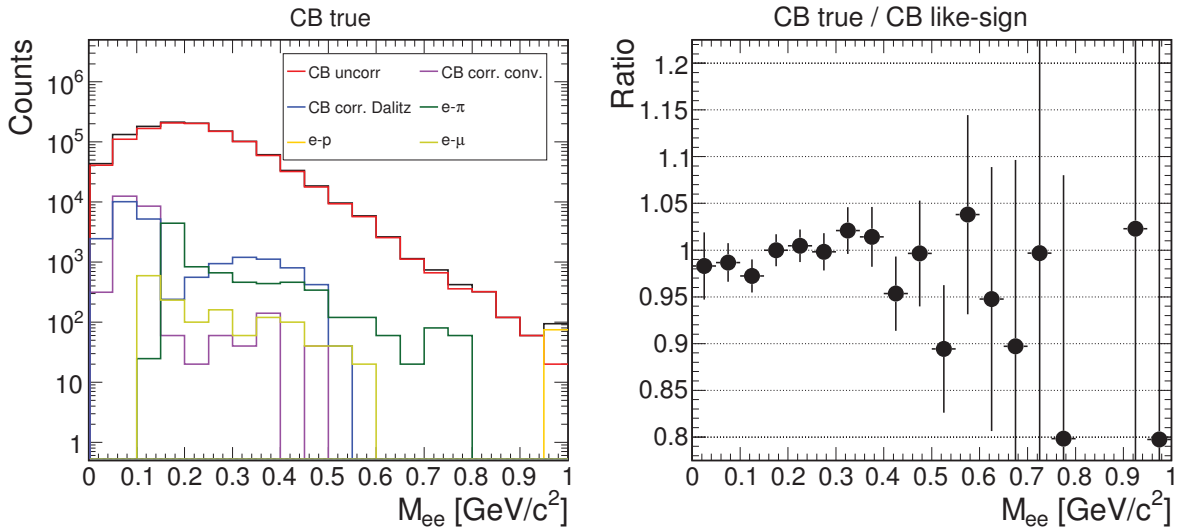
Figure 5.8.: Left: cocktail of the dilepton combinatorial background contributions in UrQMD. Right: ratio of the true unlike-sign combinatorial background to its like-sign estimator.

to misidentification of muons, pions or protons as electrons or positrons. The largest is electron-pion

---

[2] In the future, UrQMD events will be processed through GEANT only once and combined with GEANT output for different embedded particles directly before the DST calculation. Then using combined data samples will not be appropriate.

[3] With deuteron and Λ embedded, as well as pure UrQMD simulations with two sets of GEANT material budget parameters of RICH.

contribution, containing both $e^+\pi^-$ and $e^-\pi^+$ pairs. Electron-muon pairs ($e^+\mu^-$ and $e^-\mu^+$) follow. The contribution of e^-p is negligible. This is expected, since pions are the main source of contamination in electron sample: only small number of muons are produced and protons are better separated from leptons already by kinematics. Within the statistics that has been analyzed, pairs of two misidentified particles never appear, which confirms the very high purity of lepton PID.

The cocktail of true combinatorial background is compared with its estimation by like-sign pairs yield in the right panel of Fig. 5.8 by making a ratio of the two. Like-sign background was multiplied by the k-factor obtained from event mixing of real data. The result is consistent with unity within statistical errors and consequently systematic uncertainty of the combinatorial background cannot be estimated with the precision higher, than the statistics of the simulation allows to.

Based on the difference from unity of the point values below 0.4 GeV/c^2, where statistical error and fluctuations of the simulation are still reasonably small, the upper limit on the like-sign combinatorial background uncertainty can be estimated to be 2%. This translates to $0.02 \cdot B/S$ (S - signal, B - background) uncertainty on the signal and this is taken as a conservative evaluation for all invariant mass values.

6 Summary of systematic uncertainties

Systematic uncertainties for each analysis step that may lead to the emergence of systematics were described in the corresponding chapters. The comments about the uncertainty contributions are highlighted with colored boxes in respective sections. To summarize, the following contributions are taken into account (they are listed in the order in which they are discussed in text):
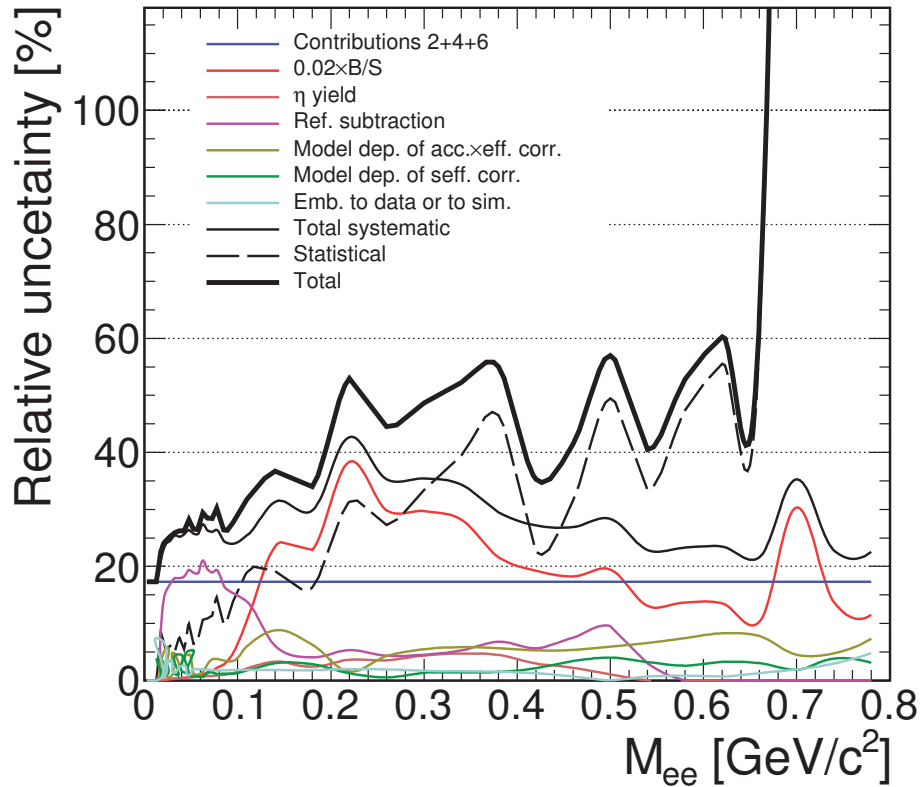
Figure 6.1.: Relative systematic, statistical and total uncertainty as a function of the dilepton invariant mass for the case of spectra, where all the sources of systematic uncertainty contributions are present. The individual contributions to the systematic uncertainty are shown as well, the three of them which were estimated to be 10% each, independently of mass, are shown as one, after adding them in squares.

1. Calculating single lepton efficiency by embedding simulated electrons and positrons to UrQMD events or to real data (Section 5.2.1). This contribution was estimated bin-by-bin in pair observables and is smaller than 2%.

2. Self-consistency check of the efficiency correction allows to estimate the uncertainty of the correction procedure to 10% (Section 4.4).

3. Using different models to calculate one-dimensional efficiency and acceptance corrections, as discussed in Section 4.5.4. This contribution is calculated bin-by-bin in pair observables and brings

4% at maximum in the case of efficiency correction and 7% at maximum in the case of efficiency and acceptance correction. In the spectra corrected for efficiency only the former contribution is included, in those corrected for efficiency and acceptance – only the latter. This allows to avoid double counting. In addition, as mentioned in Section 4.5.4, estimating the uncertainty for efficiency×acceptance correction takes into account possible cancellations of the uncertainties with respect to the case, when they are calculated for efficiency and acceptance separately and then added together as independent.

4. Correction for the acceptance of missing sectors is estimated to introduce 10% contribution to systematic uncertainty (Section 4.6).

5. Subtraction of the combinatorial background brings additional uncertainty of $0.02 \cdot B/S$ (Section 5.4). It is the largest contribution to systematic error.

6. Normalization to the number of π^0 contributes with 10% uncertainty (Section 7.1.1). This can be correlated with the error from efficiency correction if they are both driven by the track reconstruction efficiency in the drift chambers and the time-of-flight measurement. However, it is difficult to calculate the correlation coefficient and the safe assumption is to treat them as independent. This uncertainty is included only in the spectra and integrated yields which are normalized to the number of pions.

7. Uncertainty of the η yield (Section 7.2). This contribution is calculated bin-by-bin and is 5% at maximum. This uncertainty is included only in the spectra, where the η is actually subtracted.

8. Uncertainty of the reference spectra, see [83, 38]. This contribution is calculated bin-by-bin and is 20% in the π^0 region and besides that has maximum of 10% at invariant mass of around 0.5 GeV/c^2, where the difference between the reference and the Au+Au spectra is the smallest. This uncertainty is included only in the spectra, where the reference is actually subtracted.

The origins of practically all the contributions are independent of each other. It is thus assumed that the uncertainties are independent and they are added is squares to obtain the total uncertainty. Note that some of the contributions are taken into account only in the spectra, in which the reason to include them is present (acceptance correction, η or reference subtraction). The contributions to the systematic uncertainty and the total one (including all of them), together with the relative statistical error are shown in Fig. 6.1. The statistical error and the one from subtraction of combinatorial background dominate. Possibilities to estimate the uncertainty of combinatorial background with higher precision have to be further studied. The total systematic uncertainty is calculated as discussed above and represented in all plots of the next chapter as boxes.

7 Interpretation of dilepton spectra

In this chapter results of the data analysis are presented. In order to draw any conclusions about the radiation of hot and dense medium, dilepton sources emitting after the freeze-out have to be known in the first place. In the mass range accessible for present analysis these are π^0 and η. Their spectral shape is obtained from simulation and multiplicity is estimated experimentally. In the case of π^0 one possibility is to take an average of charged pions multiplicities, making use of the isospin symmetry. Both π^0 and η has been fully reconstructed from the conversion of their decay photons in detector material. Contribution of η is then subtracted from spectra for consistent comparison with previous HADES runs, although in Au+Au it is negligible. Typically, π^0 is not subtracted, but spectra are normalized to its multiplicity, which allows to compare relative radiation strength *beyond* the "trivial" freeze-out. Sections 7.1.1 and 7.2 give an overview of methods used to estimate the meson multiplicities and quote the results.

The dilepton spectra will be compared to the measured reference of elementary NN collisions at the same kinetic energy per nucleon. The reference spectrum has its respective η contribution subtracted as well. By virtue of this and of the proper normalization, it should be equivalent to incoherent superposition of collisions of single nucleons in Au nuclei.

The extracted *excess* radiation over reference (including subtraction of both NN and η) can be further studied in terms of the dependence of its integrated yield on the number of participating nucleons $\langle A_{\mathrm{part}} \rangle$ between different centrality classes of Au+Au collisions and with previous HADES measurements. Shapes of invariant as well as of transverse mass (when expansion velocity is taken into account) carry information about temperature of the medium. Interpretation in context of the existing models results in even deeper physical insights. They are summarized in the conclusions part.

7.1 Normalization to the number of π^0

Dilepton spectra from different reactions are normalized to the π^0 multiplicity in respective events. At low energies normalization to the number of charged tracks N_{ch} is inadequate, since the number is dominated by protons from projectile and target, in contrast to higher energies, where N_{ch} is dominated by newly produced particles. Neutral pion multiplicity can be obtained either from the direct reconstruction by means of the double γ conversion method or from multiplicities of charged pions. In the latter case, due to isospin symmetry, $N_{\pi^0} \approx \frac{1}{2}(N_{\pi^+} + N_{\pi^-})$ (this was also confirmed inspecting UrQMD simulation).

7.1.1 Charged pion analysis

The general features of event and track selection in the charged pion analysis are the same as for leptons [122]. Pion tracks are selected with:

1. Track is not marked as a *fake* by the track finding procedure.

2. Track has been constructed from fitted track segments and the outer segment was matched to a hit in any META detector, Runge-Kutta fit converged.

3. Runge-Kutta $\chi^2 < 400$.

4. META hit is within the cell pointed by the track.

5. The distance between the track and META hit in the direction along the META cell is smaller than 3σ

6. No sharing of MDC segments or META hits is allowed.

Particle identification is done by a 2σ cut around the kinematic curve $\beta = \frac{p/m}{\sqrt{(p/m)^2+1}}$, while restricting the momentum range to $80 \leq p \leq 1300$ MeV/c. The cuts are shown in Fig. 7.1 for the two HADES sub-systems separately.
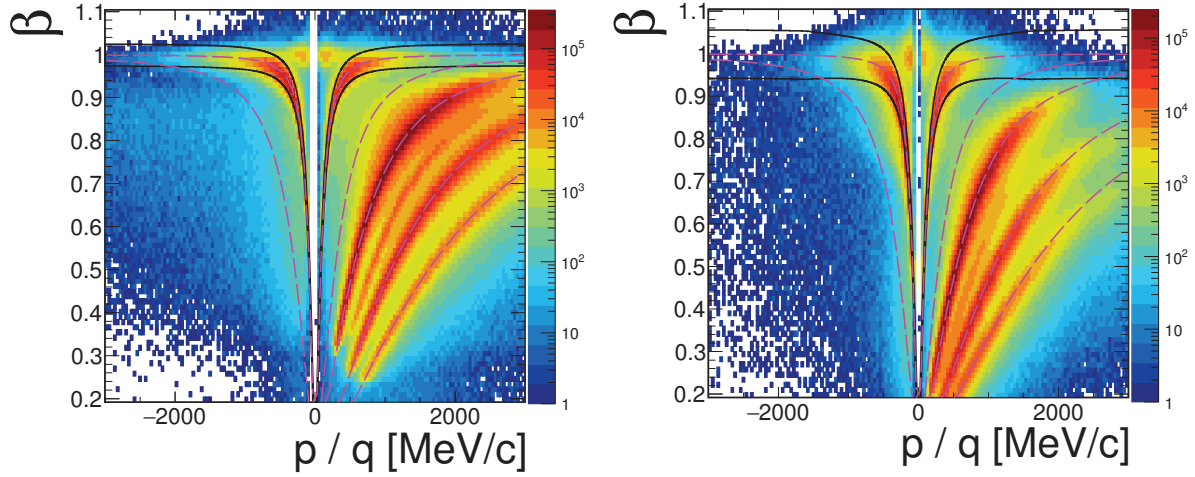
Figure 7.1.: Particle identification of hadrons in RPC (left) and TOF (right). Dashed lines represent kinematic $\beta(p)$ for pions, kaons, protons and light nuclei, solid lines are 2σ cuts for pions.

Efficiency and acceptance matrices are also calculated in similar way as in the case of single leptons, they are, however, represented in coordinates of transverse mass $m_t = \sqrt{m_\pi^2 + p_t^2}$ and rapidity y. The corrected spectra of $m_t - m_0$ are shown in Fig. 7.2 for various rapidity bins. Particles emitted from a thermal source have Boltzmann (exponential) distribution of their transverse mass:

$$\frac{1}{m_t^2}\frac{d^2N}{d(m_t - m_0)dy} = C_1(y)\exp\left(\frac{-(m_t - m_0)c^2}{k_b T_1(y)}\right) + C_2(y)\exp\left(\frac{-(m_t - m_0)c^2}{k_b T_2(y)}\right).$$

The spectra in Fig. 7.2 can in fact be described by a sum of two such exponential components. The steeper one (T_1), populating mostly low transverse mass, is interpreted as a contribution of pions from decays of Δ resonances. The less steep component (T_2), dominating higher m_t, can be attributed to pions produced thermally in the fireball (meaning excitation of $\pi^+\pi^-$ pairs) or as a superposition of pions from decays of higher lying baryonic resonances (N*(1440), N*(1520),Δ(1680),...).

The fit is used to extrapolate the pion yield to the regions of m_t, where no measurements are possible. In order to access total π^+ and π^- multiplicities, extrapolation to the unmeasured rapidity ranges is necessary as well. The rapidity density function obtained from integrating m_t spectra has a bell-like shape, see Fig. 7.3. This suggest a Gaussian fit as a first attempt to extrapolation. Alternatively, one can use the shape of rapidity distribution obtained from a transport model calculations, that includes various pion production mechanisms and absorption/rescattering processes. The yield is then scaled to reach the same value at mid-rapidity as experimental data. In HADES, UrQMD [66] transport code is used for this purpose. For the needs of this work, average pion multiplicities from Gaussian and UrQMD extrapolations are taken in all of 10% centrality bins. They are listed in Table 7.1 For 40% most central events the average from all centrality classes is taken for consistency, as the classes should be populated equally with events, by definition.
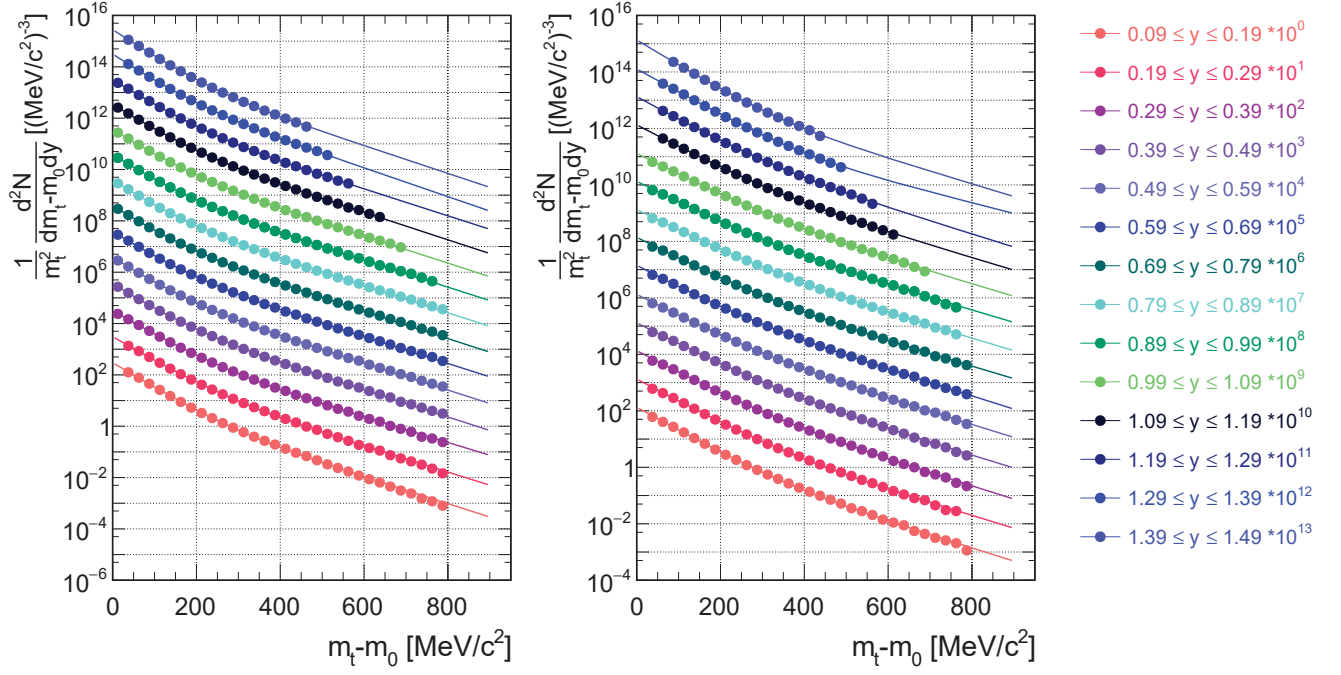
Figure 7.2.: Differential distributions of π^- **(left)** and π^+ **(right)**, corrected for acceptance and efficiency. Lines represent fits with a sum of two Boltzmann components.
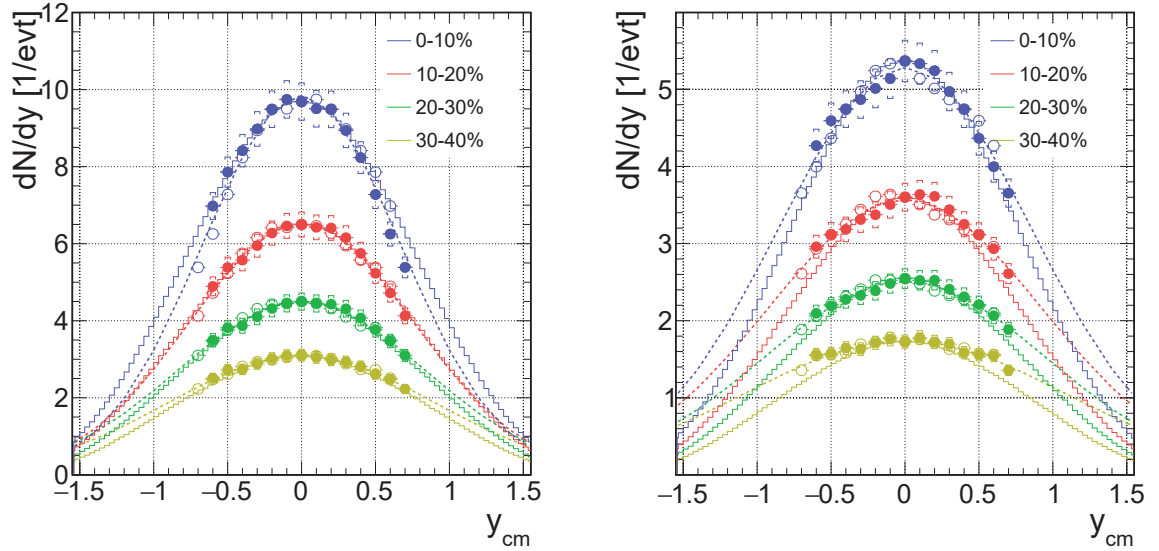
Figure 7.3.: Total corrected yield of π^- **(left)** and π^+ **(right)** as a function of the rapidity. Full points are data, open points are data reflected about $Y = 0$ axis. Dashed lines represent extrapolation with the Gauss fit, solid lines – extrapolation with UrQMD.

The statistical uncertainty in the pion yield determination is negligible. The systematic one was estimated to be of 10% and the main contribution is the extrapolation in rapidity. The same is thus the uncertainty of the $1/N_{\pi^0}$ factor used to normalize dilepton spectra.

Centrality	$\langle N_{\pi^-} \rangle$	$\langle N_{\pi^+} \rangle$	$\langle N_{\pi^0} \rangle$	$T_1^{\pi^-}$ [MeV/k_B]	$T_2^{\pi^-}$ [MeV/k_B]	$T_1^{\pi^+}$ [MeV/k_B]	$T_2^{\pi^+}$ [MeV/k_B]
0-10%	17.05	9.75	13.40	49.4 ± 2.5	93.4 ± 4.7	61.4 ± 3.1	105.4 ± 5.3
10-20%	12.20	6.75	9.48	45.3 ± 2.3	87.7 ± 4.4	55.4 ± 2.8	97.2 ± 4.9
20-30%	8.85	4.80	6.83	43.2 ± 2.2	83.7 ± 4.1	52.0 ± 2.6	91.5 ± 4.6
30-40%	6.35	3.45	4.90	41.6 ± 2.1	80.5 ± 4.0	49.4 ± 2.5	87.0 ± 4.4
0-40%	**11.10**	**6.20**	**8.65**				

Table 7.1.: Multiplicities and temperatures of charged pions and π^0 calculated as their average. Statistical error is negligible and systematic one was estimated to 10%.

7.2 Neutral meson reconstruction with γ conversion

It is also possible to fully reconstruct neutral mesons π^0 and η. This requires detection of real photons. At the time of the Au+Au experiment, HADES did not contain any detector for photon measurement using e.g. calorimetry. Still, it is possible to detect e^+e^- pairs created in external γ conversions. In this type of analysis [41] leptons are identified based on a β vs. momentum cut only – besides the low efficiency of the RICH detector, many conversions occur in its mirror and such cases would be lost when requiring a presence of a RICH ring.

Identified particles are combined into $e^+e^-e^+e^-$ multiplets and their invariant mass is investigated. Properly selected *topological* cuts on opening angles between e^+ and e^- and between dilepton pairs reduce the background – both from wrong combinations and from hadron contamination due to very conservative particle identification. The background is then fairly well described by event mixing, in this case mixed objects are whole e^+e^- pairs.

With this method π^0 multiplicity in 40% most central events was estimated to be
9.7 ± 0.27(stat) ± 1.8(syst) ± 1.3(extra) per event, where the first uncertainty takes into account all the systematics besides the one, that comes from extrapolation to full phase space. This one is given separately as the second uncertainty. The result is consistent with the one from charged pion multiplicities, but in the case of conversion method the uncertainty is larger. In fact, the low multiplicity with overwhelming background contribution makes the analysis very difficult and its result highly appreciable. The η multiplicity in the 40% most central events is estimated to be
0.107 ± 0.005(stat) ± 0.028(syst) ± 0.007(extra) per event. The uncertainty is quite large but, as it will be shown later in this chapter, since η does not play any important role in the dilepton spectra from Au+Au collisions, also its uncertainty has little impact on excess e^+e^- yield.

7.3 Invariant mass and excess radiation

Invariant mass spectrum of dilepton signal, corrected for efficiency is shown in Fig. 7.4 with statistic and systematic uncertainty (the latter are shown as boxes around the symbols). Substantial yield is visible in the mass range above π^0, what allows to interpret the origin of the virtual photon radiation.

The first step is to compare with the reference measurement of p+p and n+p [1] at E_{beam} = 1.25 GeV [83]. The difference should reveal medium radiation, not present in collisions of elementary hadrons. If there were no such a radiation, heavy-ion collisions would look like a (properly scaled) sum of individual interactions of their nucleons. In Au+Au there would be roughly the same probability for n+p collisions as for p+p and n+n together and the radiation from p+p is assumed to be the same as from n+n. As a consequence, an appropriate *reference spectrum* is an average of n+p and p+p.

For comparison, the sources, that radiate mainly after the freeze-out, have to be properly accounted for. The comparison of the measured invariant mass spectrum to the freeze-out cocktail is shown in

---

[1] It was measured in d+p reactions, with events selected, where neutron in deuteron was *quasi-free*
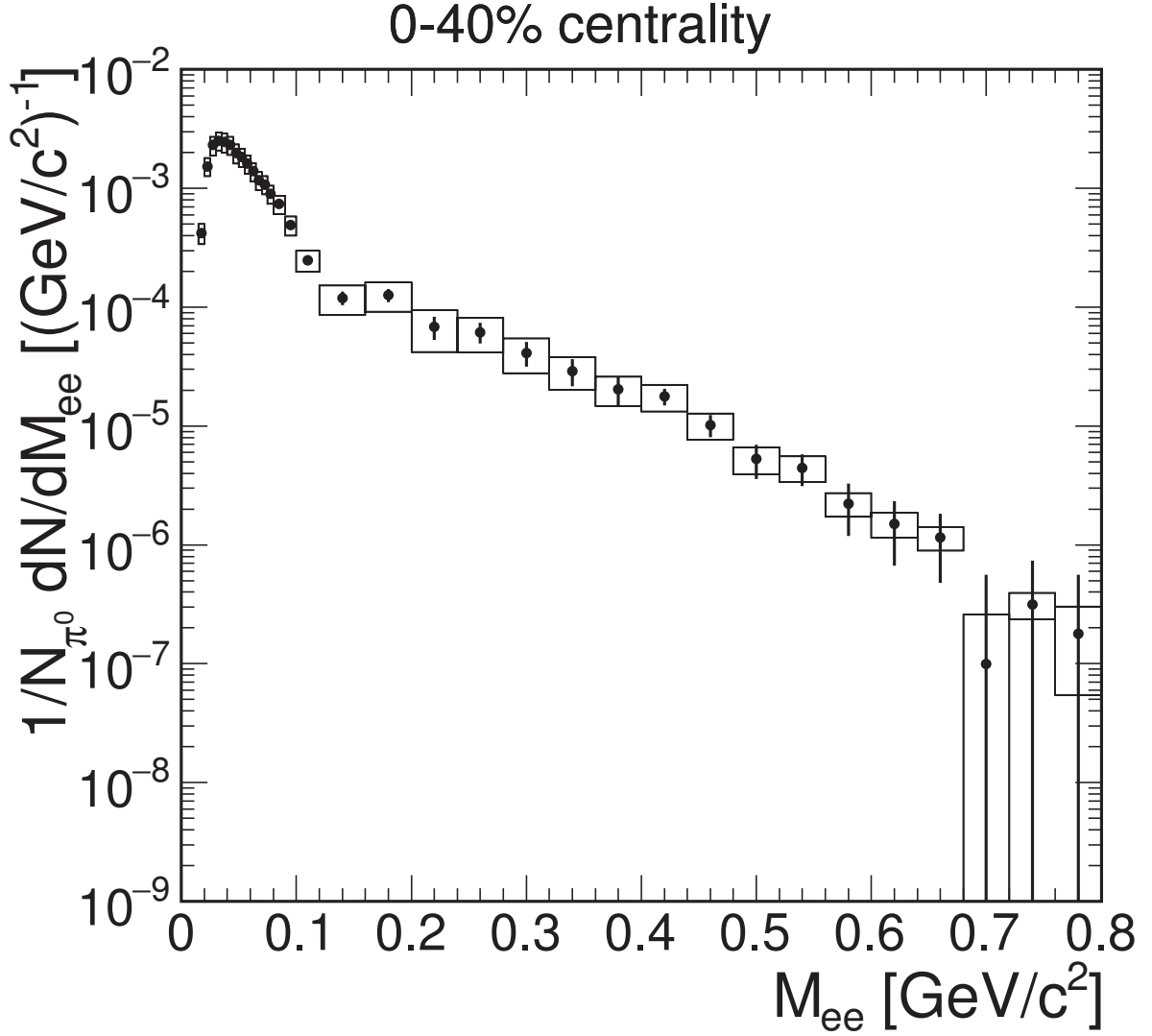
Figure 7.4.: Invariant mass distribution of dilepton signal in Au+Au at $E_{\mathrm{beam}} = 1.23A$ GeV in 40% most central collisions. It is corrected for the efficiency and normalized to the π^0 multiplicity. Error bars represent statistical error (Poisson), rectangles are the systematic.

the left panel of Fig. 7.5. The ingredients are the same as described in Section 4.5.1 with the only difference that now $\omega \rightarrow \pi^0 e^+ e^-$ channel is included (branching ratio $7.7 \cdot 10^{-4}$). The radiation beyond the freeze-out, is clearly visible.

In order to compare to reference, the spectrum has to be normalized to the number of pions produced, i.e. number of events analyzed times the π^0 multiplicity per event. As the latter is approximately proportional to the system size [38] (i.e. number of π^0 is constant as a function of $\langle A_{\mathrm{part}} \rangle$), this assumes a proper scaling for NN reactions and gives an insight into effects, that are beyond simple superposition of single colliding nucleons. From the scaled spectra, properly normalized η-Dalitz, calculated in simulation, is subtracted. Nevertheless, in Au+Au reactions this contribution is smaller than 10% and it is negligible, as it can be seen in the left panel of Fig. 7.5 and also by comparing with the right panel of the same figure, where this yield is subtracted. The comparison of Au+Au spectrum to reference is shown in Fig. 7.5 (right panel) as overlay of the two distributions. A substantial excess can be seen, which is roughly of the factor 4.
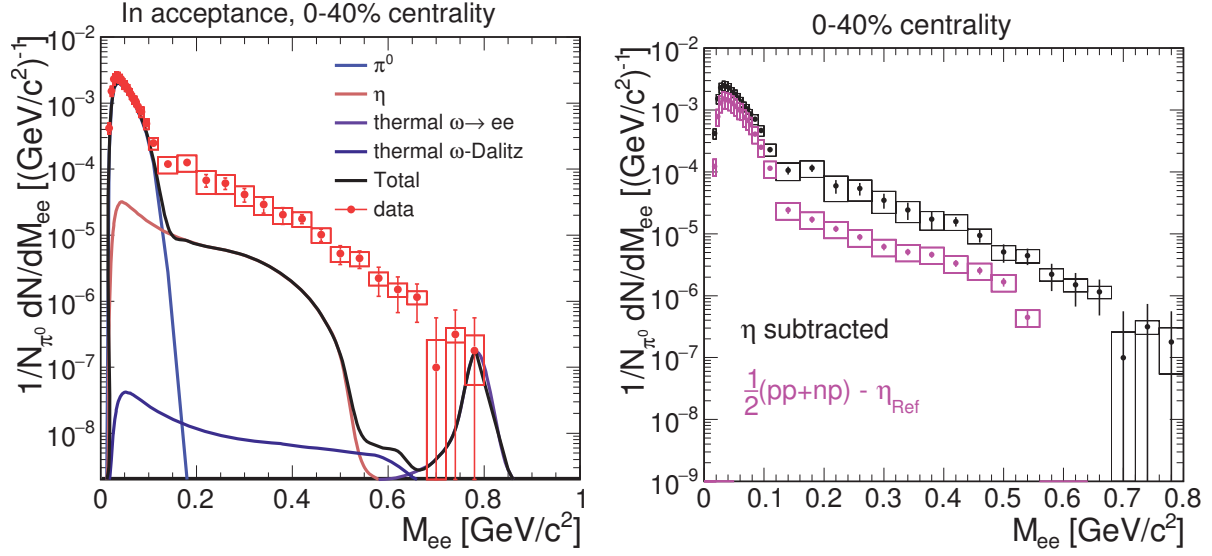
Figure 7.5.: Left panel: invariant mass distributions from 40% most central Au+Au events at $E_{\text{beam}} = 1.23A$ GeV together with the simulated cocktail of the freeze-out sources. Right: invariant mass distributions from Au+Au and average of p+p and n+p at $E_{\text{beam}} = 1.25$ GeV. In this case spectra were normalized to respective numbers of neutral pions and η contributions were subtracted.

The excess can then be compared to STAR results and provide the lowest energy point in the beam energy scan, as shown in Fig. 7.6. It turns out, that the dilepton excess yield, normalized to the number of pions is approximately constant with beam energy. As a matter of fact, the yield results from an interplay
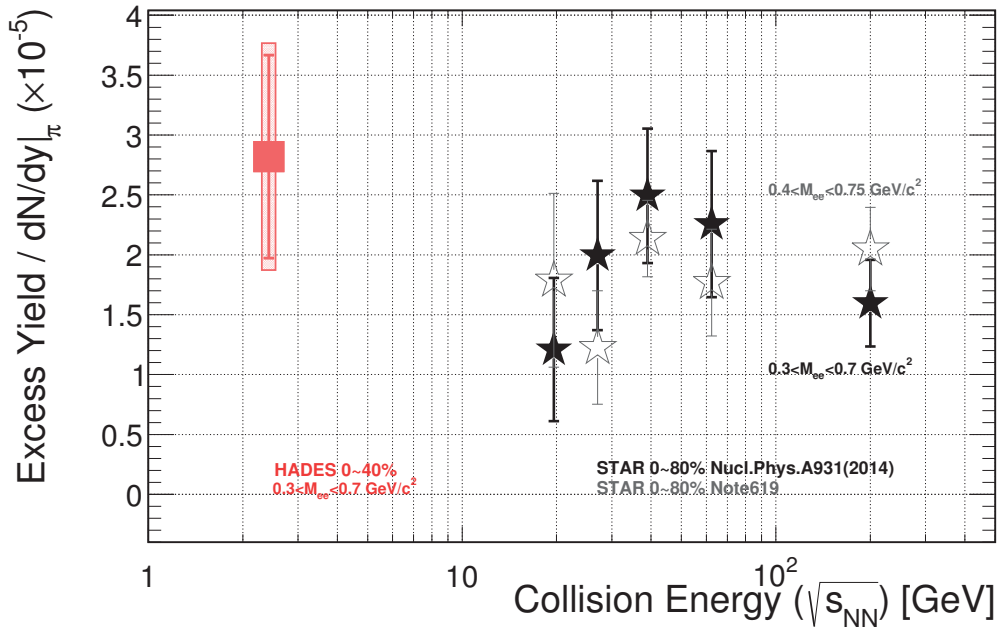
Figure 7.6.: Integrated excess dileptons yield per pion, as a function of center-of-mass beam energy, measured by HADES (present work) and STAR [29]. Note that the HADES point has been scaled up by factor 2 to account for different rapidity coverage of the two experiments.

of volume, temperature and the life-time of the system what is reflected by its $\sqrt{s_{NN}}$ dependence. This observation will be scrutinized in future in greater detail.

7.4 Centrality dependence of the integrated excess yield

Further understanding of in-medium radiation can be gained by examining it differentially. One aspect is the centrality dependence. Fig. 7.7 shows dilepton excess yield in centrality bins of 10% events. The spectra are obtained by subtracting the η-Dalitz contribution and NN reference. Next, they are normalized to the number of π^0 and extrapolated to 4π using one-dimensional acceptance correction (the mean from three models, as discussed in Section 4.5.4). The centrality dependence of the excess yield cannot be clearly seen from the spectra themselves.
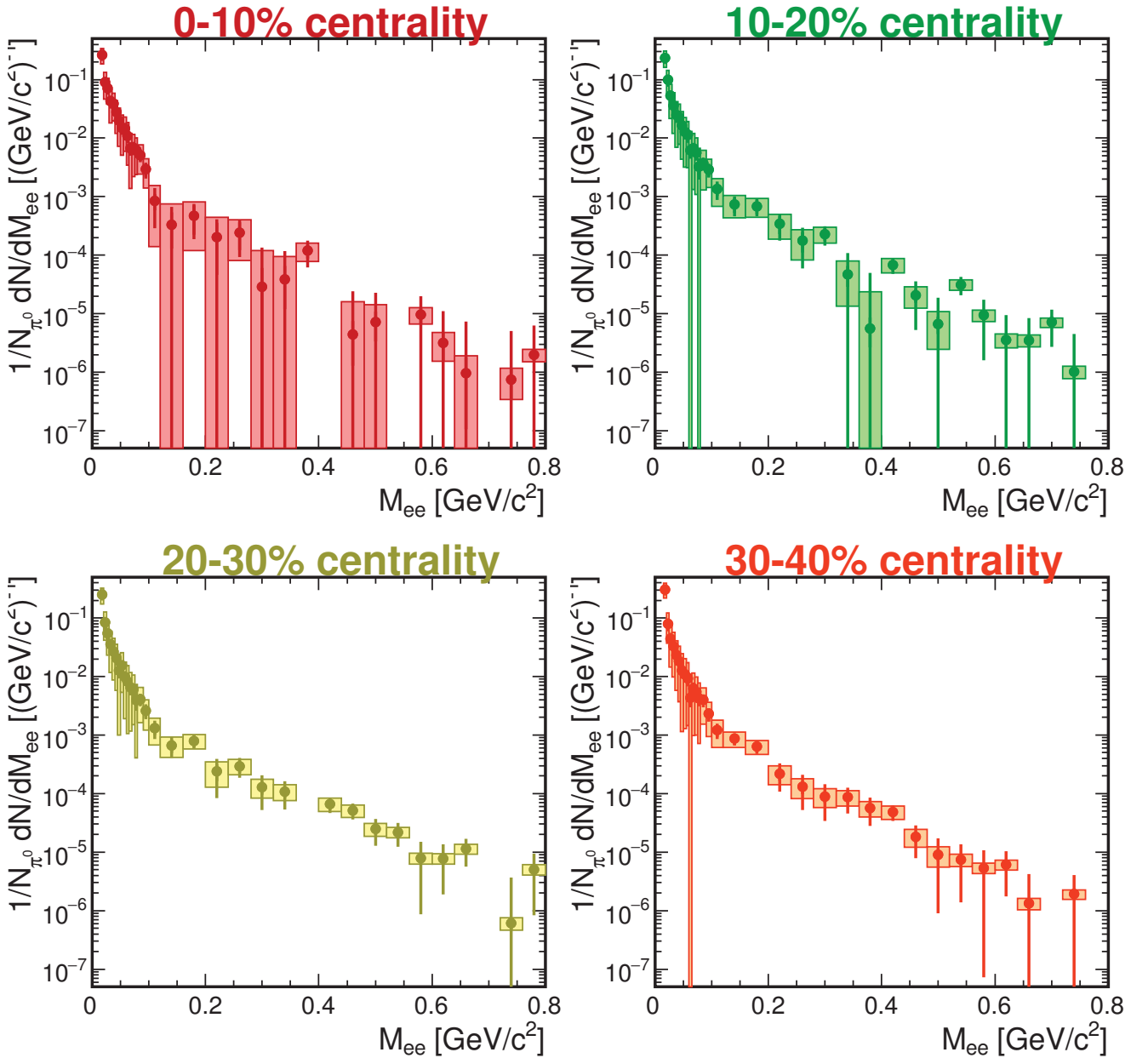
Figure 7.7.: Dilepton excess yield in four centrality bins extracted by subtracting η contribution and NN reference and extrapolating to 4π by means of one-dimensional acceptance correction.

To make a qualitative assertion spectra are integrated in the range $0.3 < M_{ee} < 0.7$ MeV/c^2. This choice has been made in view of possible relation of the dilepton yield to the lifetime of the fireball and a comparison to available STAR BES results. The integrals are shown in the left panel of Fig. 7.8 as a function of the average number of participants. Here the increasing trend is present in two more peripheral bins, which breaks down in central bins. The latter is not a physics effect but comes from insufficient data quality as can be observed in Fig. 7.7. This is due to the small efficiency and signal-to-background ratio in the analysis using RICH ring finder (the two effects are related: loosing a lepton due to inefficiency destroys the signal, but background remains almost unaffected). The problem is resolved in the backtracking (BT) analysis, where the increasing trend is visible in all centrality bins [104] and the yields in the two peripheral bins are indeed consistent with the ones from the analysis discussed here.
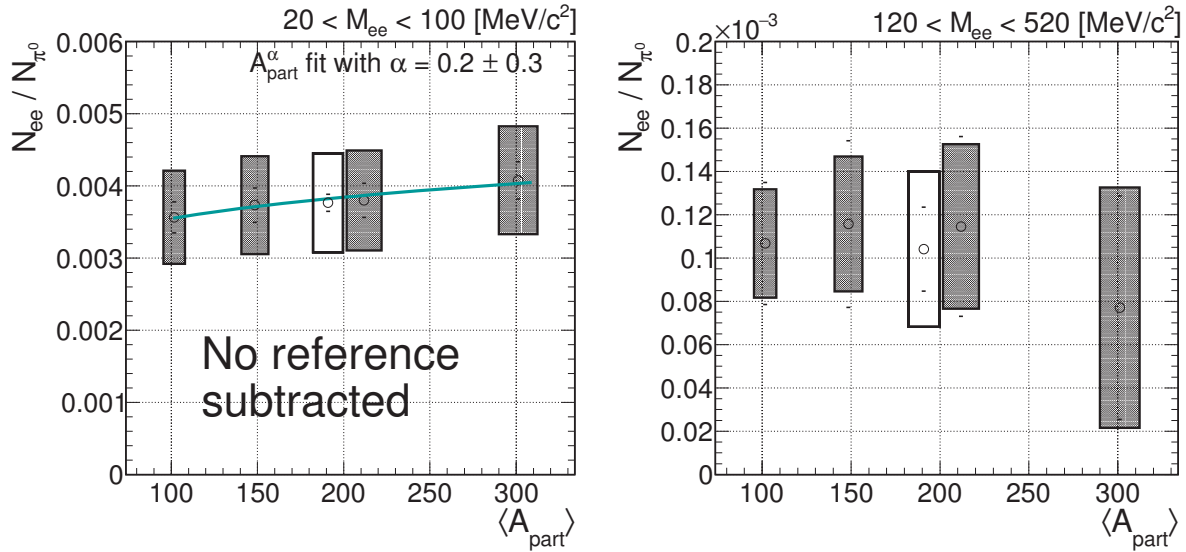
Figure 7.8.: Left panel: integrals of the spectra in the mass range dominated by π^0 after η but without the reference subtraction. Right panel: Integral of the excess yield above the π^0 mass after η and the reference subtraction as a function of the centrality. All integrals are normalized to respective numbers of π^0 deduced from charged pion multiplicities. Ticks represent statistical uncertainties, rectangles systematic (both on the integral and on $\langle A_{\text{part}} \rangle$). The non-filled rectangle in the middle corresponds to 0-40% most central events.

To verify this statement and exclude other issues like e.g. wrong normalization, one can consider integrals in the invariant mass region dominated by π^0-Dalitz decays (without subtracting the reference). In this case signal to background ratio is high in all centrality classes and the abundance of neutral pions makes the efficiency problem less important. The result is shown in the left panel of Fig. 7.8. Since the spectra are normalized to the number of π^0 deduced from charge pion multiplicities, one would expect the integrals to be constant as a function of $\langle A_{\text{part}} \rangle$. However, even in the considered mass range, there is a contribution from medium radiation of about 10-20% of the total yield, cf. Figs. 7.14 and 7.15. Therefore, what is actually expected is a slight increase and it is indeed the case, as shown in Fig. 7.8 (left panel).

7.5 Slopes of the spectra and what they tell us about the effective temperature of the source

Like in the case of charged pions, transverse mass spectra of dileptons are expected to have exponential shape, from which an inverse slope parameter can be extracted, event though caution is needed when interpreting this parameter as the temperature of emitting source.

For the π^0-Dalitz region the fits are shown in Fig. 7.9. Similar like in the case of charged pions, two-component fit consist of: (i) the steep slope up to ~ 400 MeV/c^2 dominated by $\Delta \to N\pi^0$, (ii) the flat one, in wchich π^0 from decays of various baryonic resonances are superimposed. Slope parameters extracted from the fit are summarized in the left panel of Fig. 7.10 and compared to the one obtained from π^- analysis. The values are lower than for charged pions. The reason is, that the spectra in Fig. 7.9 are not for fully reconstructed π^0, but for dileptons from its Dalitz decays and they are a convolution of the neutral pion distributions with the decay kinematics. It is illustrated in the right panel of Fig. 7.10. A simple simulation has been performed, in which a sample of π^0 with two thermal components, decaying solely to the $e^+e^-\gamma$ channel, was generated. Then transverse mass spectra of dileptons (sum of e^+ and e^- four-vectors) and of π^0 (sum of four-vectors of e^+, e^- and γ) were plotted and fitted with a sum of two exponential components. Extracted inverse slope parameter for both components turned out to be by about 12 MeV/k_B lower for the dilepton than for the π^0. When taking into account the correction, the results coincide with the ones from charged pions. Please note, that the effective temperature T_{eff} from the fit to transverse mass/momentum is subject to the blue shift. In order to extract the temperature at kinetic freeze-out T_{kin}, the averaged radial expansion velocity $\langle \beta_{\text{T}} \rangle$ has to be taken into account:

$$T_{\text{kin}} = T_{\text{eff}} - m \cdot \langle \beta_{\text{T}} \rangle^2. \tag{7.1}$$

This gives for pions with $T_{\text{eff}} = 82.8$ MeV/k_B and $\langle \beta_{\text{T}} \rangle = 0.36$ the value $T_{\text{eff}} = 64.6$ MeV/k_B.

It is often argued, that exponential (without any structure) shape of the invariant mass of the excess can be a signature of chiral restoration. The HADES spectrum is shown in Fig. 7.11 for 40% most central events. Two variants are presented: (i) η contribution is subtracted, (ii) η and NN reference (minus respective η contribution) are removed. Single exponential function was fitted to both distributions in the range 0.2-0.8 GeV/c^2. The inverse slope parameter from fit to the invariant mass has the advantage over the one from fit to transverse mass or momentum, that it is not affected by the fireball expansion velocity (i.e. it is free from the blue shift and correspondingly lower, than the T_{eff} extracted from a Boltzmann fit to transverse mass or momentum spectra). It can be therefore interpreted as the true temperature of the source. The values extracted from the two variants are consistent, subtracting the reference has no influence on them beyond the uncertainties. Taking into account that the spectra are integrated over space-time evolution of the fireball, the result is in agreement with coarse-grained UrQMD simulation, as shown in Fig. 1.23, from which the (model-dependent) values of μ_B and of quark condensate, which gets significantly depleted, can be read-off. Substantial depletion of the $\langle \bar{q}q \rangle$ in the HADES range of T and μ_B can be seen and this fact is reflected in the dilepton spectra.
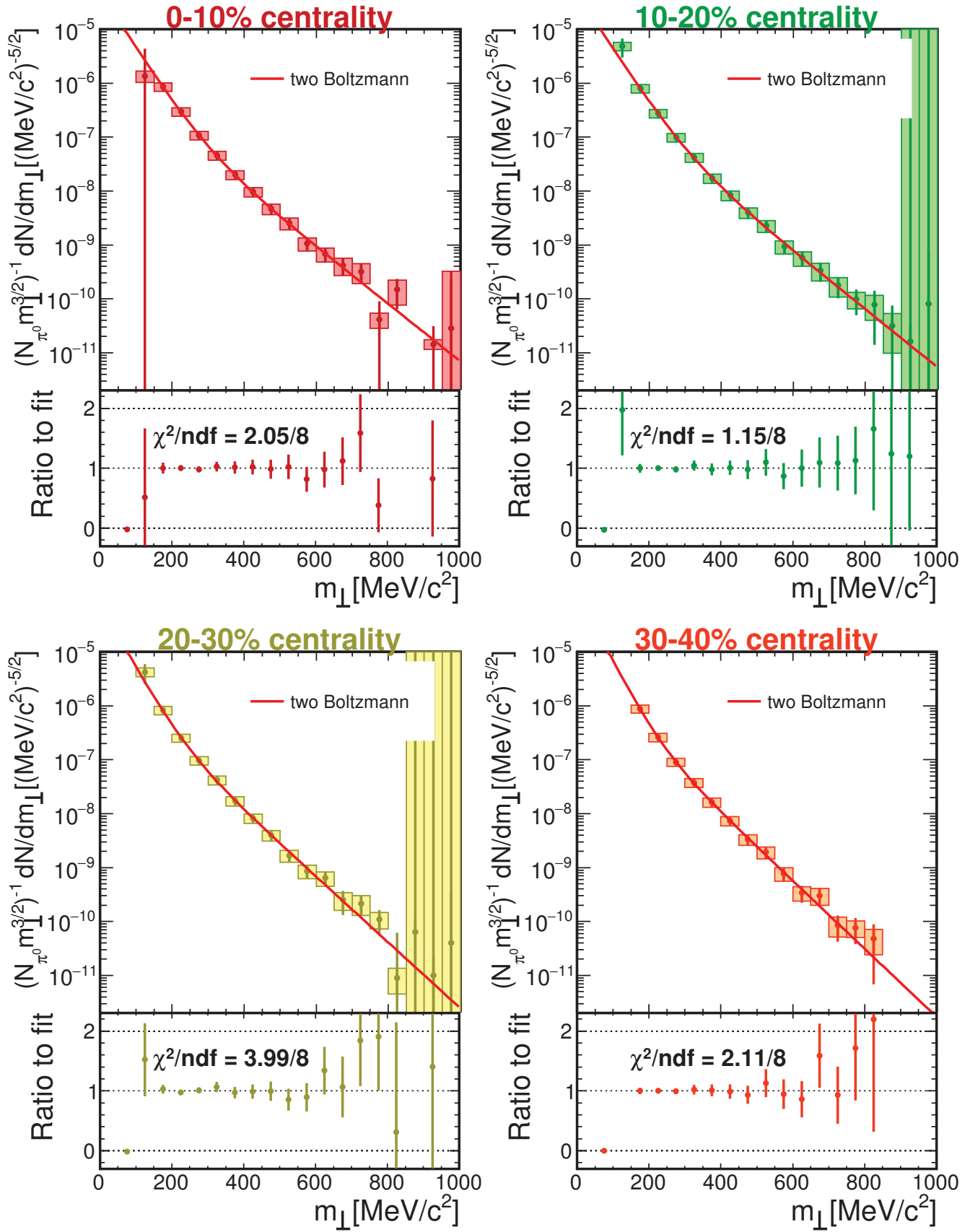
Figure 7.9.: Dilepton transverse mass spectra in four centrality bins for invariant mass $0.15 < M_{ee} < 0.55 \text{ GeV}/c^2$, fitted with a sum of two exponential functions.

7. Interpretation of dilepton spectra
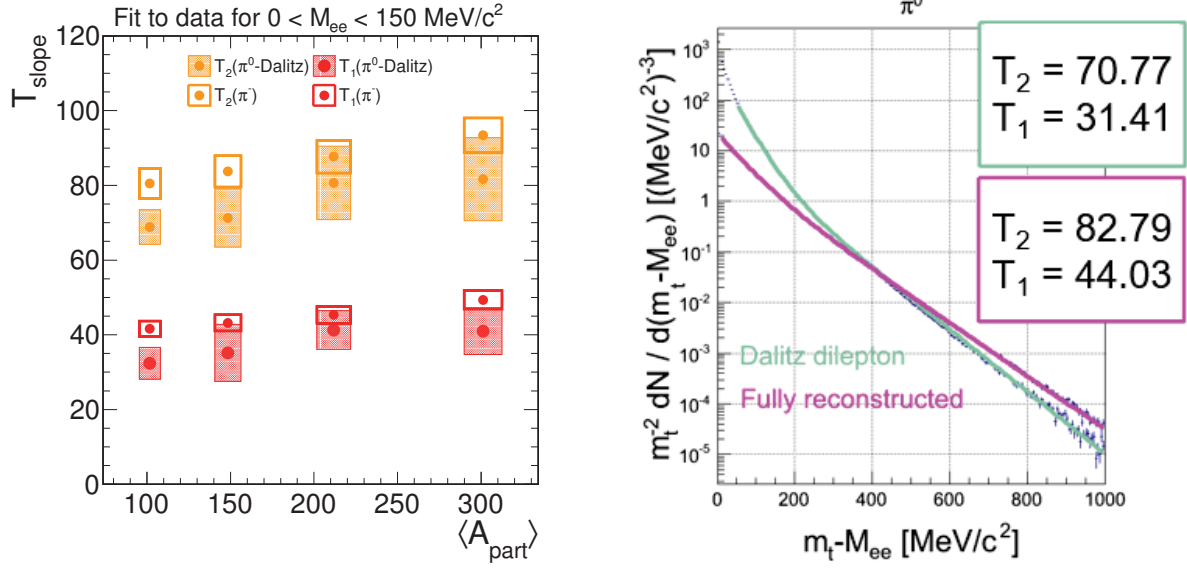
Figure 7.10.: Left: inverse slope parameters of two exponential components fitted to the transverse mass of dileptons in the invariant mass range of $0 < M_{ee} < 0.15\,\mathrm{GeV}/c^2$, compared to π^-. Right: simulated spectra of transverse mass of π^0 (magenta) and dileptons from its Dalitz decay (green) together with two exponent fit to both spectra and extracted inverse slope parameters.
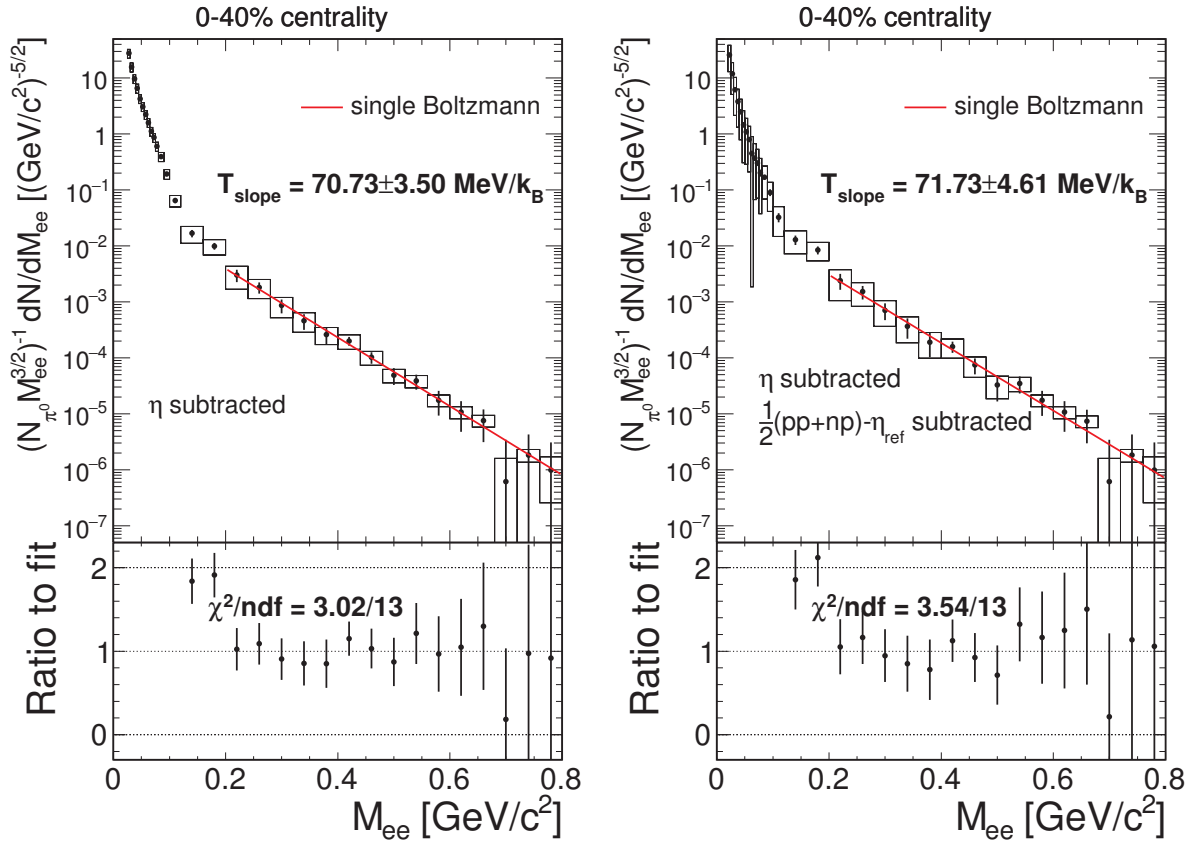
Figure 7.11.: Excess dilepton yield extracted by subtracting η contribution (left) and η as well as NN reference (right).

7.6 Comparison to previous HADES measurements

It is possible to interpret data in model-independent way by putting them in broader context of system size and collision energy dependence. The first of the two can be investigated thanks to data samples collected by HADES over years in different runs. In Fig. 7.12 ratios of dilepton yields obtained in different experiments to the NN reference are shown. All samples have their respective η contributions subtracted and they are normalized to the π^0 multiplicities. Compared in this way, C+C spectra at two beam kinetic energies [30, 37] are equivalent to the reference within errors. This means, that there are no "medium effects" that would enhance virtual photon radiation compared to the the sources at freeze-out. This also means that normalization to pions removes energy dependence – at least as long as their multiplicity is also not affected by the medium.

Situation changes in case of Ar+KCl at E_{beam} = 1.76A GeV. Here strong enhancement over the reference, of around factor 3, is visible above the π^0 mass. The enhancement is even stronger in Au+Au collisions (though only at very low invariant mass values), which can be interpreted as a confirmation of the previously observed "resonance-clock" of the fireball, i.e. the possibility to extract the lifetime of the fireball from the strength of the in-medium ρ^0 radiation. It is also noticeable from the figure, that the radiation in Au+Au is stronger than in other experiments in the region below the π^0 mass. This can be compared to Figs. 7.14 and 7.15, where the radiation due to coupling with baryons has a significant contribution in the π^0-Dalitz region. In fact, the V-like shape of the Au+Au-to-reference ratio in this region is also consistent with theoretical picture developed above, since the "baryonic" contribution relative to π^0 is smallest at mass around 0.06 GeV/c^2.

The Au+Au measurement can also contribute to the systematic study of the collision energy dependence of the excess yield. The left panel of Fig. 7.13 shows the excess over η yield, integrated in the range of $0.15 - 0.5$ GeV/c^2, as well as yields of π^0 and η. They are normalized to the average number of participants A_{part} in order to cancel different centrality selection in different experiments and of trivial system size dependence. The same energy dependence of the excess was observed in C+C (black) and Ar+KCl/Ca+Ca (blue, the two systems are considered as equivalent from the point of view of size and isospin), measured by HADES (full triangles [30, 37, 38]) and DLS (open triangles [31]). It is also nearly the same as energy dependence of π^0 production, which justifies normalization of dilepton spectra to pion multiplicity. Solid lines through the π^0 and η points are second-order polynomial fits. When they are scaled down to go through baryonic radiation points, they indicate non-linear scaling of the latter with $\langle A_{\text{part}} \rangle$ (the lines do not overlap). When it is taken into account, Au+Au may follow the energy dependence established by lighter systems, but this would need to be confirmed by another Au+Au measurement in similar energy range ($1 - 2A$ GeV).

The extensive study of system size dependence is shown in the right panel of Fig. 7.13. The integral of the excess yield is shown for two integration ranges: $0.15 < M_{ee} < 0.5$ GeV/c^2 (blue) and $0.13 < M_{ee} < 0.7$ GeV/c^2 (red). Squares are four centrality bins of Au+Au, stars are Ar+KCl at E_{beam} = 1.76A GeV and triangles are C+C at E_{beam} = 2A GeV. The latter two were scaled to E_{beam} = 1.23A GeV using energy dependence of π^0 production for the lower integration range and of η for the higher range, as in the left panel of the figure. This means, that in the lower range the Ar+KCl yield was multiplied by 0.62 and C+C by 0.53. In the higher range the corresponding factors were 0.46 and 0.38, respectively. This choice was driven by the observation, that the lower part of the integration range brings a dominant contribution to the integrated yield, due to the exponential shape of the spectra, see Fig. 7.11. Secondly, the energy dependence of the dilepton production at given invariant mass was expected to be similar to meson production at this mass. The two spectra were corrected for acceptance in analogous way as it was discussed for Au+Au, using the cocktail consisting of π^0, η and ω with acceptance matrices for single leptons from corresponding experiments.[2]

---

[2] The same as made public for theory: `https://hades-wiki.gsi.de/foswiki/bin/view/Public/` `HadesDataFilterAADileptons` (accessed December 14th, 2016)
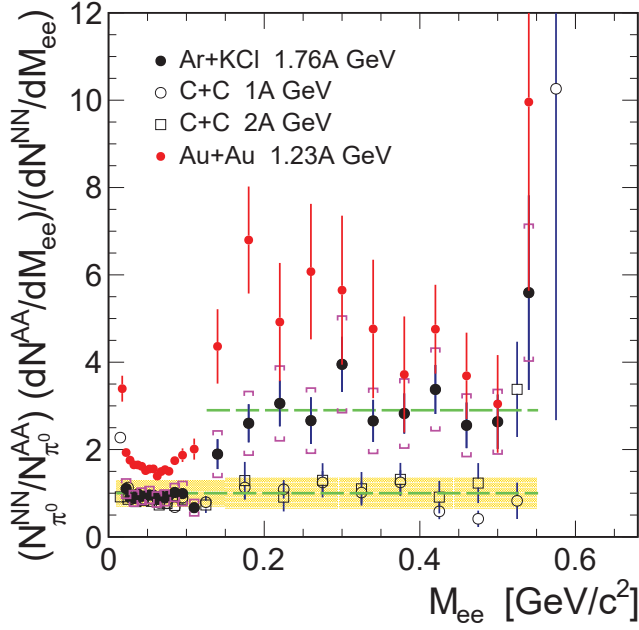
Figure 7.12: Ratio of the invariant mass yield in Au+Au, Ar+KCl and C+C to the reference. Respective η contributions are subtracted from all spectra.
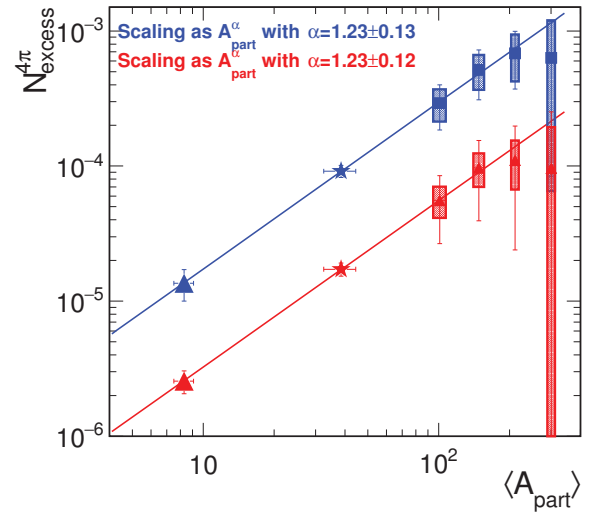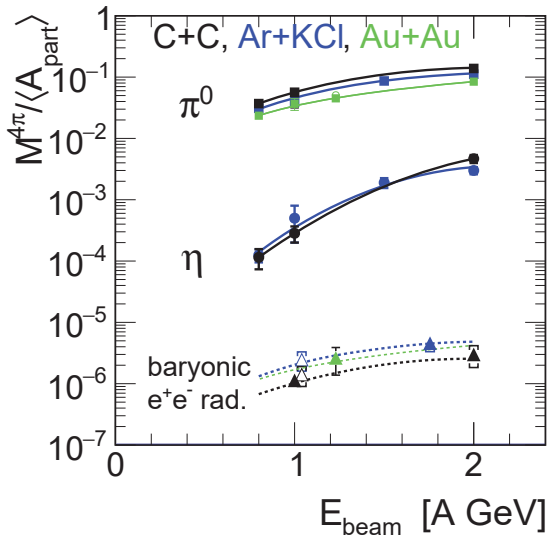
Figure 7.13.: Left: energy dependence of inclusive multiplicity per participant for dilepton excess over η-Dalitz (extrapolated to 4π) as well as π^0 and η. For the excess, full triangles are HADES measurements [30, 37, 38], open triangles – DLS [31]. π^0 and η were measured with photon calorimetry by TAPS collaboration in C+C (black) [39] and Ca+Ca (blue, equivalent to Ar+KCl) collisions [40]. Measurements of π^0 in Au+Au collisions are from HADES [41], TAPS at 0.8 and $1A$ GeV and E895 $2A$ GeV [42]. **Right:** participant number dependence of the same excess for four Au+Au centrality classes (squares) Ar+KCl (stars) and C+C at $E_{\text{beam}} = 2A$ GeV, properly scaled to $E_{\text{beam}} = 1.23A$ GeV/c^2. Blue points are integrated in $0.15 < M_{ee} < 0.5$ GeV, the red ones in $0.3 < M_{ee} < 0.7$ GeV/c^2. The power law fits to C+C, Ar+KCl and two peripheral Au+Au bins are shown and the exponents are printed.

The two central event classes of Au+Au are not reliable in the current analysis due to low efficiency of the RICH. The two remaining confirm the power law scaling of the excess yield, as in [38], shrinking at the same time the fit error. The result is $N_{\text{excess}}^{4\pi} \propto A_{\text{part}}^{\alpha}$ with $\alpha = 1.23$ for both integration ranges.

7.7 Comparison to theoretical models

Further understanding of the *excess* yield may come from the comparison to model calculations. One is the thermal emission based on the ρ^0 spectral function, with thermal parameters obtained from coarse-grained space-time cells of fireball simulated with UrQMD [89]. Freeze-out components discussed above are also added. As it can be seen in Fig. 7.14 (left panel) such a cocktail describes mass spectrum very
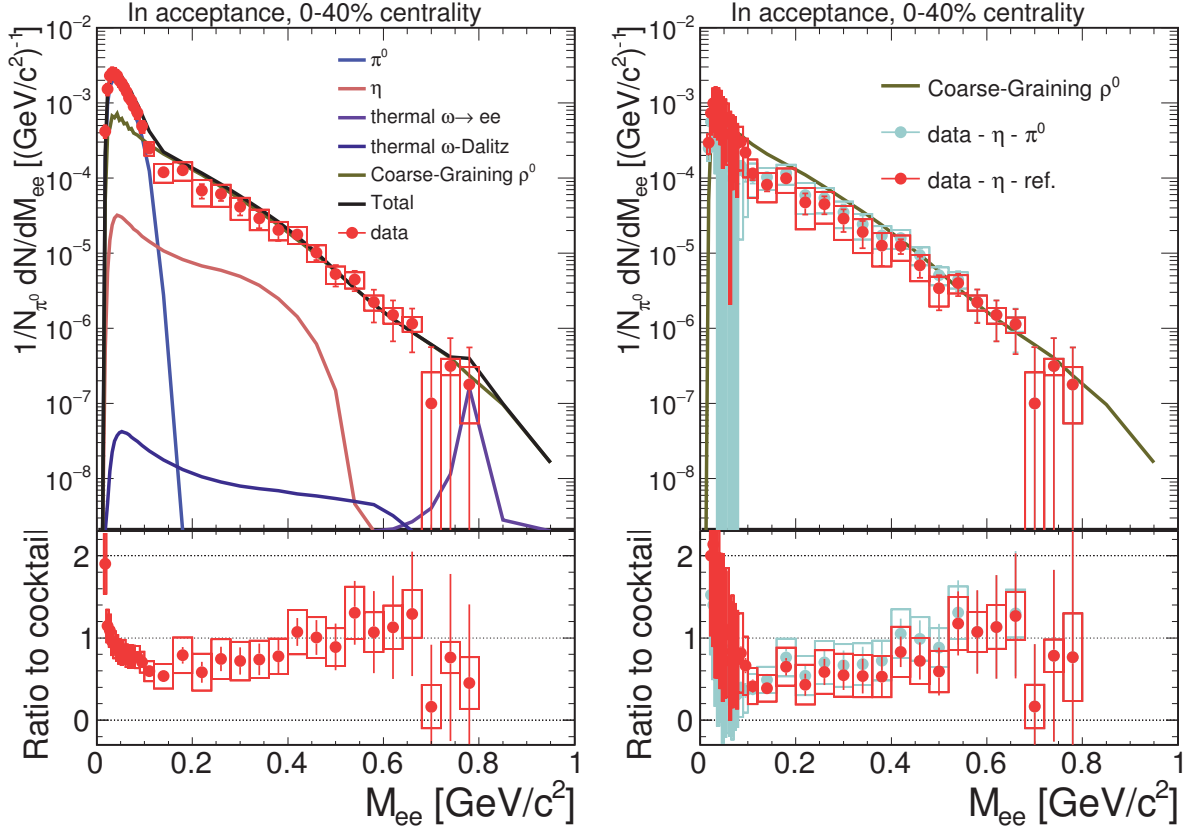
Figure 7.14.: Left panel: invariant mass distributions from 40% most central Au+Au events at $E_{\text{beam}} = 1.23A$ GeV and a cocktail comprising in-medium ρ^0 from the coarse-graining approach and freeze-out contributions from π^0, η and ω. Right panel: data points after subtracting the reference of elementary nucleon collisions (red) or main cocktail components π^0 and η (green), compared to the in-medium ρ^0 radiation only.

well in the invariant mass range above 0.4 GeV/c^2 and there is some discrepancy for lower masses. One can also attempt to extract medium radiation by subtracting the reference from the experimental spectrum (both properly normalized and after removing η contribution, as discussed above) and by comparing it with the thermal ρ^0 radiation only. This is shown in the right panel of Fig. 7.14. They still agree within experimental uncertainties, at least above 0.2 GeV/c^2. However, there is a systematic shift with respect to the left panel of the figure. A possible interpretation of this fact will be addressed later on.

Before that, one may take a look at another calculation, Hadron String Dynamics (HSD) transport model [113]. The results of the calculation are compared with the data points in Fig. 7.15. Compared to the cocktail including coarse-grained calculation of the spectral function, HSD describes data somewhat better below 0.4 GeV/c^2 invariant mass, while above there is a clear discrepancy, which gets reduced after inclusion of the ρ^0 dropping mass and broadening effects. Note, that the HSD spectra are normalized to the average number of π^0 per event obtained in the simulation, i.e. 11.2, while the experimentally measured spectra are normalized to 8.65 resulting from charged pion analysis. Note also an important
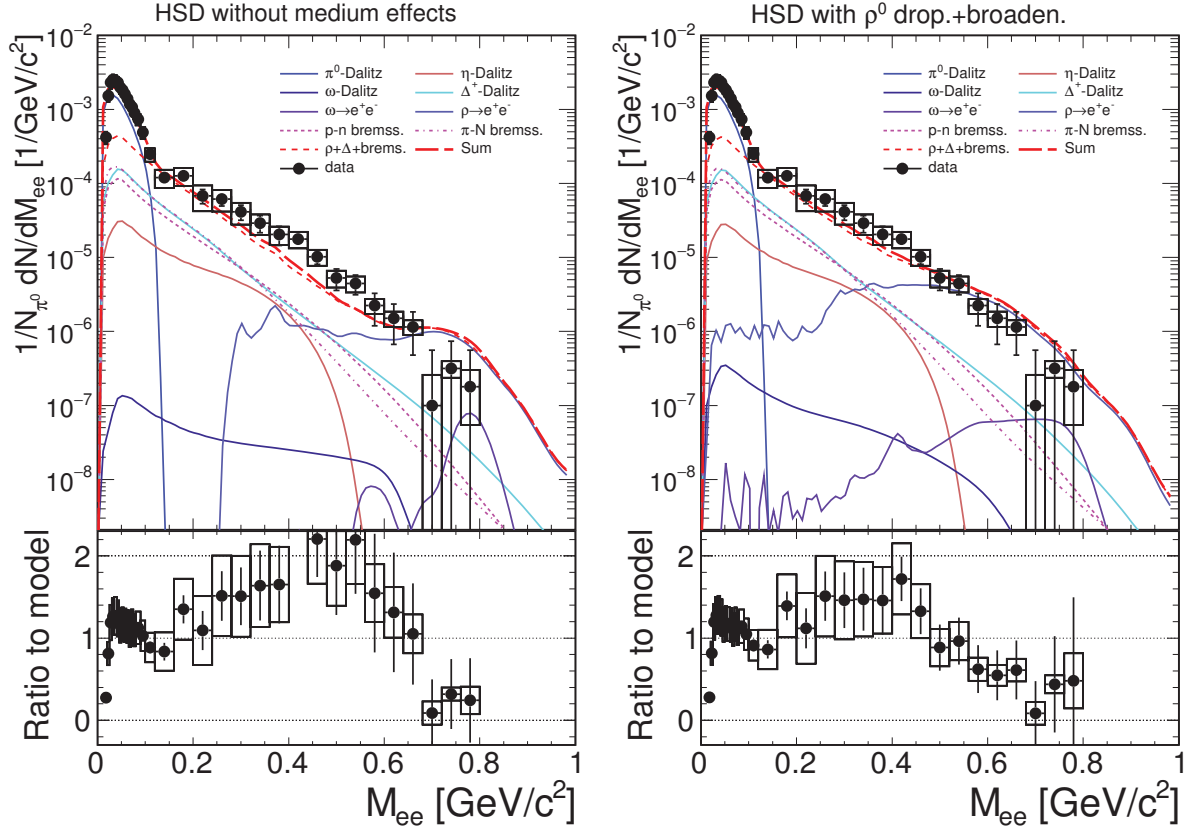
Figure 7.15.: Invariant mass distributions of 40% most central Au+Au events at $E_{\mathrm{beam}} = 1.23A$ GeV compared to the result of the HSD calculation without including medium effects on the ρ^0 (left panel) and with dropping mass and collisional broadening included (right panel).

role of the Δ regeneration in course of the heavy-ion collision in HSD [113], where up to 8 generations of Δ are needed to saturate the dilepton yield. No higher lying resonances are included, although the work of [123] implies strong ρ^0 coupling to such resonances.

Considering the two types of calculations together, one can notice, that in HSD both bremsstrahlung contributions and Δ^+-Dalitz have at low masses the spectral shape not very different from the in-medium radiation from the coarse-graining approach. In contrast, even medium-modified ρ^0 in HSD does not contribute significantly to the low mass range. However, the vector meson spectral function in the coarse-graining is calculated within the strict Vector Meson Dominance model. This assumes, that actually all dileptons are mediated through vector mesons which are interpolating fields between hadrons and virtual photons having the same quantum numbers and non-vanishing mass (due to virtuality). Therefore the ρ^0 spectrum in the coarse-graining approach saturates the dileptons radiation from the medium (there might be also contributions from other vector mesons, ω and ϕ, treated in the same way) and sums all sources coherently.

The spectral function contains not only the dilepton radiation from the medium, but also Δ and bremsstrahlung contribution, which is present to some extent in the reference spectra. Therefore one could question comparing experimentally extracted excess just with the medium ρ^0 spectrum, as in the right panel of Fig. 7.14. The ratio of the data to model after subtracting the η contribution and the reference minus its respective η (red points in the right panel of Fig. 7.14) deviates from unity stronger than the ratio after subtracting only the η from Au+Au data (green points) and also stronger than the ratio of the full experimental spectrum to the full cocktail (left panel). Desirable would be to calculate the spectral function in vacuum and check, whether it can be subtracted from the result of in-medium calculation. On the other hand, the in-medium radiation is emitted after fireball cells are thermalized

and its largest contribution comes from about 10-20 fm/c (see Fig. 7.18), thus first-chance collisions should not be included in it.

At the same time, substantial deviation is present already before any subtraction (left panel) and remains after subtraction only η from Au+Au. This suggests, that the thermodynamic parameters extracted from UrQMD differ from the real ones or that the in-medium radiation is overestimated in the coarse-grained calculation of spectral function itself and it could be further scrutinized.

In Fig. 7.16 transverse mass distributions for the invariant mass $0 < M_{ee} < 150$ MeV/c^2 are shown in four centrality bins, compared to HSD calculations and a hadronic freeze-out cocktail together with in-medium radiation according to ρ^0 spectral function calculated in the coarse-graining approach when available. The agreement between data and models is fairly good.

Similar comparisons can be done in higher invariant mass range $0.15 < M_{ee} < 0.55$ GeV/c^2, as seen in Fig. 7.17. There is in fact a very good agreement between shapes of the spectra from the two models and consequently they both describe the data as far as it can be judged from the limited statistics. Exponential function cannot be fitted to the spectra – their spectra are modified in a way typical for the radial flow, i.e. they get concave (compare e.g. to Fig. 7 in [86]). Still, good agreement between data and the model based on the coarse graining allows to infer thermal properties of the radiating source from the model. Fig. 7.18 shows a few of them. It turns out that the highest dilepton emission rate occurs in time range of 10-20 fm/c. During this period transverse velocity β_T, which is the measure of the radial fireball expansion, accelerates from about 5 to 30% of the speed of light. This is also when highest temperatures (above 70 MeV/k_B) and densities (as large as triple normal nuclear matter density) are reached. If this is the case, dilepton spectra should be sensitive to drop of the quark condensate and partial restoration of the chiral symmetry.
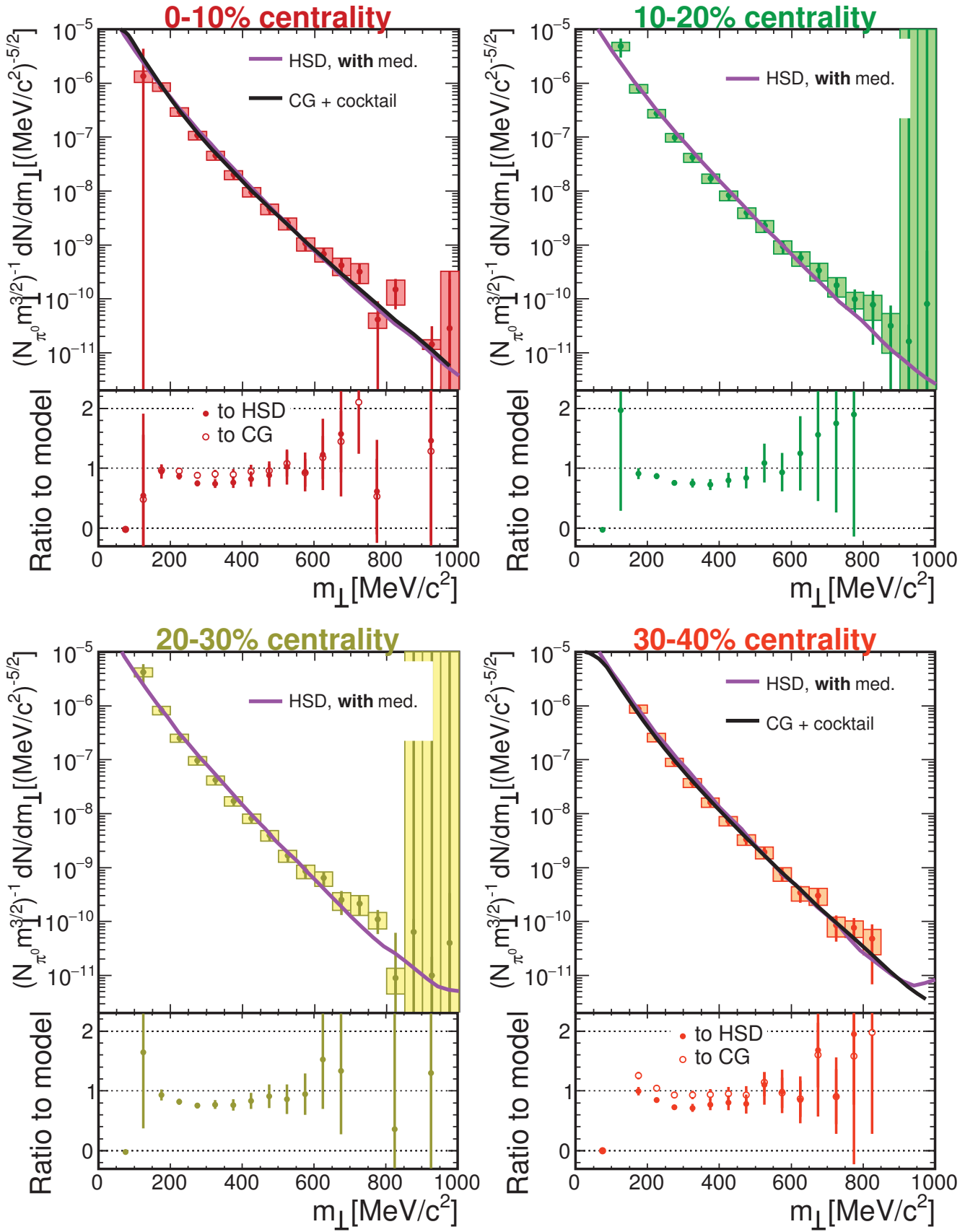
Figure 7.16.: Dilepton transverse mass spectra in four centrality bins for the invariant mass $0 < M_{ee} < 0.15 \, \text{GeV}/c^2$ compared to HSD transport model and a hadronic cocktail combined with coarse-graining calculation. Models are normalized to the same value as data at 500 MeV/c^2.
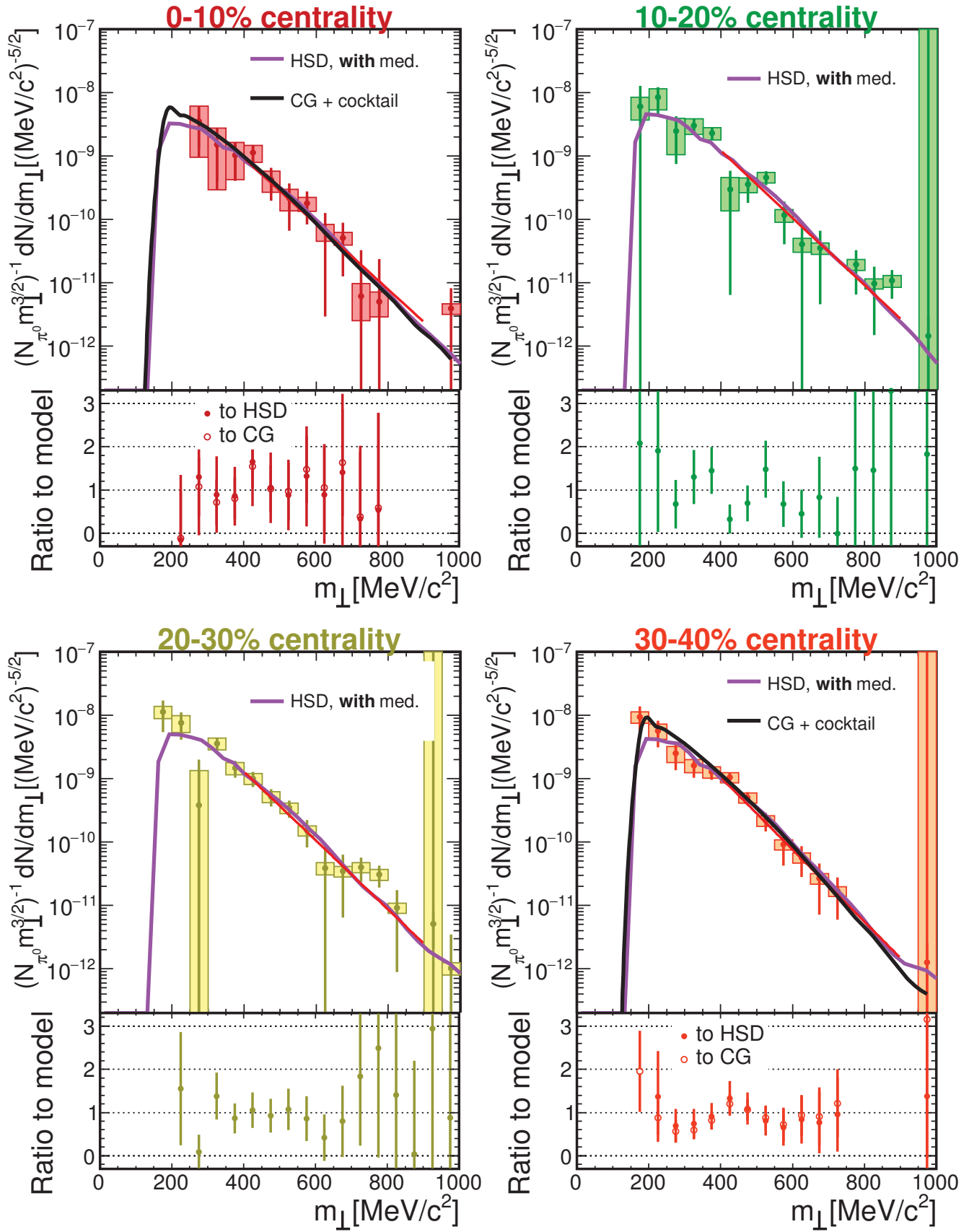
Figure 7.17.: Dilepton transverse mass spectra in four centrality bins for the invariant mass $150 < M_{ee} < 550\,\mathrm{MeV}/c^2$ compared to HSD transport model and a hadronic cocktail combined with coarse-graining calculation. Models are normalized to the same value as data at 500 MeV/c^2.
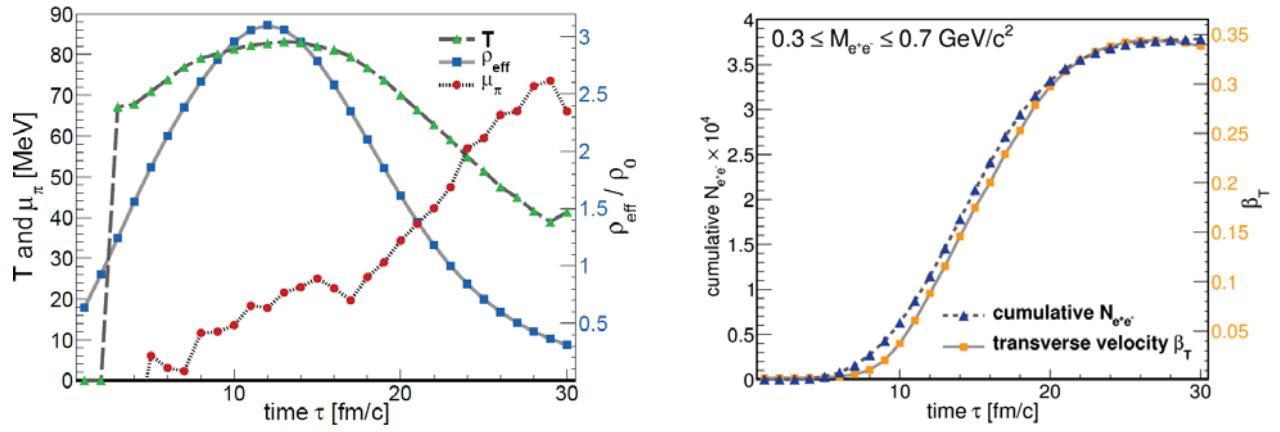
Figure 7.18.: Left: time evolution of thermodynamic properties of 7×7×7 central 1 fm³ cells of the fireball from the coarse graining. Right: time evolution of the cumulative dilepton yield in the range of $0.3 < M_{ee} < 0.7$ GeV/c^2 and of the transverse velocity.

7.8 Conclusions and outlook

The goal of this work was to reconstruct dilepton spectra in Au+Au collisions at $E_{\mathrm{beam}} = 1.23A$ GeV by means of the data analysis based entirely on RICH ring reconstruction algorithms inherited from previous HADES runs. In the course of the analysis the mathematical formalism behind combinatorial background subtraction has been understood in great detail and this has lead to the introduction of the k-factor calculated with the event mixing technique. The analysis faced large difficulties due to low efficiency of the ring reconstruction algorithms, that decreased the signal-to-background ratio. Despite that, it was possible to extract thermal dilepton radiation from hot and dense fireball. It was compared to model calculations and relatively good agreement allowed to draw certain model-dependent conclusions about the properties of nuclear matter under the conditions achieved in the energy regime under study. The quantitative results of the models can now be regarded as reflecting the reality – at least approximately. Model-independent Boltzmann fits, especially to the invariant mass spectrum, allow to extract the true temperature of the dilepton emitting source.

Even if the formalism of the two considered models, HSD and CG, is different, the qualitative physical picture that emerges to an experimenter is consistent. HSD is the transport calculation that predicts emission of dileptons in medium from Dalitz decay of Δ (regenerated appropriate number of times) and nucleon-nucleon and pion-nucleon bremsstrahlung together with the decays of thermally produced ρ^0 and adds them incoherently, on the level of probabilities. Coarse-grained calculation of the spectral function assumes strict vector meson dominance i.e. all virtual photons are mediated by ρ^0 and its spectra are modified by self-energy terms, that account essentially for the same elementary processes. Their contributions are added coherently, on the level of amplitudes. The difference between the two models is smaller than the statistical and systematic uncertainty of experimental data, this does not allow to discriminate between them, but further studies are ongoing. Also, while HSD tends to increase appropriately the abundance of Δ and CG takes higher lying resonances into account, experimental data seem to be not sensitive to which resonant state is really excited. The fact, that the spectrum has exponential shape signals thermal system. In the end, dilepton emission is enhanced due to various types of interactions between hadrons, that occur more often due to high density. The density in turn translates to change in the order parameter of chiral symmetry breaking. If it results in distinctive phase properties of the matter, it has to (and will) be further studied using observables that are yet to be proposed.

On the dilepton side, there is a number of topics that can be studied in the future. It would probably be appreciable, that this is done using the novel backtracking algorithm (BT), which provides higher reconstruction efficiency and thus signal-to-background ratio. Of course, the analysis with ring finder can also be carried out in parallel in order to validate, that higher *precision* BT analysis has also at least the same *accuracy* as ring finder. Possible future analysis could involve

1. Angular distributions, especially dilepton polar anisotropy in the center-of-mass frame and possibly also in the helicity frame. This could be a further test for theoretical models and may provide additional information on the nature of the emitting source.

2. Radial flow based on experimental data. In the current analysis it was only possible to compare the shape of transverse mass, modified by the expansion velocity, in a broad invariant mass range and after verifying the agreement, to extract the $\langle \beta_{\mathrm{T}} \rangle$ from the model. With higher statistics it should also be possible to plot m_t spectra in narrow invariant mass bins. The inverse slope should then behave like according to Eq. 7.1. By fitting to the M_{ee} dependence of the slope it should be possible to extract $\langle \beta_{\mathrm{T}} \rangle$ and confront it with models.

3. Dilepton elliptic flow coefficient v_2. It develops in the early stage of the collision and dileptons are ideal probes as they leave the fireball without reinteractions.

4. Systematic uncertainty of the combinatorial background, calculated by comparing the true background (wrong opposite-sign pairs) with its like-sign estimation, has now precision limited by the

statistics of the simulation used in the calculation. It would be impractical to simulate on present computing facilities significantly more than 10^8 UrQMD events which are currently available (disk space, computing time). One can consider using an event generator to simulate events containing only a certain number of dileptons, but it is not clear, how realistic such a model would be.

5. A more extensive study of the dependence of the transverse mass/momentum slope of dileptons from Dalitz decays on the thermal distribution of the mother particle would be interesting. This can be done by simulating Dalitz decays of π^0 or other particles decaying into Dalitz channel with different source temperatures or by finding an analytic expression.

6. Last but not least: Estimation of the upper limit for u boson/dark photon needs to be finalized. For this, finely binned invariant mass distribution of dileptons serves as an input.

Further experiments are planned in HADES, in which investigation of thermal dilepton radiation and phase structure of strongly interacting matter will play a major role. The spectrometer will be upgraded by replacing Pre-Shower with an lead glass electromagnetic calorimeter (ECAL). It will not only allow to directly detect real photons but also should have electron to pion separation power as good as it was designed for Pre-Shower. In April 2012 Au+Au beam it was hardly possible (due to aging) to maintain Pre-Shower at high voltage values at which it operates in the streamer mode needed for lepton identification. Therefore installation of the ECAL will in fact be an improvement. The other significant upgrade will be of the RICH detector. Photon detection plane based on the MWPC will be replaced by an array of photomultipliers. This is expected to increase lepton identification efficiency.

After that, Ag+Ag at E_{beam} = 1.65A GeV is going to be measured still at SIS18 accelerator (*FAIR phase 0*). As it can be presumed interpolating between coarse-graining calculations for Au+Au and Ar+KCl runs, the density should not be much lower than in the former and the temperature not much lower than in the latter. This means the most extreme combination of the two thermodynamic parameters studied up to now with HADES. The aim here is to reconstruct ω and ϕ peaks and to access intermediate-mass dileptons. Furthermore, ρ^0 and a_1 spectral functions will be measured in pion- and proton-induced reactions to address their behavior in cold nuclear matter. At future SIS100 accelerator Ag+Ag at E_{beam} = 3.5A GeV experiment is planned and it may be able to thoroughly explore the most interesting region of the phase diagram with new exotic phases. The currently developed CBM (Compressed Baryonic Matter) experiment at FAIR will then study possible first-order phase transition(s) with high-precision data from Au+Au collisionns and may have a chance to hit the critical point, if it exists.

Yet many interesting phenomena are still to be explored with HADES and still at SIS18 and even still with already existing data!

Appendices

A Tuning Pre-Shower parameters

In this appendix procedures of calibrating gain of the Pre-Shower detector in HADES and of tuning its digitization parameters are described. The calibration is needed to optimize lepton identification, The correct digitization is necessary for accurate efficiency correction based on Monte Carlo simulation.

A.1 Gain calibration

Calibration of Pre-Shower consists of two parts. One is calibration of the front-end electronics response to charge induced on pads of planar read-out electrode. This part is done by registering ADC response of each read-out channel when a well defined charge is injected into it, and when there is no input charge, only noise. This is done many times for every channel (in practice the charge is injected alternately into odd and even columns) in order to collect statistics sufficient for fitting a straight response line. Parameters of the line (slope and offset) are stored in the database for every channel. This allows to cut out the noise and equalize the response of different front-end modules. The procedure can be performed before, after and during breaks in data taking. It was done during all previous beam-times. Part of my master thesis [124] project was to adapt the software that calculates these calibration parameters to the new version of HYDRA framework, developed for the Au+Au beam.

Already the charge induced when a particle with specific properties passes through the detector can depend on the location in the chamber due to different gas or geometry conditions. This has to be taken into account if unitary particle identification condition is going to be used for the whole detector area. A placeholder for an additional, multiplicative calibration parameter that would level out such details was foreseen in the database from the very beginning. It has, however, never been used in the experiments before Au+Au, because resulting smearing of ΔQ (see Eq. 2.3), averaged over the whole detector, was not a crucial problem in lepton identification.

As described in Section 2.4.3, a Pre-Shower hit object contains information about charges integrated over corresponding 3×3 pads areas in the three chambers, while in the Pre chamber maximum charge is located in the central pad. In order to calculated the gain parameter, histograms of charge integrals Q_{Pre}, $Q_{\mathrm{Post\,I}}$, $Q_{\mathrm{Post\,II}}$ are made for every pad from hits centered at this pad and in addition global histograms are made for the whole detector. They are fitted with Landau's distribution. Examples are shown in Fig. A.1.
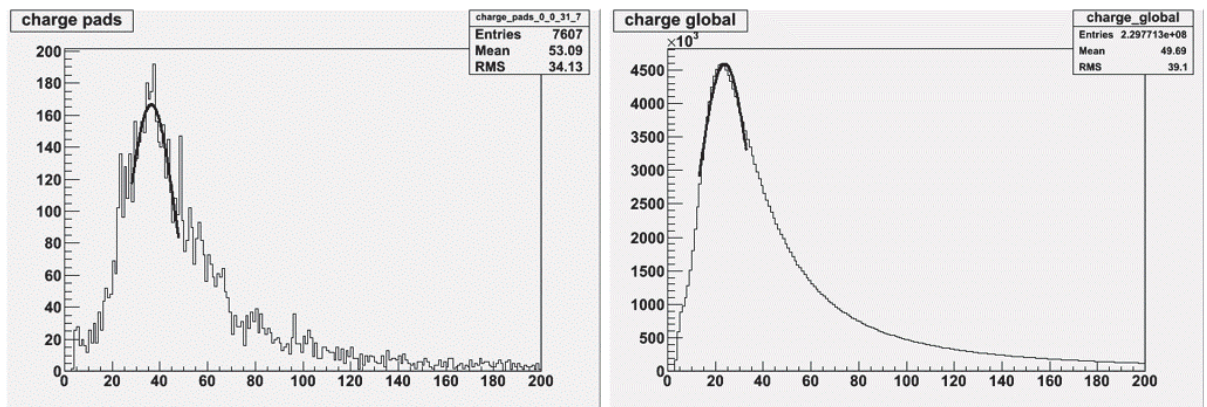
Figure A.1.: Distributions of Q_{Pre} for hits centered at one single pad (left) and for all the hits in Pre-Shower detector (right) together with Landau's fits.

The gain factor is then a ratio of the Most Probable Values (MPV) from fit to the global histogram to the one from a single pad:

$$\text{gain(pad)} = \frac{MPV(\text{global})}{MPV(\text{pad})}.$$

Figs. A.2 and A.3 show the effect of using the additional calibration parameter. Left panels of both
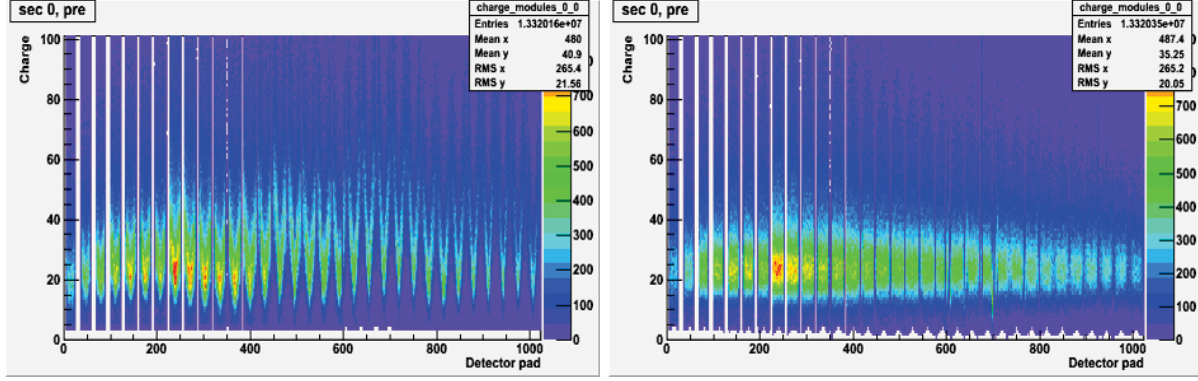
Figure A.2.: Distributions of Q_{Pre} for hits centered at one single pad (left) and for all the hits in Pre-Shower detector (right) together with Landau's fits.
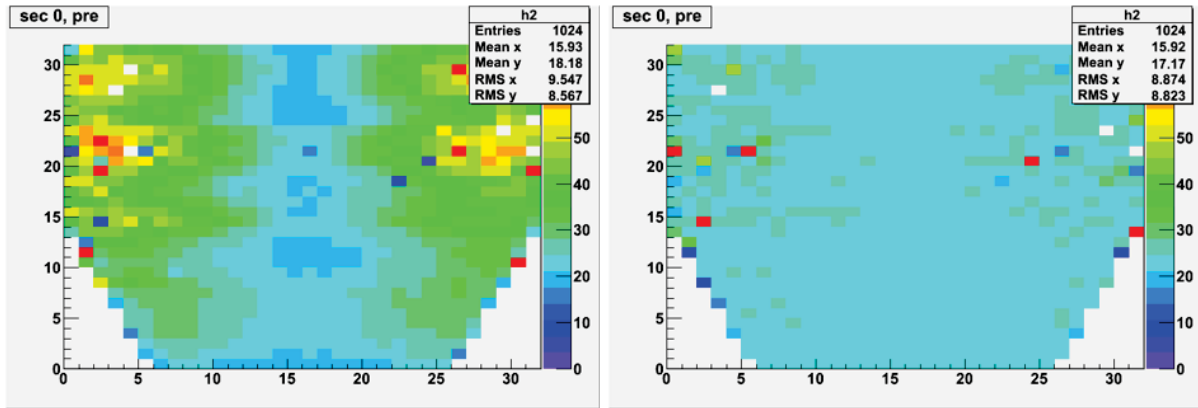
Figure A.3.: Distributions of Q_{Pre} for hits centered at one single pad (left) and for all the hits in Pre-Shower detector (right) together with Landau's fits.

figures present data with gain = 1, right panels with values calculated as above. Fig. A.2 shows Q_{Pre} distributions for all the pads in one sector, grupped by rows (gaps are between rows with less than 32 pads). Fig. A.3 shows average Q_{Pre} for every pad arranged in the way as in the real detector chamber. The calibrated gain levels out charges from different pads and makes the average distribution narrower, which results in better possibility to optimize the hard cut on $\Delta Q(p)$ (Section 3.5) as well as in better performance of the neural network with ΔQ as one of input observables.

The same gain calibration was performed (under my supervision) by A.Snoch, participant of HGS-HIRe Summer Student Program at GSI 2015 for the pion beam campaign of June-August 2014 [125]. The opportunity to revisit the procedure and its principles revealed the potential for its further optimization. It might be, that the trend of uncalibrated charge as a function of column within a single row originates mainly from the incident angle of a particle on the detector plane, which is close to right angle in the middle and smaller on the sides of each sector, due to geometry. This would be the result of longer path of particles (the primary one and secondary conversion electrons) through gas chambers and larger ionization. In this case Eq. 2.3 would need to be modified to take the angle into account and the gain parameter would involve only pure detector effects. In addition, the incident angle on the META

wall would allow to improve the track-hit matching, especially for timing detectors, but it is not yet implemented in DST.

A.2 Digitization parameters

An important step in Monte Carlo simulation of a detector system is *digitization*, generation of possibly realistic detector responses for given simulated particles. They corresponds to values measured in real experiment and to detection probability of a real detector. If models used to generate such responses are not sufficiently accurate, the statements based on Monte Carlo, especially spectra and quantities corrected for efficiency, cannot be considered as physically meaningful. In the case of Pre-Shower, digitization is based on efficiency values and charge distributions measured in experiment. More specifically, Q_{Pre}, $Q_{\text{Post I}}$ and $Q_{\text{Post I}}$ vs. particle's velocity β distributions are stored, following the assumption, that this dependence is the strongest one. Similarly, the detection efficiency is assumed to depend on the velocity. It also changes from pad to pad of the detector. It is not possible. Even the statistics from the whole experimental run is too small to calculate the efficiency as a function of velocity for each individual pad. Therefore an average distribution of Eff(β) for the whole detector was computed and also for all the pads average values, independent of velocity or any other particle's property. They were compared with the overall value for the whole detector in order to obtain a pad-dependent scaling factor, by which Eff(β) is to be multiplied.
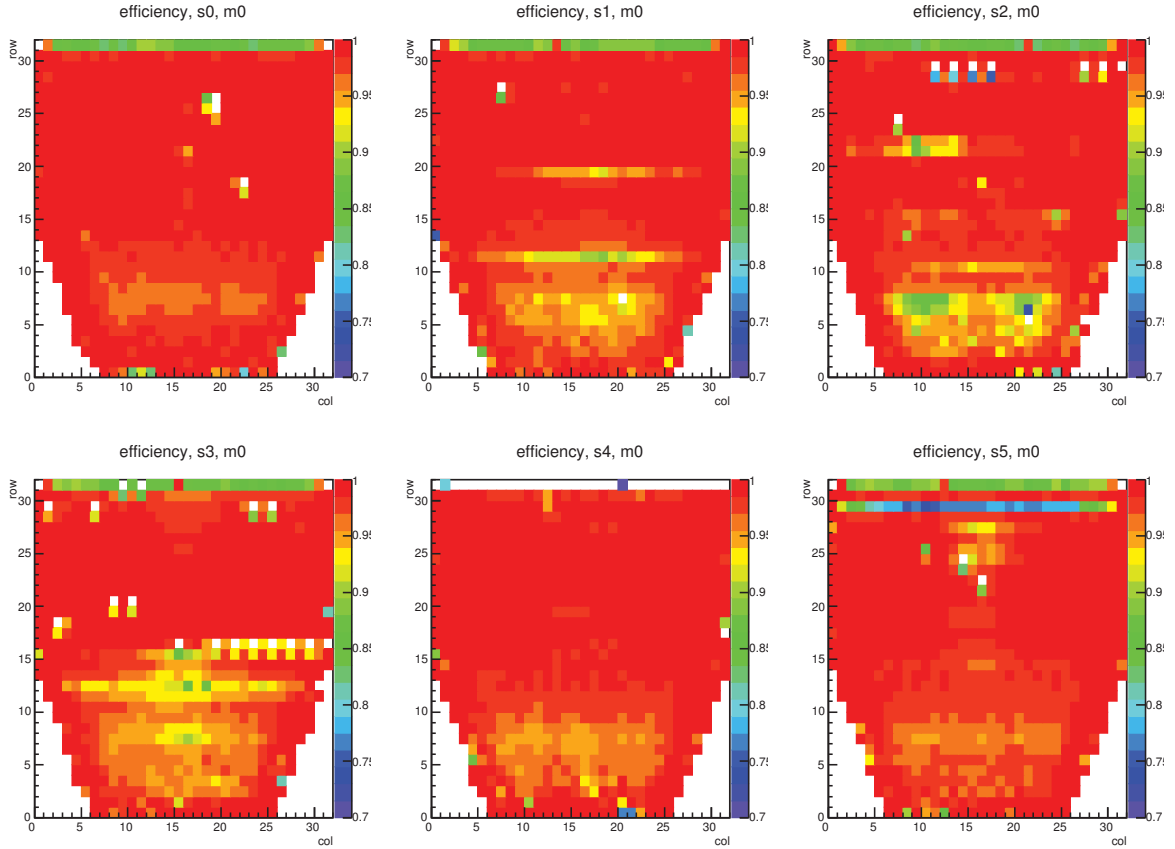
Figure A.4.: Efficiency of the Pre chamber as a function of detector pad.

Efficiency was calculated in the simplest possible way. For the Post I module, as reference detectors served Pre and Post II chambers. Therefore efficiency is the ratio:

$$\text{Eff(Post I)} = \frac{N(Q_{\text{Pre}} > 0 \wedge Q_{\text{Post I}} > 0 \wedge Q_{\text{Post II}} > 0)}{N(Q_{\text{Pre}} > 0 \wedge Q_{\text{Post II}} > 0)}.$$
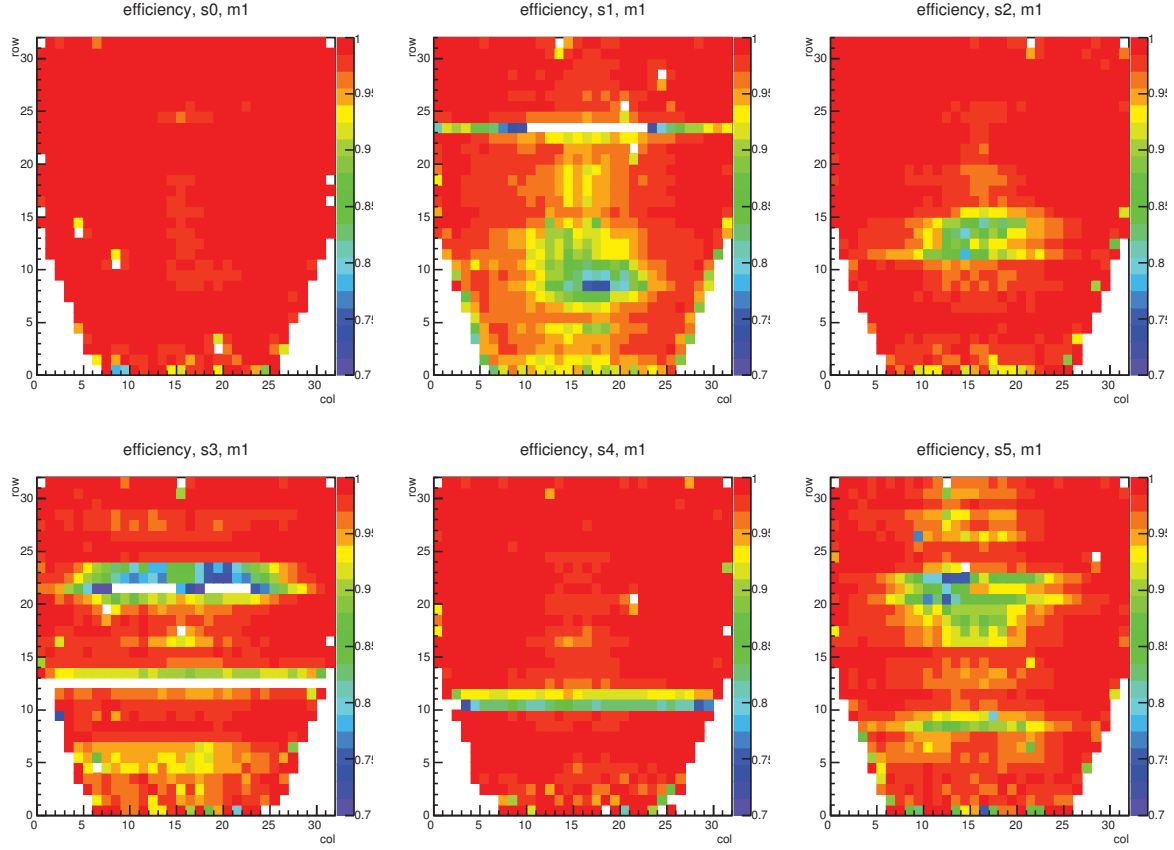
Figure A.5.: Efficiency of the Post II chamber as a function of detector pad.

There is no other detector behind the Post II chamber that could be used as a reference, so the best what could be assumed was that its efficiency is identical as the one of Post I. For Pre the whole tracking system can serve as a reference detector, second one being the Post I chamber. The efficiency can be expressed as follows:

$$\text{Eff(Pre)} = \frac{N(\text{Track exists} \wedge Q_{\text{Pre}} > 0 \wedge Q_{\text{Post I}} > 0)}{N(\text{Track exists} \wedge Q_{\text{Post I}} > 0)}.$$

The efficiency values as a function of detector pad of the Pre and Post I chambers are shown in Figs. A.4 and A.5 for the situation that corresponds to parameters stored in the database.

Pre-Shower is only used to support lepton identification and as lepton candidates only the tracks are considered with $\beta > 0.9$. Therefore it is only crucial, that charge and efficiency values for high velocity tracks come directly from measurement. Below a specified value one can interpolate. It is not possible, to use measured values for all velocities, since at some point statistics becomes too low. In the final version stored in the database the global efficiency for $\beta < 0.6$ was taken the same as for $\beta = 0.6$. The charge distributions above roughly $\beta = 0.85$ were fitted with Laundau's distributions. The fit parameters were extrapolated up to $\beta = 0$ using an exponential fit to histograms of parameters as a function of velocity. Based on the Landau's distributions with extrapolated parameters, charge vs. velocity histogram was generated in the extrapolation region. An example of extrapolated charge vs. β distribution and global efficiency as a function of β are shown in Fig. A.6.

The test of charge digitization is ΔQ vs. momentum distribution, shown in Fig. A.7 for experimental data (left) and Monte Carlo (right), for all particles after track sorting. This choice allows to select sample with significant leptons contribution and especially of particles with $\beta > 0.9$. On the other hand, it does not bring the bias on the distribution due to usage of ΔQ and p in particle identification. The central part of the two plots, where well reconstructed electrons are dominating, shows very similar trend in
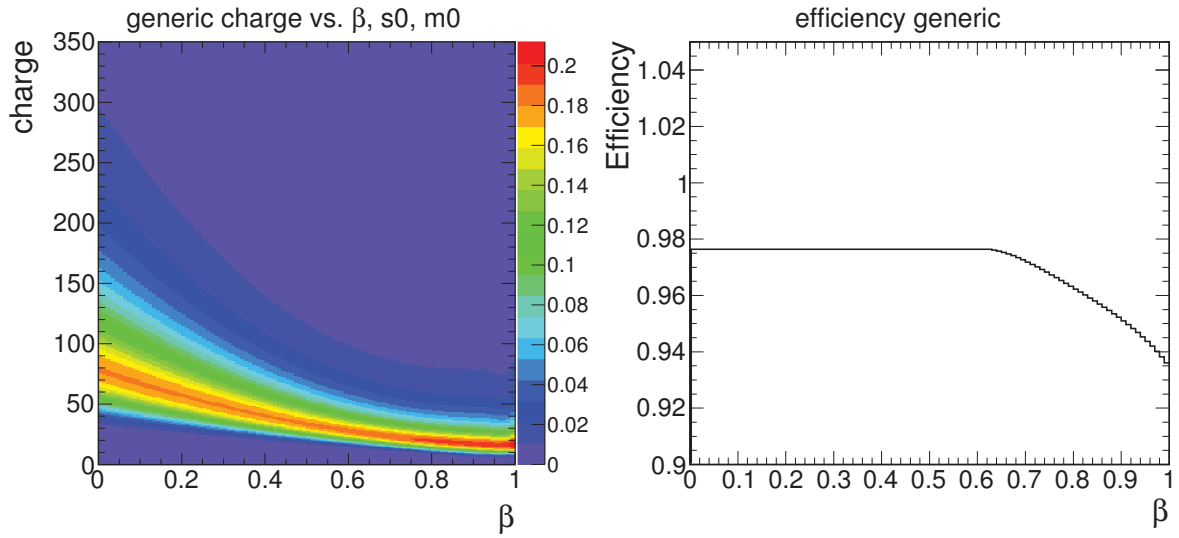
Figure A.6.: Left: xtrapolated charge vs. particle's velocity for sector 0, module Pre. Right: global efficiency as a function of velocity.

both cases. In other parts distributions are rather different. This is not due to wrong performance of digitizer, but rather due to larger amount of hadron-like background tracks in experiment.

Test of the digitizer efficiency as a function of β is shown in Fig. A.8 where it is compared between simulation and experiment for particle safter track sorting. The agreement on the level of few percent is satisfactory. As Shower observable is not the strongest particle identification criterion, it does not bring significant contribution to the overall systematic uncertainty.
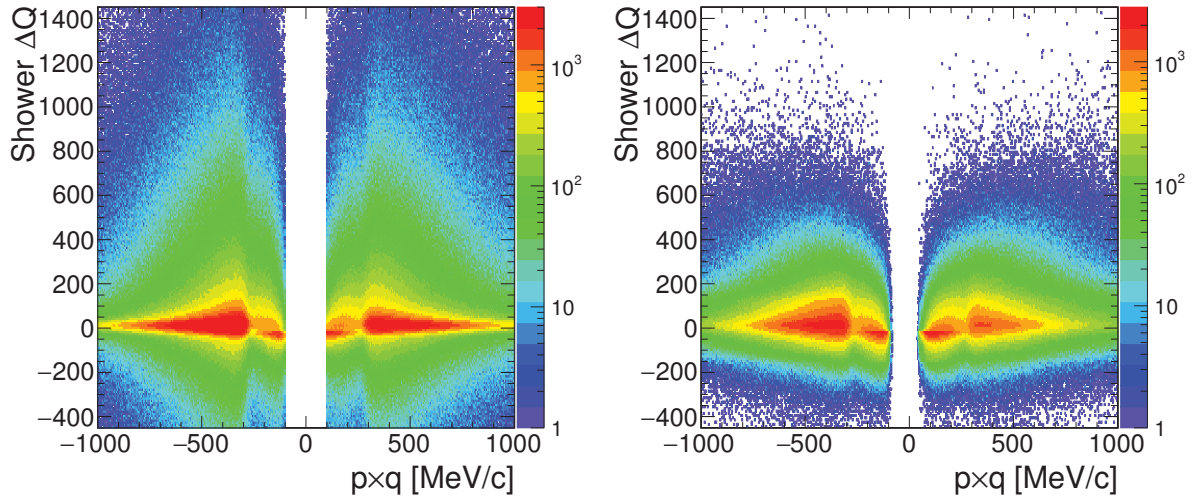
Figure A.7.: Comparison of ΔQ vs. momentum distribution in experiment (left) and simulation (right) for particles after track sorting.
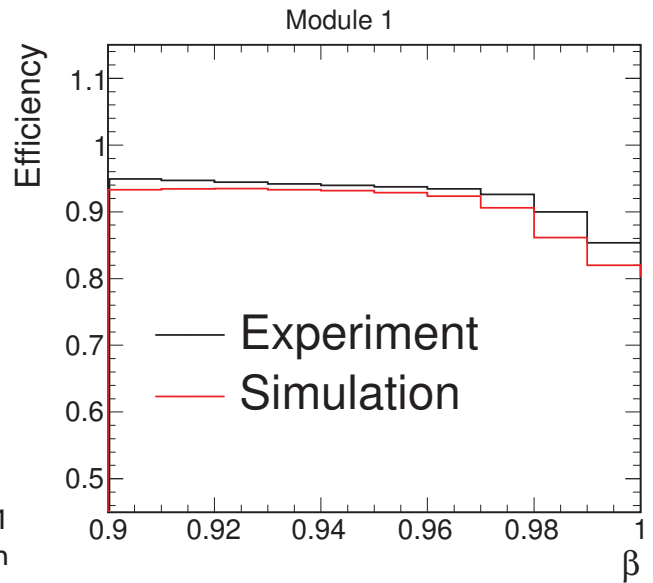
Figure A.8: Cross-check of the efficiency of module 1 (Post I) as a function of β in simulation and experiment.

Acknowledgments

In the first place I owe my deepest gratitude to my *Doktorvater* for providing me a possibility to join the HADES group in Kraków already during my Master studies and in the beginning of PhD and my *Doktormutter* Tetyana Galatyuk for allowing me to continue the PhD in the group at TU Darmstadt under the joint supervision agreement. Their guidance and discussions with them, sometimes quite lively but always deep and fruitful, enabled me to gain an understanding of what I am actually doing and, more importantly, why I am doing this. I am also very thankful for helping me to sort out all the formal and other issues that appeared during my studies.

I am indebted to "my post-doc", Gosia Gumberidze for helping me in tedious every-day details of my work. I would not go far without her continuously pointing out, that I must have a problem in some place of my analysis (also helping to solve the problems), that my plots are wrong (different ranges on the Y axis!) or that I have a typo in some PowerPoint slide. Of course my end would be even more miserable without lending me several household items and car trips to a supermarket. Also results on charged pion analysis, a crucially important input to my work, are coming from Gosia.

My deepest appreciation goes to HADES software coordinator Jochen Markert for taking care that we all can work smoothly and produce reliable results and for helping to solve the most difficult problems related to programming. To him and to other memebers of data reconstruction team, especially Vladimir and Olga Pechenov and Georgy Kornakov, special thanks go for providing all us excellent quality data, with which we could play.

I am very grateful to those who were involved in the discussions about data analysis, in particular to Joachim Stroth, Romain Holzmann, Wolfgang Koenig and Patrick Sellheim.

I also thank to the teams of HSD and coarse-graining. Their results are highly important in understanding and interpreting the experimental spectra, that I have plotted.

I would like to offer my special thanks to my colleagues from the TU Darmstadt group: Federico, Florian, Adrian and Frederic for awesome scientific discussions during our group meetings, for creating a unique team atmosphere and for the fact, that what happens in the Ratskeller stays in Ratskeller (or at least I hope so).

One should not forget all the colleagues from neighbor HADES groups in GSI and Frankfurt, who created a very friendly working environment: Christoph, Ilse, Jurek, Christian M., Manuel, Christian W., Christina, Erwin, Claudia (also for telling the η multiplicity), Heidi, Timo, Erik, Behruz (also for determining centrality selection) and all the others.

I want to thank also Witek and Jacek from Kraków for assisting me with bits of paper work, that I came across.

I am also very thankful to the whole HADES Collaboration for building the spectrometer and running the experiment, data from which I had a great pleasure to analyse. It is necessary to mention fantastic atmosphere of the Collaboration Meetings.

I thank the HGS-HIRe team for valuable support and organization of very interesting Lecture Weeks, Power Weeks and Soft-skill Courses as part of the Graduate Program. I spent a great time and have learned a lot. I thank also prof. dr. Bengt Friman for the time devoted to our PhD Committee meetings.

I want also to express my gratitude to the proofreaders of the thesis: Piotr, Tetyana, Gosia and Florian (who corrected the German version of the abstract) – you did a huge amount of work! If the manuscript has still some flaws, then it is only my fault.

I would like to thank my all my family, my parents and brothers for strong support and believing in me, especially my Mom for accepting the fact that her little baby decided to move abroad.

Bibliography

[1] **Particle Data Group** Collaboration, K. A. Olive *et al.*, "Review of Particle Physics," *Chin. Phys.* **C38** (2014) 090001.

[2] H. Satz, *Extreme States of Matter in Strong Interaction Physics*. Springer-Verlag Berlin Heidelberg, 2012.

[3] R. Barate et al., "Measurement of the axial-vector τ spectral functions and determination of $\alpha_s(M_\tau^2)$ from hadronic τ decays," *The European Physical Journal C - Particles and Fields* **4** no. 3, (1998) 409–431. http://dx.doi.org/10.1007/s100529800895.

[4] M. Davier, A. Höcker, B. Malaescu, C.-Z. Yuan, and Z. Zhang, "Update of the ALEPH non-strange spectral functions from hadronic τ decays," *Eur. Phys. J.* **C74** no. 3, (2014) 2803, arXiv:1312.1501 [hep-ex].

[5] S. Zschocke, B. Kampfer, O. Pavlenko, and G. Wolf, "Evaluation of QCD sum rules for HADES," 2002.

[6] W. Peters, M. Post, H. Lenske, S. Leupold, and U. Mosel, "The Spectral function of the rho meson in nuclear matter," *Nucl. Phys.* **A632** (1998) 109–127, arXiv:nucl-th/9708004 [nucl-th].

[7] B. Friman, C. Hohne, J. Knoll, S. Leupold, J. Randrup, R. Rapp, and P. S. (Eds.), *The CBM Physics Book*. Springer-Verlag Berlin Heidelberg, 2011.

[8] R. Rapp and J. Wambach, "Low-mass dileptons at the CERN-SpS: evidence for chiral restoration?," *Eur. Phys. J. A* **6** no. 4, (1999) 415–420. http://dx.doi.org/10.1007/s100500050364.

[9] V. L. Eletsky, M. Belkacem, P. J. Ellis, and J. I. Kapusta, "Properties of ρ and ω mesons at finite temperature and density as inferred from experiment," *Phys. Rev. C* **64** (Jul, 2001) 035202. http://link.aps.org/doi/10.1103/PhysRevC.64.035202.

[10] J. H. Hetherington and F. D. C. Willard, "Two-, Three-, and Four-Atom Exchange Effects in bcc ^{3}He," *Phys. Rev. Lett.* **35** (Nov, 1975) 1442–1444. http://link.aps.org/doi/10.1103/PhysRevLett.35.1442.

[11] K. Fukushima and T. Hatsuda, "The phase diagram of dense QCD," *Rept.Prog.Phys.* **74** (2011) 014001, arXiv:1005.4814 [hep-ph].

[12] K. Fukushima and C. Sasaki, "The phase diagram of nuclear and quark matter at high baryon density," *Prog. Part. Nucl. Phys.* **72** (2013) 99–154, arXiv:1301.6377 [hep-ph].

[13] P. de Forcrand and O. Philipsen, "The curvature of the critical surface (m(u,d),m(s))**crit(mu): A Progress report," *PoS* **LATTICE2008** (2008) 208, arXiv:0811.3858 [hep-lat].

[14] O. Philipsen and C. Pinke, "The $N_f = 2$ QCD chiral phase transition with Wilson fermions at zero and imaginary chemical potential," *Phys. Rev.* **D93** no. 11, (2016) 114507, arXiv:1602.06129 [hep-lat].

[15] **STAR** Collaboration, M. M. Aggarwal *et al.*, "An Experimental Exploration of the QCD Phase Diagram: The Search for the Critical Point and the Onset of De-confinement," 2010.

[16] A. Andronic, P. Braun-Munzinger, and J. Stachel, "Thermal hadron production in relativistic nuclear collisions: The Hadron mass spectrum, the horn, and the QCD phase transition," *Phys. Lett.* **B673** (2009) 142–145, `arXiv:0812.1186 [nucl-th]`. [Erratum: Phys. Lett.B678,516(2009)].

[17] J. Cleymans, H. Oeschler, K. Redlich, and S. Wheaton, "Comparison of chemical freeze-out criteria in heavy-ion collisions," *Phys. Rev. C* **73** (Mar, 2006) 034905. `http://link.aps.org/doi/10.1103/PhysRevC.73.034905`.

[18] J. Stachel, A. Andronic, P. Braun-Munzinger, and K. Redlich, "Confronting LHC data with the statistical hadronization model," *Journal of Physics: Conference Series* **509** no. 1, (2014) 012019. `http://stacks.iop.org/1742-6596/509/i=1/a=012019`.

[19] **HADES** Collaboration, G. Agakishiev *et al.*, "Statistical model analysis of hadron yields in proton-nucleus and heavy-ion collisions at SIS 18 energiesStatistical hadronization model analysis of hadron yields in p + Nb and Ar + KCl at SIS18 energies," *Eur. Phys. J.* **A52** no. 6, (2016) 178, `arXiv:1512.07070 [nucl-ex]`.

[20] **FOPI Collaboration** Collaboration, X. Lopez *et al.*, "Subthreshold production of $\Sigma(1385)$ baryons in Al+Al collisions at 1.9A GeV," *Phys. Rev. C* **76** (Nov, 2007) 052203. `http://link.aps.org/doi/10.1103/PhysRevC.76.052203`.

[21] **NA60** Collaboration, H. J. Specht, "Thermal Dileptons from Hot and Dense Strongly Interacting Matter," *AIP Conf. Proc.* **1322** (2010) 1–10, `arXiv:1011.0615 [nucl-ex]`.

[22] **CBM** Collaboration, S. Chattopadhyay *et al.*, "Challenges in QCD matter physics - The Compressed Baryonic Matter experiment at FAIR," `arXiv:1607.01487 [nucl-ex]`.

[23] **CERES Collaboration** Collaboration, G. Agakichiev *et al.*, "Enhanced Production of Low-Mass Electron Pairs in 200 GeV/Nucleon S-Au Collisions at the CERN Super Proton Synchrotron," *Phys. Rev. Lett.* **75** (Aug, 1995) 1272–1275. `http://link.aps.org/doi/10.1103/PhysRevLett.75.1272`.

[24] **CERES** Collaboration, A. Marin *et al.*, "Dilepton measurements with CERES," *PoS* **CPOD07** (2007) 034, `arXiv:0802.2679 [nucl-ex]`.

[25] J. Ruppert *et al.*, "Low Mass Dimuons Produced in Relativistic Nuclear Collisions," *Phys. Rev. Lett.* **100** (Apr, 2008) 162301. `http://link.aps.org/doi/10.1103/PhysRevLett.100.162301`.

[26] H. van Hees and R. Rapp, "Dilepton radiation at the CERN super-proton synchrotron," *Nuclear Physics A* **806** no. 1–4, (2008) 339 – 387. `http://www.sciencedirect.com/science/article/pii/S0375947408004144`.

[27] K. Dusling and I. Zahed, "Transverse momentum spectra of dileptons measured by the NA60 Collaboration in In+In collisions at 158 GeV/nucleon," *Phys. Rev.* **C80** (2009) 014902, `arXiv:hep-ph/0701253 [HEP-PH]`.

[28] **ALICE** Collaboration, D. Lohner, "Measurement of Direct-Photon Elliptic Flow in Pb-Pb Collisions at $\sqrt{s_{NN}} = 2.76$ TeV," *J.Phys.Conf.Ser.* **446** (2013) 012028, `arXiv:1212.3995 [hep-ex]`.

[29] **STAR** Collaboration, P. Huck, "Beam Energy Dependence of Dielectron Production in Au + Au Collisions from STAR at RHIC," *Nucl. Phys.* **A931** (2014) 659–664, `arXiv:1409.5675 [nucl-ex]`.

[30] **HADES** Collaboration, G. Agakishiev *et al.*, "Study of dielectron production in C+C collisions at 1-A-GeV," *Phys. Lett.* **B663** (2008) 43–48, `arXiv:0711.4281 [nucl-ex]`.

[31] **DLS** Collaboration, R. J. Porter *et al.*, "Dielectron cross-section measurements in nucleus-nucleus reactions at 1-A/GeV," *Phys. Rev. Lett.* **79** (1997) 1229–1232, `arXiv:nucl-ex/9703001` `[nucl-ex]`.

[32] **CBM** Collaboration, S. Chattopadhyay *et al.*, "Challenges in QCD matter physics - The Compressed Baryonic Matter experiment at FAIR," `arXiv:1607.01487 [nucl-ex]`.

[33] S. Tavernier, *Experimental Techniques in Nuclear and Particle Physics*. Springer-Verlag, Berlin Heidelberg, 2010.

[34] T. Filippas *et al.*, "Precision measurements of gas refractivity by means of a Fabry–Perot interferometer illustrated by the monitoring of radiator refractivity in the DELPHI RICH detectors," *Nuclear Instruments and Methods in Physics Research Section B: Beam Interactions with Materials and Atoms* **196** no. 3–4, (2002) 340 – 348. `http://www.sciencedirect.com/science/article/pii/S0168583X02012910`.

[35] "Rich Detector Principles." `http://physics.syr.edu/hep/rich.html`. Accessed: 2014-12-24.

[36] L. Fabbietti *et al.*, "Photon detection efficiency in the CsI based HADES RICH," *Nuclear Instruments and Methods in Physics Research Section A: Accelerators, Spectrometers, Detectors and Associated Equipment* **502** no. 1, (2003) 256 – 260. `http://www.sciencedirect.com/science/article/pii/S0168900203002845`. Experimental Techniques of Cherenkov Light Imaging. Proceedings of the Fourth International Workshop on Ring Imaging Cherenkov Detectors.

[37] **HADES Collaboration** Collaboration, G. Agakichiev *et al.*, "Dielectron Production in ^{12}C $+^{12}$C Collisions at 2A GeV with the HADES Spectrometer," *Phys. Rev. Lett.* **98** (2007) 052302.

[38] **HADES** Collaboration, G. Agakishiev *et al.*, "Dielectron production in Ar+KCl collisions at 1.76A GeV," *Phys. Rev.* **C84** (2011) 014902, `arXiv:1103.0876 [nucl-ex]`.

[39] **TAPS Collaboration** Collaboration, R. Averbeck *et al.*, "Production of π^0 and η mesons in carbon-induced relativistic heavy-ion collisions," *Zeitschrift für Physik A Hadrons and Nuclei* **359** no. 1, (1997) 65–73.

[40] **TAPS Collaboration** Collaboration, R. Holzmann *et al.*, "Contribution of π^0 and η Dalitz decays to the dilepton invariant-mass spectrum in 1A GeV heavy-ion collisions," *Phys. Rev. C* **56** (1997) R2920–R2923.

[41] C. Behnke, *Reconstruction of π^0 and η Mesons via Conversion in Au+Au at 1.23 Gev/u with the HADES Spectrometer*. PhD thesis, Goethe Universität Frankfurt, 2017.

[42] **E895 Collaboration** Collaboration, J. L. Klay *et al.*, "Charged pion production in 2A to 8A GeV central Au + Au Collisions," *Phys. Rev. C* **68** (2003) 054905.

[43] D. H. Perkins, *Introduction to high energy physics, 4th ed.* Press Syndicate of the University of Cambridge, 2000.

[44] B. Martin and G. Shaw, *Particle Physics, 2nd ed.* John Wiley & Sons, 1997.

[45] **ATLAS** Collaboration, G. Aad *et al.*, "Observation of a new particle in the search for the Standard Model Higgs boson with the ATLAS detector at the LHC," *Phys. Lett.* **B716** (2012) 1–29, `arXiv:1207.7214 [hep-ex]`.

[46] M. Maggiore, *A Modern Introduction to Quantum Field Theory*. Oxford University Press, 2005.

[47] **LHCb Collaboration** Collaboration, R. Aaij *et al.*, "Observation of $J/\psi p$ Resonances Consistent with Pentaquark States in $\Lambda_b^0 \to J/\psi K^- p$ Decays," *Phys. Rev. Lett.* **115** (Aug, 2015) 072001.

[48] M. E. Peskin and D. V. Schroeder, *An Introduction to Quantum Field Theory*. Westview Press, 1995.

[49] R. Hagedorn, "On the hadronic mass spectrum," *Nuovo Cim.* **A52** no. 4, (1967) 1336–1340. [,223(2016)].

[50] M. Gell-Mann, R. J. Oakes, and B. Renner, "Behavior of current divergences under SU(3) x SU(3)," *Phys. Rev.* **175** (1968) 2195–2199.

[51] S. Weinberg, "Precise Relations between the Spectra of Vector and Axial-Vector Mesons," *Phys. Rev. Lett.* **18** (Mar, 1967) 507–509. `http://link.aps.org/doi/10.1103/PhysRevLett.18.507`.

[52] T. Das, V. S. Mathur, and S. Okubo, "Low-Energy Theorem in the Radiative Decays of Charged Pions," *Phys. Rev. Lett.* **19** (Oct, 1967) 859–861. `http://link.aps.org/doi/10.1103/PhysRevLett.19.859`.

[53] **OPAL** Collaboration, K. Ackerstaff *et al.*, "Measurement of the strong coupling constant $\alpha(s)$ and the vector and axial vector spectral functions in hadronic τ decays," *Eur.Phys.J.* **C7** (1999) 571–593, `arXiv:hep-ex/9808019 [hep-ex]`.

[54] R. Rapp, J. Wambach, and H. van Hees, "The Chiral Restoration Transition of QCD and Low Mass Dileptons," *Landolt-Bornstein* **23** (2010) 134, `arXiv:0901.3289 [hep-ph]`.

[55] R. D. Pisarski, "Phenomenology of the Chiral Phase Transition," *Phys. Lett.* **B110** (1982) 155–158.

[56] G. E. Brown and M. Rho, "Scaling effective Lagrangians in a dense medium," *Phys. Rev. Lett.* **66** (May, 1991) 2720–2723. `http://link.aps.org/doi/10.1103/PhysRevLett.66.2720`.

[57] G. Brown and M. Rho, "Chiral restoration in hot and/or dense matter," *Physics Reports* **269** no. 6, (1996) 333 – 380. `http://www.sciencedirect.com/science/article/pii/0370157395000674`.

[58] C. Song, "Properties of vector mesons at finite temperature: Effective Lagrangian approach," *Phys. Rev. D* **53** (Apr, 1996) 3962–3966. `http://link.aps.org/doi/10.1103/PhysRevD.53.3962`.

[59] H. Gomm, O. Kaymakcalan, and J. Schechter, "Anomalous spin-1-meson decays from the gauged Wess-Zumino term," *Phys. Rev. D* **30** (Dec, 1984) 2345–2355. `http://link.aps.org/doi/10.1103/PhysRevD.30.2345`.

[60] **HADES** Collaboration, P. Salabura, J. Stroth, and L. Fabbietti, "The HADES Pion Beam Facility," *Nucl. Phys. News* **25** no. 2, (2015) 22.

[61] P. M. Hohler and R. Rapp, "Is ρ-Meson Melting Compatible with Chiral Restoration?," *Phys. Lett.* **B731** (2014) 103–109, `arXiv:1311.2921 [hep-ph]`.

[62] F.-L. V. *et al.*, "Crystalline and amorphous ices," in *Proceedings of the International School of Physics "Enrico Fermi" Course 187 "Water: Fundamentals as the Basis for Understanding the Environment and Promoting Technology"*, P. G. Debenedetti, M. A. Ricci, and F. Bruni, eds. IOS, Amsterdam, SIF, Bologna, 2015.

[63] P. Chomaz, "The Nuclear liquid gas phase transition and phase coexistence: A Review," 2004.

[64] A. Kurkela and A. Vuorinen, "Cool quark matter," *Phys. Rev. Lett.* **117** no. 4, (2016) 042501, `arXiv:1603.00750 [hep-ph]`.

[65] **STAR Collaboration** Collaboration, L. Adamczyk *et al.*, "Inclusive charged hadron elliptic flow in Au + Au collisions at $\sqrt{s_{NN}} = 7.7$–39 GeV," *Phys. Rev. C* **86** (Nov, 2012) 054908. `http://link.aps.org/doi/10.1103/PhysRevC.86.054908`.

[66] M. Bleicher *et al.*, "Relativistic hadron hadron collisions in the ultrarelativistic quantum molecular dynamics model," *J.Phys.* **G25** (1999) 1859–1896, `arXiv:hep-ph/9909407 [hep-ph]`.

[67] O. Buss *et al.*, "Transport-theoretical Description of Nuclear Reactions," *Phys.Rept.* **512** (2012) 1–124, `arXiv:1106.1344 [hep-ph]`.

[68] W. Ehehalt and W. Cassing, "Relativistic transport approach for nucleus-nucleus collisions from SIS to SPS energies," *Nuclear Physics A* **602** no. 3–4, (1996) 449 – 486. `http://www.sciencedirect.com/science/article/pii/0375947496000978`.

[69] P. Romatschke and U. Romatschke, "Viscosity Information from Relativistic Nuclear Collisions: How Perfect is the Fluid Observed at RHIC?," *Phys. Rev. Lett.* **99** (Oct, 2007) 172301. `http://link.aps.org/doi/10.1103/PhysRevLett.99.172301`.

[70] C. Nonaka and S. A. Bass, "Space-time evolution of bulk QCD matter," *Phys. Rev. C* **75** (Jan, 2007) 014902. `http://link.aps.org/doi/10.1103/PhysRevC.75.014902`.

[71] J. Auvinen and H. Petersen, "Evolution of elliptic and triangular flow as a function of $\sqrt{s_{NN}}$ in a hybrid model," *Phys. Rev.* **C88** no. 6, (2013) 064908, `arXiv:1310.1764 [nucl-th]`.

[72] M. Bleicher, S. Endres, J. Steinheimer, and H. van Hees, "Recent results from the UrQMD hybrid model for heavy ion collisions," in *International Workshop on Collectivity in Relativistic Heavy Ion Collisions (IWoC 2014) Kolymbari, Crete, Greece, September 14-20, 2014.* 2015. `arXiv:1503.07371 [nucl-th]`. `http://inspirehep.net/record/1355583/files/arXiv:1503.07371.pdf`.

[73] **ALICE** Collaboration, B. B. Abelev *et al.*, "Elliptic flow of identified hadrons in Pb-Pb collisions at $\sqrt{s_{NN}} = 2.76$ TeV," *JHEP* **06** (2015) 190, `arXiv:1405.4632 [nucl-ex]`.

[74] J. Cleymans, H. Oeschler, and K. Redlich, "Influence of impact parameter on thermal description of relativistic heavy ion collisions at (1-2) A-GeV," *Phys.Rev.* **C59** (1999) 1663, `arXiv:nucl-th/9809027 [nucl-th]`.

[75] F. Becattini, J. Manninen, and M. Gazdzicki, "Energy and system size dependence of chemical freeze-out in relativistic nuclear collisions," *Phys.Rev.* **C73** (2006) 044905, `arXiv:hep-ph/0511092 [hep-ph]`.

[76] A. Andronic, P. Braun-Munzinger, and J. Stachel, "Thermal hadron production in relativistic nuclear collisions: The Hadron mass spectrum, the horn, and the QCD phase transition," *Phys.Lett.* **B673** (2009) 142–145, `arXiv:0812.1186 [nucl-th]`.

[77] R. Rapp and J. Wambach, "Chiral symmetry restoration and dileptons in relativistic heavy ion collisions," *Adv. Nucl. Phys.* **25** (2000) 1, `arXiv:hep-ph/9909229 [hep-ph]`.

[78] **NA60** Collaboration, R. Arnaldi *et al.*, "First measurement of the rho spectral function in high-energy nuclear collisions," *Phys. Rev. Lett.* **96** (2006) 162302, `arXiv:nucl-ex/0605007 [nucl-ex]`.

[79] **PHENIX** Collaboration, A. Adare *et al.*, "Enhanced production of direct photons in Au+Au collisions at $\sqrt{s_{NN}} = 200$ GeV and implications for the initial temperature," *Phys. Rev. Lett.* **104** (2010) 132301, arXiv:0804.4168 [nucl-ex].

[80] **PHENIX** Collaboration, A. Adare *et al.*, "Azimuthally anisotropic emission of low-momentum direct photons in Au+Au collisions at $\sqrt{s_{NN}} = 200$ GeV," *Phys. Rev.* **C94** no. 6, (2016) 064901, arXiv:1509.07758 [nucl-ex].

[81] H. van Hees, C. Gale, and R. Rapp, "Thermal photons and collective flow at energies available at the BNL Relativistic Heavy-Ion Collider," *Phys. Rev. C* **84** (Nov, 2011) 054906. http://link.aps.org/doi/10.1103/PhysRevC.84.054906.

[82] H. van Hees, M. He, and R. Rapp, "Pseudo-critical enhancement of thermal photons in relativistic heavy-ion collisions?," *Nucl. Phys.* **A933** (2015) 256–271, arXiv:1404.2846 [nucl-th].

[83] **HADES** Collaboration, G. Agakishiev *et al.*, "Origin of the low-mass electron pair excess in light nucleus-nucleus collisions," *Phys. Lett.* **B690** (2010) 118–122, arXiv:0910.5875 [nucl-ex].

[84] R. Averbeck, R. Holzmann, V. Metag, and R. S. Simon, "Neutral pions and η mesons as probes of the hadronic fireball in nucleus-nucleus collisions around 1A GeV," *Phys. Rev. C* **67** (Feb, 2003) 024903. http://link.aps.org/doi/10.1103/PhysRevC.67.024903.

[85] R. Scheibl and U. W. Heinz, "Coalescence and flow in ultrarelativistic heavy ion collisions," *Phys. Rev.* **C59** (1999) 1585–1602, arXiv:nucl-th/9809092 [nucl-th].

[86] U. W. Heinz, "Concepts of heavy ion physics," in *2002 European School of high-energy physics, Pylos, Greece, 25 Aug-7 Sep 2002: Proceedings*, pp. 165–238. 2004. arXiv:hep-ph/0407360 [hep-ph]. http://doc.cern.ch/yellowrep/CERN-2004-001.

[87] S. Endres, H. van Hees, J. Weil, and M. Bleicher, "Dilepton production and reaction dynamics in heavy-ion collisions at SIS energies from coarse-grained transport simulations," *Phys. Rev. C* **92** (Jul, 2015) 014911.

[88] F. Seck, "Towards realistic event generator for in-medium signals," Master's thesis, Technische Universität Darmstadt, 2015.

[89] T. Galatyuk, P. M. Hohler, R. Rapp, F. Seck, and J. Stroth, "Thermal Dileptons from Coarse-Grained Transport as Fireball Probes at SIS Energies," *Eur. Phys. J.* **A52** no. 5, (2016) 131, arXiv:1512.08688 [nucl-th].

[90] G. Agakishiev *et al.*, "Statistical hadronization model analysis of hadron yields in p + Nb and Ar + KCl at SIS18 energies," *The European Physical Journal A* **52** no. 6, (2016) 178. http://dx.doi.org/10.1140/epja/i2016-16178-x.

[91] **HADES** Collaboration, *Proposal for a High-Acceptance Di-Electron Spectrometer*. GSI, 1994.

[92] G. Agakichiev *et al.*, "The high-acceptance dielectron spectrometer HADES," *The European Physical Journal A* **41** no. 2, (2009) 243–277. http://dx.doi.org/10.1140/epja/i2009-10807-5.

[93] J. D. Jackson, *Classical Electrodynamics 3rd ed.* John Wiley & Sons Inc., New York, 1999.

[94] M. Artuso *et al.*, "The CLEO RICH detector," *Nuclear Instruments and Methods in Physics Research Section A: Accelerators, Spectrometers, Detectors and Associated Equipment* **554** no. 1–3, (2005) 147 – 194. http://www.sciencedirect.com/science/article/pii/S016890020501524X.

[95] C. Matteuzzi, "The LHCb RICH system: Detector performance," *Nuclear Instruments and Methods in Physics Research Section A: Accelerators, Spectrometers, Detectors and Associated Equipment* **766** no. 0, (2014) 245 – 249. http://www.sciencedirect.com/science/article/pii/S0168900214004896. RICH2013 Proceedings of the Eighth International Workshop on Ring Imaging Cherenkov Detectors Shonan, Kanagawa, Japan, December 2-6, 2013.

[96] G. Kornakov, "Time of Flight calibration and reaction time determination," 2014. Talk in the HADES Collaboration Meeting XXVIII, Bratislava, Slovakia.

[97] D. Belver *et al.*, "The HADES RPC inner TOF wall," *Nuclear Instruments and Methods in Physics Research Section A: Accelerators, Spectrometers, Detectors and Associated Equipment* **602** no. 3, (2009) 687 – 690. http://www.sciencedirect.com/science/article/pii/S0168900208019633. Proceedings of the 9th International Workshop on Resistive Plate Chambers and Related Detectors RPC08.

[98] A. Blanco *et al.*, "{RPC HADES-TOF} wall cosmic ray test performance," *Nuclear Instruments and Methods in Physics Research Section A: Accelerators, Spectrometers, Detectors and Associated Equipment* **661, Supplement 1** (2012) S114 – S117. X. Workshop on Resistive Plate Chambers and Related Detectors (RPC 2010).

[99] G. Kornakov *et al.*, "Time of flight measurement in heavy-ion collisions with the HADES RPC TOF wall," *Journal of Instrumentation* **9** no. 11, (2014) C11015. http://stacks.iop.org/1748-0221/9/i=11/a=C11015.

[100] W. Koenig and J. Pietraszko, "Beam detectors in Au+Au run," 2012. Talk in the HADES Collaboration Meeting XXIV, Cracow, Poland.

[101] J. Pietraszko *et al.*, "Radiation damage in single crystal CVD diamond material investigated with a high current relativistic 197Au beam," *Nuclear Instruments and Methods in Physics Research Section A: Accelerators, Spectrometers, Detectors and Associated Equipment* **763** no. 0, (2014) 1 – 5. http://www.sciencedirect.com/science/article/pii/S0168900214007013.

[102] J. Michel *et al.*, "The HADES DAQ System: Trigger and Readout Board Network," *Nuclear Science, IEEE Transactions on* **58** no. 4, (2011) 1745–1750.

[103] J. Markert, "Software and DST status," 10, 2015. Talk on the XXX Hades Collaboration Meeting, Estoril, Portugal.

[104] P. Sellheim, *Reconstruction of the low-mass dielectron signal in 1.23A GeV Au+Au collisions*. PhD thesis, Goethe Universität Frankfurt, 2017.

[105] B. Kardan, *Centrality Determination at* 1.23*A GeV Gold-Gold Collisions and Readout-Electronics for the HADES Electromagnetic Calorimeter*. PhD thesis, Goethe Universität Frankfurt, 2015.

[106] C. Ungethüm, "Searching for the Dark Photon," Master's thesis, Technische Universität Darmstadt, 2015.

[107] O. Pechenov and V. Pechenov, "News from Tracking in Low and High Multiplicities," 10, 2014. Talk on the XXVIII Hades Collaboration Meeting, Bratislava, Slovakia.

[108] A. Hoecker *et al.*, "TMVA: Toolkit for Multivariate Data Analysis," *PoS* **ACAT** (2007) 040, arXiv:physics/0703039.

[109] L. Fabietti, *Study of the e^+e^- pair acceptance in the dilepton spectrometer HADES*. PhD thesis, Technische Universität München, 2003.

[110] I. Frohlich *et al.*, "Pluto: A Monte Carlo Simulation Tool for Hadronic Physics," *PoS* **ACAT2007** (2007) 076, `arXiv:0708.2382 [nucl-ex]`.

[111] T. Kunz, "Photon Signal Response of the RICH Detector," 2014. Talk in the HADES Collaboration Meeting XXVII, Munich, Germany.

[112] P. Huck, "Suche nach einem seltenen Zerfall des η-Mesons in pp-Reaktionen bei $E_{kin} = 3.5$ GeV," Master's thesis, Technische Universität München, 2009.

[113] E. L. Bratkovskaya *et al.*, "System size and energy dependence of dilepton production in heavy-ion collisions at 1-2 GeV/nucleon energies," *Phys. Rev.* **C87** (2013) 064907.

[114] S. Constantinescu, S. Dita, and D. Jouan, "Study of the estimation of the combinatorial muon pair background," 1996. Report PNO–DER–96–01.

[115] M. Gazdzicki and M. I. Gorenstein, "Background subtraction from the dilepton spectra in nuclear collisions," `arXiv:hep-ph/0003319 [hep-ph]`.

[116] M. Abreu et al., "Dimuon and charm production in nucleus-nucleus collisions at the CERN-SPS," *The European Physical Journal C - Particles and Fields* **14** no. 3, (2000) 443–455. `http://dx.doi.org/10.1007/s100520000373`.

[117] **PHENIX Collaboration** Collaboration, A. Adare *et al.*, "Detailed measurement of the e^+e^- pair continuum in $p + p$ and Au + Au collisions at $\sqrt{s_{NN}} = 200$ GeV and implications for direct photon production," *Phys. Rev. C* **81** (Mar, 2010) 034911. `http://link.aps.org/doi/10.1103/PhysRevC.81.034911`.

[118] A. Toia, *Performance of the HADES Spectrometer for Dilepton Identification in the Reaction C+C at 1-2 AGeV*. PhD thesis, Justus-Liebig-Universität Giessen, 2004.

[119] **STAR** Collaboration, L. Adamczyk *et al.*, "Measurements of Dielectron Production in Au+Au Collisions at $\sqrt{s_{NN}} = 200$ GeV from the STAR Experiment," *Phys. Rev.* **C92** no. 2, (2015) 024912, `arXiv:1504.01317 [hep-ex]`.

[120] **ALICE** Collaboration, M. K. Köhler, "Dielectron measurements in pp, p-Pb and Pb-Pb collisions with ALICE at the LHC," *Nucl. Phys.* **A931** (2014) 665–669, `arXiv:1407.7809 [nucl-ex]`.

[121] M. K. Köhler, *Dielectron production in proton-proton collisions with ALICE*. PhD thesis, Technische Universität Darmstadt, 2014.

[122] H. Schuldes, *Charged Kaon and ϕ Reconstruction in Au+Au Collisions at 1.23 AGeV*. PhD thesis, Goethe Universität Frankfurt, 2016.

[123] A. V. Anisovich, R. Beck, E. Klempt, V. A. Nikonov, A. V. Sarantsev, and U. Thoma, "Properties of baryon resonances from a multichannel partial wave analysis," *Eur. Phys. J.* **A48** (2012) 15, `arXiv:1112.4937 [hep-ph]`.

[124] S. Harabasz, "Procedury kalibracji i wizualizacji danych detektora kaskady elektromagnetycznej w zderzeniach ciezkich jonow," Master's thesis, Jagiellonian University, Cracow, 2011.

[125] A. Snoch, "Calibration of Pre-Shower detector gain for HADES," 2015. HGS-HIRe Summer Student Program at GSI – Book of Reports.

Curriculum vitae

Szymon Harabasz
e-mail: s.harabasz@gsi.de

Education

2011 - 2017
Doctoral studies in Physics under a joint supervision agreement between Jagiellonian University in Cracow and Technische Universität Darmstadt

2011
Master of Science in Physics
Jagiellonian University in Cracow

2005
Maturity exam
I Liceum Ogólnokształcące im. Bartłomieja Nowodworskiego w Krakowie

Additional experience

July - August 2009
Participation in the *GSI Summer Student Programm* in Darmstadt, Germany

July 2012
HGS-HIRe soft-skills course I *Making an Impact as an Effective Researcher*

June 2013
HGS-HIRe soft-skills course II *Leading Teams in a Research Environment*

April 2013 - July 2015
Participation in tutoring the Physics Lab Course for the Advanced in the Institute of Nuclear Physics of the Technical University Darmstadt

Major international scientific conference contributions

September 2013
Fairness 2013 Workshop for young scientists with research interests focused on physics at FAIR, Berlin, Germany
Talk title: *Electron identification in Au+Au collisions at 1.23 GeV/u using multivariate analysis*

May 2014
Quarm Matter 2014, Darmstadt, Germany
Poster title: *Di-electron reconstruction in Au+Au@1.23 GeV/u*

June 2016
Critical Point and Onset of Deconfinement 2016, Wrocław, Poland
Talk title: *Measurement of virtual photons radiated from Au+Au collisions at $E_{beam} = 1.23A$ GeV with HADES*

Awards

October 2016
Giersch Excellence Award

Personal interests

- Computing, programming languages and technologies

- Culture tourism

- Poland's and world history